UNCLASSIFIED

AD NUMBER

AD819299

NEW LIMITATION CHANGE

TO

Approved for public release, distribution unlimited

FROM

Distribution authorized to U.S. Gov't. agencies and their contractors; Administrative/Operational Use; Aug 1967. Other requests shall be referred to Air Force Rocket Propulsion Laboratory, Attn: RPPR-STINFO, Edwards AFB, CA 93523.

AUTHORITY

AFRPL ltr, 27 Oct 1971

THIS PAGE IS UNCLASSIFIED

Best Available Copy

AFRPL-TR-67-211- VOL I

AD819299

# PROJECT SOPHY - SOLID PROPELLANT HAZARDS PROGRAM

R. B. Elwell
O. R. Irwin
R. W. Vail, Jr.
Aerojet-General Corporation

TECHNICAL REPORT AFRPL-TR-67-211 - VOL I

August 1967

"This document is subject to special export controls and each transmittal to foreign governments or foreign nationals may be made only with prior approval of AFRPL (RPPR-STINFO), Edwards, California 93523."

Air Force Rocket Propulsion Laboratory
Research and Technology Division
Edwards Air Force Base, California
Air Force Systems Command, United States Air Force

Best Available Copy

## NOTICES

"When U. S. Government drawings, specifications, or other data are used for any purpose other than a definitely related Government procurement operation, the Government thereby incurs no responsibility nor any obligation whatsoever, and the fact that the Government may have formulated, furnished or in any way supplied the said drawings, specifications, or other data, is not to be regarded by implication or otherwise, as in any manner licensing the holder or any other person or corporation, or conveying any rights or permission to manufacture, use, or sell any patented invention that may in any way be related thereto."

# PROJECT SOPHY - SOLID PROPELLANT HAZARDS PROGRAM

R. B. Elwell
O. R. Irwin
R. W. Vail, Jr.

"This document is subject to special export controls and each transmittal to foreign governments or foreign nationals may be made only with prior approval of AFRPL (RPPR-STINFO), Edwards, California 93523."

## FOREWORD

This final report, submitted in two volumes, was prepared by Aerojet-General Corporation, Downey, California, on Air Force Contract AF04(611)-10919, which supports the USAF Solid Propellant Hazards Study Program (Project SOPHY), Project No. 63A00201.

This report was submitted to the Procuring Contracting Officer on 16 June 1967, and covers the period beginning 1 September 1965 through 17 May 1967. The contractor's report number is 0977-01(01)FP. The AFRPL Project Officers were Maj. Bryan A. Giesler, until March 1966, and Capt. Norman H. Valor, for the remainder of the contract. The Aerojet-General Corporation Program Managers were Mr. Glenn L. Roark, until April 1966, and Mr. Robert B. Elwell, for the remainder of the contract. The principal investigators were R. B. Elwell, Dr. O. R. Irwin, Dr. M. Nishibayashi, P. K. Salzman, and R. W. Vail, Jr.

The authors express their gratitude to these persons who made significant contributions to the execution of this program: R. B. Coley, Project Engineer; B. L. Cooper and A. F. Van Ryckeghen, Test Engineers; D. G. Frutchey, J. T. Knight, R. S. Precht, and C. R. Woods, Data Reduction; F. J. Adams, Liaison; C. K. Mattson, Cost Accounting; W. L. Mattson, Propellant Production; F. A. Hettinger and W. L. McGurk, Synthesis and Analysis of Propellant with Defects; and R. F. Chaiken, Consultant. The suggestions and assistance received from Maj. Giesler and Capt. Valor, of the Air Force Rocket Propulsion Laboratory, are also gratefully acknowledged.

This technical report has been reviewed and is approved.

Norman H. Valor
Captain, USAF
Project Officer, Solid Propellant Hazards Study Program
Solid Rocket Division
Air Force Rocket Propulsion Laboratory

## ABSTRACT

The critical diameter of a typical composite propellant was determined to be between 60 and 72 in. The selection of test sample sizes was facilitated by the detonation model developed during the solid propellant hazards program, under Contracts AF04(611)9945 and AF04(611)10919. The final form of the critical geometry relationship states that for any shape other than the right solid circular cylinder, four times the cross sectional area of the critical sample, divided by its total perimeter, equals 92% of the critical diameter. The minimum shock pressure required to initiate detonation of composite propellant is estimated to be 25 to 30 kbar for a critical size sample, and 8 to 10 kbar for an ideal diameter sample. A study of the effect of pulse width on the minimum initiating shock pressure for 4-in. diameter samples of an adulterated propellant showed that with a 2 mm pulse the minimum pressure is between 50 and 64 kbar, and that the minimum pressures approach a lower limit of 26 to 32 kbar as the pulse width increases. New techniques were developed to prepare and characterize porous and cracked propellant samples. Correlations of the blast and fireball data from 22 propellant tests have been made. The average TNT equivalence of the peak overpressure data is 197%. The average TNT equivalence of the positive-phase impulse data is 138%, for those samples that detonated.

[illegible]

TABLE OF CONTENTS


| | | Page No. |
|---|---|---|
| I. | INTRODUCTION | 1 |
| | The Overall SOPHY Program | 2 |
| | SOPHY I Program Summary | 6 |
| | Specific Objectives, SOPHY II | 8 |
| II. | SUMMARY | 11 |
| III. | DETONATION MODEL | 15 |
| | Introduction | 15 |
| | Estimation of Coefficients | 15 |
| | Generalization of Detonation Model | 24 |
| | Use of Jones' Expression | 30 |
| IV. | LARGE CRITICAL DIAMETER TESTS | 57 |
| | Selection of Sample Sizes | 57 |
| | Test Site | 58 |
| | Test CD-96 (72-in. Diameter) | 58 |
| | Test CD-98 (60-in. Diameter) | 76 |
| | Conclusions | 88 |
| V. | THE CRITICAL GEOMETRY FOR SUSTAINMENT OF DETONATION | 91 |
| | Background | 91 |
| | Technical Approach | 92 |
| | Test Results | 96 |
| | Conclusions | 116 |
| VI. | EVALUATION OF THE CRITICAL GEOMETRY THEORY FOR SUSTAINMENT OF DETONATION | 121 |
| | Technical Approach | 121 |
| | Test Results | 122 |
| | Conclusions | 134 |
| VII. | INITIATION CRITERION THEORY | 137 |
| | Introduction | 137 |
| | Initiation Criteria Determinations | 138 |
| | Evaluation of the Initiation Criterion for AAB-3139 | 154 |
| | Initiation Pressure vs Pulse Width | 173 |
| | Predicted Initiation Criterion for Unadulterated Propellant | 183 |
| | Conclusions | 188 |

TABLE OF CONTENTS (Concluded)


| | | Page No. |
|---|---|---|
| VIII. | SYNTHESIS OF DEFECTIVE PROPELLANT..... | 193 |
| | Introduction..... | 193 |
| | Production of Propellant with Unconnected Pores ..... | 193 |
| | Production of Connected Voids..... | 210 |
| IX. | CHARACTERIZATION OF DEFECTIVE PROPELLANT..... | 211 |
| | Pore Volume Measurement..... | 211 |
| | Pore Diameter Distribution..... | 211 |
| | Measurement of Surface Area..... | 212 |
| | Conclusions..... | 216 |
| X. | REPORTED MISHAPS OF SOLID MOTORS..... | 219 |
| XI. | BLAST AND REFALL CORRELATION..... | 223 |
| | Airblast Data..... | 223 |
| | Analysis of Fireball Data..... | 228 |
| | Conclusions..... | 241 |
| XXI. | CONCLUSIONS AND RECOMMENDATIONS..... | 247 |
| | Suscainment of Detonation..... | 247 |
| | Initiation of Detonation..... | 248 |
| | Propellant with Defects..... | 250 |
| | Blast and Fireball..... | 250 |
| | REFERENCES..... | 251 |

## LIST OF ILLUSTRATIONS


| Figure No. | | Page No. |
|---|---|---|
| 1. | Operational Hazards of Large Solid Motors..... | 3 |
| 2. | Detonation Model for ANB-3226 Propellant Adulterated with RDX..... | 23 |
| 3. | Generalized Model for Hot-Spot Initiation of AP Propellant..... | 25 |
| 4. | Correlation Between Probe Position in Reaction Zone and Oscillograph Pulse Shape..... | 44 |
| 5. | Mapping of Conductance-Zone Profile, 4-in. Diameter Sample..... | 45 |
| 6. | Blast Instrumentation Legs, AFRPL 1-36D Facility..... | 59 |
| 7. | Critical-Diameter Test Setup for 72-in.-Diameter Sample..... | 62 |
| 8. | 72-in. Critical-Diameter Test Setup, CD-96.... | 63 |
| 9. | Test CD-96 (Frames 0 to 5): Camera Speed 6 fps..... | 66 |
| 10. | Test CD-96 (Frames 7 to 21, selected): Camera Speed 6 fps..... | 67 |
| 11. | Fragments of Aluminum Sheet from Test CD-96... | 68 |
| 12. | Crater, Test CD-96..... | 69 |
| 13. | Detonation Velocity vs Distance Along Charge, CD-96..... | 71 |
| 14. | Peak Side-On Overpressures, CD-96..... | 72 |
| 15. | CD-96 Fireball Growth..... | 74 |
| 16. | CD-96 Fireball History..... | 75 |
| 17. | Test CD-98 (Frames 0 to 5): Camera Speed 6 fps..... | 78 |
| 18. | Test CD-98 (Frames 7 to 17, selected): Camera Speed 6 fps..... | 79 |
| 19. | Detonation Velocity vs Distance, CD-98..... | 80 |
| 20. | Peak Side-On Overpressures, CD-98..... | 81 |
| 21. | CD-98 Fireball Growth..... | 84 |
| 22. | CD-98 Fireball History..... | 85 |
| 23. | Shock Attenuation in Plexiglas..... | 87 |
| 24. | 72-in. and 60-in. Test Data Compared with Data from Plexiglas and AP-PBAN Propellant.... | 89 |
| 25. | Critical Diameter Results, Batch 4EH-85..... | 97 |
| 26. | Critical Diameter Results, Batch 4EH-86..... | 99 |
| 27. | Combined Results: SOPHY I and SOPHY II, AAB-3189..... | 101 |
| 28. | 95% Joint Confidence Ellipses for $\mu$ and $\sigma$, AAB-3189..... | 102 |
| 29. | Critical-Geometry Results (Square Columns).... | 106 |
| 30. | Critical-Geometry Results (Equilateral Triangles)..... | 108 |

LIST OF ILLUSTRATIONS (Continued)


| Figure No. | | Page No. |
|---|---|---|
| 31. | Critical-Geometry Results (1.75-in.-Thick Rectangles) | 110 |
| 32. | Hollow-Core Cylindrical Charge Undergoing Abortment of Steady-State Detonation | 111 |
| 33. | Test Results for 1.5-in. ID Hollow Cylinders | 114 |
| 34. | Test Results for 3.0-in. ID Hollow Cylinders | 115 |
| 35. | Test Results for Cross-Core Cylinders ($\ell$ = 0.5 in.) | 117 |
| 36. | Test Results for Cross-Core Cylinders ($\ell$ = 1.0 in.) | 118 |
| 37. | Average Detonation Velocity vs Reduced Size, AAB-3189 | 120 |
| 38. | Critical Diameter Results, Batch 4EH-44 | 124 |
| 39. | Sectioning Plan for Microscopic Analysis | 126 |
| 40. | Photomicrograph of AAB-3225 Propellant, Batch 4EH-44 (Specimen 6A) | 127 |
| 41. | Photomicrograph of AAB-3225 Propellant, Batch 4EH-44 (Specimen 2R) | 128 |
| 42. | Shock Pressure Attenuation in PMMA, Using TNT Boosters ($P_o$ = 118 kbar) | 141 |
| 43. | Shock Pressure Attenuation in PMMA -- Various Donors | 142 |
| 44. | Normalized Shock-Pressure Attenuation Curves for Plexiglas and Lucite | 144 |
| 45. | Shock-Pressure Attenuation in PMMA | 145 |
| 46. | 42-in. Diameter Card-Gap Setup | 153 |
| 47. | Initiation Criterion for AAB-3189 | 158 |
| 48. | Initiation Criterion for AAB-3225 | 159 |
| 49. | Initiation Criterion for AAB-3267 | 160 |
| 50. | Normalized Initiation Criteria | 161 |
| 51. | Evaluation of Initiation Criterion with Unattenuated Booster Shock Wave | 165 |
| 52. | Evaluation of Initiation Criterion with Attenuated Booster Shock Wave | 167 |
| 53. | Evaluation of Initiation Criterion, Miscellaneous Tests | 168 |
| 54. | Evaluation of Initiation Criterion, Rectangular Acceptor | 172 |
| 55. | Pressure in PBAN Propellant as a Function of Flyer Plate Velocity | 175 |
| 56. | Pulse Width of Shock Wave in PBAN Propellant | 176 |
| 57. | Experimental Test Configuration | 178 |
| 58. | Test Setup Using Flash X-Ray | 179 |

LIST OF ILLUSTRATIONS (Concluded)


| Figure No. | | Page No. |
|---|---|---|
| 59. | Effect of Pulse Width on Minimum Initiating Shock Pressure | 181 |
| 60. | Effect of Pulse Width (mm) on Minimum Initiating Shock Pressure | 182 |
| 61. | Axial-Resistance Probe | 186 |
| 62. | Minimum Initial Pressure-Area Requirements for Shock Initiation of Detonation in AAB-3189 | 190 |
| 63. | The Effect of Temperature on the Viscosity of ANB-3226 Binder | 197 |
| 64. | Distributions of Pore Diameters | 203 |
| 65. | The Effect of Vacuum Level During Casting on Pore Formation | 207 |
| 66. | The Effect of Pressure Cure on ANB-3226 Propellant Containing Micropores | 209 |
| 67. | Distributions of Pore Diameters in ANB-3226 Propellant Cured Under Pressure | 213 |
| 68. | Apparatus for Surface Area Determination | 214 |
| 69. | Inclined-Tube Pressure Gauge | 215 |
| 70. | Peak Overpressure vs Scaled Distance. TNT and RDX-Adulterated PBAN Propellants | 225 |
| 71. | Comparison of TNT Impulse with Best Fit of the Pooled Propellant Data | 227 |
| 72. | Comparison of TNT Impulse with Best Fits of Propellant Go and No Go Data | 229 |
| 73. | Maximum Height of Fireball | 233 |
| 74. | Maximum Diameter of Fireball | 234 |
| 75. | Time to Maximum Height | 235 |
| 76. | Time to Maximum Diameter | 236 |
| 77. | Total Fireball Duration | 237 |
| 78. | Fireball Size History (Measured vs Predicted), Test CD-98 | 241 |

## LIST OF TABLES


| Table No. | | Page No. |
|---|---|---|
| I. | Frequency Distribution of Zero-Percent RDX Critical-Diameter Estimates for Solutions Satisfying all Ranges..... | 18 |
| II. | Results of Least-Squares Fits to Critical-Diameter Data..... | 19 |
| III. | Least-Squares Fit to Critical-Diameter Data..... | 20 |
| IV. | Best Least-Squares Fit to Critical-Diameter Data..... | 22 |
| V. | Computed Detonation Parameters for PETN at $\rho_o$ = 1.7800 g/cm$^3$..... | 32 |
| VI. | RUBY Calculations for Ammonium Perchlorate.. | 34 |
| VII. | Covolumes Used in RUBY Code Calculations for AP Detonation..... | 35 |
| VIII. | RUBY Calculations for RDX-Wax..... | 37 |
| IX. | Covolumes Used in RUBY Code Calculations.... | 38 |
| X. | RUBY Calculations for Propellant..... | 39 |
| XI. | RUBY Calculations for RDX/Aluminum (80% RDX, 20% Al; $\rho_o$ = 1.94 g/cc)..... | 41 |
| XII. | Average Detonation Velocities for Super-critical 9.2% RDX Adulterated Samples..... | 47 |
| XIII. | Conductance-Probe Measurements..... | 48 |
| XIV. | Average Detonation Velocity and Conductance-Zone Length..... | 49 |
| XV. | Correlation of Detonation Model in the Nonideal Region for AAB-3189 Propellant (f = 0.092)..... | 53 |
| XVI. | Estimates of $K_1^*$, $K_2^*$, $C_1^*$, $C_2^*$, $g_c(f)$, $k_1$, and $k_2$..... | 55 |
| XVII. | Observed and Calculated Side-On Overpressure and TNT Equivalences in the 72-in. and the 60-in. Critical Diameter Tests..... | 82 |
| XVIII. | Comparison of Critical-Diameter Estimates, AAB-3189..... | 100 |
| XIX. | Batch-Control Tests, AAB-3189..... | 104 |
| XX. | Critical and Pseudocritical Geometries for Various Shapes, AAB-3189..... | 116 |
| XXI. | Critical Diameter Results, Batch 4EH-44..... | 123 |
| XXII. | Critical-Diameter Results, Batch 4EH-84..... | 129 |
| XXIII. | Critical-Diameter Results, Batch 4EH-107.... | 131 |
| XXIV. | Comparison of Critical-Diameter Estimates for AAB-3225..... | 132 |
| XXV. | Verification-Test Results, Using AAB-3225 Propellant..... | 135 |

LIST OF TABLES (Concluded)


| Table No. | | Page No. |
|---|---|---|
| XXVI. | Attenuation of Shock from TNT Booster by Stacked Squares of Plexiglas..... | 140 |
| XXVII. | Hugoniot Computations for AAB-3189..... | 148 |
| XXVIII. | Hugoniot Computations for AAB-3225..... | 149 |
| XXIX. | Hugoniot Computations for AAB-3267..... | 149 |
| XXX. | Hugoniot Equations of State for Polymethylmethacrylate..... | 150 |
| XXXI. | Transmitted Shock Pressures in AAB-3189 for Several Incident Shock Pressures in PMMA, Using Various Hugoniot Equations of State..... | 152 |
| XXXII. | Card-Gap Test Results, AAB-3189 Propellant. | 155 |
| XXXIII. | Card-Gap Test Results, AAB-3225 Propellant. | 156 |
| XXXIV. | Card-Gap Test Results, AAB-3267 Propellant. | 157 |
| XXXV. | Initiation Criterion Evaluation for Cylindrical Acceptor..... | 162 |
| XXXVI. | Evaluation of Initiation Criterion, Using 4-in. by 8-in. Rectangular Acceptors..... | 169 |
| XXXVII. | Results of Flyer-Plate Tests..... | 180 |
| XXXVIII. | The Effect of Cowles Dissolver Speed..... | 194 |
| XXXIX. | The Effect of Cowles Dissolver and Aeration Technique..... | 195 |
| XL. | The Solid Density of ANB-3226 Propellant Prepared from Aerated Binder with Various Aeration Methods..... | 198 |
| XLI. | The Effect of Mixing Conditions..... | 199 |
| XLII. | Effect of Mixing Technique on 60-lb Batches of ANB-3226 Propellant..... | 200 |
| XLIII. | Effect of Dissolved Nitrogen, in ANB-3226 Binder, on Pore Formation..... | 202 |
| XLIV. | The Effect of Chloroform on Pore Formation..... | 204 |
| XLV. | The Effect of Freon-TF and Methyl Chloroform on Pore Formation..... | 205 |
| XLVI. | The Effect of Delay in the Vacuum Cure of ANB-3226 Propellant..... | 208 |
| XLVII. | Adsorption of Toluene Vapor..... | 217 |
| XLVIII. | Percent TNT Impulse Equivalences for RDX-Adulterated PBAN Propellants..... | 230 |
| XLVIX. | Fireball Data..... | 232 |
| L. | Correlation Coefficients, Fireball Data.... | 238 |
| LI. | Coefficients of Fireball Equation..... | 239 |
| LII. | Estimates of Fireball Characteristics as a Function of Diameter..... | 242 |
| LIII. | Estimates of Fireball Characteristics as a Function of Weight..... | 243 |

# SECTION I

## INTRODUCTION

Large solid rocket motors, cast with composite propellant, are being designed for use in military applications and in space exploration programs, some of which are already in operation. The clustered large solid boosters of the Titan III-C system, for example, have already been flown. Motors as large as 260-in.-diameter have been successfully test fired. The trend toward larger diameter solid rocket motors is being paralleled by the development of increasingly more energetic propellant formulations. Of prime concern is the potential hazard that large motors may present when they are involved in an accidental mishap, whether it should occur during handling or transportation of the motor, or on the launch site, or after the launch has been effected. The motors contain from 300,000 lb to over 1 million lb of propellant. The reaction of this large a quantity of propellant to any of several stimuli, applied either individually or in conjunction with other stimuli, must be subject to realistic prediction, to allow proper design of operating procedures and facilities to restrict the personnel and materiel losses to a minimum. Not having the ability to make such predictions risks serious consequences resulting from either underestimating or overestimating the damage potential. Severe damage to neighboring structures and complexes and the real possibility that lives could be lost illustrate clearly the dangers of underestimation. An error in the opposite direction, caused by overestimating the hazard, would create the need for unnecessary expenditures such as would be required to acquire sufficient land, for example, and to build facilities capable of withstanding the imagined stresses. This type of error conceivably could delay the advancement of new systems to an operational level.

The needless costs incurred by either type of erroneous estimation not only justify, but demand, an intensive theoretical and experimental investigation of the hazards associated with large solid propellant systems. To determine these hazards for one specific system, limited to a fixed quantity of a particular propellant formulation in a specific configuration, by an empirical approach alone, would not satisfy the basic requirements that are established by the overall problem. Such an approach could not provide any basis for estimating the hazards of a different system. The need for theoretical analysis of propellant hazards is precisely to develop tools by which the general problem can be described in terms of parameters peculiar to any system, where some of these parameters may have to be determined from a number of subscale tests. Only by attacking the hazards problem with a combined theoretical and experimental approach can the end results be obtained economically.

## THE OVERALL SOPHY PROGRAM

The Air Force Rocket Propulsion Laboratory, Edwards Air Force Base, California, is conducting a solid-propellant hazards study program to analyze the potential explosives hazard created by handling, transporting, testing, and launching large solid propellant systems. This program is identified by the acronym SOPHY.

Shock, impact, fire, and mechanical failure each are potential causes for steady-state detonation or thermal explosion of the propellant. By detonation is meant an exothermic reaction characterized by a rapid combustion or thermal decomposition reaction zone preceded by a shock wave and propagating through the material at a velocity greater than the sonic velocity in the material. An essential feature of detonation is the movement of product gases toward the burning surface and unreacted material. The propagation mechanism is shock compression. Steady-state detonation proceeds at a constant velocity. Thermal explosion, on the other hand, is used to describe the violent consequence of an exothermic reaction that releases heat at a greater rate than the rate of heat loss from the reacting medium, reaching the point where the reaction produces an explosion because of the increasing temperature and reaction rate.

An analysis of operational mishaps to which large solid motors could react catastrophically is given in Figure 1. Shown are several paths by which the propellant reaction could proceed to either a detonation or a thermal explosion. In most cases the paths to detonation require a mechanism that relies on increased surface area or porosity, to lead from deflagration to detonation or thermal explosion; i.e., they require modification of the propellant.

The hazards problem clearly can be relegated to two general fields of investigation: (1) the hazards created by the unmodified propellant and (2) the hazards created after the propellant has been modified by exposure to any one, or several, of those stresses that have been described. In both categories, the hazards of detonation and thermal explosion must be studied. The general objectives of the SOPHY program are discussed within this context.

### Unmodified-Propellant Hazards

#### Detonation

For any motor to sustain detonation it must be of supercritical size and it must be subjected to a shock stimulus sufficient to initiate detonation. Since solid motors are conventionally of

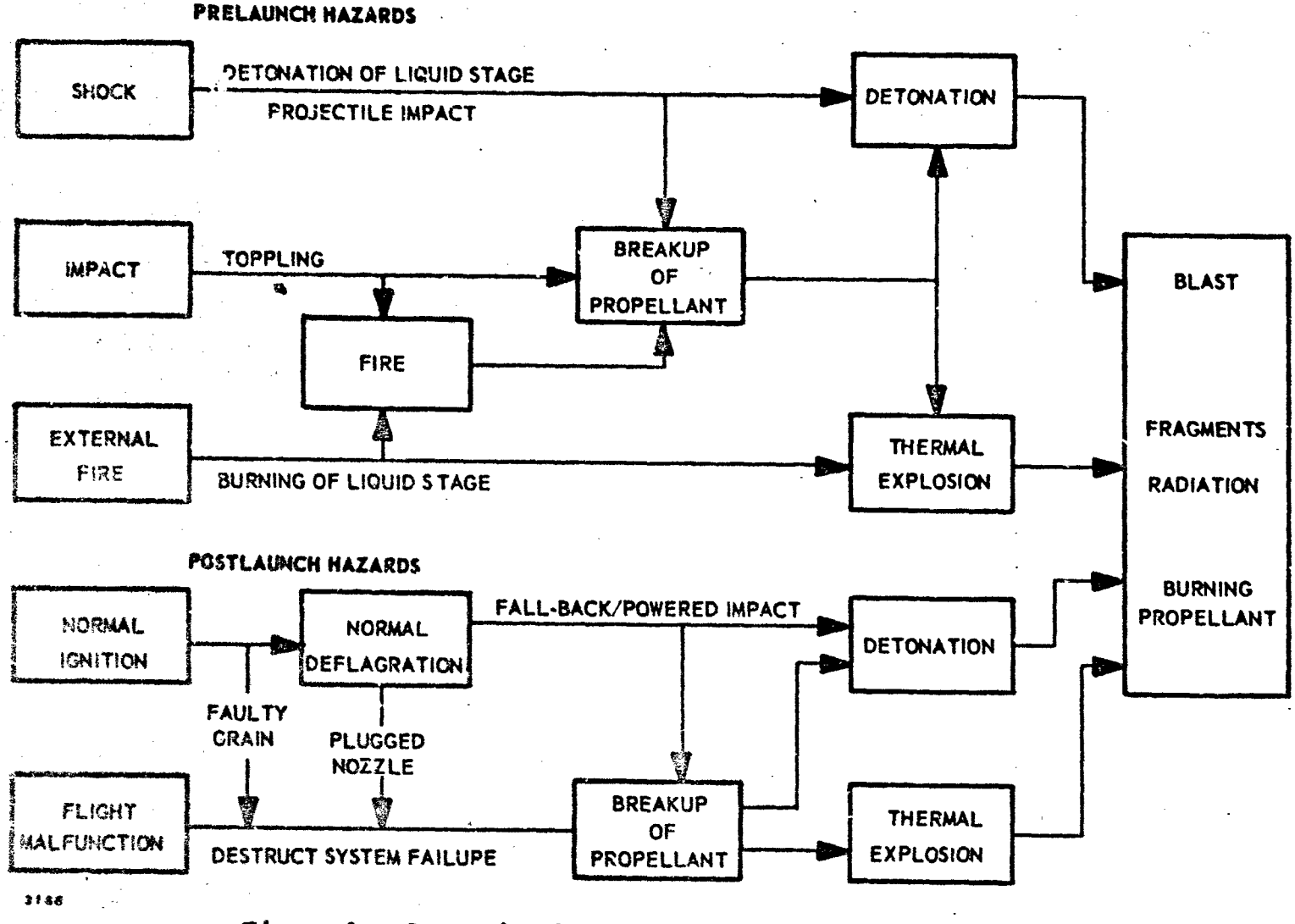


Figure 1. Operational Hazards of Large Solid Motors.

hollow-core design, existing detonation theories, which consider propagation of detonation only in solid cylindrical charges, are not directly applicable to this analysis. The SOPHY approach is to estimate the critical dimensions of a charge of any shape by determining a relationship between the charge dimensions and the critical diameter of the material of which the charge is composed. Since the critical diameter of a composite propellant is expected to be relatively large, to determine the critical diameter by conventional means for each propellant would be prohibitively expensive, particularly without a reasonable initial estimate of the critical diameter.

The SOPHY objective in this case is to develop a theoretical model and associated test program that will produce an estimate of sufficient accuracy to preclude performance of large full-scale tests.

A sustainment theory of critical geometry, relating the dimensions of any shape to the critical diameter, is required to predict the critical size of hollow grains. With this theory, given the critical diameter, it will be possible to specify the critical dimensions of any particular shape motor. The immediate question then is whether sufficient shock forces exist to initiate the detonation.

Since the applied shock wave can be delivered by any of a wide range of sources, its parameters must be identified individually and their separate roles determined. The shock pressure, shock wave area, and pulse width are postulated to be those parameters that sufficiently define a shock wave. The initiation criterion hypothesis states that, for any detonable material, initiation of detonation will occur only when the shock wave meets certain conditions of pressure, area, and pulse width, and that the set of such minimal conditions is a smooth curved surface generated in the three-dimensional space defined by those coordinates. This surface is the initiation criterion for the material.

## Thermal Explosion

If a given motor is detonable, an energetic reaction also could occur if the motor is not shocked sufficiently to cause detonation. If the motor is subcritical, a fading detonation could occur from sufficient shock loading of the grain. These nonsteady-state reactions must be predicted from knowledge of the attenuation of shock waves in a reactive medium. A theoretical interpretation of empirical results must be developed for predicting the nature and extent of propellant reaction under such conditions.

Fragments of burning propellant, distributed over a wide area and capable of inflicting heavy damage to above-ground facilities and equipment, are an obvious hazard produced by thermal explosion. Blast and fireball characteristics would be expected to differ from those associated with detonation in that their values would be heavily dependent on the initiating source strength. These relationships must be determined. It would be totally inadequate to ignore the hazards produced by thermal explosion and to substitute the detonation hazards as approximate upper limits for the hazards of any particular system.

Theoretical understanding of the sustainment of detonation has advanced to its present level primarily because sustained detonation can be treated as a steady-state phenomenon. Initiation theory has reached a degree of sophistication, which nevertheless is primitive in comparison with sustainment theory. Even less understood are thermal-explosion and fading-detonation reactions, simply due to their transitional character. Despite the magnitude of the challenge, theoretical understanding of these transient, nonsteady, propellant reactions is demanded by the very fact that current and projected large propellant systems are of such size that their behavior under catastrophic conditions must be predictable.

## Modified-Propellant Hazards

It is clear that the types of mishaps most likely to occur, particularly at the launch site and during the post-launch operations, can produce propellant modification in combination with thermal or shock stresses. Two such cases, for example, would be an external fire caused by a liquid propellant stage rupture, or spill, and powered impact to earth due to guidance system failure. An external fire may alter the physical integrity of a solid motor, perhaps by creating a porous region in the propellant grain which would become a region of accelerated burning should the grain ignite. It may cause autoignition of the grain, under certain favorable circumstances. A third possibility is that the heat would cause the motor to become supercritical, or more supercritical, as the case may be, and possibly more sensitive to initiation by shock. On powered impact, the grain would be expected to break up and, since it would already have been ignited, to enter an increased burning-rate regime that quite possibly could lead to violent thermal explosion.

The SOPHY objectives in this area are to determine (1) whether heat can cause significant propellant porosity, (2) the effect of heat (propellant temperature) on the critical diameter and on the initiation criterion, (3) the reactions of porous propellant to subsequent fire or shock stimuli, (4) the reactions of cracked propellant, in a confining medium, to fire or shock, and (5) the relation of blast, fireball, and fragmentation data to propellant mass, environment, and stimuli. Inherent in these studies is a theoretical advancement of the state of the art relating propellant reaction to the thermo-physical condition of the material.

## General Comments

Project SOPHY is an ambitious and realistic approach to an immediate problem that involves the investment of billions of dollars in both propellant and support systems. The constant advancement in propellant and engineering technology must be matched by similar capabilities in the hazards analysis field. The goals of SOPHY extend beyond predicting the nature of catastrophic propellant reactions into the area of preventive action. With a thorough scientific understanding of the fundamental mechanisms that are involved, certain steps might be taken in propellant formulation, for example, that would either decrease the possibilities of such occurrences or minimize the consequences: by increasing the critical diameter, reducing the sensitivity, or improving the resistance of solid propellant to extreme thermal and mechanical stimuli.

Large solid propellant systems are no longer an exclusive property of the future. They exist today. The objectives of Project SOPHY more desirably should have directed research activity in these various areas at an earlier stage in rocket motor development, but the present existence of large solid propellant systems has provided these objectives with an undeniable exigency.

## SOPHY I PROGRAM SUMMARY

Aerojet conducted the initial Project SOPHY investigation, identified herein as SOPHY I, under Air Force Contract AF04(611)9945. The results of that study have been described in a final report (Reference 1). To provide continuity for the reader of this Introduction, and to establish the orientation of the current SOPHY project (SOPHY II) a very brief summary of the objectives and results of SOPHY I is presented.

The SOPHY I program consisted entirely of an investigation of the detonation hazards of unmodified solid composite propellant. To determine the critical diameter of typical Class II propellants, a theoretical model was developed which assumed a grain-burning mechanism and applied the Jones expression that relates the diameter of a charge to (1) its detonation velocity at that diameter, (2) the ideal detonation velocity, at infinite diameter, and (3) the detonation reaction time. This model was formulated to predict critical diameter as a function of hot-spot initiation-site concentration. The coefficients in the final expression were determined from the results of a large number of critical diameter tests of adulterated propellant, in which the hot-spot concentration was effectively controlled by substitution of certain weight fractions of RDX explosive for corresponding weights of the ammonium perchlorate oxidizer in a representative PBAN-type composite propellant formulation. The model gave a preliminary prediction of 75.6 in. for the critical diameter of basic, unadulterated propellant. The data from SOPHY I have been analyzed more thoroughly in SOPHY II to obtain a statistically supported estimate.

A critical geometry theory for sustainment was developed and evaluated. Analyzing the sustainment phenomenon in terms of energy gains and losses, and relating these to the cross-sectional area and total perimeter, respectively, the theory produced a method by which the critical dimensions of a sample of any shape could be predicted, once the critical diameter were known. The critical geometry defined by the theory is assumed to be a property of the material and independent of shape. Experimental evaluation of this theory, using both an adulterated propellant formulation and an RDX-wax explosive, disclosed that the predicted critical dimensions differed from the experimental by as little as 3 to 20%. The higher percentage differences were due in large measure to the choice of size increments in the test designs. The results of the tests, when reduced to an "equivalent diameter" based on the equations of the original theory, were found to compare to within 5% of the predicted critical geometry when the latter was assumed to be 89% of the critical diameter.

The initiation criterion was measured for an RDX-adulterated PBAN propellant, in terms of shock pressure and shock wave area, from the results of card-gap tests. This criterion was tested by shock loading supercritical right-solid-cylindrical acceptors, using axially-centered cylindrical high-explosive boosters of different diameters to vary the initial shock wave area in the acceptor. The expanding shock wave was mapped for each test at several discrete times, and the average pressures and wave areas were plotted against the initiation criterion. In one test the analytical

results contradicted the initiation criterion hypothesis; in the others, the pressure-area parameters intersected the initiation criterion only when the sample sustained detonation. The exception was a test in which the sample did not detonate but the pressure-area parameters briefly "entered", then "left," the region bounded by the initiation criterion. It was not possible to determine whether this behavior was fictitious and due simply to errors accumulated in the reduction of the data. The general conclusion drawn from the tests of the initiation criterion was that it is more accurate when expressed as a relationship between pressure and wave diameter, since the criterion was not violated when so represented.

## SPECIFIC OBJECTIVES, SOPHY II

Aerojet has conducted the second segment of the solid-propellant hazards study program under Air Force Contract AF04(611)10919. This program, which is identified as SOPHY II, has the following objectives:

- Statistically analyze the critical-diameter test results of SOPHY I to determine the least squares best fit to the Aerojet detonation model.
- Using the detonation model, predict the critical diameter of the unadulterated propellant.
- Perform experimental tests, bracketing the predicted critical diameter, to evaluate the theoretical prediction.
- Develop the critical-geometry theory of sustainment by statistically designed and analyzed experiments.
- Evaluate the final expression of the critical-geometry theory by testing its applicability to various shapes cast from another adulterated propellant formulation.
- Determine experimentally the initiation criteria for three different adulterated propellant formulations.
- From the initiation criteria thus determined, predict the initiation criterion for the unadulterated formulation.

- Attempt an experimental method to determine the minimum shock pressure required to initiate detonation of an adulterated propellant, using subcritical samples.

- If the method is successfully demonstrated, determine the minimum shock pressure required to initiate detonation of the unadulterated formulation.

- Evaluate the initiation criterion for an adulterated propellant, using cylindrical and rectangular acceptors, each shocked by a booster centered on the end face of the acceptor.

- Develop methods to synthesize and characterize propellant with controlled physical defects.

- Examine the literature to compile data on accidental mishaps involving solid-composite propellant motors, and on the nature and extent of defects that might be induced in propellant as the result of such mishaps.

- Reduce and analyze air blast and fireball data acquired under SOPHY I and SOPHY II; attempt correlations and scaling relationships for both sets of data.

REPRODUCED FROM BEST AVAILABLE COPY

## SECTION II

## SUMMARY

The statistical best-fit of the detonation model to the critical-diameter data obtained under the SOPHY programs states that for AP/PBAN propellant formulations containing f wt fraction RDX, where $0 \leq f \leq 0.10$, the estimated critical diameter $d_c$ is given by

$$d_c = 17.32\ (f + 0.00533)^{-1/3} - 34.94 \text{ in.}$$

By this model the critical diameter of the unadulterated parent formulation, ANB-3226, is estimated to be 64 in. The accuracy of this estimate was demonstrated experimentally by the fact that a 72-in. diameter sample of ANB-3226 propellant did sustain a steady-state detonation, whereas a 60-in. diameter sample of the same propellant failed to sustain detonation.

The critical geometry of a nonsolid-circular shape is defined as four times the ratio of cross-sectional area to total perimeter, for the smallest sample size that can sustain detonation. Experimental evidence shows that this critical geometry is approximately equal to 92% of the critical diameter of the material, for these shapes: square, equilateral triangle, rectangle, and circular-core and cross-core right cylinders. The within-batch standard deviation in the critical geometry test results for AAB-3189 propellant (9.2% RDX) is 0.04 in. The between-batch standard deviation in critical diameter data is 0.07 in.

Critical geometry theory evaluation tests using AAB-3225 (7.1% RDX) confirmed the predictions of the theory for squares and circular-core and cross-core hollow cylinders. The confirmation tests were statistically designed to test the hypothesis that the respective critical geometries were within the region of the predicted mean plus or minus three standard deviations. The results showed no reason to reject the hypothesis.

The minimum shock pressure required to initiate detonation was determined as a function of charge diameter for 3 RDX-adulterated propellants, using the card-gap test technique. These data were extrapolated to unadulterated propellant by comparing the trends, with respect to RDX content, of the minimum shock pressure required near the critical diameter and the minimum pressure required in the ideal-diameter region. From the data near the critical diameters, it is estimated that for unadulterated propellant the minimum shock pressure required at the critical diameter is 25 to 30 kbar. This estimate would be greatly improved by acquisition of

additional data from adulterated propellants near their critical diameters. In the ideal-diameter region, the data indicate that the minimum initiating pressure required for ANB-3226 is 8 to 10 kbar.

The experimental determination of the minimum pressure required to initiate unadulterated propellant, by testing subcritical samples instrumented with an axial resistance probe, failed to produce intelligble data during preliminary evaluation tests, using adulterated propellant, and was not attempted with unadulterated samples.

Shock waves of various initial pressures and areas were applied to supercritical samples of an RDX-adulterated propellant, and the attenuation and expansion of the waves were monitored. In all but one test where detonation ensued, the pressure-area wave parameters exceeded the initiation criterion; in all failures to detonate, the pressure-area parameters did not reach the initiation criterion. These results tend to support the initiation criterion hypothesis.

Several techniques have been developed for preparing small-batch samples of porous or cracked propellant and characterizing the samples in terms of pore size, pore distribution, and void surface area, to gain the technical capability needed to study the effect of these defects on propellant reaction to shock and/or fire. This preliminary study anticipates investigation of the detonation and thermal explosion hazards of motors that have undergone physical modification as the result of such stimuli as are exerted by powered impact, fire, and shock.

The peak side-on overpressure data from 22 large-diameter tests with adulterated and unadulterated propellant were correlated with the reduced range $\lambda$ (range divided by the cube root of the propellant weight) to fit this equation:

$$\ln P = 7.4228 - 1.9925 \ln\lambda$$

where P is in psi and $\lambda$ is in $ft/lb^{1/3}$.

The impulse data from the detonating samples could not be pooled with that from the nondetonating samples. Consequently two correlations were developed. Over the range in which the measured data were obtained, these correlations were, respectively

$$\ln\left(\frac{I}{W^{1/3}}\right) = 3.71 - 0.717 \ln\left(\frac{R}{W^{1/3}}\right)$$

additional data from adulterated propellants near their critical diameters. In the ideal-diameter region, the data indicate that the minimum initiating pressure required for ANB-3226 is 8 to 10 kbar.

The experimental determination of the minimum pressure required to initiate unadulterated propellant, by testing subcritical samples instrumented with an axial resistance probe, failed to produce intelligble data during preliminary evaluation tests, using adulterated propellant, and was not attempted with unadulterated samples.

Shock waves of various initial pressures and areas were applied to supercritical samples of an RDX-adulterated propellant, and the attenuation and expansion of the waves were monitored. In all but one test where detonation ensued, the pressure-area wave parameters exceeded the initiation criterion; in all failures to detonate, the pressure-area parameters did not reach the initiation criterion. These results tend to support the initiation criterion hypothesis.

Several techniques have been developed for preparing small-batch samples of porous or cracked propellant and characterizing the samples in terms of pore size, pore distribution, and void surface area, to gain the technical capability needed to study the effect of these defects on propellant reaction to shock and/or fire. This preliminary study anticipates investigation of the detonation and thermal explosion hazards of motors that have undergone physical modification as the result of such stimuli as are exerted by powered impact, fire, and shock.

The peak side-on overpressure data from 22 large-diameter tests with adulterated and unadulterated propellant were correlated with the reduced range $\lambda$ (range divided by the cube root of the propellant weight) to fit this equation:

$$\ln P = 7.4228 - 1.9925 \ln\lambda$$

where P is in psi and $\lambda$ is in $ft/lb^{1/3}$.

The impulse data from the detonating samples could not be pooled with that from the nondetonating samples. Consequently two correlations were developed. Over the range in which the measured data were obtained, these correlations were, respectively

$$\ln \left(\frac{I}{W^{1/3}}\right) = 3.71 - 0.717 \ln \left(\frac{R}{W^{1/3}}\right)$$

and

$$\ln\left(\frac{I}{W^{1/3}}\right) = 4.25 - 0.953 \ln\left(\frac{R}{W^{1/3}}\right)$$

where the impulse I is in psi-msec, R in ft, and W in lb.

The fireball data were correlated to charge diameter and to total weight by linear equations in which the dependent variable is any one of the following: maximum fireball height, maximum fireball diameter, time to maximum height, time to maximum diameter, and total fireball duration.

In summary, the critical geometry theory predicts that ANB-3226 is detonable in a circular-core cylindrical configuration if the web thickness exceeds 27 to 33 in. The initiation criterion estimated for ANB-3226 indicates that the minimum shock pressure required to initiate detonation may be as low as 10 kbar, but this estimate may vary significantly with the pulse width of the entering shock wave. The need for defining the initiation criterion fully, i.e., in terms of all its parameters, is of major importance at this stage in the SOPHY program. Sharing priority with the pulse width studies are investigations of the validity of the initiation criterion for hollow-core acceptors initiated at the web end or at the side, and theoretical understanding of the wave expansion process under such conditions. These large study areas, when completed, would fulfill the SOPHY objectives regarding the detonation hazards of unmodified composite propellant. Thermal explosion hazards and the reactions of modified composite propellant then must be investigated and characterized in their own right.

[illegible] FOR [illegible]

# SECTION III

# DETONATION MODEL

## INTRODUCTION

In the SOPHY I program, theoretical and experimental approaches were combined to generate a detonation model for a typical composite propellant (Reference 1). This model relates the critical diameter to RDX weight fraction, for any propellant formulation derived from the basic unadulterated propellant, ANB-3226, by substituting a specific RDX weight fraction for the same weight of ammonium perchlorate oxidizer. Aerojet propellant ANB-3226, which is the propellant selected by SOPHY to be representative of composite propellants presently in use, is composed of 69 wt % ammonium perchlorate ( AP), 15 wt % aluminum, and 16 wt % PBAN binder (polybutadiene, acrylic acid, and acrylonitrile) and additives.

The general form of the detonation model developed in SOPHY I is

$$d_c = k_1 (f + c)^{-1/3} + k_2 \qquad (1)$$

where $d_c$ is the critical diameter, f is the RDX weight fraction, and $k_1$, $k_2$, and c are constants. By trial and error fitting of Equation 1 to the critical diameter data obtained in SOPHY I, the final form of the model became

$$d_c = 15.3 (f + 0.003)^{-1/3} - 30.4 \text{ in.} \qquad (2)$$

Using more sophisticated techniques, under the SOPHY II program the best values of the constants in Equation 1 were re-estimated. Also, the detonation model was stated in a more generalized form that essentially defined the critical diameter as a function of the number and distribution of hot-spot initiation sites. Furthermore, in SOPHY II, attempts were made to evaluate the applicability of the modified Jones expression, which was used in the development of the detonation model, since the Jones expression had been derived to describe nonideal detonation behavior of high explosives and the SOPHY detonation model was developed for composite propellants.

## ESTIMATION OF COEFFICIENTS

The detonation model of SOPHY I was to guide the selection of sample sizes to be used in SOPHY II critical diameter tests of the unadulterated propellant. It was necessary that the SOPHY I

data be analyzed thoroughly, and that the distribution of all the possible fits of Equation 1 to the data be found, before selection of the proper test sizes could be made.

Two distinct approaches to this problem were investigated. The first was a nonstatistical approach consisting of finding those solutions for $k_1$, $k_2$, and c which were consistent with all the go-no go ranges determined by the SOPHY I data. The second was a statistical approach that consisted of fitting best-estimate values of the mean critical diameter for each range, by least squares, to estimate values of $k_1$ and $k_2$ for selected values of c. Both methods produced nearly identical limiting values of $d_c$ (for zero-percent RDX). The results of each approach are discussed independently in the following sections.

## Nonstatistical Approach

The results from the SOPHY I tests produced the following go-no go ranges:

| Weight Fraction RDX | Critical-Diameter Range (in.) |
|---|---|
| 0.10 | 1.75 to 2.50 |
| 0.092 | 2.66 to 2.80 |
| 0.090 | 3.00 to 4.00 |
| 0.0675 | 6.00 to 8.00 |
| 0.0475 | 11.00 to 12.00 |
| 0.018 to 0.024 | 23.5 |
| 0.0025 to 0.0050 | 48.0 |

The nonstatistical approach consisted of finding those combinations of $k_1$, $k_2$, and c which were consistent with all ranges. In doing this, 441,471 unique combinations of these constants were tested, using the IBM 7094 computer. Values of $k_1$ ranged from 15.00 to 10.00, in intervals of 0.05; values of $k_2$ from 28.0 to 42.0, in intervals of 0.1; and values of c from 0.0020 to 0.0080, in intervals of 0.0002. Of the 263 total solutions that satisfied all ranges, the following solutions provided the maximum and minimum critical-diameter values for zero-percent RDX, respectively:

$$d_c\ (\max) = 79.13 = 16.1 \left(\frac{1}{f + 0.003}\right)^{1/3} - 32.5 \qquad (3)$$

$$d_c \text{ (min)} = 56.15 = 18.75 \left(\frac{1}{f + 0.008}\right)^{1/3} - 37.6 \qquad (4)$$

The midrange between the two extremes is 67.54 in. Table I presents a frequency distribution of the zero-percent RDX critical diameter estimates for all solutions satisfying all ranges. From this table, the median (50%) value of the critical diameter is found to be 64 in.

## Statistical Approach

The statistical approach consisted of fitting best-estimate values of the mean critical diameter, by least squares, to estimate values of $k_1$ and $k_2$ for selected values of c. The values of mean critical diameter, at the corresponding RDX percentages, that were used for these fits are given below:

| Critical Diameter (in.) | Weight Fraction RDX |
|---|---|
| 2.125 | 0.10 |
| 2.73 | 0.092 |
| 3.50 | 0.090 |
| 6.50 | 0.0675 |
| 11.25 | 0.0475 |
| 23.5 | 0.021 |
| 48.0 | 0.00375 |

Those critical-diameter values at RDX weight fractions of 0.0675 and 0.0475 are not the midpoints of the respective go-no go ranges. They are considered best-estimate values, based on interpretation of velocity data and other technical judgments that were made.

As stated, the values of $k_1$ and $k_2$ in the model were estimated by least squares for selected values of c. This was necessary since $k_1$ and c are not linearly independent in the model. The values of c fitted ranged from 0.0133 to 0.0900 in increments of 0.0033. Table II presents the results of these fits. The fit for c = 0.00533 was considered best since it resulted in the smallest standard error of estimate, 0.224 in. The equation of this fit is

$$d_c = 17.208 \left(\frac{1}{f + 0.00533}\right)^{1/3} - 34.472 \text{ in.} \qquad (5)$$

The equation for zero-percent RDX gives a critical diameter of 64.0 in.

Table I. Frequency Distribution of Zero-Percent RDX Critical-Diameter Estimates for Solutions Satisfying all Ranges.

| Critical Diameter (in.) | Frequency Tally | Number | Cumulative Number | Cumulative Percent |
|---|---|---|---|---|
| 56 | 𝍸 | 5 | 5 | 1.9 |
| 57 | 𝍸 𝍸 II | 12 | 17 | 6.5 |
| 58 | 𝍸 𝍸 𝍸 I | 16 | 33 | 12.5 |
| 59 | 𝍸 𝍸 𝍸 𝍸 | 20 | 53 | 20.2 |
| 60 | 𝍸 𝍸 𝍸 𝍸 III | 23 | 76 | 28.9 |
| 61 | 𝍸 𝍸 𝍸 II | 17 | 93 | 35.4 |
| 62 | 𝍸 𝍸 I | 11 | 104 | 39.5 |
| 63 | 𝍸 𝍸 𝍸 | 15 | 119 | 45.2 |
| 64 | 𝍸 𝍸 𝍸 III | 18 | 137 | 52.1 |
| 65 | 𝍸 𝍸 IIII | 14 | 151 | 57.4 |
| 66 | 𝍸 𝍸 𝍸 I | 16 | 167 | 63.5 |
| 67 | 𝍸 𝍸 II | 12 | 179 | 68.1 |
| 68 | 𝍸 𝍸 II | 12 | 191 | 72.6 |
| 69 | 𝍸 𝍸 | 10 | 201 | 76.4 |
| 70 | 𝍸 𝍸 III | 13 | 214 | 81.8 |
| 71 | 𝍸 IIII | 9 | 223 | 84.8 |
| 72 | 𝍸 𝍸 | 10 | 233 | 88.6 |
| 73 | 𝍸 IIII | 9 | 242 | 92.0 |
| 74 | 𝍸 I | 6 | 248 | 94.3 |
| 75 | IIII | 4 | 252 | 95.8 |
| 76 | IIII | 4 | 256 | 97.3 |
| 77 | IIII | 4 | 260 | 98.9 |
| 78 | I | 1 | 261 | 99.2 |
| 79 | II | 2 | 263 | 100.0 |

Table II. Results of Least-Squares Fits to Critical-Diameter Data.

| c | $k_1$ | $k_2$ | $s_e$* | Critical Diameter at 0% RDX (in.) |
|---|---|---|---|---|
| 0.00133 | 12.580 | 24.001 | 1.55 | 90.4 |
| 0.00167 | 13.015 | 25.015 | 1.39 | 84.7 |
| 0.002 | 13.427 | 25.971 | 1.24 | 80.6 |
| 0.00233 | 13.831 | 26.901 | 1.09 | 77.4 |
| 0.00267 | 14.239 | 27.834 | 0.96 | 74.8 |
| 0.003 | 14.627 | 28.718 | 0.82 | 72.7 |
| 0.00333 | 15.009 | 29.583 | 0.70 | 70.9 |
| 0.00367 | 15.396 | 30.454 | 0.59 | 69.4 |
| 0.004 | 15.766 | 31.283 | 0.48 | 68.0 |
| 0.00433 | 16.131 | 32.096 | 0.39 | 66.9 |
| 0.00467 | 16.502 | 32.918 | 0.30 | 65.8 |
| 0.005 | 16.857 | 33.701 | 0.24 | 64.9 |
| 0.00533 | 17.208 | 34.472 | 0.224 | 64.0 |
| 0.00567 | 17.566 | 35.253 | 0.24 | 63.3 |
| 0.006 | 17.909 | 36.00 | 0.30 | 62.6 |
| 0.00633 | 18.249 | 36.736 | 0.37 | 61.9 |
| 0.00667 | 18.595 | 37.483 | 0.44 | 61.3 |
| 0.007 | 18.929 | 38.199 | 0.52 | 60.8 |
| 0.00733 | 19.259 | 38.905 | 0.60 | 60.2 |
| 0.00767 | 19.597 | 39.624 | 0.68 | 59.7 |
| 0.008 | 19.922 | 40.314 | 0.75 | 59.3 |
| 0.00833 | 20.245 | 40.995 | 0.82 | 58.9 |
| 0.00867 | 20.575 | 41.689 | 0.90 | 58.5 |
| 0.009 | 20.893 | 42.356 | 0.96 | 58.1 |

*$s_e$ = standard error of estimate = $\sqrt{\frac{\Sigma (y - \hat{y})^2}{n - 1}}$

The closeness of the fit to the best-estimate mean critical-diameter values is shown in Table III. The largest errors occur at f = 0.10, 0.092, and 0.090. The large error at f = 0.10 was anticipated, because the model begins to break down at RDX percentages in the region of 10% and above. The deviations at f = 0.092 and 0.090 also are expected because of the relatively large difference between the assumed critical diameters (0.77 in.) when compared with the very small difference in RDX percentages (0.2%). The estimate of 2.73 in. for the critical diameter at f = 0.092 was based on test results obtained from 20 closely-spaced samples. The best-estimate at f = 0.090 of 3.50 in. apparently was slightly higher than the true mean at that RDX level.

Table III. Least-Squares Fit to Critical-Diameter Data.

| f | $d_c$ (data) | $d_c$ (estimated) | Residual | Relative Error (%) |
|---|---|---|---|---|
| 0.10 | 2.125 | 1.966 | 0.159 | 7.5 |
| 0.092 | 2.73 | 2.938 | -0.208 | -7.6 |
| 0.090 | 3.50 | 3.197 | 0.303 | 8.6 |
| 0.0675 | 6.50 | 6.734 | -0.234 | -3.6 |
| 0.0475 | 11.25 | 11.388 | -0.138 | -1.2 |
| 0.021 | 23.50 | 23.37 | 0.129 | 0.6 |
| 0.00375 | 48.00 | 48.011 | -0.011 | -0.02 |

Two least-squares curve-fits also were made, using only the upper values of the ranges, and using only the lower values, excluding the data at f = 0.10 and 0.092. The best fits yielded the following equations, respectively:

$$d_c = 17.598 \left(\frac{1}{f + 0.00567}\right)^{1/3} - 33.743 \text{ in.} \quad (6)$$

$$d_c = 14.984 \left(\frac{1}{f + 0.00567}\right)^{1/3} - 29.725 \text{ in.} \quad (7)$$

at zero-percent RDX, these functions give critical diameters of 70.7 and 59.9 in.

## Analysis

To obtain an estimate of the variance of critical diameter at zero-percent RDX, it is necessary to have estimates of the variances of $k_1$, $k_2$, and c. The variance of $d_c$ can then be estimated, using the standard propagation-of-error technique:

$$V(d_c) = \left(\frac{\partial d_c}{\partial k_1}\right)^2 V(k_1) + \left(\frac{\partial d_c}{\partial k_2}\right)^2 V(k_2) + \left(\frac{\partial d_c}{\partial c}\right)^2 V(c) \quad (8)$$

where V(x) is the variance of x, and the partial derivatives are evaluated at their expected values. The variances of $k_1$ and $k_2$ are, by standard least-squares regression formulas, equal to 0.008806 and 0.07688, respectively.

The variance in c cannot be obtained from the least-squares fit. To estimate its variance it was assumed that the $6\sigma$ spread for c was 0.005. This value was deduced from the nonstatistical approach results, which revealed that, for all the solutions satisfying all ranges, the value of c varied from 0.003 to 0.008. Assuming c to be distributed normally and the $6\sigma$ range to be 0.005, the variance of c is calculated to be $6.94 \times 10^{-7}$. Using these values as the estimated variances of $k_1$, $k_2$, and c, the variance in $d_c$ at zero-percent RDX becomes 26.85 in. squared. The estimated standard deviation at zero-percent RDX is 5.18 in. This produces $3\sigma$ limits of from 48.5 to 79.5 in. about the mean value of 64.0 in.

## Final Estimations

Following the completion of the critical geometry subtasks of SOPHY II (see Sections V and VI), the best least-squares fit of Equation 1, to all the critical diameter data of both SOPHY projects, was found to be

$$d_c = 17.32\ (f + 0.00433)^{-1/3} - 34.94 \text{ in.} \quad (9)$$

The estimated critical diameters obtained from application of Equation 9 are compared with the experimental data in Table IV and Figure 2. Equation 9 is the final expression of the detonation model evaluated for ANB-3226 propellant.

Table IV. Best Least-Squares Fit to Critical-Diameter Data.

| f | $d_c$ (experimental estimate) | $d_c$ (theoretical estimate) | Residual | Relative Error (%) |
|---|---|---|---|---|
| 0.10 | 2.125 | 1.725 | 0.400 | 18.8 |
| 0.092 | 2.69 | 2.703 | -0.013 | - 0.5 |
| 0.090 | 3.00 | 2.964 | 0.036 | 1.2 |
| 0.071 | 5.24 | 5.880 | -0.640 | -12.2 |
| 0.0475 | 11.25 | 11.207 | 0.043 | 0.4 |
| 0.021 | 23.50 | 23.265 | 0.235 | 1.0 |
| 0.00375 | 48.00 | 48.061 | -0.061 | - 0.1 |

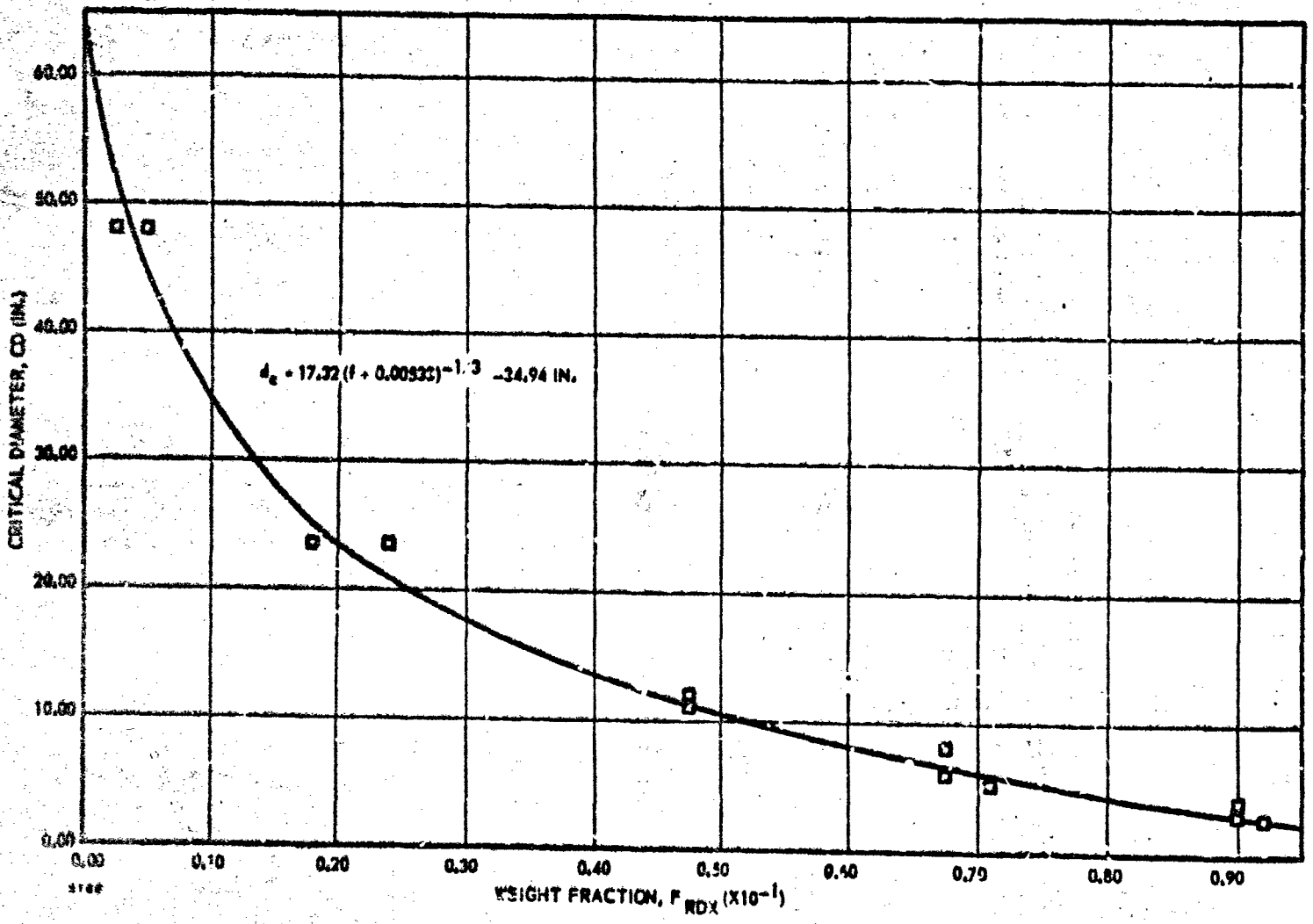


Figure 2. Detonation Model for ANB-3226 Propellant Adulterated with RDX.

## GENERALIZATION OF DETONATION MODEL

### Development of the Model

In the previously developed detonation model for RDX-adulterated propellant (Reference 1) all hot-spot initiation sites were assumed to be contributed either by RDX particles or by inherent sites such as voids, crystal defects, or heterogeneities. For convenience, the inherent sites were considered to be of the same density and size distribution as the RDX particles. This assumption permitted certain simplifications in the model since the expression for the number of inherent sites could be combined with that for the number of RDX hot-spot sites into a single term.

In reality, different types of hot-spot initiation sites may vary widely with respect to average size, density, and concentration. To permit consideration of such differences, the expression for the effective AP grain-burning radius $R_e$ in the SOPHY model has been generalized as follows:

Consider an AP propellant containing a cubical array of hot-spot initiation sites (Figure 3). Let the distance between the centers of adjacent sites of average diameter $\bar{d}$ be $\ell$. Then the effective AP grain radius $R_e$, which is defined as one-half the distance between the surfaces of adjacent sites, is

$$R_e = \frac{1}{2} (\ell - \bar{d}) \tag{10}$$

Let N be the total number of hot-spot sites, of L kinds, per cc of propellant, i.e.,

$$N = \sum_{i}^{L} n_i \tag{11}$$

where $n_i$ is the number of sites of the ith kind per cc of propellant.

Since $\ell = N^{-1/3}$, Equation 10 becomes

$$R_e = \frac{1}{2} (N^{-1/3} - \bar{d}) \tag{12}$$

or

$$R_e = \frac{1}{2} \left[ \left( \sum_{i}^{L} n_i \right)^{-1/3} - \bar{d} \right] \tag{13}$$

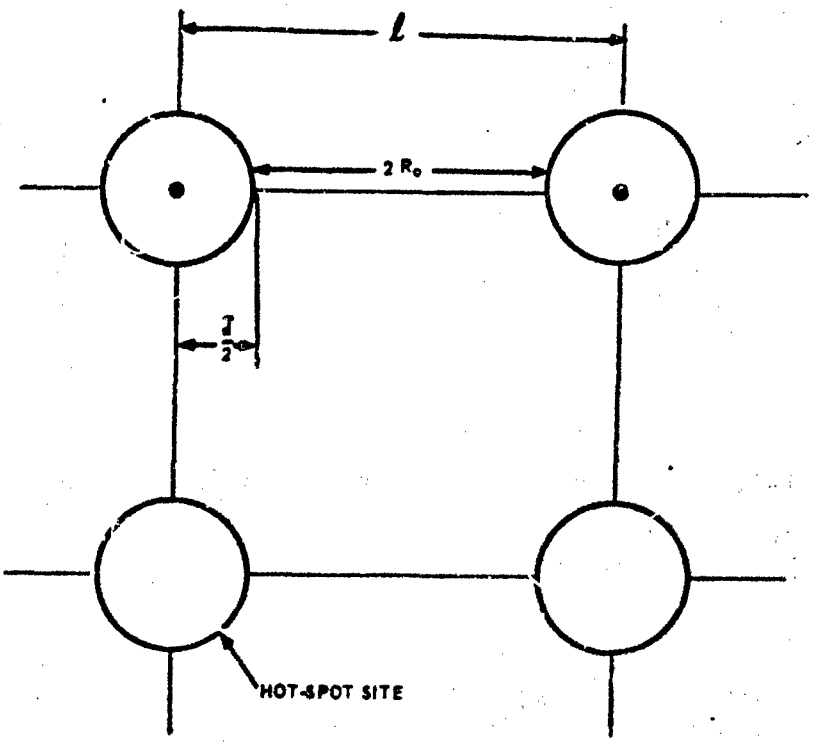


Figure 3. Generalized Model for Hot-Spot Initiation of AP Propellant.

Now $n_i$ is given by

$$n_i = \frac{V_i}{\bar{v}_i} \tag{14}$$

where $V_i$ is the volume fraction of ith type sites and $\bar{v}_i$ is the average volume of an ith type site. We may define $\bar{v}_i$ as

$$\bar{v}_i = \frac{\sum_j^M n_{ij} v_{ij}}{\sum_j^M n_{ij}} \tag{15}$$

or

$$\bar{v}_i = \frac{\pi/6 \sum_j^M n_{ij} d_{ij}^3}{\sum_j^M n_{ij}} \tag{16}$$

where $n_{ij}$ is the number of ith type sites in the jth subset of a total of M subsets of sizes, and $d_{ij}$ is the diameter of an ith type site in the jth subset. But

$$\frac{\sum_j^M n_{ij} d_{ij}^3}{\sum_j^M n_{ij}} = \overline{d_i^3} \tag{17}$$

so that

$$\bar{v}_i = \pi/6 \, \overline{d_i^3} \tag{18}$$

Substituting Equations 14 and 18 and the relationship between volume fraction $V_i$ and weight fraction $f_i$, i.e.,

$$V_i = f_i \left(\frac{\rho_p}{\rho_i}\right) \tag{19}$$

where $\rho_p$ and $\rho_i$ are the densities of propellant and ith type sites, respectively, into Equation 11 gives

$$N = \sum_{i}^{L} \frac{f_i \left(\frac{\rho_p}{\rho_i}\right)}{\pi/6 \; \overline{d_i^3}} \tag{20}$$

The effective AP grain radius $R_e$ is, therefore, from Equations 13 and 20,

$$R_e = \frac{\bar{d}}{2} \left[ \left( \sum_{i}^{L} f_i \frac{6}{\pi} \frac{\rho_p}{\rho_i} \frac{\bar{d}^3}{\overline{d_i^3}} \right)^{-1/3} - 1 \right] \tag{21}$$

where $\bar{d}$, the average diameter of all hot-spot sites, is defined as

$$\bar{d} = \frac{\sum_{i}^{L} \sum_{j}^{M} n_{ij} \, d_{ij}}{N} \tag{22}$$

Letting the coefficient of $f_i$ in Equation 21 be $a_i$, the expression for $R_e$ becomes

$$R_e = \frac{\bar{d}}{2} \left[ \left( \sum_{i}^{L} a_i \, f_i \right)^{-1/3} - 1 \right] \tag{23}$$

COMPARISON OF GENERALIZED MODEL WITH ORIGINAL MODEL

In the case of a propellant containing only one type of added hot-spot site (e.g., RDX), and one type of inherent site (e.g., an assumed single type of heterogeneity giving rise to hot spots by generation of converging shocks), Equation 23 reduces to

$$R_e = \frac{\bar{d}}{2} \left[ a_1^{-1/3} \left( f_1 + \frac{a_2}{a_1} f_2 \right)^{-1/3} - 1 \right] \tag{24}$$

In the original model, the inherent initiation sites were assumed to have the same density and size distribution as the added sites (RDX). The expression for the effective grain radius then becomes

$$R_e = \frac{\bar{d}_{RDX}}{2}\left[\frac{\left(\pi/6\frac{\rho_{RDX}}{\rho_p}\frac{\overline{d_{RDX}^3}}{\bar{d}_{RDX}^3}\right)^{1/3}}{(f_{RDX} + f'_{RDX})^{1/3}} - 1\right] \quad (25)$$

The form of Equation 25 is identical to that of the original model (Reference 1), i.e.,

$$R_e = \frac{\bar{d}_{RDX}}{2}\left[\frac{G}{(f + c)^{1/3}} - 1\right] \quad (26)$$

where G is a constant[1], determined by the type of assumed hot-spot lattice, the hot-spot particle-size distribution, and the propellant composition, and f and c are, respectively, the weight fractions of RDX adulterant and the additional (constant) amount of RDX needed to account for other (inherent) initiation sites.

## Discussion of the Generalized Model

The success of the SOPHY detonation model in predicting the critical diameter for an AP composite propellant without RDX adulterant provides some support for one of the basic postulates of that model, i.e., that the hot-spot sites leading to the initiation of detonation must include those inherent in the propellant (e.g., voids, crystal defects, and heterogeneities) as well as any sites created by the addition of adulterants such as RDX.

Further support for the SOPHY concept of the existence of inherent sites other than voids, as well as for the overall SOPHY hot-spot model, is provided by the recent work of Apin and Stesik in Russia (Reference 2). These workers investigated the effect of adding inert grit particles of various kinds on the critical diameter of an explosive in which initiation would be expected to occur by a

[1] Actually, C will be a weak function of the f's because of the dependency of $\rho_p$ and d on composition.

hot-spot mechanism. They found that relatively high-density additives (e.g., MgO, $Bi_2O_3$, and tungsten powder) were relatively efficient hot-spot generators. All of their data could be correlated by a model which assumed that the effective burning distance in the detonation reaction zone is one-half the distance between adjacent hot-spot initiation sites, and that the initiation sites must include both added sites (grit) and inherent sites (heterogeneities). Their final expression for the effective radius is

$$R_e = \frac{1}{2} \left[ \frac{1}{(N_a + N_i)^{1/3}} - \bar{d} \right] \tag{27}$$

where $N_a$ = number of added grit particles per cc

and $N_i$ = number of inherent hot-spot sites per cc

This may be compared with the corresponding form for $R_e$ in the original SOPHY model

$$R_e = \frac{1}{2} \left[ \frac{1}{(N_{RDX} + N_i)^{1/3}} - \bar{d}_{RDX} \right] \tag{28}$$

and the present generalized expression for $R_e$

$$R_e = \frac{1}{2} \left[ \frac{1}{\left( \sum_{i=1}^{L} N_i \right)^{1/3}} - \bar{d} \right] \tag{29}$$

The fact that both the SOPHY studies and the experiments of Apin and Stesik, using widely differing basic formulations and types of additives, lead to the same form of the expression for $R_e$ suggests that the hot-spot model of the detonation process employed in both studies contains certain elements of physical reality. Hopefully, then, the generalized model may be useful when systems more complex than the present RDX-adulterated AP propellant are considered. For example, future systems may contain blends of AP with fast-reacting oxidizers other than RDX, that serve as hot-spot generators for initiation of AP grain burning, plus one or more heavy-metal additives such as zirconium corresponding to the grit-type additives of Apin and Stesik, plus inherent sites due to voids, AP crystal defects, and heterogeneities created by the AP particles themselves.

While in principle the generalized SOPHY expression for $R_e$ permits calculation of the effective grain-burning radius from a knowledge of the size distributions, densities, and concentrations of all potential hot-spot sites, such complete information may not always be available (e.g., the size and density of hot-spot sites created by shock focusing near various heterogeneities). In addition, the particle-size distribution of a hot-spot-forming adulterant (e.g., a metal powder), as determined by conventional techniques, may not be the same as the effective hot-spot size distribution since some of the particles will be too small (and possibly too large) to function as hot-spot sites.

It is further apparent that the assumption of the present SOPHY model that all initiation sites are activated in a time that is very short compared to the AP grain-burning time (which is considered to be the total reaction time) is probably an oversimplification of the real situation. It seems more reasonable to assume that the induction time for activation of a hot-spot site by a shock wave will depend on the nature of the potential hot-spot site; i.e., the induction time will be determined by the kinetics of the activation process. As a first step in the eventual inclusion of a time-dependent hot-spot site activation process in the SOPHY model, a one-dimensional lattice model of the detonation reaction zone, in which the various types of hot spots are allowed to assume their characteristic induction times, has been developed by R. F. Chaiken and is presented in Appendix I. In the limit of negligible induction time for all hot-spot sites, the Chaiken model reduces to the SOPHY expression.

## USE OF JONES' EXPRESSION

A basic assumption of the SOPHY detonation model is that the nonideal detonation behavior of composite propellant can be described by the Jones expression that was derived from analysis of high-explosive detonation:

$$\left(\frac{D}{D_i}\right)^2 = 1 - K_j \left(\frac{a}{d}\right)^2 \qquad (30)$$

in which D is the detonation velocity in a cylindrical charge of diameter d, $D_i$ is the ideal detonation velocity ($\lim_{d\to\infty} D = D_i$), a is the reaction zone thickness, and $K_j$ is the Jones constant. In developing the detonation model (Reference 1), it was shown that by assuming

$$a = 3/4\ Dt \qquad (31)$$

where t, the reaction time, is given by

$$t = R_e/B \tag{32}$$

Equation 30 can be expressed by an equivalent explicit function in d, which is

$$d = \frac{kR_e D}{B\left[1 - (D/D_i)^2\right]^{1/2}} \tag{33}$$

where k is $3/4\ K_j^{1/2}$, $R_e$ is the effective AP grain burning radius, and B is the AP linear-burning rate.

Three attempts to validate the use of Jones' expression were made in SOPHY II: (1) a theoretical approach, using the RUBY computer code to calculate the detonation parameters for composite propellant; (2) an experimental measurement of D and a for an adulterated propellant, at various diameters, to test Equation 30; and (3) an analysis of the detonation velocity vs diameter data, to test Equation 33.

## Detonation Properties of Composite Propellant

The RUBY computer code, developed by Levine and Sharples (Reference 3) solves the simultaneous algebraic equations that describe the Chapman-Jouguet (C-J) conditions, the shock conservation laws, the Becker-Kistiakowsky-Wilson (BKW) equation of state, and the chemical reactions, to calculate the C-J detonation properties of an explosive. Until recently the code was applied exclusively to high explosives of the carbon, hydrogen, oxygen, and nitrogen (CHON) group. The RUBY calculations for ammonium perchlorate (Reference 4) mark a significant advancement in the use of this code because AP has a relatively low reaction energy compared to that of high explosives, and because it contains chlorine and no carbon, which introduces a new set of reaction products to the calculations.

### RUBY Application

Preliminary checkout of the RUBY code, by computing the detonation properties of PETN explosive and comparing these to published data (Reference 5), showed only minor discrepancies between the two (Table V). These differences may be entirely the result of slight differences between the input data used in the two runs. Unfortunately, the exact input that produced the reference data was not available.

Table V. Computed Detonation Parameters for PETN at $\rho_o$ = 1.7800 g/cm$^3$.

| Property | Units | NOL | Aerojet (LRL Coefficients of Heat Capacity Equations) | Aerojet (JANAF Coefficients of Heat Capacity Equations) |
|---|---|---|---|---|
| D | mm/$\mu$ sec | 8.323 | 8.427 | 8.342 |
| $P_J$ | meg b | 0.3233 | 0.3386 | 0.3248 |
| $T_J$ | $10^3$ °K | 2.790 | 3.110 | 2.931 |
| $\rho_J$ | gm/cc | 2.412 | 2.431 | 2.413 |
| $\gamma$ | N/A | 2.815 | 2.734 | 2.814 |
| $E_J - E_O$ | cal/gm HE | 568.9 | 616.6 | 579.2 |
| $S_J - S_o$ | cal/°K/gm HE | -0.1658 | 0.0932 | -0.1631 |
| Composition | | | | |
| $H_2O$ | $10^{-3}$ moles/gm HE | 11.42 | 11.30 | 11.96 |
| $H_2$ | $10^{-3}$ moles/gm HE | 0.0039 | 0.0128 | 0.0046 |
| $CO_2$ | $10^{-3}$ moles/gm HE | 12.80 | 12.62 | 12.49 |
| CO | $10^{-3}$ moles/gm HE | 0.9406 | 1.410 | 1.028 |
| $N_2$ | $10^{-3}$ moles/gm HE | 6.211 | 6.322 | 6.200 |
| $NH_3$ | $10^{-3}$ moles/gm HE | 0.279 | 0.0064 | 0.2484 |
| $CH_4$ | $10^{-3}$ moles/gm HE | 0.4454 | 0.6634 | 0.1587 |
| C(graphite) | $10^{-3}$ moles/gm HE | 1.630 | 1.122 | -- |
| moles gas | $10^{-3}$ moles/gm HE | 32.05 | 32.34 | 32.08 |
| $V_g$ | cc/mole | 12.75 | 12.59 | 12.67 |

The next step was to perform calculations with ammonium perchlorate. Satisfactory solutions were generated for ammonium perchlorate at each of several loading densities. Computed detonation properties for AP at densities of 1.50 and 0.08 g/cm$^3$ are presented in Table VI.

The particular loading densities chosen by Aerojet unfortunately did not coincide with those selected by Evans (Reference 4). To make a comparison between the two sets of data requires interpolation. Evans reports an ideal detonation velocity for AP of 3.67 mm/μsec at a loading density of 0.75 g/cm$^3$ and 4.13 mm/μsec at 0.95 g/cm$^3$. The Aerojet calculations yield a velocity of 3.82 mm/μsec at a loading density of 0.080 g/cm$^3$, and an interpolated velocity of 4.20 mm/μsec at 0.95 g/cm$^3$.

The small differences between the two sets of calculations may result from the differences in the covolume inputs used, since some uncertainty exists as to the correct covolume values for specific compounds. RUBY is particularly sensitive to covolume input values. These values used in the work by Evans are not reported. Those used in the Aerojet calculations are given in Table VII.

Experimental detonation velocities for AP, at various densities and charge diameters, are reported by Andersen and Pesante (Reference 6). At a loading density of 0.80 g/cm$^3$ and a charge diameter of 4 in. the detonation velocity was observed to be 3.0 mm/μsec. Furthermore, from the shape of the velocity vs diameter curve, ranging from diameters of 0.75 in. to 4 in., it appears that 3.0 mm/μsec approximates the ideal detonation velocity. The RUBY program is approximately 25% high, with its calculation of 3.82 mm/μsec.

Three separate experimental values are reported for AP detonation velocity at a 1.50 g/cm$^3$ packing density (Reference 6). The values were obtained from 2.5 in. diameter samples, and averaged to 4.3 mm/μsec. No evidence is given to indicate that 2.5 in. is near the ideal diameter at this density; therefore, the data cannot be compared with the predicted 5.55 mm/μsec ideal velocity.

The low predicted values of the C - J temperature for AP are worth noting. They are indicative of a fundamental weakness in the RUBY calculation.

Table VI. RUBY Calculations for Ammonium Perchlorate.

| Property | Units | $\rho_o$ = 0.80 g/cc | $\rho_o$ = 1.50 g/cc |
|---|---|---|---|
| D | mm/μ sec | 3.824 | 5.554 |
| $P_{C-J}$ | Mbar | 0.032 | 0.110 |
| $T_{C-J}$ | $10^3$ °K | 1.227 | 0.795 |
| $\rho_{C-J}$ | gm/cc | 1.105 | 1.968 |
| $\gamma$ | (dimensionless) | 2.621 | 3.208 |
| $E_{C-J} - E_o$ | cal/gm HE | 133.3 | 208.1 |
| $S_{C-J} - S_o$ | cal/°K/gm HE | -0.346 | -0.834 |
| $\gamma$ moles gas | $10^{-3}$ moles/gm HE | 36.32 | 36.32 |
| $V_g$ | cc/mole | 24.91 | 13.99 |
| Composition | | | |
| $H_2O$ | $10^{-3}$ moles/gm HE | 12.82 | 12.82 |
| $N_2$ | $10^{-3}$ moles/gm HE | 4.27 | 4.27 |
| $O_2$ | $10^{-3}$ moles/gm HE | 10.68 | 10.67 |
| $NO_2$ | $10^{-3}$ moles/gm HE | 0.00 | 0.01 |
| HCl | $10^{-3}$ moles/gm HE | 8.56 | 8.55 |

| Symbols | |
|---|---|
| D | detonation velocity |
| $\rho$,T,$\gamma$,E,S,V | standard thermodynamic quantities |
| Subscripts | |
| C-J | Chapman-Jouguet conditions |
| o | original condition |
| g | gas |

Table VII. Covolumes Used in RUBY Code Calculations for AP Detonation.

| Product | Covolume |
|---|---|
| $H_2O$ | 250 |
| $H_2$ | 180 |
| $CO_2$ | - |
| $N_2$ | 380 |
| $O_2$ | 350 |
| $NO_2$ | 600 |
| $NH_3$ | 476 |
| $CH_4$ | - |
| HCl | 643 |

RUBY calculations also have been made for an explosive composed of 30 wt % RDX and 70 wt % wax -- a material similar to that which was used in the SOPHY I program. The purposes of making these calculations were (1) to compare the experimental detonation-velocity results obtained in the nonideal region with the calculated ideal detonation velocity, and (2) to test the ability of RUBY to handle a composition similar to a composite propellant -- fast-reacting oxidizer distributed in a slow-reacting fuel. The results of these computations are given in Table VIII. Again, the low temperatures must be noted. The detonation-velocity vs diameter relationship of RDX-wax (Reference 1) indicates that the ideal detonation velocity is greater than 6.5 mm/μsec (D = 6.57 mm/μsec at d = 1.75 in. for the material, which has a critical diameter of approximately 1.5 in.). The upper bound would appear to be influenced by the fact that the velocity-diameter function for this type of material closely approaches its asymptote $D_i$ at diameters $d > 2d_c$. The RUBY program predicts an ideal detonation velocity of 6.9 mm/μsec when the input parameter, heat of formation of graphite, is chosen to be zero (Table VIII). With the heat of formation of carbon chosen to be 10.75 kcal/mole, RUBY predicts an ideal detonation velocity of 6.2 mm/μsec. The first computation, which agrees with the experimental evidence, was encouraging and indicated that RUBY could handle propellant-like materials as well as high explosives.

The low, 1058°K, C-J temperature, predicted by RUBY, was of some concern. However, the extremely low oxygen content in the material does suppress the reaction kinetics and may do so to sufficiently account for this temperature. Since no experimental measurement of this temperature has been made, it was not possible to reject the value calculated by RUBY.

A later version of the RUBY computer code for calculating detonation properties was obtained with the cooperation of the U.S. Naval Ordnance Test Station, China Lake, California. The NOTS version, using thermodynamic data presented in the JANAF tables, had been successfully applied by NOTS personnel to several ammonium perchlorate systems that consisted of AP plus an explosive binder. The NOTS program received by Aerojet was used to calculate the ideal detonation properties for two propellants, ANB-3226 and AAB-3189, which is identical to ANB-3226 except for the substitution of 9.2 wt % RDX for the equivalent weight of AP. The gaseous constituents of the reaction products that were used as input for the computer calculations are listed in Table IX, together with their respective covolume values. The ideal detonation properties for unadulterated AP-PBAN (ANB-3226) and for AAB-3189 are presented in Table X.

Table VIII. RUBY Calculations for RDX-Wax.
$\rho_o$ = 1.11 g/cc

| Property | Units | Δ $H_f$ of Graphite = 0.0 Kcal/mole | Δ $H_f$ of Graphite = 10.75 Kcal/mole |
|---|---|---|---|
| D | mm/μsec | 6.906 | 6.211 |
| $P_{C-J}$ | Mbar | 0.123 | 0.091 |
| $T_{C-J}$ | $10^3$ °K | 1.058 | 0.707 |
| $\rho_{C-J}$ | gm/cc | 1.444 | 1.408 |
| $\gamma$ | (dimensionless) | 3.315 | 3.729 |
| $E_{C-J} - E_o$ | cal/gm HE | 306.5 | 206.1 |
| $S_{C-J} - S_o$ | cal/°K/gm HE | -0.844 | -1.112 |
| $\gamma$ moles gas | $10^{-4}$ moles/gm HE | 349.168 | 351.437 |
| $V_g$ | cc/mole | 15.89 | 16.76 |
| Composition | | | |
| $H_2O$ | $10^{-4}$ moles/gm HE | 30.993 | 39.776 |
| $H_2$ | $10^{-4}$ moles/gm HE | 0.002 | -- |
| $CO_2$ | $10^{-4}$ moles/gm HE | 0.003 | 20.612 |
| $N_2$ | $10^{-4}$ moles/gm HE | 35.816 | 40.376 |
| $NH_3$ | $10^{-4}$ moles/gm HE | 9.368 | 0.248 |
| $CH_4$ | $10^{-4}$ moles/gm HE | 222.957 | 250.425 |
| C (graphite) | $10^{-4}$ moles/gm HE | -- | 269.962 |
| C (diamond) | $10^{-4}$ moles/gm HE | 318.029 | -- |

| Symbols | |
|---|---|
| D | detonation velocity |
| $\rho, T, \gamma, E, S, V$ | standard thermodynamic quantities |
| Subscripts | |
| C-J | Chapman-Jouguet conditions |
| o | original condition |
| g | gas |

Table IX. Covolumes Used in RUBY Code Calculations.

| Gaseous Element or Compound | Covolume ($cm^3$/mole) |
|---|---|
| C | 180 |
| $CH_4$ | 528 |
| CO | 390 |
| $CO_2$ | 670 |
| Cl | 57 |
| $Cl_2$ | 1157 |
| HCl | 1588 |
| ClO | 656 |
| $ClO_2$ | 847 |
| $H_2$ | 180 |
| $H_2O$ | 360 |
| $N_2$ | 380 |
| $NH_3$ | 476 |
| NO | 386 |
| $O_2$ | 350 |
| Al | 350 |
| AlCl | 880 |
| AlOCl | 2143 |
| $AlCl_2$ | 2118 |
| $AlCl_3$ | 2619 |
| AlO | 1160 |
| $Al_2O_2$ | 1800 |

Table X. RUBY Calculations for Propellant.

| Property | Units | ANB-3226 ($\rho_o$=1.73 g/cc) | AAB-3189 ($\rho_o$=1.72 g/cc) |
|---|---|---|---|
| $D_i$ | mm/μsec | 7.142 | 7.257 |
| $P_{C-J}$ | Mbar | 0.226 | 0.233 |
| $T_{C-J}$ | $10^3$ °K | 3.198 | 3.216 |
| $\rho_{C-J}$ | gm/cc | 2.327 | 2.313 |
| $\gamma$ | (dimensionless) | 2.899 | 2.893 |
| $E_{C-J} - E_o$ | cal/gm HE | 400.87 | 414.97 |
| $S_{C-J} - S_o$ | cal/°K/gm HE | -0.254 | -0.236 |
| Σ moles gas | $10^{-3}$ moles/gm HE | 28.855 | 28.655 |
| $V_g$ | cc/mole | 12.39 | 12.58 |
| Composition (Major Products) | | | |
| $CH_4$ | $10^{-3}$ moles/gm HE | 5.190 | 5.764 |
| CO | $10^{-3}$ moles/gm HE | 4.251 | 4.690 |
| $CO_2$ | $10^{-3}$ moles/gm HE | 1.652 | 1.882 |
| Cl | $10^{-3}$ moles/gm HE | 5.734 | 4.915 |
| $H_2$ | $10^{-3}$ moles/gm HE | 0.189 | 0.152 |
| $H_2O$ | $10^{-3}$ moles/gm HE | 8.437 | 6.944 |
| $N_2$ | $10^{-3}$ moles/gm HE | 2.610 | 3.440 |
| $NH_3$ | $10^{-3}$ moles/gm HE | 0.653 | 0.693 |
| AlCl | $10^{-3}$ moles/gm HE | 0.139 | 0.174 |
| $Al_2O_3$(solid) | $10^{-3}$ moles/gm HE | 2.710 | 2.692 |

Symbols

D detonation velocity

P,T,γ,E,S,V standard thermodynamic quantities

Subscripts

C-J Chapman-Jouguet conditions

o original state

g gas

The best fit of ideal detonation velocity $D_i$ versus RDX weight fraction, as calculated by the expression of Andersen and Parlin (reference 1), was given by

$$D_i = 6700 - 500\ f \quad \text{m/sec} \tag{34}$$

The predicted ideal detonation velocity for ANB-3226 from this expression is 6700 m/sec, which is not comparable to the RUBY prediction (Table X), which is 7142 m/sec. With no other basis upon which to estimate $D_i$, neither of these values can be preferred over the other. The RUBY computer program for calculation of detonation properties was subjected to further evaluation for the purpose of determining its applicability to solid composite propellants. Additional evidence has been found to support a conclusion that the RUBY program is not particularly suitable for propellant materials. Such evidence is subjective, however, because of the lack of experimental techniques or data on which to base an objective appraisal.

As an example, the RUBY program was used to calculate the detonation properties for an 80/20 mixture of RDX and aluminum under each of two conditions. In the first case, the aluminum was allowed to participate in the reaction; in the second case, it was not. Control over the reaction or nonreaction of aluminum is accomplished in the computer program simply by selection of the byproducts allowed by the programer. Thus, the various aluminum suboxides and aluminum oxide were permitted as byproducts in the first instance, but only aluminum (liquid) was permitted in the second case.

The purpose behind the deliberate restrictions placed upon the second run was to approximate conditions under which aluminum could not react within the C-J reaction zone. Considering the reaction times involved, this is a real possibility in the detonation of composite propellant. Probably a more accurate guess would be that some of the aluminum does react in the C-J zone and some does not. The necessity of forcing aluminum to do nothing but melt, in the second case, is brought about by the fact that RUBY, a one-dimensional code, does not consider reaction kinetics in solving for the detonation properties of a material. The artificial handling of the input data to RUBY is one way for the computed data to account arbitrarily for the reaction kinetics.

The results of the two computer runs were compared. As expected, lower energy and pressure were predicted in the C-J region when aluminum could not react. However, the calculated ideal detonation velocity in this case was higher than that calculated when aluminum was allowed to react (Table XI). This computation is not immediately acceptable, because a higher energy and C-J pressure

Table XI. RUBY Calculations for RDX/Aluminum (80% RDX, 20% Al; $\rho_o$ = 1.94 g/cc).

| Property | Units | Al (reactive) | Al (nonreactive) |
|---|---|---|---|
| $D_i$ | mm/μsec | 8.555 | 9.114 |
| $P_{C-J}$ | Mbar | 0.395 | 0.332 |
| $T_{C-J}$ | $10^3$ °K | 3.882 | 2.262 |
| $\rho_{C-J}$ | gm/cc | 2.60 | 2.44 |
| $\gamma$ | (dimensionless) | 2.957 | 3.856 |
| $E_{C-J} - E_o$ | cal/gm HE | 469.94 | 420.70 |
| $S_{C-J} - S_o$ | cal/°K/gm HE | -0.188 | 0.144 |
| Σ moles gas | $10^{-3}$ moles/gm HE | 25.32 | 27.06 |
| $V_g$ | cc/mole | 12.28 | 11.36 |
| Composition | | | |
| $Al_2O$ | $10^{-3}$ moles/gm HE | 0.909 | -- |
| CO | $10^{-3}$ moles/gm HE | 4.479 | 0.171 |
| $CO_2$ | $10^{-3}$ moles/gm HE | 2.485 | 5.454 |
| $CH_4$ | $10^{-3}$ moles/gm HE | 3.331 | 0.036 |
| $H_2$ | $10^{-3}$ moles/gm HE | 0.038 | 0.007 |
| $H_2O$ | $10^{-3}$ moles/gm HE | 2.854 | 10.531 |
| $N_2$ | $10^{-3}$ moles/gm HE | 10.385 | 10.737 |
| $NH_3$ | $10^{-3}$ moles/gm HE | 0.833 | 0.134 |
| $Al_2O_3$ (condensed) | $10^{-3}$ moles/gm HE | 2.796 | -- |
| Al (liquid) | $10^{-3}$ moles/gm HE | -- | 7.412 |
| Graphite | $10^{-3}$ moles/gm HE | 0.509 | 5.144 |

logically require that a higher detonation velocity should result. It has been demonstrated by this set of data that it is possible for the RUBY program to produce apparently erroneous data with reference to the predicted relationship of the detonation properties to the input parameters.

## Conclusions

The RUBY computer code was evaluated regarding its applicability to solid composite propellants. A series of compounds ranging from conventional high explosives to ammonium perchlorate, and formulations that included oxidizer plus aluminum or aluminum and binder, were subjected to the RUBY program and the respective predictions analyzed. The evaluation process has included comparison with known experimental data, investigation of the trends that the principal parameters follow as functions of compositions and density, and occasionally, comparison of the output with theoretically expected values.

A critique of RUBY, as an instrument for predicting the detonation parameters of composite propellant, is presented as Appendix II to this report. It is the conclusion of this analysis that the RUBY code is not applicable, in present form, to solid propellant. The principal disqualifying feature of RUBY is that the equation of state it uses is an unrealistic characterization of those conditions that are thought to apply in propellant detonation processes. Furthermore, RUBY is an empirical tool which must be adjusted internally by selection of the proper values of certain constants in the equation of state to agree in its predictions with experimental fact. It cannot be applied confidently to any compound or formulation that differs only slightly from the materials used to determine a particular set of its constants.

During the course of the evaluation of RUBY, considerable assistance has been given by individuals and organizations already experienced with RUBY and its operation. Among those to whom particular acknowledgment must be [illegible] are Dr. L. B. Seely of Stanford Research Institute, and J. Dieroff of the U.S. Naval Ordnance Test Station, China Lake.

## Reaction-Zone Measurements

To evaluate the use of the Jones expression directly, an attempt was made to measure the detonation velocity and reaction-zone thickness in samples of AAB-3189 RDX-adulterated propellant, and to attempt a fit of these data using the Jones equation (Equation 30).

## Test Description

Instrumentation. It has been shown that the reaction zone in high explosives is characterized by high conductivity (Reference 7). Using this fact as a starting point, a probe and associated circuit were designed that would permit the direct measurement of the length or this region. The conductance probe consists of a No. 60 drill rod (0.040-in. diameter) wrapped with an enamel-insulated 30-gauge copper wire. The probe is in series with a fixed, known resistor in a constant-voltage circuit. The voltage across the known resistor is monitored on an oscilloscope, provided with a Polaroid camera to make a permanent record of the pulse. Since it is a simple voltage-divider circuit, the monitored voltage is inversely related to the change in resistance of the probe, which in turn depends upon the length of the probe extended into the conductive region.

When the probe is placed in the side of a cylindrical charge, and inserted to the charge axis, the results shown schematically in Figure 4 are expected. The circuit closes as soon as the ionized region contacts the probe. Since the wave front is convex forward, the first contact should be made at the charge axis. The maximum conductivity should occur when the total inserted length of the probe extends into the zone, i.e., when the full diameter zone passes the probe. Subsequent "tailing-off" of the zone, in diameters near the critical diameter, and more abrupt cut-off, at the near-ideal diameters, should be indicated by a similar reduction of the probe conductivity.

The results from one of the preliminary tests are shown in Figure 5, where the close agreement between probes inserted to different depths is shown. One probe was inserted to the sample axis. The pulse resulting from this probe will show the profile of one-half the conductive zone. The second probe was inserted one-half radius toward the axis; its output will show the shape of the outer portion only of the zone which envelopes the probe. The overlapping of these traces, when an appropriate scale adjustment was made, indicated good support for the basic hypothesis upon which this method is based. The only adjustment required was to shift zero-time on the pulse obtained from the shorter probe to that time on the longer pulse which represented the time of arrival of the front to the tip of the short probe. The agreement in rising and falling slopes was excellent. Since the diameter of 4 in. is near the critical diameter (2.7 in.), the shape of this zone is as expected.

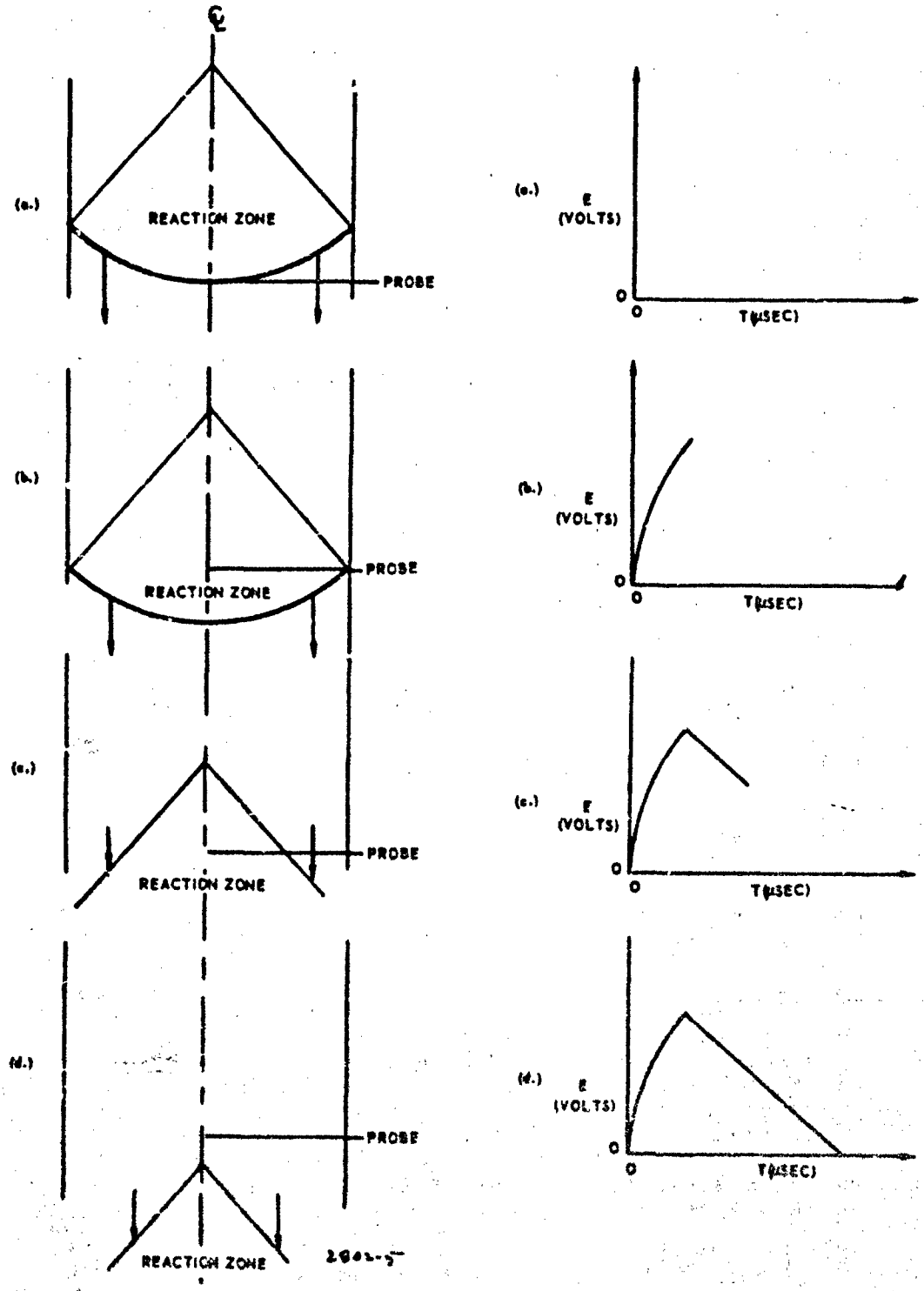


Figure 4. Correlation Between Probe Position in Reaction Zone and Oscillograph Pulse Shape.

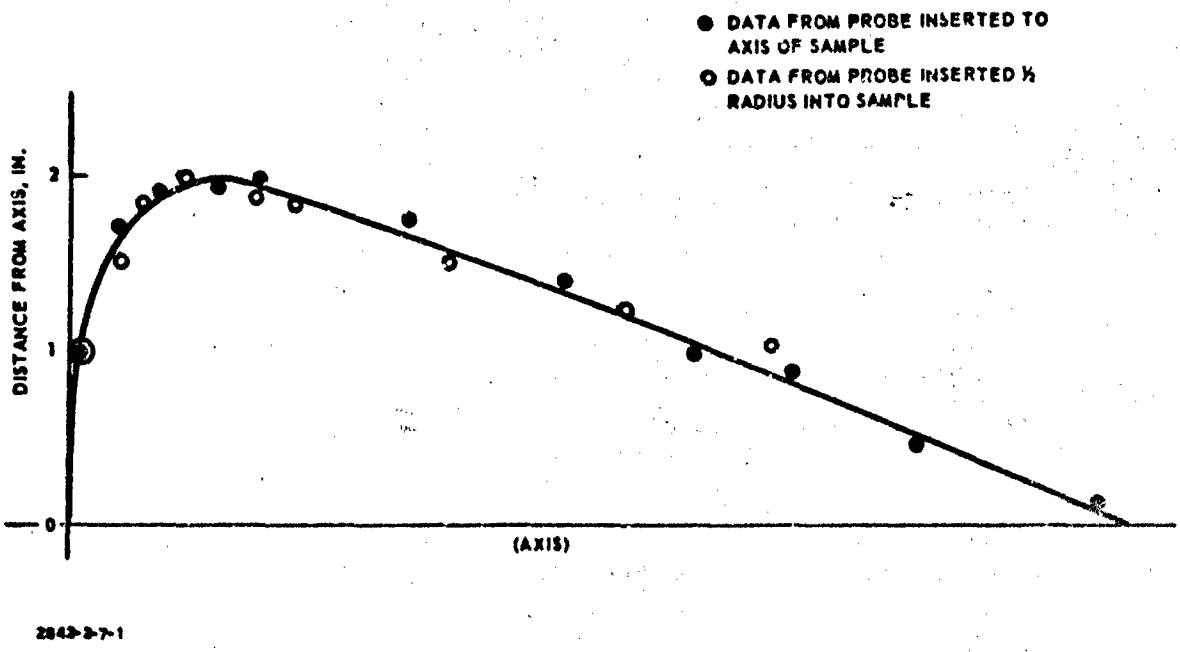


Figure 5. Mapping of Conductance-Zone Profile, 4-in. Diameter Sample.

Subsequent tests of this system, with an explosive linewave generator, showed that the inherent rise time was better than 0.2 μsec. Since the rise times of these pulses were near 4 μsec, no serious masking of the wavefront curvature could be attributed to the electronic system and, therefore, considerable confidence could be placed in the curvature deduced from the pulse shape.

In addition to the conductance probes, conventional ionization-type probes in circuit with a rasteroscillograph are placed at points along the sample length to provide detonation-velocity data. The length of the conductance zone then is calculated by multiplying the detonation velocity by the conductance-probe pulse duration time.

Setup. Propellant samples were selected in two shapes: solid right circular cylinders and square cross-section columns. The latter were chosen in anticipation of extending the theoretical detonation model to include geometrical effects. Subsequent experimental analysis of the critical-geometry theory (Section V) concluded that there was no significant advantage to be gained by pursuing in this direction.

The sample length was at least 4 times the charge diameter or the square side, to ensure stabilization of the detonation velocity. Only the lower half of each sample was instrumented for the velocity and zone-thickness determinations. The samples were initiated by Composition B boosters of matching cross section and 3/4 the length of the acceptor.

Results

The results of the tests are given in Tables XII to XIV. The pulse shapes obtained from conductance probes in the larger samples differed considerably from those obtained in the preliminary tests (e.g., Figure 5). The "ice-cream cone" was replaced by a trapezial shape, rising rapidly to its peak amplitude, decaying linearly at a slow rate, then dropping off rapidly to the original zero level. Several tests were conducted with heavier gauge probes, to determine whether the new pulse shape had been caused by consumption of the thinner probes. The pulse shapes and widths did not differ significantly with variation of the probe diameter, establishing the validity of the earlier tests.

Table XII. Average Detonation Velocities for Supercritical 9.2% RDX Adulterated Samples.

Solid Circular Cylinders

| Size (in) | Average Velocity (mm/μsec) | Standard Deviation of Velocity (mm/μsec) | Test No. |
|---|---|---|---|
| 12 (dia) | 4.74 | 0.180 | 3.2.3.1 |
| | 4.77 | 0.100 | 3.2.3.2 |
| | 4.77 | 0.083 | 3.2.3.3 |
| 8 | 4.70 | 0.065 | 3.2.3.4 |
| | 4.71 | 0.035 | 3.2.3.5 |
| | 4.71 | 0.081 | 3.2.3.6 |
| | 4.70 | 0.110 | 3.2.3.7 |
| | 4.67 | 0.160 | 3.2.3.8 |
| | 4.72 | 0.029 | 3.2.3.10 |
| | 4.69 | 0.012 | 3.2.3.11 |
| 6 | 4.62 | 0.096 | 3.2.3.23 |
| | 4.68 | 0.140 | 3.2.3.28 |
| | 4.52 | 0.085 | 3.2.3.37 |
| 4(dia) | 4.46 | 0.086 | 3.2.3.25 |
| | 4.48 | 0.051 | 3.2.3.31 |
| | 4.54 | 0.100 | 3.2.3.35 |
| Solid Square Columns | | | |
| 6.0 (side) | 4.62 | 0.057 | 3.2.3.27 |
| | 4.64 | 0.049 | 3.2.3.22 |
| | 4.64 | 0.197 | 3.2.3.38 |
| 4.5 | 4.63 | 0.105 | 3.2.3.21 |
| | 4.55 | 0.077 | 3.2.3.26 |
| | 4.54 | 0.001 | 3.2.3.36 |
| | 4.56 | - | 3.2.3.30 |
| 3.5 | 4.53 | 0.091 | 3.2.3.19 |
| | 4.45 | 0.046 | 3.2.3.24 |
| | 4.45 | 0.121 | 3.2.3.29 |
| | 4.44 | 0.035 | 3.2.3.34 |
| 3.0 (side) | 4.39 | 0.029 | 3.2.3.15 |
| | 4.44 | 0.085 | 3.2.3.16 |
| | 4.47 | 0.244 | 3.2.3.17 |
| | 4.36 | 0.082 | 3.2.3.18 |

Table XIII. Conductance-Probe Measurements.

| Test No. 3.2.3- | Size (in.) | Detonation Velocity (mm/μ sec) | Pulse Width (μsec) | Conductance-Zone Thickness (in.) |
|---|---|---|---|---|
| **Cylinders** | | | | |
| 1 | 12 (dia) | 4.74 | No data | No data |
| 2 | 12 | 4.77 | No data | No data |
| 3 | 12 | 4.77 | 56 | 10.5 |
| 4 | 8 | 4.70 | 33 | 6.1 |
| 5 | 8 | 4.71 | 37 | 6.8 |
| 6 | 8 | 4.71 | 37 | 6.8 |
| 7 | 8 | 4.70 | 50 | 9.2 |
| 8 | 8 | 4.67 | 30 | 5.6 |
| 9 | 8 | No data | 34 | No data |
| 10 | 8 | 4.72 | 38 | 7.0 |
| 11 | 8 | 4.69 | 50 | 9.2 |
| 23 | 6 | 4.62 | 40 | 7.3 |
| 28 | 6 | 4.68 | 42 | 7.2 |
| 33 | 6 | No data | 40 | No data |
| 37 | 6 | 4.52 | 40 | 7.3 |
| 20 | 4 | No data | 40 | 7.1 |
| 25 | 4 | 4.46 | 34 | 6.0 |
| 31 | 4 | 4.48 | 32 | 5.6 |
| 35 | 4 (dia) | 4.54 | 32 | 5.6 |
| **Square Columns** | | | | |
| 22 | 6 (side) | 4.64 | 35 | 6.4 |
| 27 | 6 | 4.62 | 33 | 6.0 |
| 38 | 6 | 4.65 | Not clear | No data |
| 21 | 4.5 | 4.63 | 30 | 5.4 |
| 26 | 4.5 | 4.55 | 33 | 5.9 |
| 30 | 4.5 | No data | 30 | No data |
| 36 | 4.5 | 4.54 | 32 | 5.8 |
| 19 | 3.5 | 4.53 | 22 | 3.9 |
| 24 | 3.5 | 4.45 | 30 | 5.3 |
| 29 | 3.5 | 4.45 | Not clear | No data |
| 34 | 3.5 | 4.44 | 30 | 5.3 |
| 15 | 3 | 4.39 | 14 | 2.4 |
| 16 | 3 | 4.44 | 13 | 2.3 |
| 17 | 3 | 4.47 | 22 | 3.8 |
| 18 | 3 (side) | 4.36 | 22 | 3.8 |

Table XIV. Average Detonation Velocity and Conductance-Zone Length.

| Size (in.) | Average Detonation Velocity (mm/μsec) | Average Conductance-Zone Length (in.) |
|---|---|---|
| 12 (dia) | 4.76 | 10.5* |
| 8 | 4.70 | 7.0 |
| 6 | 4.61 | 7.2 |
| 4 (dia) | 4.49 | 6.1 |
| 6 (side) | 4.64 | 6.2 |
| 4.5 | 4.57 | 5.6 |
| 3.5 | 4.47 | 4.8 |
| 3 (side) | 4.42 | 3.1 |

*This is the result of one test and should be so weighted.

## Conclusions

Concurrent with the experimental execution of this subtask, a theoretical study was made of the use of conductance probes to measure reaction-zone thickness. The basic problem in the case of detonable propellants is related to identification of the C-J surface and establishing whether the high-conductance region necessarily lies completely within the volume enclosed by the shock wave and C-J surface. In conventional high explosives the C-J surface is identical with the completed reaction surface. Since explosives generally are composed of one homogeneous compound or two highly reactive compounds, the reaction times are short and the reaction-zone thicknesses are relatively small. The assumption that the reaction-zone and high-conductance zone are the same is therefore quite logical.

In composite propellant, however, it is known that reaction times are long for some of the side reactions, notably the aluminum oxidation reaction. Using an alternate definition of the C-J surface, i.e., that surface that describes the region behind which there is no energy contribution in the forward direction to support the shock wave, then the difficulty in locating such a surface for detonating propellant can be appreciated. The C-J surface most probably is not coincident with the completion of all reactions. Therefore it must be assumed that the C-J reaction zone cannot be measured by the conductivity method. This interpretation leaves only the detonation velocity vs size data to be used in analyzing the validity of the Jones expression for propellants.

## Analysis of D(d) Data

The SOPHY detonation model (Reference 1) is expressed by

$$d = \frac{3/4\ K_J^{1/2} \left(\frac{d_{RDX}}{2}\right)\left[\left(\frac{G}{f+c}\right)^{1/3} - 1\right] D}{B\left[1 - (D/D_i)^2\right]^{1/2}} \qquad (35)$$

where

- $d$ = charge diameter
- $K_J$ = the constant in the Jones expression, left unspecified in the Aerojet model
- $d_{RDX}$ = average RDX particle diameter
- $G$ = a constant, unspecified

$f$ = wt fraction RDX

$c$ = equivalent wt fraction RDX for other initiation sites

$D$ = detonation velocity

$B$ = linear burning rate of ammonium perchlorate (AP)

$D_i$ = ideal detonation velocity

The AP burning rate can be expressed as a function of $T_s$, the surface temperature of the regressing AP, by

$$B = 2.1 \times 10^{-4} T_s \exp(-21{,}500/T_s) \text{ mm/}\mu\text{sec} \quad (36)$$

and $T_s$ by

$$T_s = 1824 + 18.4\, \rho_o D^2 - 0.137\, \rho_o^2 D^4 \ ^\circ\text{K} \quad (37)$$

where $\rho_o$ is the AP bulk density. Thus d can be related uniquely to D if $d_{RDX}$ and f are fixed. In this case, Equation 35 can be written

$$d = K_f g(f) \quad (38)$$

where

$$K_f = 3/4\, K_J^{1/3} \left(\frac{d_{RDX}}{2}\right) \left[\left(\frac{G}{f + c}\right)^{1/3} - 1\right] \quad (39)$$

and

$$g(f) = \frac{D}{B\left[1 - (D/D_i)^2\right]^{1/2}} \quad (40)$$

Therefore with D(d) data and an estimate of $D_i$ it is possible to compute g(f) from Equations 36, 37, and 40. If the detonation model is applicable to nonideal detonation, a plot of d vs g(f) should produce a straight line with slope $K_f$, for a propellant containing f weight fraction RDX.

The indicated correlation was carried out for AAB-3189 propellant (f = 0.092), using data obtained under this subtask for both circular cylinders and square columns. A computer program carried out the computations of Equations 36, 37, and 40 and determined $K_f$ by two methods: (1) by calculating the best value (denoted $K_c$) from the critical dimension and the critical detonation velocity estimates, and (2) by computing the least-squares best-fit, denoted $K_f$, from all the data.

Equation 38 could possibly be fit best with an additive constant, so a third value of $K_f$ (denoted $K^*_f$) was calculated for a fit to

$$d = K^*_f \, g(f) + C^*_f \tag{41}$$

where $C^*_f$ is the finite intercept.

The results of these calculations are shown in Table XV. The "residual variance" estimates give a measure of how well the best values of $K_f$ actually fit the data. Table XV reveals that the fit of Equation 41 is considerably superior to that of Equation 38. Although there are no residual variance estimates for Equation 33 using the critical values, a plot of g(f) vs d (and s, the side of the square columns) using $K_c$, yields a poor fit to the data. It may be assumed, therefore, that the best correlation of the non-ideal detonation data for AAB-3189 is represented by Equation 41.

Since this correlation differs from the assumed form (Equation 38), it is desirable to determine its effect when the SOPHY model is used to fit the critical diameter vs weight fraction RDX data generated on Contract AF 04(611)9945. At critical conditions, Equation 41 becomes

$$d_c = K^*_f \, g_c(f) + C^*_f \tag{42}$$

However, since it was shown (Reference 1) that $d_c$ is linearly dependent on $(1/f + c)^{1/3}$, $K^*_f$ or $C^*_f$ may depend on $(1/f + c)^{1/3}$. Therefore, in the general case,

$$K^*_f = K^*_1 \left(\frac{1}{f + c}\right)^{1/3} + K^*_2 \tag{43}$$

$$C^*_f = C^*_1 \left(\frac{1}{f + c}\right)^{1/3} + C^*_2 \tag{44}$$

where $K^*_1$, $K^*_2$, $C^*_1$, and $C^*_2$ are constants independent of $(1/f + c)^{1/3}$.

Substituting Equations 43 and 44 into Equation 42 gives, after rearranging,

$$d_c = \left[K^*_1 \, g_c(f) + C^*_1\right] \left(\frac{1}{f + c}\right)^{1/3} + \left[K^*_2 \, g_c(f) + C^*_2\right] \tag{45}$$

Table XV. Correlation of Detonation Model in the Nonideal Region for AAB-3189 Propellant (f = 0.092).

SQUARE COLUMNS

| Equation | Slope (in.) | Intercept (in.) | Residual Variance ($in.^2$) |
|---|---|---|---|
| $s = \bar{K}_f g(f)$ | $\bar{K}_f = 3.03 \times 10^{-4}$ | -- | 5.31 |
| $s_c = K_c g_c(f)$ | $K_c = 8.08 \times 10^{-4}$ | -- | -- |
| $s = K^*_f g(f) + C^*_f$ | $K^*_f = 18.8 \times 10^{-4}$ | $C^*_f = -3.52$ | 0.0092 |

CIRCULAR CYLINDERS

| Equation | Slope (in.) | Intercept (in.) | Residual Variance ($in.^2$) |
|---|---|---|---|
| $d = \bar{K}_f g(f)$ | $\bar{K}_f = 11.2 \times 10^{-4}$ | -- | 2.01 |
| $d_c = K_c g_c(f)$ | $K_c = 8.73 \times 10^{-4}$ | -- | -- |
| $d = K^*_f g(f) + C^*_f$ | $K^*_f = 23.3 \times 10^{-4}$ | $C^*_f = -4.87$ | 0.197 |

Combining Equations 35 and 40, at the critical case, gives

$$d_c = \left[\frac{3}{4} K_J^{1/2} \left(\frac{d_{RDX}}{2}\right) G^{1/3} g_c(f)\right] \left(\frac{1}{f + c}\right)^{1/3} - \left[\frac{3}{4} K_J^{1/2} \left(\frac{d_{RDX}}{2}\right) g_c(f)\right] \quad (46)$$

or

$$d_c = k_1 (f + c)^{-1/3} + k_2 \quad (47)$$

By Equation 9, $k_1 = 17.32$ and $k_2 = -34.94$ are the best estimates of these constants in the detonation model.

For Equations 45 and 46 to be compatible the following must be true:

$$K^*_1 g_c(f) + C^*_1 = \frac{3}{4} K_J^{1/2} \left(\frac{d_{RDX}}{2}\right) G^{1/3} g_c(f) = k_1 \quad (48)$$

$$K^*_2 g_c(f) + C^*_2 = \frac{3}{4} K_J^{1/2} \left(\frac{d_{RDX}}{2}\right) g_c(f) = k_2 \quad (49)$$

Since $K_J$, $d_{RDX}$, and G are constants, Equations 43, 44, 48, and 49 state that $K^*_1$, $K^*_2$, $C^*_1$, and $C^*_2$ depend only on $g_c(f)$. However, since it was found that $g_c(f)$ is itself a constant independent of f (Reference 1), the equations require that $K^*_1$, $K^*_2$, $C^*_1$, and $C^*_2$ be constants also independent of f. To determine if Equations 48 and 49 are satisfied, it is necessary to specify all these constants. However, examination of Equations 43 and 44 shows that this cannot be done until other values of K* and C* are determined at other f's.

Such data became available during the performence of the initiation criteria tests (Section VII), in which AAB-3225 (7.1% RDX) was tested in diameters ranging from 6 in. to 24 in. The detonation velocity data were fit to Equation 41, yielding

$$d = 3.72 \times 10^{-3} g(f) - 4.565 \text{ in.} \quad (50)$$

The standard deviation of $K^*_f$ is $2.4 \times 10^{-4}$ in. and that of $C^*_f$ is 1.022 in., for f = 0.071.

Solving Equations 43 and 44, and using Equation 42, the values of $K^*_1$, $K^*_2$, $C^*_1$, $C^*_2$, and $g_c(f)$ were obtained. Because the least squares estimates of $K^*_f$ and $C^*_f$ possess statistical uncertainties (standard deviations), the estimates of $K^*_1$, $K^*_2$, $C^*_1$, and $C^*_2$ will possess them also. The standard deviations of the least squares estimates are calculated by standard propagation-of-error techniques. The estimate of $g_c(f)$ is subject to statistical variation because detonation velocity measured near the critical diameter contains random variation.

Substitution of these values into Equations 48 and 49 yields the values of $k_1$ and $k_2$ that have been estimated from the detonation velocity data. Standard deviations of these estimates were obtained, again by the propagation-of-error technique.

The expected values and their standard deviations are shown in Table XVI.

Table XVI. Estimates of $K_1^*$, $K_2^*$, $C_1^*$, $C_2^*$, $g_c(f)$, $k_1$, and $k_2$.

| | Expected Value | Standard Deviation |
|---|---|---|
| $K_1^*$ (in.) | 0.00688 | 0.00135 |
| $K_2^*$ (in.) | - 0.01265 | 0.00297 |
| $C_1^*$ (in.) | 1.59499 | 5.92641 |
| $C_2^*$ (in.) | - 8.32503 | 12.76201 |
| $g_c(f) \times 10^3$ | 3.305 | 0.258 |
| $k_1$ (in.) | 24.34175 | 7.56003 |
| $k_2$ (in.) | -50.14478 | 16.43279 |

The standard deviations of $k_1$ and $k_2$ are quite large, primarily due to the large standard deviations calculated for the estimated intercepts $C_f^*$.

The estimated standard deviations for the $k_1$ and $k_2$ determined from critical diameter data are 0.148 and 0.441, respectively, which shows practically no variation when compared with those estimated from the detonation velocity data. In view of the large standard deviations associated with the $k_1$ and $k_2$ estimates

obtained from the detonation velocity data, it is impossible to state that the estimates differ significantly from those obtained from the critical-diameter data least squares fit. If it is assumed that these least squares k values are not subject to statistical error, an assumption that only affects the simplicity of the statistical test and not the conclusion, then the following normal deviate statistic can be used to test for a significant difference between the two corresponding k estimates:

$$Z = \frac{k_{vel} - k_{l\text{-}s}}{s_{k_{vel}}} \qquad (51)$$

where $k_{vel}$ is the k value obtained from the velocity data, $k_{l\text{-}s}$ is the least squares estimate obtained from the critical diameter data, and $s_{k_{vel}}$ is the standard deviation of the velocity data estimate. For $k_1$, $Z = -0.929$; for $k_2$, $Z = -0.925$.

The Z values have an associated significance level of 0.18. Usually, Z values below 0.05 are considered by statisticians to infer a significant difference. Therefore, it may be concluded that the k values determined from the detonation velocity data do not statistically differ from the k values obtained from the critical diameter data.

It may be concluded that the correlation found with Equation 41 is not inconsistent with the Aerojet detonation model. It should be noted that Equations 48 and 49 must be satisfied for values of the constants determined from any pair of(K*, C*) data and must therefore hold for all RDX contents from $0 \leq f \leq 0.10$ if the SOPHY model is to be generally valid for nonideal detonation.

## SECTION IV

## LARGE CRITICAL DIAMETER TESTS

### SELECTION OF SAMPLE SIZES

The best statistical fit to the detonation model that was available in the early stages of SOPHY II predicted that the critical diameter of AAB-3226 propellant was 64.0 in. (Equation 5). The standard deviation limits were at 48.5 and 79.5 in. A conventional critical diameter test program requires multiple testing at several sizes within the region of the predicted critical diameter. The high expense of performing such a series of tests at the large scale indicated by the theoretical predictions was sufficient to preclude the adoption of a conventional critical diameter approach.

It was agreed to limit the number of tests to three, and to conduct these tests at three different diameters instead of repeating tests at any particular diameter. Greater information value would be obtained under these conditions. The test program, instead of attempting an estimate of the mean critical diameter, is designed to determine the approximate range within which the critical diameter could be found.

The first sample size to be selected was one that the theoretical model predicted would sustain detonation. That selection was a 72-in. diameter sample. The probability that this size will detonate is not 100%, but it is high enough to justify the selection. As is shown in Table I, the nonstandardized solution of the detonation model indicates a probability that the critical diameter will be below 72.0 in. is that 88.6% or 233 of the 263 solutions gave solutions for the critical diameter less than or equal to 72 in.

This probability is indicated to be even higher by the statistical approach. Assuming that critical diameters are normally distributed at zero-percent RDX with a mean of 64.0 in. and a standard deviation of 5.18 in., a 72-in. diameter would be 1.54 standardized normal units above the mean value. Thus, the probability of 72 in. equalling or exceeding the critical diameter is approximately 0.94. Giving equal weight to both analyses, the probability of a detonation at 72 in. is greater than 0.90.

The second sample could not be selected finally until the first sample had been tested. The two possible sizes for the second sample were 60-in. and 96-in. diameter, depending on whether the 72-in. diameter sample did or did not detonate. An RDX-adulterated

propellant (f = 0.0025) was tested under SOPHY I, in a 48-in. diameter, and it did not detonate (Reference 1). It is reasonable to assume, therefore, that the unadulterated propellant is subcritical at 48-in. diameter also. The 60-in. sample size is midway between 72 in. diameter and 48 in. diameter, so that its test result would reduce the range to 12 in. between the smallest detonable and the largest nondetonable sizes.

The results of the 72-in. diameter test, discussed fully in the paragraph entitled Test CD-96, were positive. The detonation at 72 in. made the 60-in. diameter sample the choice for the second test. The optional third test was eliminated in favor of redirection of that funding toward expansion of the overall SOPHY II technical objectives in the areas of critical geometry sustainment and initiation studies.

## TEST SITE

The large critical diameter tests were conducted at the 1-36D Hazardous Test Facility, Air Force Rocket Propulsion Laboratory, Edwards Air Force Base, California. This facility is designed to accommodate test articles of up to 1 million lb of high explosive. The field area contains three instrumentation legs at 120° spacing, along which are installed the necessary mounts for air blast and radiation measuring devices at several distances from ground zero (Figure 6). The maximum range is 1500 ft. Eight permanent field housings are provided for high-speed and documentary camera coverage.

## TEST CD-96 (72-IN. DIAMETER)

### Test Setup

The propellant acceptor charge was constructed at the test site from five 6-ft-diameter by 4.8-ft-high segments of ANB-3226 propellant. Each segment contained more than 14,000 lb of propellant; the total propellant weight was approximately 74,000 lb. The segments were shipped in their molds from Aerojet's Solid Rocket Operations Plant at Sacramento. At the test site each mold was removed and an 0.080-in.-thick aluminum cylindrical restraining fixture was fastened around the bare propellant. The excessive loading experienced by the propellant in its final test position required the application of a restraining fixture to preserve dimensional uniformity and physical integrity. The aluminum

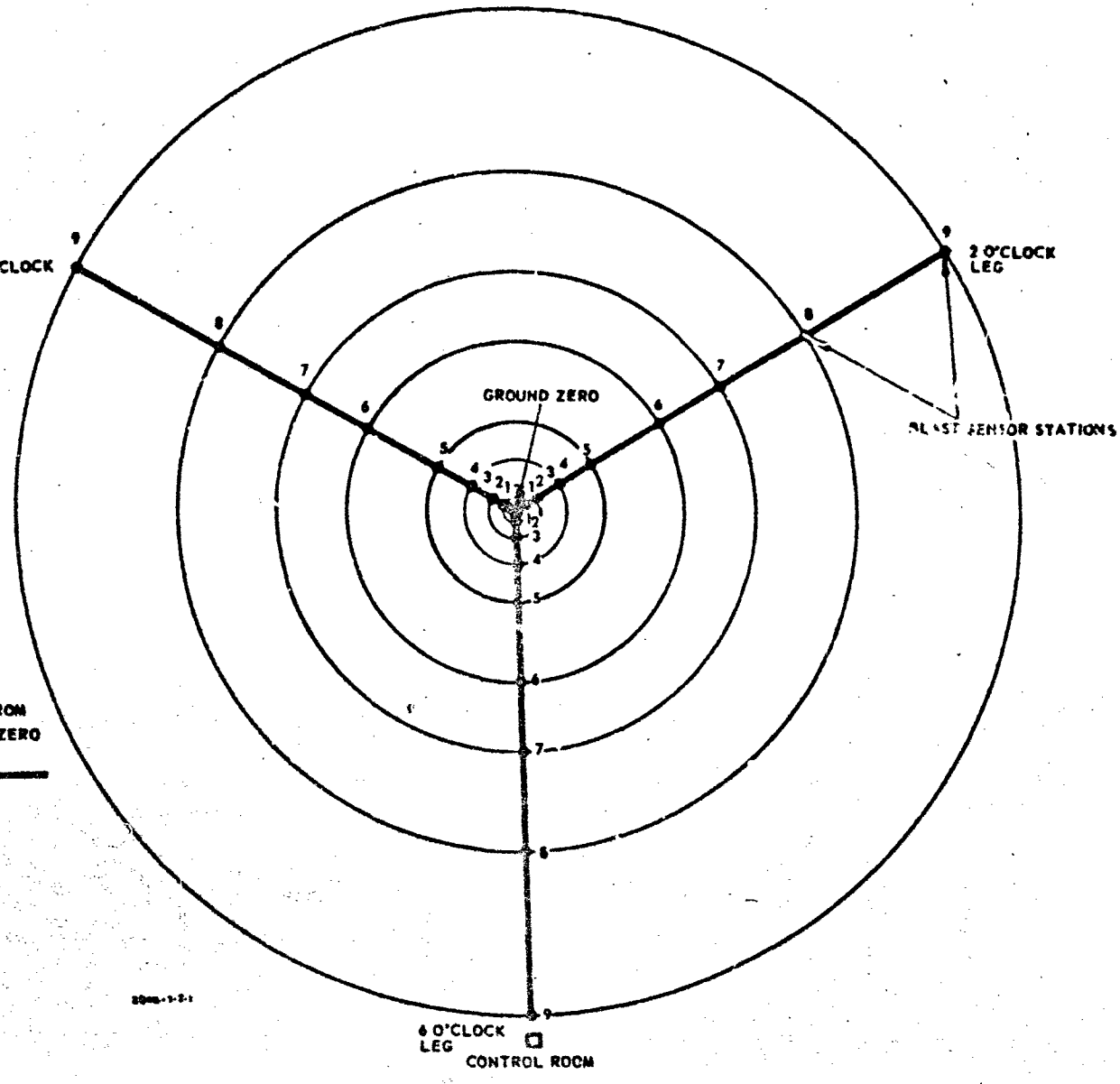


| STATION NO. | DIST. FROM GROUND ZERO (FT) |
|---|---|
| 1 | 25 |
| 2 | 40 |
| 3 | 70 |
| 4 | 140 |
| 5 | 250 |
| 6 | 500 |
| 7 | 700 |
| 8 | 1000 |
| 9 | 1500 |

Figure 6. Blast Instrumentation Legs, AFRPL 1-36D Facility.

girdle design represented the minimum confinement consistent with meeting the stress loads that were anticipated.[2]

The girdles provided sites from which tie-down cables were attached to secure the segments in a four-point pattern to "deadmen" buried 40 ft. from the charge. The segments were positioned and tied down to form an exactly vertical column, determined by triangulation with a pair of transits.

The propellant segments were lifted into their final positions by a vacuum chuck assembly capable of handling propellant in diameters up to 96 in. Woven straps beneath the segments provided physical support against a vacuum failure. Each segment-lifting operation proceeded without event, proving out the vacuum chuck design.

The TNT booster consisted of stacked segments, each measuring 3 ft thick. The shape of each segment resembled three 1-ft-thick cylindrical sections, whose diameters decreased by 4 in. progressing toward the top of the segment. Thus, a 3-to-1 height-to-base-diameter cone was approximated by the completely assembled booster.

The estimated weight of the booster was 18,000 lb. The booster molds, in and by which the segments were lifted, were removed after each segment was finally positioned. Tie-down cables were attached to rings placed at two levels on the booster to secure the TNT.

This configuration was 42 ft high. The detonator was placed in a final cone of C-4 explosive placed on top of the stacked TNT booster.

---

[2]These necessary modifications to the design of the acceptor charge differentiate the 72-in. diameter and the 60-in. diameter tests from the smaller tests performed in SOPHY I, where the charges were cast full length and tested in the unconfined state. The results of these two tests cannot properly qualify for inclusion with the SOPHY I data in determining the best values of the coefficients of the detonation model. However, the effect of the 0.080-in. confinement on lowering the critical diameter is certainly minor, and the segment interfaces are practically nonexistent under the stress loading imposed by the total assembly. Therefore, despite the difference between the two series of tests, the 72-in. and 60-in. tests are considered to be acceptable confirmatory tests of the model.

The test setup is shown schematically in Figure 7. The leveled test pad consisted of a square concrete footing measuring 10 ft on a side. The individual sides of the footing were 1 ft wide at the top, 21 in. wide at the bottom, and 4 ft deep, buried in the soil. The soil inside the ring was removed to a depth of approximately 8 in. to provide the customary air gap beneath that portion of the steel witness plate under the charge.

The need for this support arrangement was dictated by the questionable ability of the soil, at ground zero, to provide stable support for wood beams under the plate. Because of the refilling of craters left after each 48-in.-diameter test in SOPHY I, it was estimated that the ground was not strong enough to support the 60-ton load imposed by the witness plate, propellant, and booster.

The witness plate was a mild-steel plate, 6 in. thick by 10 ft square, weighing approximately 12 tons. The handling of this plate was facilitated by ear lugs welded at its edges. A 45-ton-capacity crane provided by the Air Force was used to lift the plate and the propellant and booster segments. Figure 8 shows the complete test configuration standing on the witness plate, at the moment when the ionization probes were being inserted and checked out. The uppermost segment of the booster assembly, made available from the SOPHY I project, was not designed to be removed from its mold; consequently, this configuration had plywood strengthening rings and an aluminum sheet around that segment.

## Instrumentation

### Detonation-Velocity Measurement

Ionization probes of two designs were used with rasteroscillograph systems to provide detonation-velocity data. These probes were placed along the length of the propellant sample in two rows, one for each type of probe, located 90° apart on the charge surface. Holes in the restraining girdles provided access to the propellant surface at the locations selected as probe sites.

To provide a streak record of the event, a modified Beckman & Whitley Model 318B camera with 35mm film was synchronized with the firing of the charge.

The low level of luminosity from detonating adulterated propellant, which is also expected to be characteristic of unadulterated propellant, plus the distance the camera had to be placed from ground zero, put a heavy demand upon the lens system of the camera. The camera employed in this test includes a 629mm objective lens.

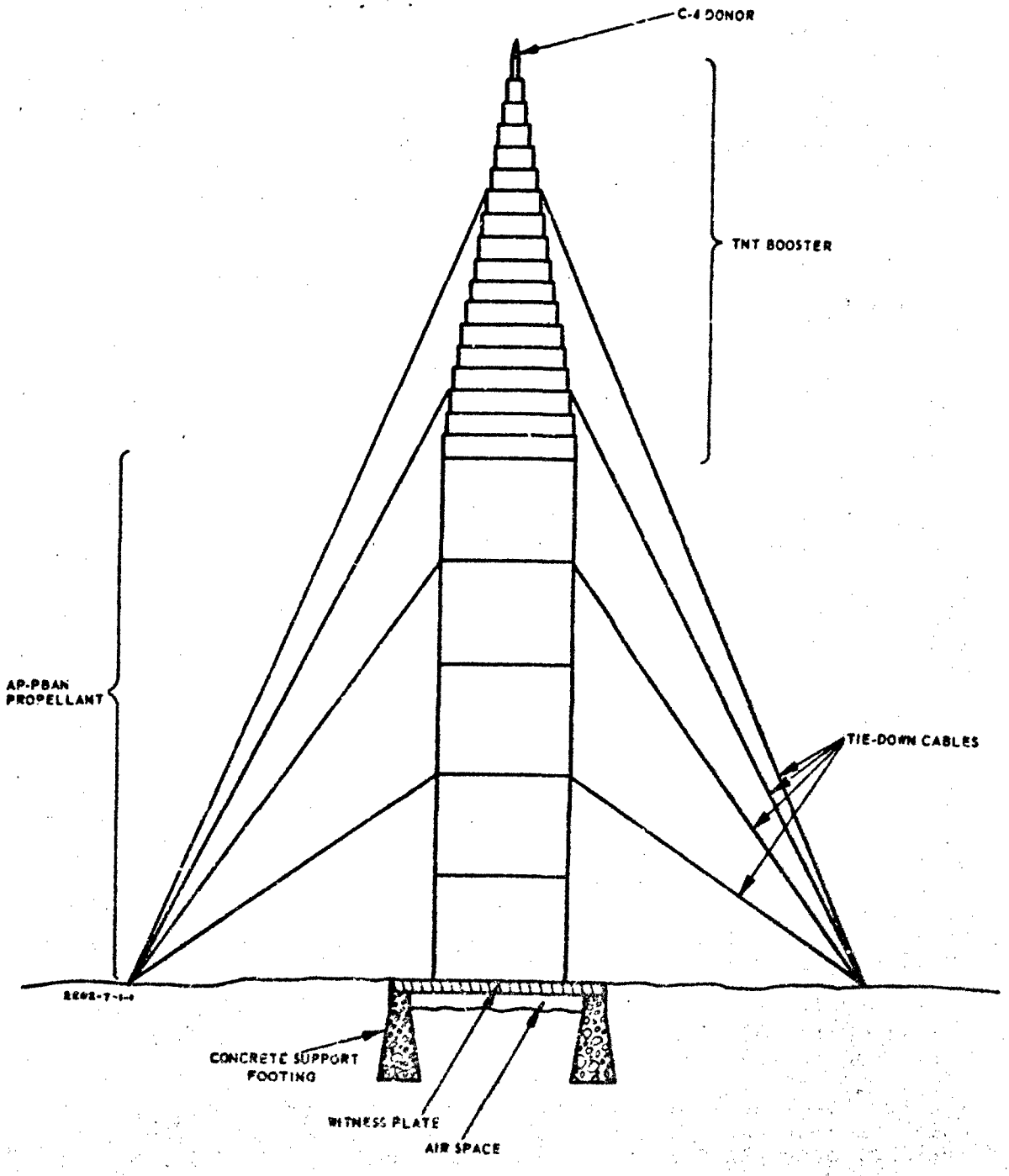


Figure 7. Critical-Diameter Test Setup for 72-in.-Diameter Sample.

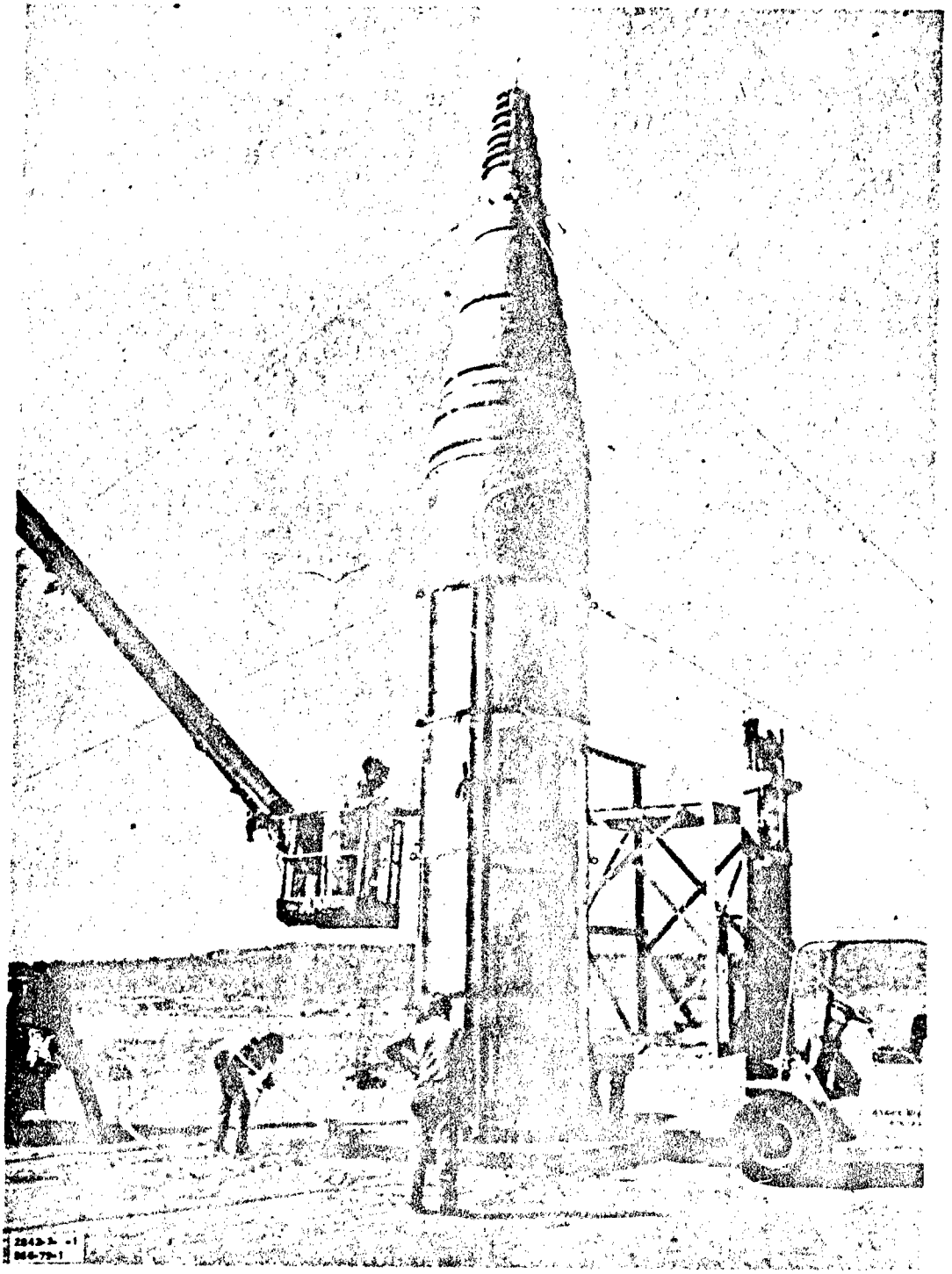

Figure 8. 72-in. Critical-Diameter Test Setup, CD-96.

## Blast Overpressure and Impulse Measurement

A Kistler system provided side-on and face-on blast pressure data. This system consists of Type 601A and 701A side-on gauges, Type 601A face-on gauges, and Kistler amplifiers. The output from the system was recorded directly on FM tape, using Ampex FR 1200 (120 ips) and Ampex ES100 (60 ips) recorders.

## Fireball Growth Rate

Documentary and high-speed photographic coverage of the test was provided by five Fastax cameras, two Milliken cameras, and a 35mm camera. The Fastax and Milliken cameras were operated at film speeds ranging from 64 fps to 8000 fps and the 35mm camera at 6 fps. Helicopter-borne cameras recorded the event on 70mm film at 20 fps and 16mm film at 200 fps. Except for the black-and-white 70mm film, all the film used was color.

The principal purpose of this camera coverage is to provide records from which the fireball growth rate can be calculated. In addition, the coverage makes it possible to measure the wave velocity along the ground independently of the blast gauges. It also provides a means of detecting the emergence of burning propellant fragments from the fireball; such fragments are characteristic of nondetonating propellant charges.

## Fireball Radiation

Instrumentation placed within the expected 700-ft-radius fireball region to measure fireball heat flux and radiation included two pairs of Deltacouples and two radiometers. These were located in two stations, each consisting of a Deltacouple pair and a radiometer. In addition, the instrumentation included a pyrometer to measure the fireball temperature.

## Audio Level

As part of the instrumentation designed for this test, it was decided to include a sound-level record at the 1/2-psi overpressure level. Assuming 100% TNT equivalence for the propellant, the gauge site was determined to be 3400 ft from ground zero. The system employed was a B&K Instrument No. 2203 sound-level meter with a No. 4133 1/2-in. microphone.

## Test Results

### General Observations

Eyewitness observation of the test, and subsequent examination of the photographic records, revealed that no burning propellant was expelled in the test. Based on these observations, no evidence of a no go can be found in the photographic records. The event as recorded by a 35mm camera at 6 fps is shown in Figures 9 and 10.

Fragments of the aluminum restraining fixtures used in CD-96 were collected after considerable searching of the area. The recovered fragments are shown in Figure 11. The size and condition of these fragments offer further evidence for the detonation of this propellant. These are the only fragments that have been sighted.

The witness plate was severely broken up by the detonation. In all previous no go's in the large critical-diameter tests on Contract AF 04(611)9945, the witness plates were dished but not broken. In all previous go's the plates were punched, and strong evidence of flow was observed at the portions of the plates beneath the periphery of the charges.

The witness plate fragments from the 72-in. diameter test did not show the characteristic flow. However, the velocity data (discussed below) provide the most probable answer to this problem. The calculated shock pressure corresponding to a detonation velocity of approximately 3.2 mm/μsec in this propellant is 45 kbar. Transitted to steel, this pressure would not exceed 90 kbar. Yet NOL data indicate that 95 kbar is required to punch a 3/8-in.-thick, mild-steel plate (Reference 8). Therefore, it may be concluded that the witness plate reaction to the low-velocity detonation produces results different from those generally observed with high-velocity detonations. Concerning the witness-plate technique, the presence of a characteristic punch is ample evidence of a go, but the absence of such a reaction is not sufficient proof of a no go.

The crater left by the shot measured 32 ft in diameter and 10 ft deep (to the backfill level). Figure 12 is a photograph of the crater, showing the largest piece of broken witness plate in the foreground.

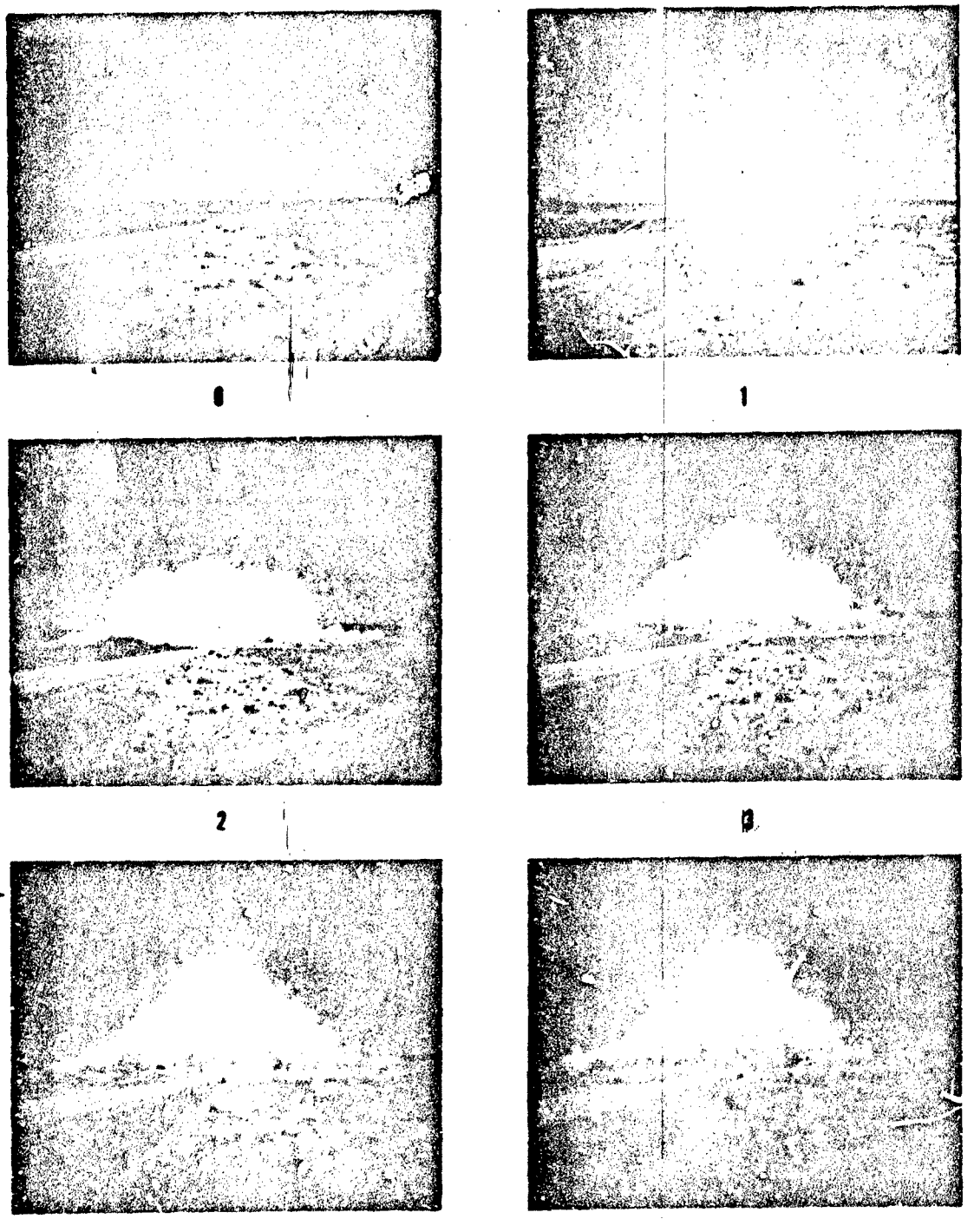


Figure 9. Test CD-96 (Frames 0 to 5): Camera Speed 6 fps.

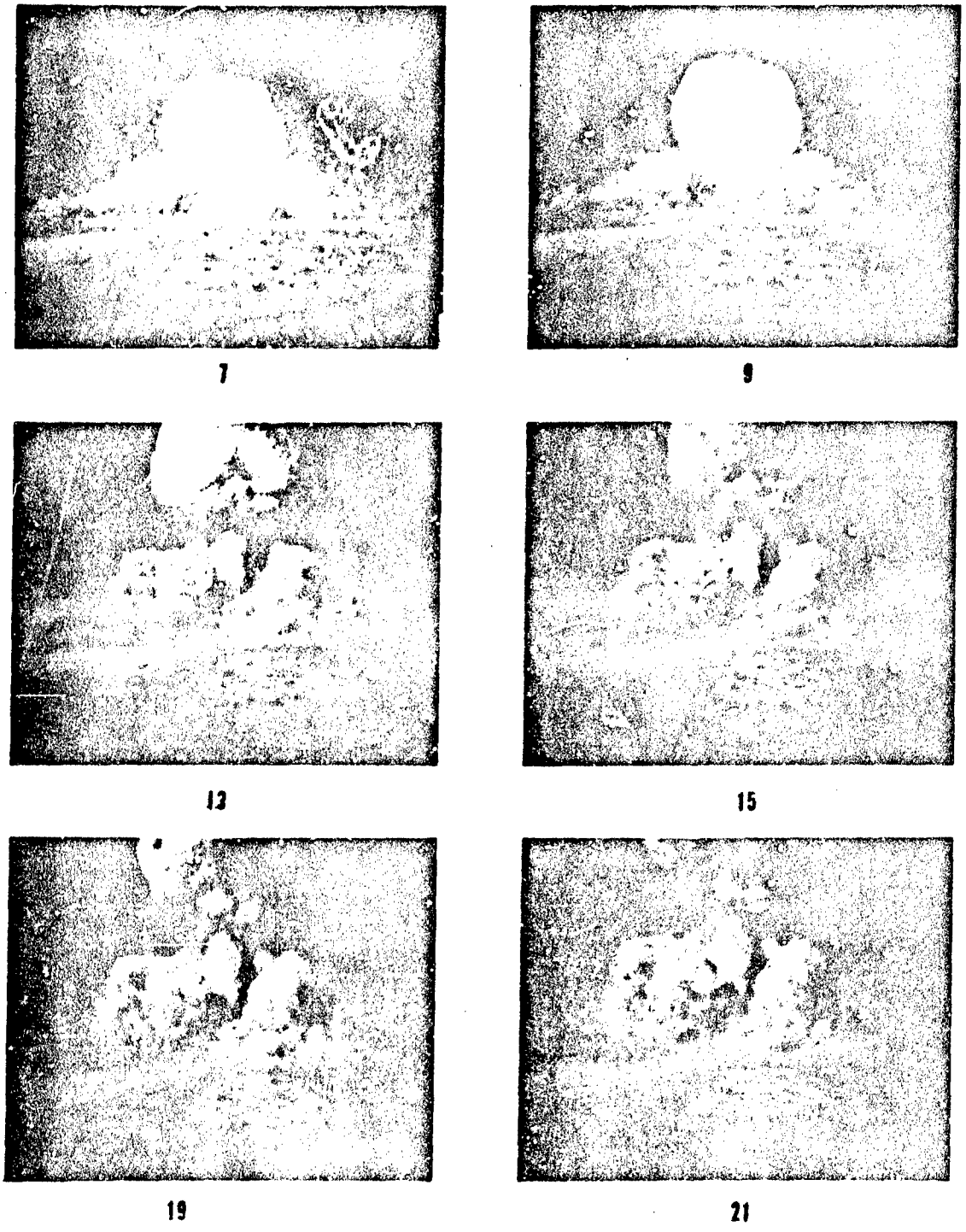


Figure 10. Test CD-96 (Frames 7 to 21, selected): Camera Speed 5 fps.

Figure 11. Fragments of Aluminum Sheet from Test CD-96.

Figure 12. Crater, Test CD-96.

## Detonation Velocity

The probe-rasteroscillograph systems produced excellent records of a sustained detonation over the lower 2-1/2 diameters of the charge. The average detonation velocity from these probe records is 3.2 mm/μsec. Sonic velocity in this propellant is estimated at 1.9 mm/μsec. The observed velocity is clearly supersonic and steady-state. From these data there can be no doubt that the sample did detonate. Figure 13 shows the plotted values of detonation velocity vs distance down the charge. The split-probe data were generated from an experimental probe design being evaluated in the test. While not accurate, perhaps because of nonuniform fabrication, these probes did provide nominal support to the ion-probe data and for that reason their data are shown. The streak record for CD-96 was lost because of a failure by the film cassette to properly engage the film for removal from the camera. As the result of this failure, the entire film length was exposed to daylight.

## Blast Overpressure and Impulse

The records obtained from the Kistler blast gauges have been read for peak overpressure and impulse at the various gauge stations. Reproductions of the actual profiles are presented in Appendix III to show the generally excellent quality of the raw data. The calibration step represents the overpressure level that is indicated by the adjacent numerical value, and the overpressure-time profile is shown at the right. The calibration steps are generated artifically by applying a certain voltage to the system. They are evaluated in psi by knowing the transducer sensitivity (picocoulombs per psi) and the amplifier gain-setting.

The peak overpressures obtained from the records were corrected after an intensive and thorough calibration of the pressure transducers, amplifiers, recording system, and playback system. The overpressures contributed by the propellant are shown in Figure 14, plotted with reference to the overpressures expected from various weights of TNT. Sample-contributed overpressures calculated from the shock velocity data are also shown. The TNT equivalence of the propellant, in terms of peak side-on overpressure, ranged from 200% at the closer distances to 175% at the farther distances.

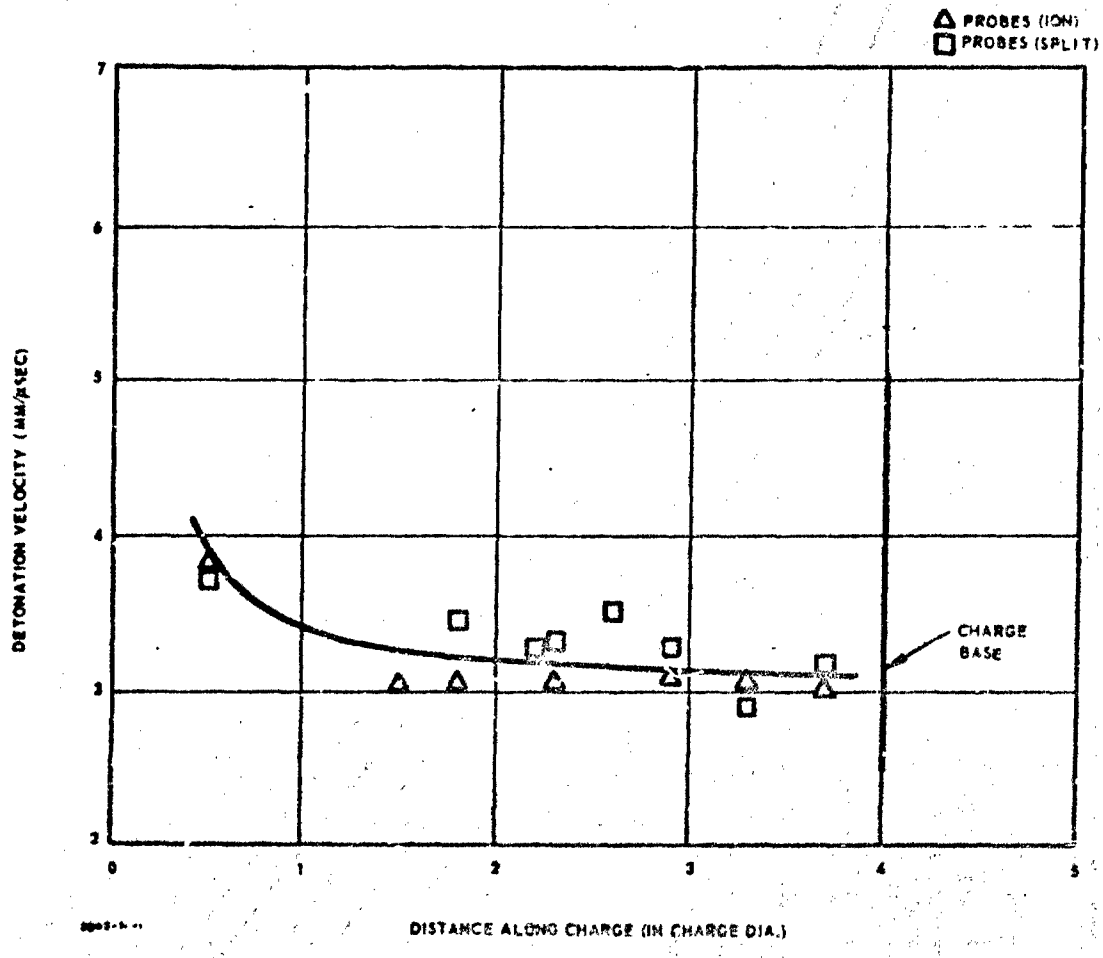


Figure 13. Detonation Velocity vs Distance Along Charge, CO-96.

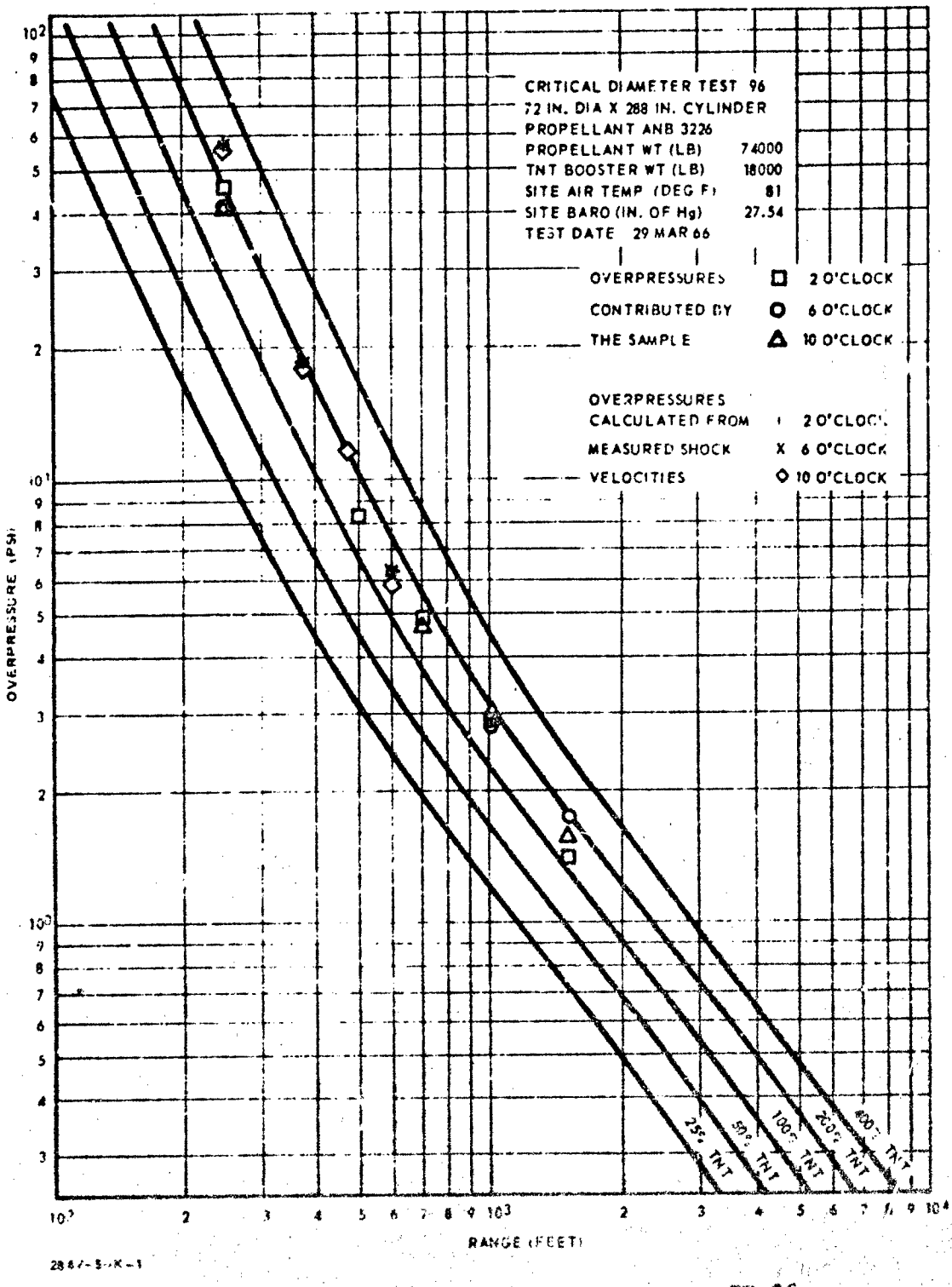


Figure 14. Peak Side-On Overpressures, CD-96.

## Radiation Data

The thermal radiation data, gathered by means of radiometers, Deltacouples, and a pyrometer, could not be reduced. The extremely high level of electromagnetic radiation produced by the detonation detrimentally affected all channels by producing excessive noise in the initial portions of the pulses. The shock wave arrival on the output of the radiometer stations was marked by an abrupt negative sweep. The Deltacouple signals contained extraneous noise and appeared to cross-talk. The pyrometer data are unusually low, probably because the fireball was obscured from the pyrometer by the dust clouds along the surface of the ground. Study of the film records suggests that the pyrometer should have been placed farther above ground level.

## Fireball

The 72-in. diameter test (CD-96) was recorded by a number of high-speed cameras. The films were read for fireball diameter and height. The data were finally plotted as fireball growth, over the first 100 msec, and fireball size history, during the first 5 sec. Fireball diameter is taken to be the maximum horizontal dimension of the fireball; fireball height is the maximum vertical dimension of the fireball, not the height of the fireball above ground. That is, when the fireball lifts off the ground, height becomes the vertical diameter of the fireball.

The fireball growth in CD-96 is shown in Figure 15. Only the fireball diameter is graphed, because all the cameras had the charge so high in the frame that the top of the fireball was very quickly out of frame, which prevents height measurement. Excellent agreement is seen to have been reached in the films taken at camera stations F and G. Other records are not reducible, either because of (1) poor focus, (2) too great a range of camera speed from the beginning of the event to the end, or (3) because the posts near the charge, which are used to obtain a distance-scaling factor, were not detected in the film. The fireball history is shown in Figure 16. The short duration (375 msec) of the information is the result of poor framing.

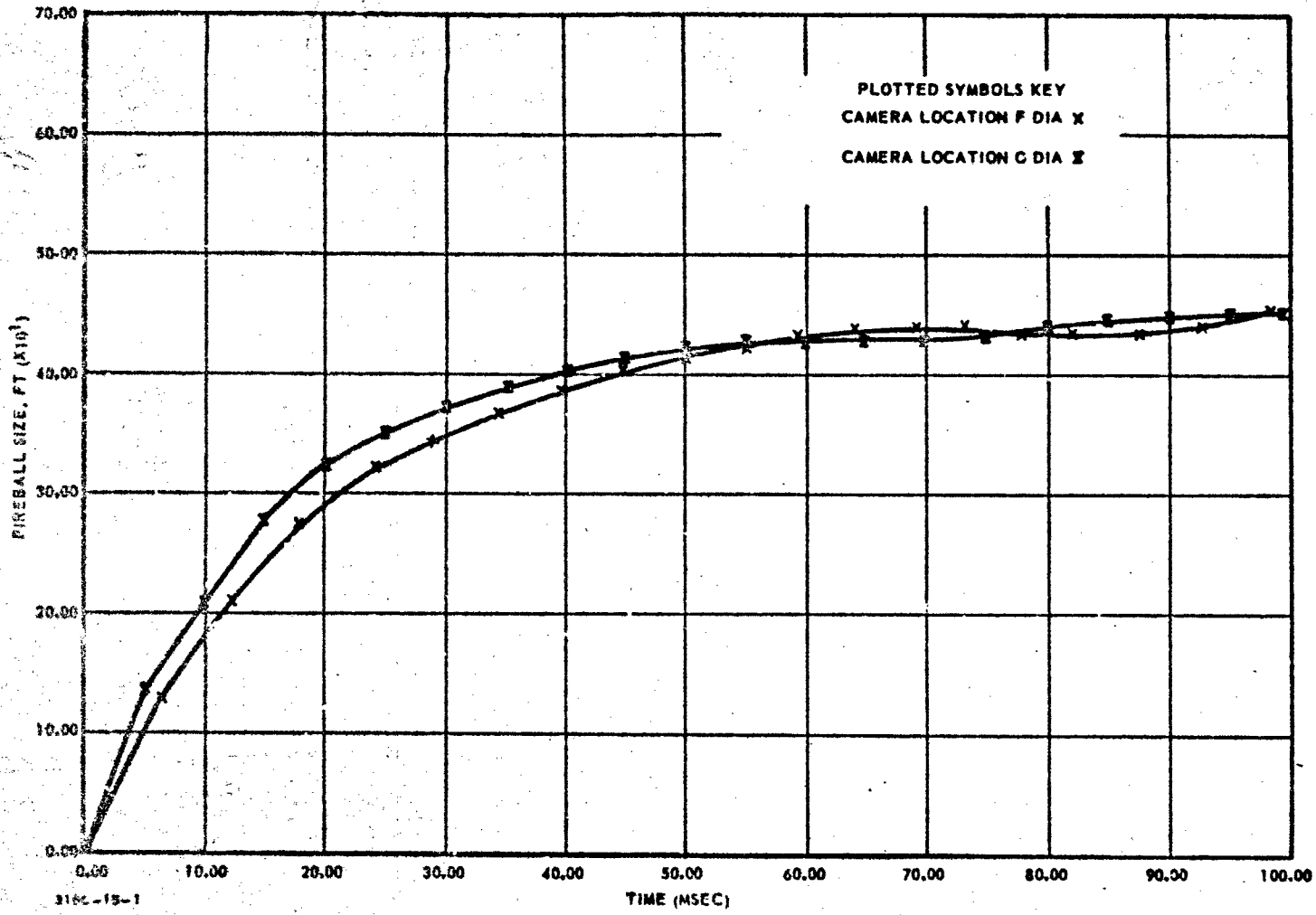


Figure 15. CD-96 Fireball Growth.

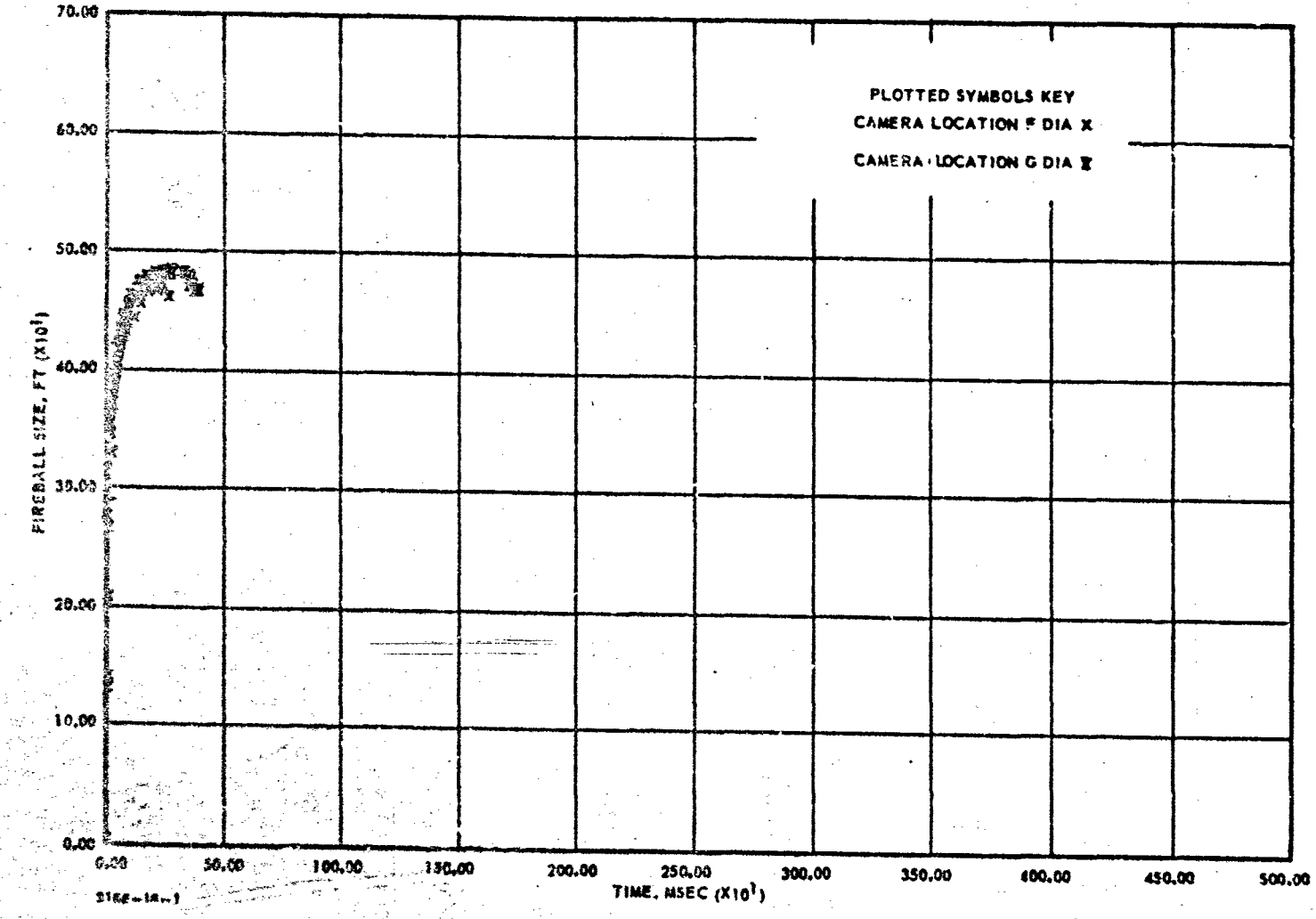


Figure 16. CD-96 Fireball History.

## TEST CD-98 (60-IN. DIAMETER)

### Test Setup

The test article consisted of a 60-in.-diameter by 240-in. high, four-segment solid-cylindrical propellant acceptor weighing 43,200 lb, and a 60-in. base diameter by 180-in. high, stacked, conical TNT booster that weighed approximately 10,700 lb. A steel plate, 10 ft square by 1/2 ft thick, was used as the witness plate. As in the 72-in. diameter test, a concrete box which supported the plate along its edges allowed an air gap beneath that portion of the plate upon which the 60-in. diameter sample rested. The completed assembly wss the same as that shown in Figure 7 except that the acceptor was made up of four segments and the booster was made up of fewer tiers because of its smaller overall height.

### Instrumentation

The instrumentation for CD-98 was basically the same as for CD-96 except for the omission of the audio level monitor.

The propellant sample was instrumented with T-2 targets, ionization probes, and ionization-mechanical probes to provide three velocity-measuring systems, each of which covered the full length of the sample. The progressive electrical shortings of the probes and T-2 targets were recorded on separate rasteroscillographs located in the control building.

The propellant sample was also fitted with an argon window, 6-in. wide, along the full length of the acceptor. The Beckman & Whitley streak camera recorded the event; the camera slit was lined up with the argon window to ensure sufficient luminosity to obtain a distinct streak record.

The problem of obtaining reducible radiometer data had been studied during the weeks prior to this test; it was finally attributed to the fact that the radiometers were mounted in steel-supported enclosures. Evaluation tests showed that the radiometers were very effective when they were shock mounted in a simple wooden stand. This radiometer mount design isolates the detector from the severe high frequency vibrational waves, which can be transmitted to it by a steel structure. The excessive noise on the records, such as those produced in the 72-in. diameter test, originated from the steel support.

Photographic coverage from the ground included (1) 16mm cameras, using color film, running at framing speeds of 64, 400, 1000, 4000, and 8000 fps; (2) a 35mm camera running at 6 fps; and (3) an infrared sensitive film in a camera operating at 400 fps. Helicopter-borne coverage of the event was cancelled because the helicopter encountered stability problems. Documentary coverage of the event, with a 16mm camera located 1-3/4 mi from the test site, used color film, at 50 fps.

## Test Results

### General Observations

High-speed cameras recorded, and eyewitnesses observed, that many burning propellant fragments were thrown off by the 60-in.-diameter sample. The propellant fragments were thrown to a distance of 2500 ft, and appeared to emanate from the lower third of the charge. The trajectory of most of the fragments from a distance appeared to be nearly horizontal; a few large chunks were sent high in the air. Burnt propellant and burning brush were in evidence through the test area. Figures 17 and 18 may be compared to Figures 9 and 10 to illustrate the difference between the two large tests.

Large pieces of the aluminum restraint fixtures were recovered, some as large as 4 ft by 1 ft. Their size was typical of that expected from a nondetonation.

The witness plate was in position at ground zero, resting on a slight mound. The plate was slightly dished, but bore no sign of indentation, and it was intact except for the loss of the lifting lugs that had been welded upright at the corners.

The detonation-velocity data obtained from three sets of probes, each different, and from the streak camera record, are shown in Figure 19. The rate of attenuation of the velocity is more gradual than has been observed in most no go tests, but the data do agree with the expected behavior of an attenuating wave near the hydrodynamic sound velocity. This is discussed in the paragraphs entitled Interpretation of SOPHY II Critical-Diameter Data.

Peak overpressures from the 60-in. test are shown against a series of TNT curves in Figure 20. It is interesting to note that the TNT equivalences in terms of peak side-on overpressure did not differ significantly in the 60-in. test from that observed in the 72-in. test (Table XVII). The fading detonation, which proceeded to the bottom of the acceptor, might lead one to expect that the propellant contribution to the air blast would be comparable to that from a steady-state detonation.

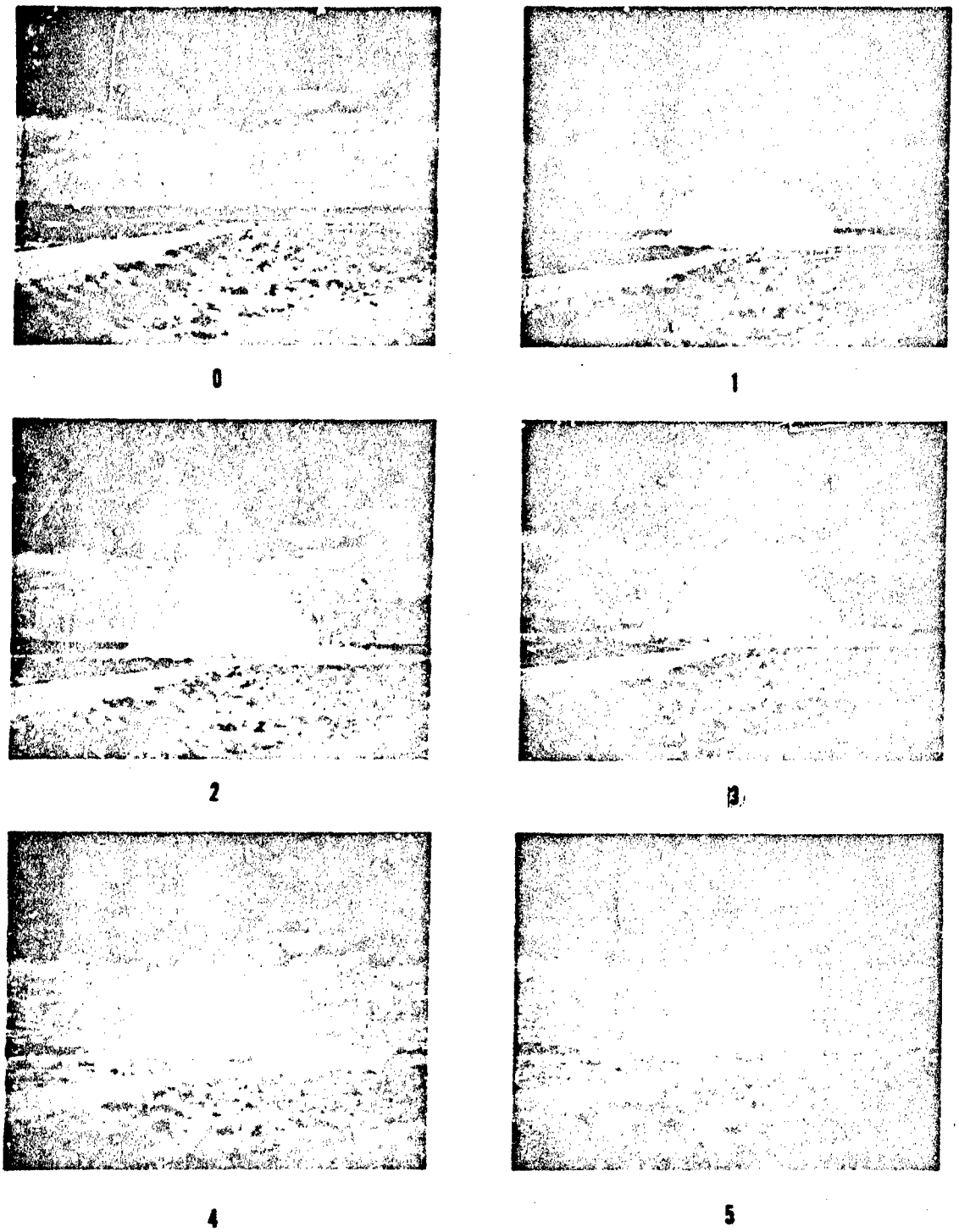


Figure 17. Test CD-98 (Frames 0 to 5): Camera Speed 6 fps.

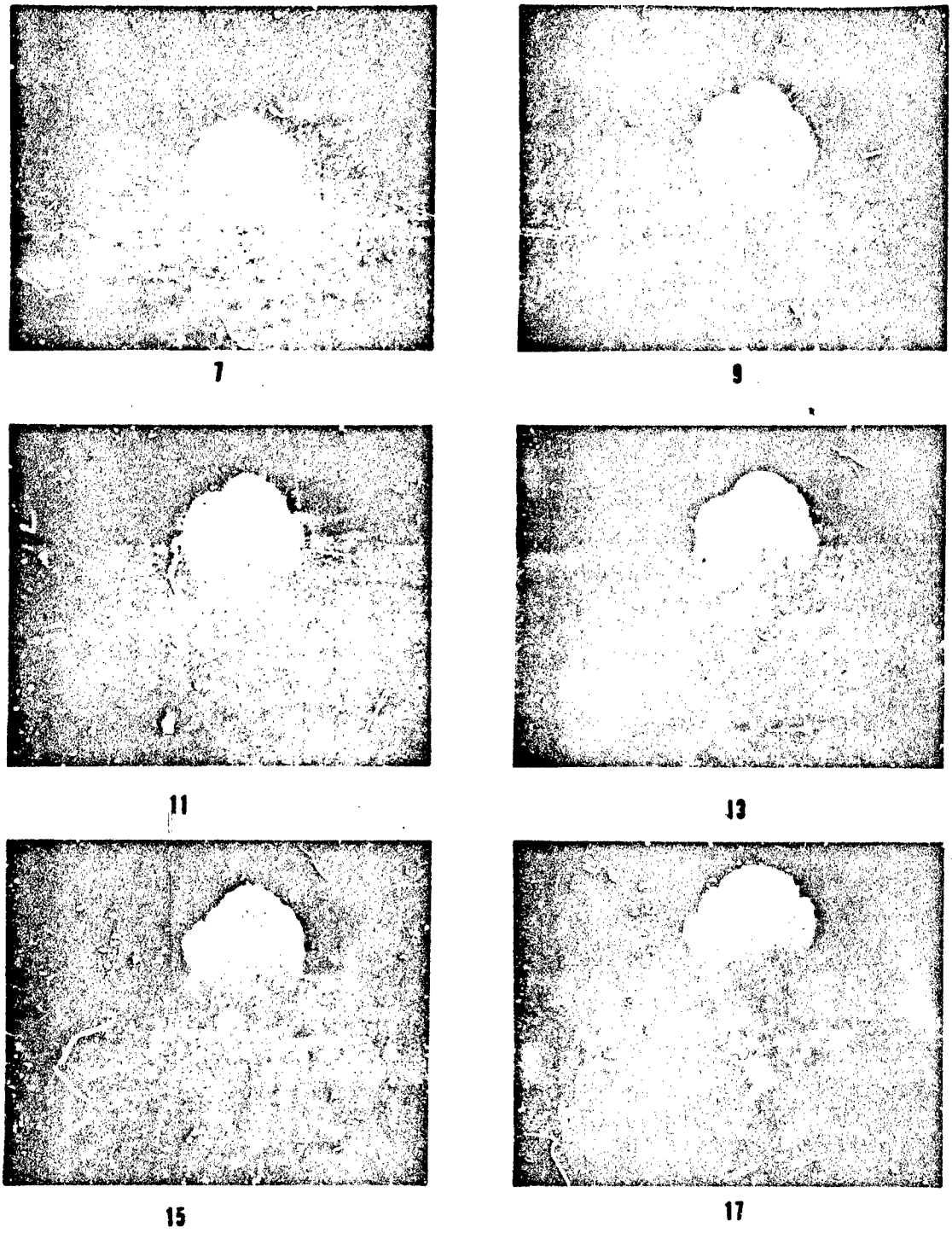


Figure 18. Test CD-98 (Frames 7 to 17, selected); Camera Speed 6 fps.

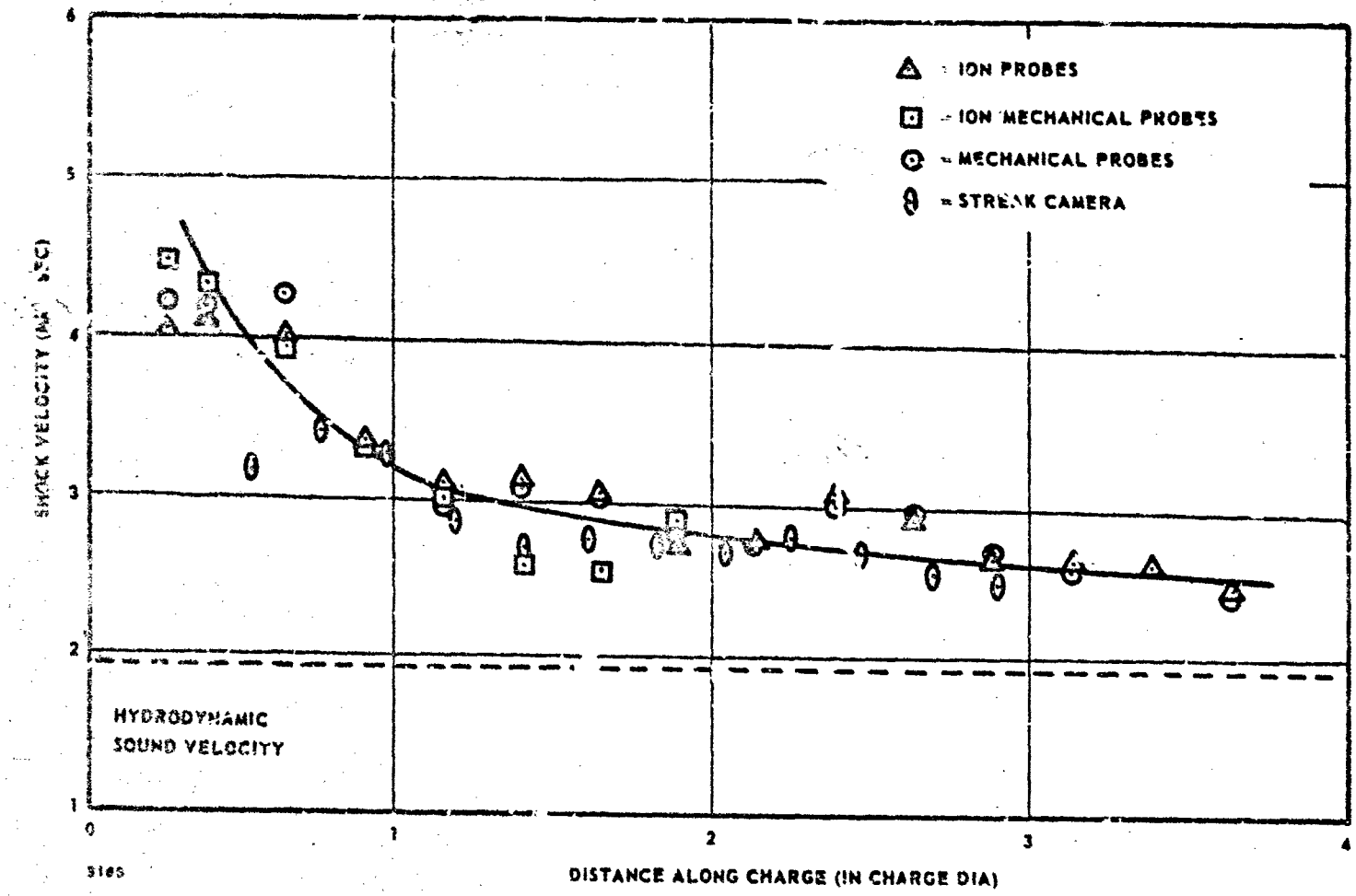


Figure 19. Detonation Velocity vs Distance, CD-98.

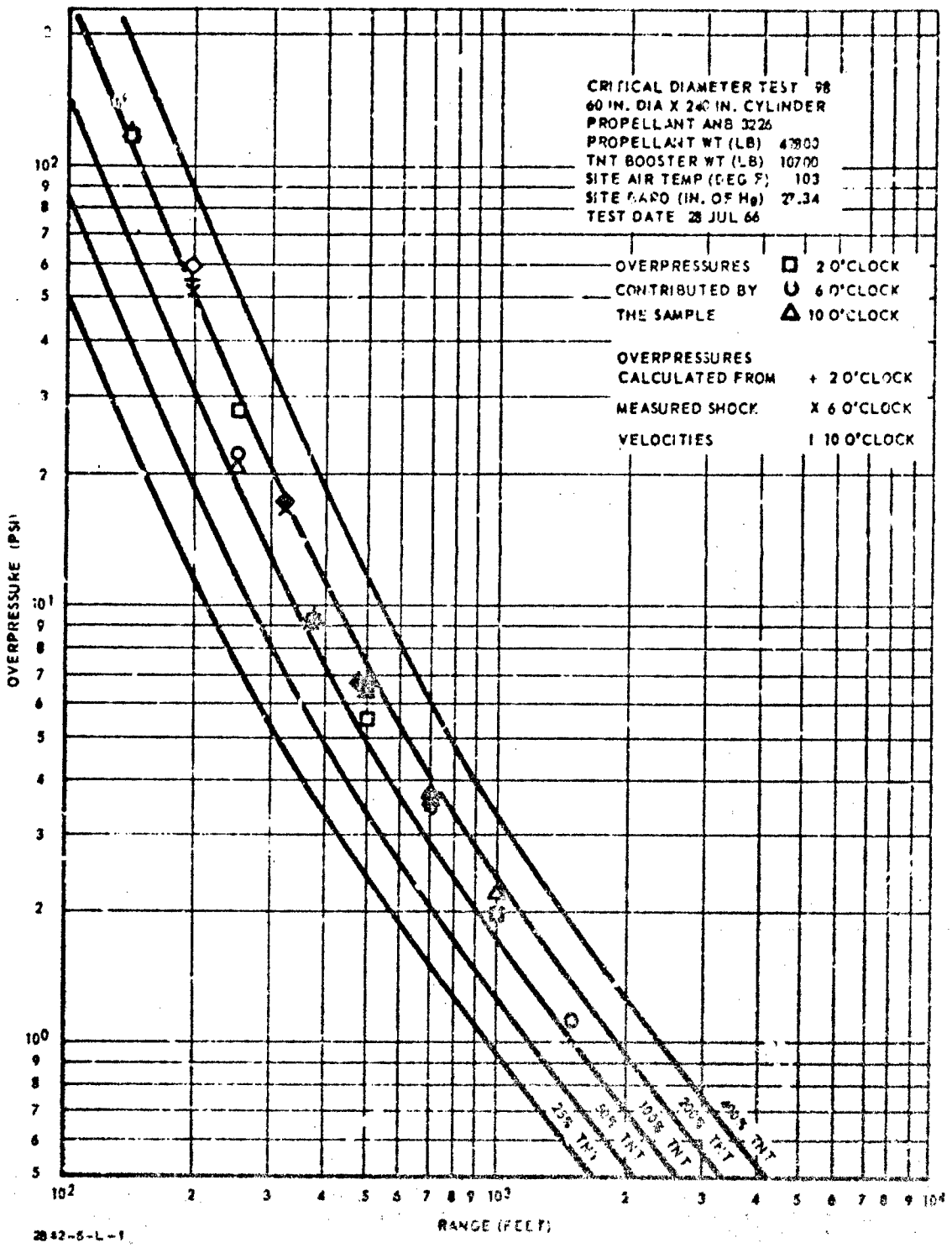


Figure 20. Peak Side-On Overpressures, CD-98.

## Table XVII. Observed and Calculated Side-On Overpressure and TNT Equivalences in the 72-in. and the 60-in. Critical Diameter Tests.

| Radial Distance from Charge (ft) | Radial Direction (o'clock) | Peak Side-On Overpressure* Measured (psi) 72-in. Test | Peak Side-On Overpressure* Measured (psi) 60-in. Test | Peak Side-On Overpressure* Calculated (psi) 72-in. Test | Peak Side-On Overpressure* Calculated (psi) 60-in. Test | TNT Equivalence* From Measured Overpressure (%) 72-in. Test | TNT Equivalence* From Measured Overpressure (%) 60-in. Test | TNT Equivalence* From Calculated Overpressure (%) 72-in. Test | TNT Equivalence* From Calculated Overpressure (%) 60-in. Test |
|---|---|---|---|---|---|---|---|---|---|
| 140 | 2 | ** | 127 | -- | -- | ** | 203 | -- | -- |
| | 6 | ** | ** | -- | -- | ** | ** | -- | -- |
| | 10 | ** | 128 | -- | -- | ** | 206 | -- | -- |
| 250 | 2 | 50.0 | 30.6 | -- | -- | 195 | 173 | -- | -- |
| | 6 | 45.7 | 25.2 | -- | -- | 171 | 128 | -- | -- |
| | 10 | 44.5 | 23.8 | -- | -- | 164 | 116 | -- | -- |
| 375 | 2 | ** | ** | 20.2 | 10.7 | ** | ** | 196 | 128 |
| | 6 | ** | ** | 19.9 | 10.4 | ** | ** | 190 | 121 |
| | 10 | ** | ** | 19.6 | 10.4 | ** | ** | 186 | 121 |
| 500 | 2 | 9.2 | 6.12 | -- | -- | 140 | 124 | -- | -- |
| | 6 | ** | 7.04 | -- | -- | ** | 162 | -- | -- |
| | 10 | ** | 6.90 | -- | -- | ** | 156 | -- | -- |
| 600 | 2 | ** | ** | 6.86 | 4.11 | ** | ** | 154 | 103 |
| | 6 | ** | ** | 6.77 | 3.98 | ** | ** | 151 | 95 |
| | 10 | ** | ** | 6.40 | 4.24 | ** | ** | 135 | 110 |
| 700 | 2 | 5.29 | 3.90 | -- | -- | 159 | 159 | -- | -- |
| | 6 | ** | 3.73 | -- | -- | ** | 144 | -- | -- |
| | 10 | 5.11 | 3.99 | -- | -- | 148 | 167 | -- | -- |
| 1000 | 2 | 3.08 | 2.14 | -- | -- | 172 | 135 | -- | -- |
| | 6 | 3.03 | 2.13 | -- | -- | 165 | 134 | -- | -- |
| | 10 | 3.13 | 2.33 | -- | -- | 178 | 167 | -- | -- |
| 1500 | 2 | 1.51 | ** | -- | -- | 118 | ** | -- | -- |
| | 6 | 1.82 | 1.21 | -- | -- | 193 | 123 | -- | -- |
| | 10 | 1.66 | ** | -- | -- | 152 | ** | -- | -- |

*Measured overpressures are derived from Kistler transducer measurements. The calculated overpressures are calculated at midpoint distances between Kistler transducer stations from which time-of-arrival data are available. The calculations are performed using an equation derived from the Rankine-Hugoniot equations:

$$p = \frac{2\gamma}{\gamma + 1} P_o \left( \frac{U^2}{c_o^2} - 1 \right)$$

where

$p$ = peak overpressure on the shock front
$\gamma$ = ratio of specific heats for air
$P_o$ = test-site atmospheric pressure
$U$ = velocity of shock front
$c_o$ = sound velocity at test site

TNT equivalence is determined by subtracting the weight of the booster from the theoretical weight of TNT that would have given the measured (or calculated) peak side-on overpressures recorded in this table. The difference is the weight of TNT that corresponds to the propellant weight. The ratio of these two, times 100, is the TNT equivalence in percent.

*No side-on overpressure gauge placed at this location.
**No data, because of gauge failure.

The radiometer data, measuring the thermal flux at 400 ft and 500 ft ranges, reduced to a maximum flux of 3.5 w/cm$^2$ at the near station and 2.5 w/cm$^2$ at the far station. These fluxes represent the level incident on the radiometers at the distances and are not meant to be estimations of the radiation flux at the fireball surface. Both radiometers recorded the thermal pulse duration to be 6.5 sec.

The CD-98 fireball growth, from the film taken at camera position D, is shown in Figure 21. The "spikes" at the very start of the curves are the measurement of the initial flash size. The fireball history, plotted in Figure 22, shows the fireball had a total duration time of 4.25 sec, a maximum diameter of 410 ft, and a maximum height of 345 ft.

A complete correlation of blast and fireball parameters, including data acquired in SOPHY I and II, is presented in Section XI.

## Interpretation of SOPHY II Critical-Diameter Data

### SOPHY I Criteria

In the SOPHY I critical diameter program the nature of the detonation velocity-distance curves obtained from pin-probe and streak-camera data and the effects of the steady-state or fading detonation waves on steel witness plates were used to classify the detonation behavior of RDX-adulterated propellant samples as supercritical or subcritical (Reference 1). Samples whose velocity-distance curve became essentially horizontal after the initially overdriven wave had propagated about halfway along the charge, and which either punched the witness plate or produced definite metal flow, were considered supercritical. If the wave velocity showed a nearly continuous decrease along the entire length of sample, and if the witness plate was intact and either dished or undamaged, the sample was considered subcritical.

These criteria clearly distinguish between supercritical and subcritical behavior in a material if the steady-state detonation velocity is (1) high enough to transmit a sufficiently strong shock wave to the steel witness plate to punch it or cause metal flow, and (2) is sufficiently above the hydrodynamic sound velocity so that the fading detonation wave in a subcritical sample will not fade so slowly that its velocity-distance curve is indistinguishable from that of a supercritical sample. In the SOPHY I tests, although the steady-state velocity at the critical diameter was found to decrease with decreasing RDX content, the value for the samples of lowest RDX content was high enough so that all of the critical diameter data could be interpreted in terms of the criteria as originally formulated.

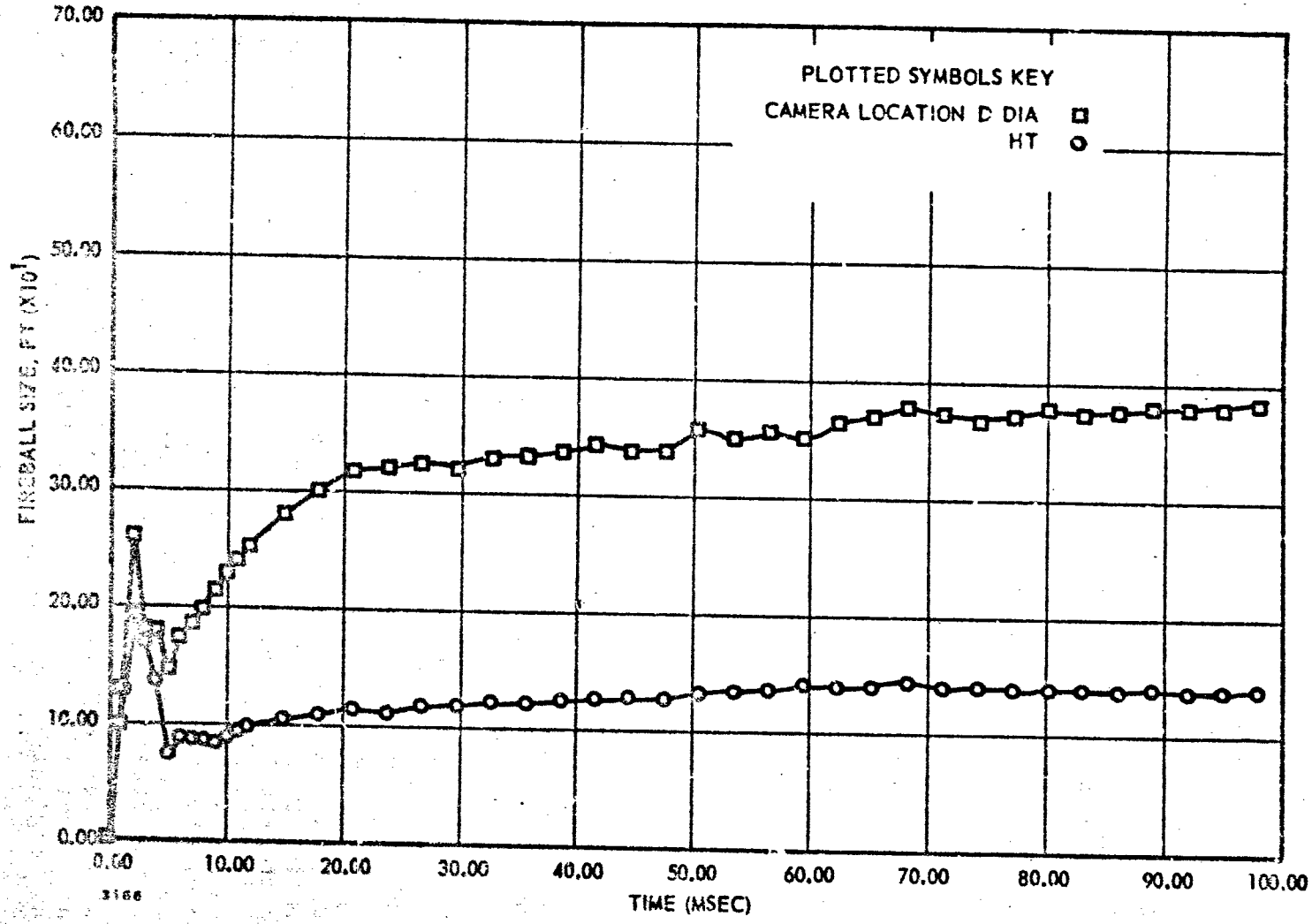


Figure 21. CD-98 Fireball Growth.

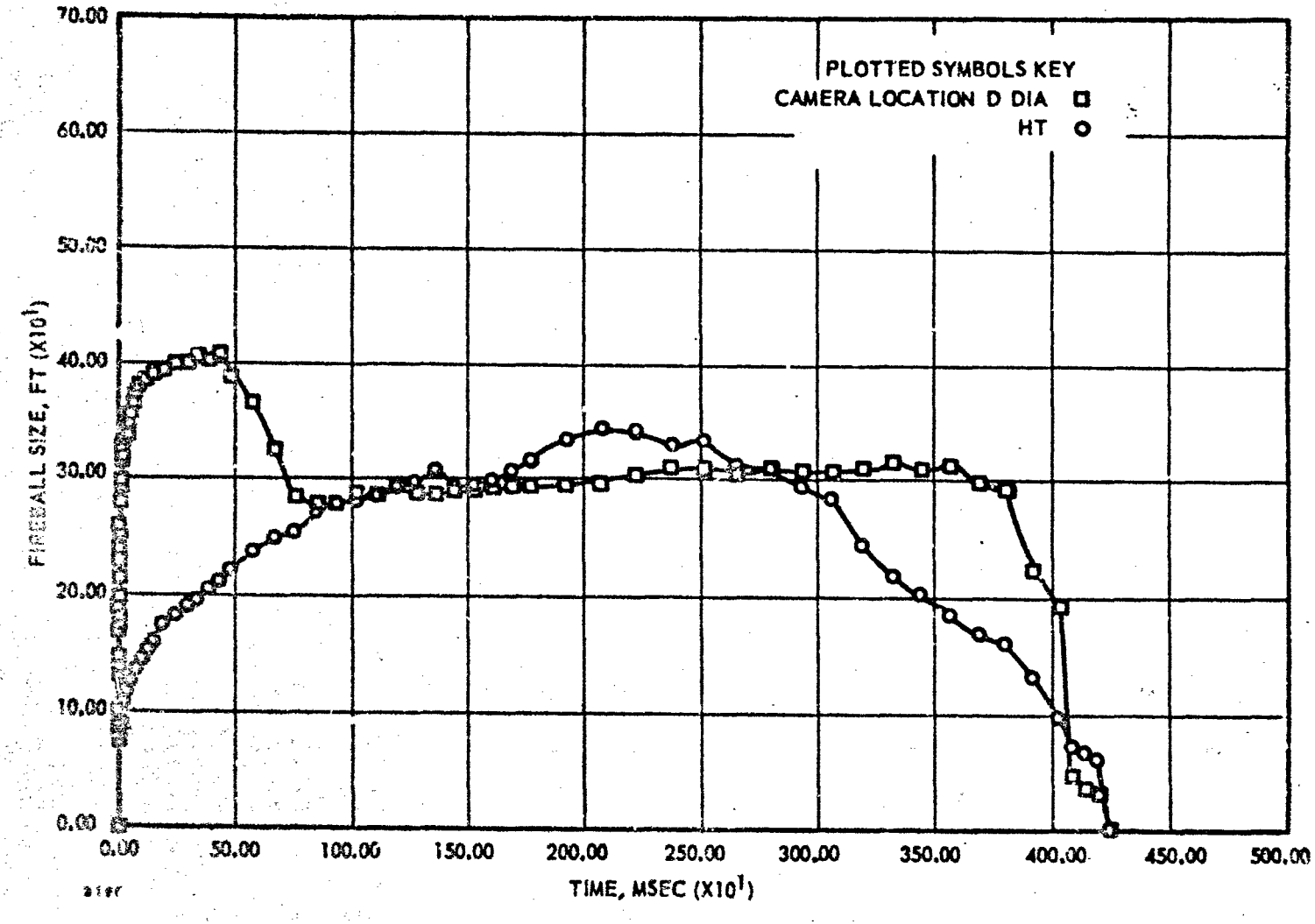


Figure 22. CD-98 Fireball History.

In the course of the SOPHY I program two phenomena were noted which correlated perfectly with the velocity-distance and witness-plate criteria, and which could serve as supplemental criteria for classifying detonation behavior. First, it was noted that the witness plates from go reactions with propellants of low RDX content were extensively broken up while those from no go's were dished but intact. Second, examination of the documentary and Fastax films showed that in all of the tests that were classified as no go's by the velocity-distance and witness-plate criteria, pieces of burning propellant were expelled laterally from the charge. No burning propellant could be detected in the film records of the go's.

## Analysis of SOPHY II Test Results

The two SOPHY II large-critical-diameter test sizes (72-in. and 60-in. diameter) were chosen to give a go and a no go reaction with unadulterated propellant, according to predictions of the model. In terms of the supplemental criteria developed in the SOPHY I program, the 72-in. diameter test was an unequivocable go and the 60-in. diameter test was an unequivocable no go; i.e., in the 72-in. diameter test, no burning propellant could be detected in the documentary and Fastax film records, and the witness plate was extensively fractured; in the 60-in. diameter test, considerable burning propellant was ejected from the charge and the witness plate was dished but unbroken. A cursory examination of the velocity-distance data showed that the curves for the two tests were quite similar (Figures 13 and 19), confirming an earlier conjecture that at sufficiently low critical detonation velocities, there might be no apparent differences between subcritical and supercritical curves.

Because of the similarity between the D vs x curves for the 72-in. and 60-in. diameter tests it has been necessary to examine them in greater detail in order to use them to classify the tests as supercritical or subcritical. For this purpose, both curves have been compared with D vs x data for a subcritical sample of an aluminized AP-PBAN propellant sample of similar composition (Reference 9). and with data for the attenuation of an unreactive shock in Plexiglas (Reference 10). The data for Plexiglas are shown in Figure 23, where the observed velocity is plotted vs the reduced distance, x/d, that the shock wave has progressed into the Plexiglas. (Although the data are for a 0.5-in. Plexiglas column, a previous, unpublished analysis indicates that the plot of shock strength vs x/d is nearly identical for Plexiglas columns with diameters varying by a factor of 12.)

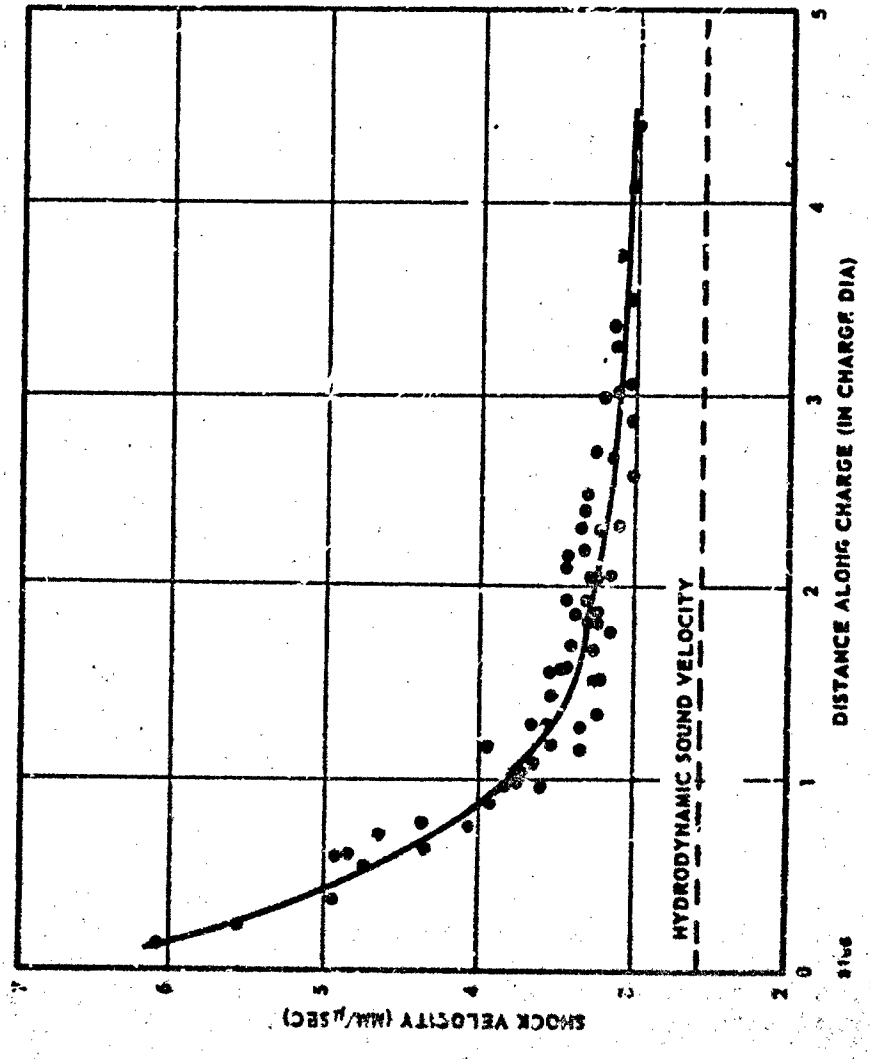


Figure 23. Shock Attenuation in Plexiglas.

It is apparent from this plot that even in the case of a nonreactive shock, the rate of decay is so gradual at x/d = 4 that the curve appears essentially flat, although still appreciably above its hydrodynamic sound velocity. Had the material been a propellant instead of Plexiglas, the original D vs x criterion would have classified the behavior as supercritical.

In Figure 24 the data for the 72-in. and 60-in. diameter tests are compared with that for Plexiglas and the data for a subcritical (22-in. diameter) sample of aluminized AP-PBAN propellant. The velocity data for the three propellant samples is expressed as the difference between the observed velocity and the (estimated) hydrodynamic sound velocity (assumed to be the same as that determined for RDX-adulterated propellant containing 9.2 weight percent RDX, i. e., 1900 mm/μsec (Section VII).

The comparison of Figure 24 indicates that the D vs x curve for the 60-in. diameter test closely follows the curve for the subcritical (22-in. diameter) test and the curve for the attenuation of an unreactive shock in Plexiglas. The curve for the 72-in. test, however, is distinctly different. It approaches a steady-state velocity (3200 mm/μsec) which is considerably above that reached in the nonreactive curves at the same position (x/d = 4). The 60-in. test is therefore judged subcritical and the 72-in. test supercritical, in agreement with the clear-cut classification by the supplemental criteria.

This analysis clearly demonstrates that the approach of a detonation wave to an apparently steady-state value somewhat above the hydrodynamic sound velocity is not adequate evidence of supercriticality when the critical velocity of the composition is near its hydrodynamic sound velocity. In the present case, consideration of this data in conjunction with the other evidence has permitted a clear distinction to be made.

## CONCLUSIONS

The results of the two large critical-diameter tests have shown that the detonation model developed in the SOPHY program is capable of predicting the critical diameter from the results of small-scale tests performed with adulterated compositions.

The fact that a typical composite propellant is detonable, in a lightly-confined 72-in. diameter cylindrical configuration, requires serious consideration of the implications bearing on the large-solid rocket programs of the present and future. Of particular

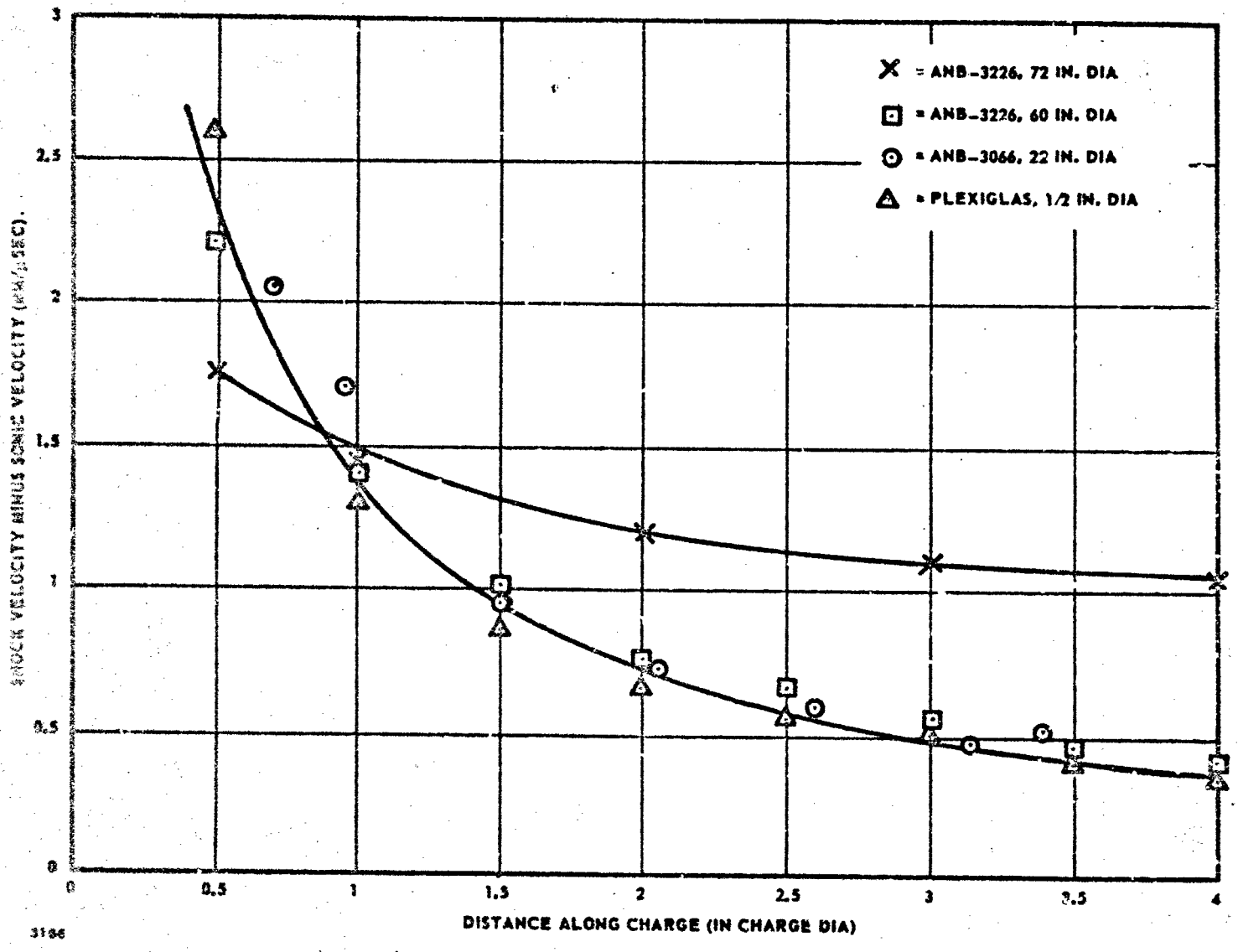


Figure 24. 72-in. and 60-in. Test Data Compared with Data from Plexiglas and AP-PBAN Propellant.

importance are the SOPHY studies regarding (1) the effect of acceptor shape on the critical geometry for sustainment (Sections V and VI) and (2) the conditions required for initiation of detonation (Section VII). A preliminary discussion of the total hazards of large solid motors is given in Section XII -- preliminary, because even with the extensive research that has been conducted, there are many important areas of investigation that have not as yet been opened.

## SECTION V

## THE CRITICAL GEOMETRY FOR SUSTAINMENT OF DETONATION

### BACKGROUND

The detailed development of the Aerojet critical-geometry theory for sustainment of detonation was reported in SOPHY I (Reference 1). In brief, the important conclusion reached by this theory is that there is a unique and explicit relationship between the critical diameter of a material and the critical dimensions of a charge of any shape with uniform cross section cast from that material. This relationship is the critical geometry, $\sigma_c$, which is defined by

$$\sigma_c = \left(\frac{4A}{P}\right)_c \tag{52}$$

where A is the area of the cross section, P is its total perimeter, and the subscript c refers to the critical conditions. For a right solid circular cylinder, Equation 52 becomes

$$\sigma_c = d_c \tag{53}$$

where $d_c$ is the critical diameter. If the critical diameter is known, Equations 52 and 53 define the critical ratio of cross sectional area to perimeter for any shape. Since area and perimeter can be expressed in terms of the dimensions of the cross section, the critical value of the dimensions (i.e., the critical size) of any shape is thereby defined.

In an experimental program conducted in SOPHY I, the critical dimensions were determined for several noncylindrical slopes and the critical geometries were calculated by Equation 52. These were compared to the experimentally determined critical diameters of the materials used and found to be lower by within 3 to 20%. Relatively large increments between consecutive sample sizes had made it impossible to determine the critical geometries accurately enough to avoid having to report the critical geometry data as a range, limited by the largest size that did not detonate and the smallest size that did detonate. Under these circumstances, the comparison between $\sigma_c$ and $d_c$ also had to be given within corresponding limits.

## TECHNICAL APPROACH

### Statistical Design

Accurate estimations of the mean critical geometries for several shapes are required before the critical geometry theory of sustainment can be tested meaningfully. This clearly demands a statistical design and analysis of the experiment. To apply statistical methods to the reduction of critical geometry data, for the purpose of relating the experimental and theoretical values, it is essential that the standard deviations, as well as the mean critical dimension, be determined for the propellant involved. Proper test design requires knowledge of the standard deviation before size increments and distribution can be assigned. A large standard deviation would require that sample sizes be selected that lie within the expected region of mixed results and that a particular distribution of these sizes be selected to permit an accurate estimation of the mean critical geometry. On the other hand, should the material exhibit a relatively small standard deviation of the order of the smallest increment in charge size that the particular series reasonably would allow, the number and distribution of the sample sizes that should be tested would be quite different from that required under the previous set of conditions.

To obtain a satisfactory estimate of the standard deviation requires a large statistical sample. A minimum of 50 tests was felt to be desirable. Since the critical geometry determinations were to be made for squares, equilateral triangles, rectangles, and circular-core cylinders and cross-core cylinders, each with two different core sizes, determination of the standard deviation for each particular shape would require a minimum of 350 tests. This does not include determination of the standard deviation of critical diameter data from each propellant batch that is cast, which obviously also must be accomplished. The total number of tests easily could reach 600. To circumvent this possibility, the test program was designed so that the standard deviation in critical geometry data for one noncircular shape would be determined and compared with that found for critical diameter data, to reveal whether the shape of the sample has any significant effect on the standard deviation of the data. The square shape was selected to be compared with the circular cylinder in this respect, with both shapes cast from one batch of propellant.

If the standard deviation within a batch does not depend upon the shape of the samples, to be judged from the results of the square and circle tests, the value of the standard deviation obtained from these tests can be assumed valid for all shapes that are cast from the particular propellant involved.

Selection of sample sizes in the critical geometry tests depends on the theoretical prediction and on the standard deviation between batches, as well as the standard deviation within a batch. To obtain an estimate of the between-batch standard deviation, a large set of cylindrical samples was cast from another batch of propellant and the pooled standard deviation (from the combined data of both batches) computed. The between-batch standard deviation can be calculated by the equation:

$$S_b^2 = S_p^2 - S_w^2 \qquad (54)$$

where S is the estimated standard deviation and the subscripts b, p, and w refer respectively to the between-batch, pooled, and within-batch estimates.

## Test Setup

### Test Assembly

The length (or height) of the acceptor charge in all critical geometry tests is at least four times the major cross-sectional exterior dimensions, which, for solid cylinders, is the diameter; for squares, the side of the square; for equilateral triangles, the side of the triangle; for rectangles, the width; and for hollow-core cylinders, the outer diameter. This proportion provides sufficient length to assure that the presence of a sustained detonation can be determined from velocity records.

The booster charges used in the critical geometry determinations for nonperforated shapes are of the same cross sectional shape and size as the acceptors. Booster lengths are three-fourths the lengths of the corresponding acceptors, which is adequate length for establishing steady-state detonation in the explosive. The booster is placed on the upper end of the acceptor; good interfacial contact is assured because of the smooth, level surfaces which are mated.

For the hollow-core, or perforated, charges the booster shapes and placement do not follow this procedure. The variation in the setup, and its justification, are discussed in detail in Appendix IV.

The assembled booster-acceptor stands on a 3/8-in.-thick, or 3/4-in. thick mild steel witness plate, depending on the size of the charge. The witness plate is supported at least 1-in. above ground to remove any possibility of shock reflection into the plate, which could alter the appearance of the witness plate.

## Instrumentation

Witness plate appearance after the test gives preliminary evidence of whether the sample sustained detonation. Conclusive evidence is obtained from velocity measurements. The sample is instrumented with ionization probes placed at a uniform depth into the side of the sample, at regular intervals down the length of the charge. These probes are connected via a mixer box to a rasteroscillograph which records the time each probe is triggered by the passing shock front with a distinctive capacitor-discharge pulse. The probes are coded by reversing the polarity applied to successive probes or groups of probes. This identification system removes doubt as to which probe is triggered when there are some probe failures, an occurrence that is commonly experienced when a sample fails to detonate.

Probe placement accuracy is an essential prerequisite to obtaining reliable velocity data. Probes must be spaced at accurately determined intervals, and their direction must be perpendicular to the axis of the charge. The third essential is that all the probes in a sample be inserted the same depth. A guide block was fabricated that contained evenly-spaced holes, to guide the piercing tool in the proper direction. By marking the tool, all of the holes made in the propellant were held to a uniform depth.

## Data Analysis

In the work under this contract, the principal evidence used in determining whether or not a sample sustained steady-state detonation is the record of detonation velocity vs reduced distance. In Section IV an exception to this criterion is discussed that applies to materials such as unadulterated AP-PBAN propellant, for which the critical detonation velocity is near the hydrodynamic sound velocity in the material. In the adulterated-propellant formulations that comprise the samples used in the present program, the critical detonation velocities are sufficiently above the hydrodynamic sound velocity to justify application of the sustained-velocity criterion: A sample is considered to have detonated if, after approximately two diameters of travel, the detonation wave proceeds at a constant velocity over the remaining sample length; a sample is considered to have failed to detonate if the velocity of the detonation wave decreases in a nearly continuous manner along the full length of the sample.

A statistical test for steady-state detonation over the lower several diameters has been programed as part of a computer program that reduces distance-time data to velocity-distance data by numerical differentiation and prints the results in tabular and graphical

form. It is assumed that if steady-state detonation is to occur, the detonation velocity will approach a constant value at some determinable distance (x) away from the initiated end. The value of x is variable from sample to sample and test to test, because it depends upon the overboostering level of the initiating stimulus and upon the charge diameter.

In this computer program, the initial value of x/d (the reduced distance in diameters) from which the computations progress, is part of the input data, in recognition of the need for flexibility. A linear least-squares fit to the velocity (D) vs x/d data first is calculated using those data obtained at all probe positions beyond the arbitrary start points except the last. (The numerical-differentiation method employed to determine velocity is not as accurate at the end points as when applied to interior points. Thus, exaggerated and suspect values of velocity are commonly calculated at the end points.) The final exclusion of the end point is determined by comparing it with the least-squares predicted value, using the t-statistic

$$t = \frac{\hat{D} - D_{obs}}{s_{\hat{D}}} \tag{55}$$

where $\hat{D}$ is the estimated velocity, $D_{obs}$ is the observed velocity calculated through the numerical-differentiation process, and $s_{\hat{D}}$ is the standard deviation of the estimate. If the calculated value of t exceeds the theoretical value at the 0.05 significance level, the end point is excluded. Otherwise the point is included and the least-squares solution recomputed to fit all the data points.

The test of whether the event is a steady-state detonation is accomplished by applying another t-statistic to the hypothesis that the slope of the least-squares best-fit linear solution is not significantly different from zero. The statistic is

$$t = \frac{b}{s_b} \tag{56}$$

where b is the estimated slope calculated by the least-squares fit and $s_b$ is the standard deviation of that estimate, given by

$$s_b^2 = \frac{\Sigma (D - \hat{D})^2}{(n - 2) \Sigma (X - \bar{X})^2} \tag{57}$$

where X = x/d and n equals the number of data points involved in the calculation. Since b is the slope of the line, this statistic has n - 2 degrees of freedom. If the calculated value of t exceeds the theoretical value at the 0.05 significance level, it is inferred that steady-state detonation did not occur.

The computer prints out on the tabular page the results of the statistical analysis of the velocity data. Included in this printout are (1) the x/d starting point, (2) the number of points used in the calculation, (3) whether or not the end point was included, (4) slope of the least-squares fit solution, (5) standard deviation of the slope, (6) whether or not the slope is essentially zero, (7) average velocity, and (8) the standard deviation of the velocity data.

## TEST RESULTS

The propellant used in this series of tests was AAB-3189, which contains 9.2 wt % RDX. Several batches of propellant were cast to provide all the samples needed in the critical geometry tests. The detailed test results are tabulated in Appendix V with respect to sample shape and, where applicable, according to batch number.

### Nonperforated Shapes

#### Circle

The two batches of propellant that contained cylindrical samples specifically designed for determining the mean critical diameter and the standard deviation of the data were Batches No. 4EH-85 and -86.

Batch 4EH-85. The results obtained from the Batch 4EH-85 tests are shown as a histogram in Figure 25. Forty-six samples were tested. An attempt to obtain maximum-likelihood estimates of the mean ($\mu$) and standard deviation ($\sigma$) was made using the computer program described in Reference 11, but the program would not converge to a maximum. For situations in which mixed results occur only at the lowest test level, the maximum-likelihood estimate of $\mu$ is the test level itself. The maximum-likelihood estimate of $\sigma$ is zero. For such cases it is difficult to accept the maximum-likelihood estimates as being best estimates.

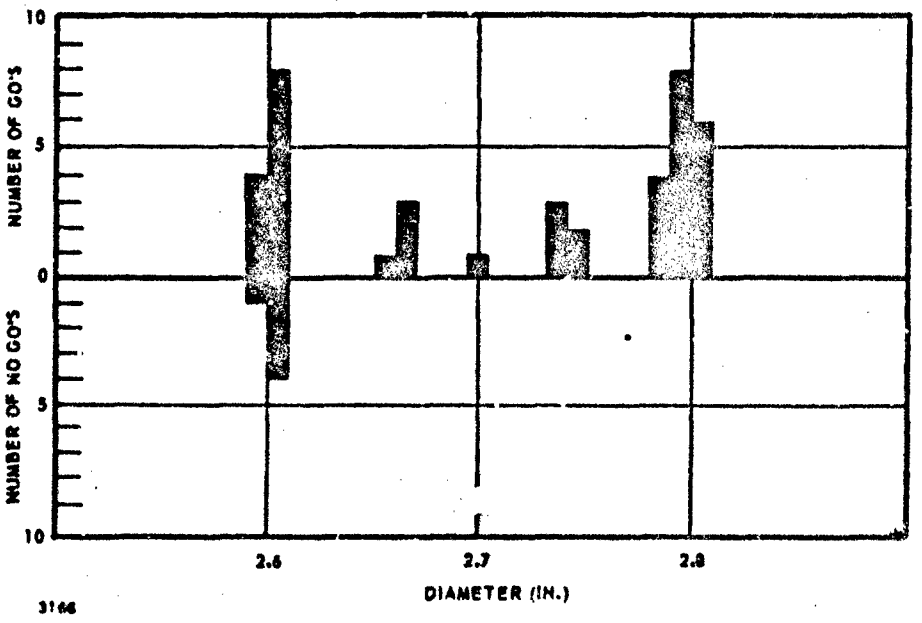


Figure 25. Critical Diameter Results, Batch 4EM-85.

Better estimates might be those which the computer program uses as its first-guess estimates for the maximum-likelihood solution. These are obtained by combining the estimates derived by two other estimation techniques: the minimum overlapping subset method and the two subset method. Both of these methods and the method of combining them are described fully in Reference 11. From the data obtained in these tests, this estimating system calculates $\hat{\mu}$ = 2.59 in. and $\hat{\sigma}$ = 0.04 in.

Batch 4EH-86. The results of 48 critical diameter tests of samples cast from Batch 4EH-86 are shown in Figure 26. Maximum likelihood estimates of the mean critical diameter and the standard deviation of the Batch 4EH-86 material are 2.71 in. and 0.04 in., respectively.

Pooled Results. The data previously reported in SOPHY I (Reference 1) were combined with the SOPHY II data to obtain a pooled estimate of the mean and standard deviation for AAB-3189 propellant. Comparative statistics from the three populations are shown in Table XVIII, and a graph of the combined go-no go results is shown in Figure 27. It should be pointed out that the SOPHY I data, although it is treated as one population, actually includes the combined results from three batches of propellant. The total number of samples, however, is still much less than the number tested in either of the recent batches. Also, the SOPHY I material was mixed and cast on a different line area at Sacramento; the batch size was 800 lb, compared to the 2000-lb batch size in SOPHY II. Different mixing equipment and personnel were used in the previous effort. It might be expected that under these circumstances, with the large number of differences between the two casting operations, the data could reflect the introduction of such parameters.

Inspection of Table XVIII reveals that the results from Batch 4EH-86 are almost identical to those from SOPHY I. In fact, the 95% confidence ellipses for the mean ($\mu$) and the standard deviation ($\sigma$) calculated for this batch, are completely contained within the ellipse drawn from the SOPHY I data (Figure 28). This figure shows the ellipse drawn for Batch 4EH-85 as well, and the data indicate that a significant difference does exist between this batch and the two other sets of data.

Another statistical test, the likelihood ratio statistic, shows that the three sets do not come from populations with the same cumulative normal response function. This test states that -2 $\ln\lambda$ follows the chi-square distribution approximately, where

$$\ln\lambda = \ln L_0 - \ln L_1 - \ln L_2 - \ln L_3 \qquad (58)$$

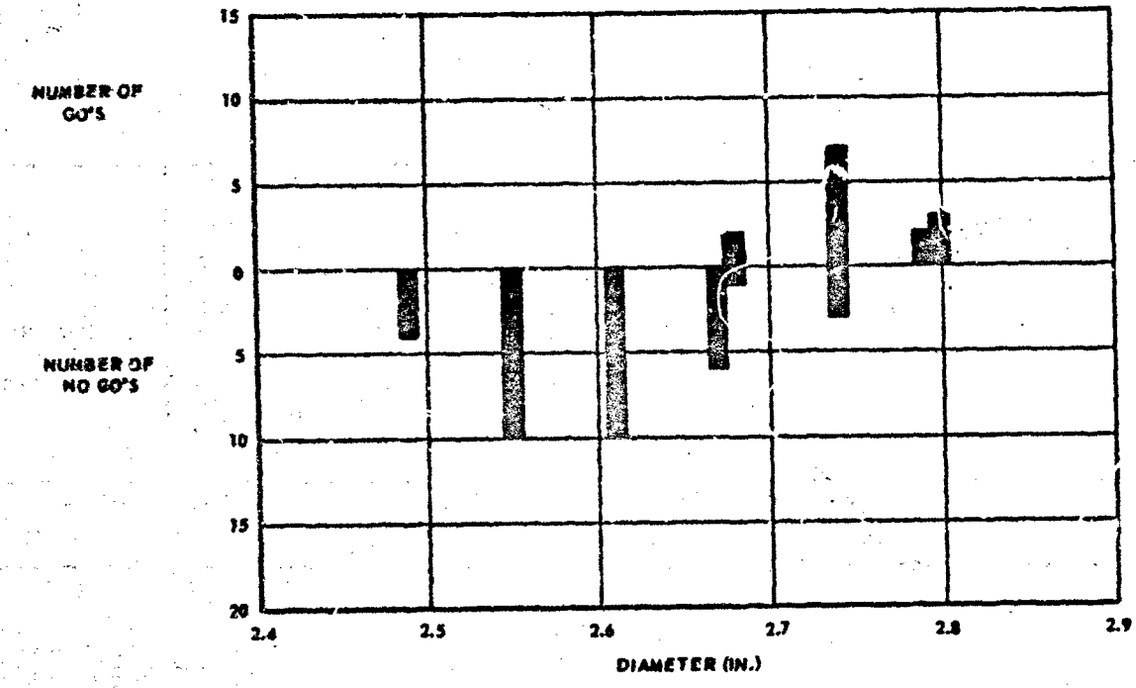


Figure 26. Critical Diameter Results, Batch 4EH-86.

Table XVIII. Comparison of Critical-Diameter Estimates, AAB-3189.

| Estimate of Quantity | Symbol | SOPHY I AF04(611)9945 | SOPHY II Batch 4EH-85 | SOPHY II Batch 4EH-86 | All Data Combined | 4EH-85 Combined with 4EH-86 |
|---|---|---|---|---|---|---|
| Mean (in.) | $\mu$ | 2.71 | 2.59* | 2.71 | 2.66 | 2.65 |
| Standard Deviation (in.) | $\sigma$ | 0.06 | 0.04* | 0.04 | 0.08 | 0.08 |
| Covariance (sq in.) | $\sigma_{\mu\mu}$ | 0.00053 | - | 0.00016 | 0.00014 | 0.00017 |
| | $\sigma_{\mu\sigma}$ | 0.00001 | - | 0.000004 | 0.00002 | 0.00002 |
| | $\sigma_{\sigma\sigma}$ | 0.00052 | - | 0.00014 | 0.00017 | 0.00019 |
| ln Likelihood | ln L | -6.46 | -8.65* | -11.00 | -47.53 | -39.11 |

*Not maximum - likelihood estimates.

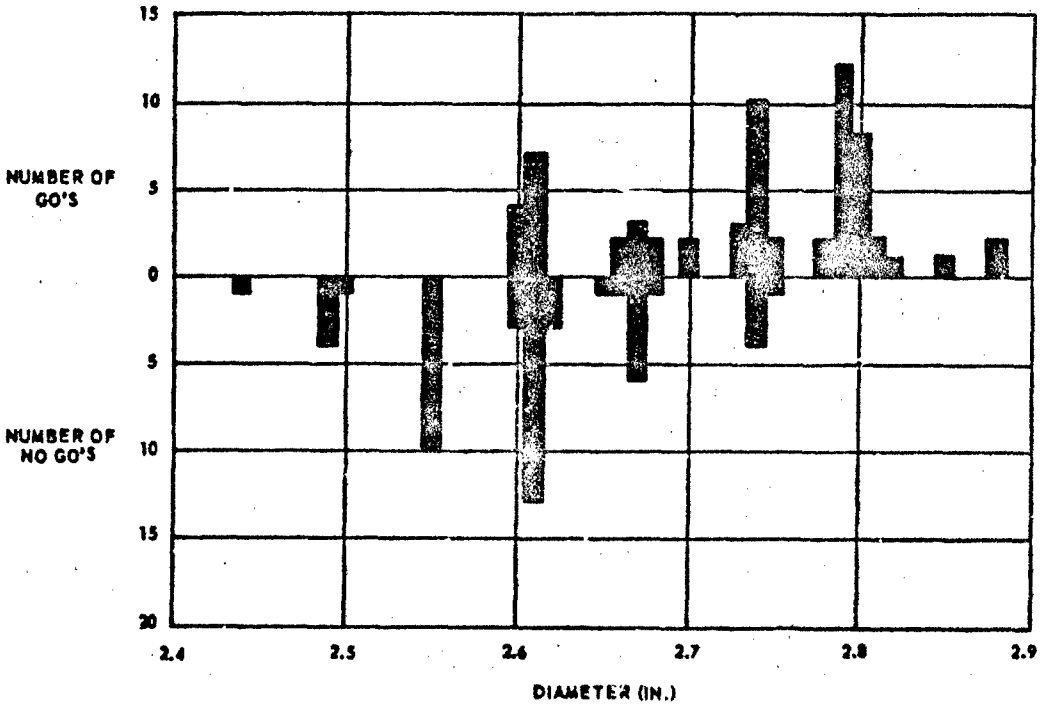


Figure 27. Combined Results: SOPHY I and SOPHY II, AAB-3189.

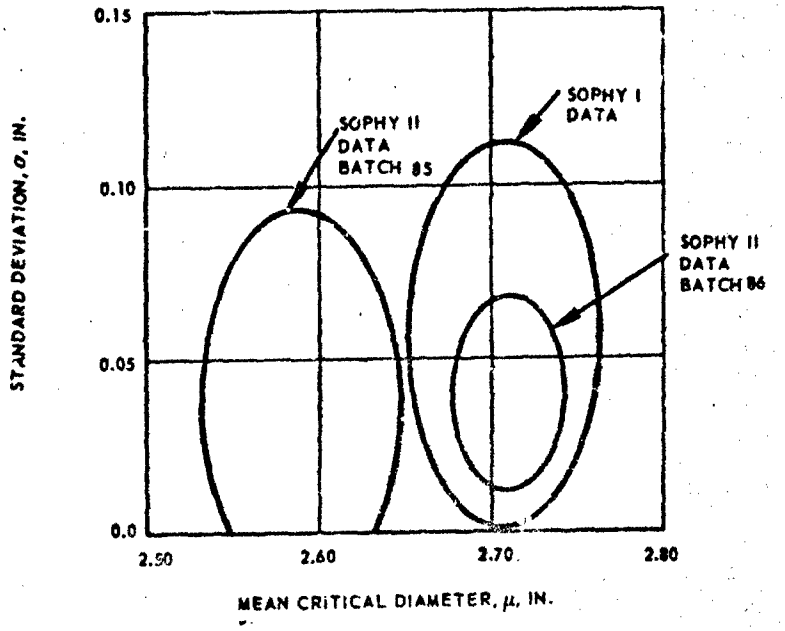


Figure 28. 95% Joint Confidence Ellipses for $\mu$ and $\sigma$, AAB-3189.

$L_0$ is the maximized sample likelihood of the combined set of data and $L_1$, $L_2$, and $L_3$ are the maximized sample likelihoods for the individual sets. In this case, the chi-square distribution has three degrees of freedom. Substituting in Equation 58 the ln-likelihoods presented in Table XVIII,

$$\ln\lambda = -20.12 \qquad (59)$$

Therefore, $\chi^2 = 40.24$. The probability of observing this value, with three degrees of freedom, is less than 0.0001. It must be inferred by this test that the samples do come from different populations.

The within-batch standard deviations for Batches 4EH-85 and -86 ar identical (Table XVIII). The standard deviation from the SOPHY I data includes batch-to-batch variation as well as within-batch variation, since it is a pooled set of data from three batches. Similarly, when all the AAB-3189 data are pooled, giving a mean critical diameter of 2.66 in., the standard deviation (0.08 in.) contains both the within-batch and the batch-to-batch variations. Subtracting the within-batch variance (0.0016-in. squared) from the total variance (0.0064-in. squared), the batch-to-batch standard deviation is estimated to be 0.07 in.

In all these calculations, the standard deviation resulting from the measurement errors and dimensional nonuniformity is one order of magnitude less than those calculated from the go-no go data. The effect of these human errors is therefore trivial.

Batch-Control Data. Since AAB-3189 is used in several subtasks of this program, additional critical-diameter data are available from the batch-control tests, which were performed with samples from each propellant batch that was cast for the critical geometry series to obtain an estimate of the critical diameter of each batch. In each batch there were included eight solid-cylindrical batch-control samples, two each at nominal diameters of 2.56, 2.63, 2.69, and 2.75 in.

Propellant Batch 4EH-108, which included triangular samples, had a critical diameter of 2.73 in. This value is consistent with the estimates derived from the previous data. Combining the results of the Batch 4EH-108 tests with all previous data changes the estimated mean critical diameter of AAB-3189 to 2.69 in. but does not affect the estimate of the standard deviation (0.08 in.)

Batches 4EH-109 and -110 contained rectangular cross-section samples and hollow cylinders. The results of the batch-control tests from both batches were negative; i.e., no detonation occurred in samples of up to 2.75 in. nominal diameter. These batches differ significantly from all previously tested batches of AAB-3189. The critical diameters of these two batches were found by testing larger diameter samples, which were prepared by turning down several surplus samples from the batches. The critical diameter of Batch 4EH-110 was between 2.90 and 2.95 in. Careful study of the batch mixing records did not show cause for the anomalous behavior of these batches. Since the samples cast were destined for use in the critical geometry subtask, they were allowed to qualify for testing, because the test results could be compared to the individual critical diameters of these batches and they did not need to be compared directly with data obtained from other AAB-3189 tests.

The results of the batch-control tests for Batches 4EH-108, -109, and -110 are shown in Table XIX.

Table XIX. Batch-Control Tests, AAB-3189.

| Batch No. | Diameter (in.) | Result | Test No. |
|---|---|---|---|
| 4EH-108 | 2.55 | No Go | 3.2.1.175 |
| 4EH-108 | 2.54 | No Go | 3.2.1.176 |
| 4EH-108 | 2.62 | No Go | 3.2.1.177 |
| 4EH-108 | 2.62 | No Go | 3.2.1.178 |
| 4EH-108 | 2.67 | No Go | 3.2.1.179 |
| 4EH-108 | 2.67 | No Go | 3.2.1.180 |
| 4EH-108 | 2.73 | Go | 3.2.1.181 |
| 4EH-108 | 2.74 | No Go | 3.2.1.182 |
| 4EH-109 | 2.73 | No Go | 3.2.1.183 |
| 4EH-109 | 2.73 | No Go | 3.2.1.184 |
| 4EH-109 | 2.80 | No Go | 3.2.1.187 |
| 4EH-109 | 2.90 | No Go | 3.2.1.188 |
| 4EH-109 | 2.95 | No Go | 3.2.1.191 |
| 4EH-109 | 3.00 | Go | 3.2.1.192 |
| 4EH-110 | 2.73 | No Go | 3.2.1.185 |
| 4EH-110 | 2.73 | No Go | 3.2.1.186 |
| 4EH-110 | 2.90 | No Go | 3.2.1.189 |
| 4EH-110 | 2.95 | Go | 3.2.1.190 |

Square

The critical geometry theory defines the critical geometry of a square, by Equation 52, to be

$$\sigma_c = s_c \tag{60}$$

where $s_c$ is the critical length of a side of the square. The theory predicts therefore, by Equation 53, that the critical length of a side should equal the critical diameter. Fifty-four square-column samples were cast from Batch 4EH-86, which material had a critical diameter of 2.71 in. and a standard deviation in the critical diameter data of 0.04 in.

Figure 29 shows the results of the square critical geometry tests. Since there was one reversal in these data the maximum-likelihood estimates of the mean critical side (or geometry) and the standard deviation could be calculated. These values are 2.49 in. and 0.04 in., respectively.

The experimental critical geometry for the square shape is 92% of the theoretical prediction. Since the standard deviations from the circle and square data are identical, no statistical test of their similarity is required.

An estimate of the within-batch standard deviation for AAB-3189 has been determined, therefore, and found not to be affected by sample shape.

Equilateral Triangle

AAB-3189 propellant from Batch 4EH-108 (2.73 in. critical diameter) was cast into equilateral triangular cross-section columns for testing to determine the critical geometry of this shape. Five samples were to be cast at each of the following nominal sizes: 4.05, 4.15, 4.25, 4.35, 4.45, and 4.55-in. Modifications to the molds before the casting took place raised each of the sets of dimensions by approximately 0.20 in., which produced a series of samples ranging from 4.25 to 4.75 in. All the columns had a length-to-side ratio of 4.

For the equilateral triangular column, the theory of critical geometry defines the critical geometry to be

$$\sigma_c = \frac{b_c}{\sqrt{3}} \tag{61}$$

where $b_c$ is the critical length of a side of the triangle.

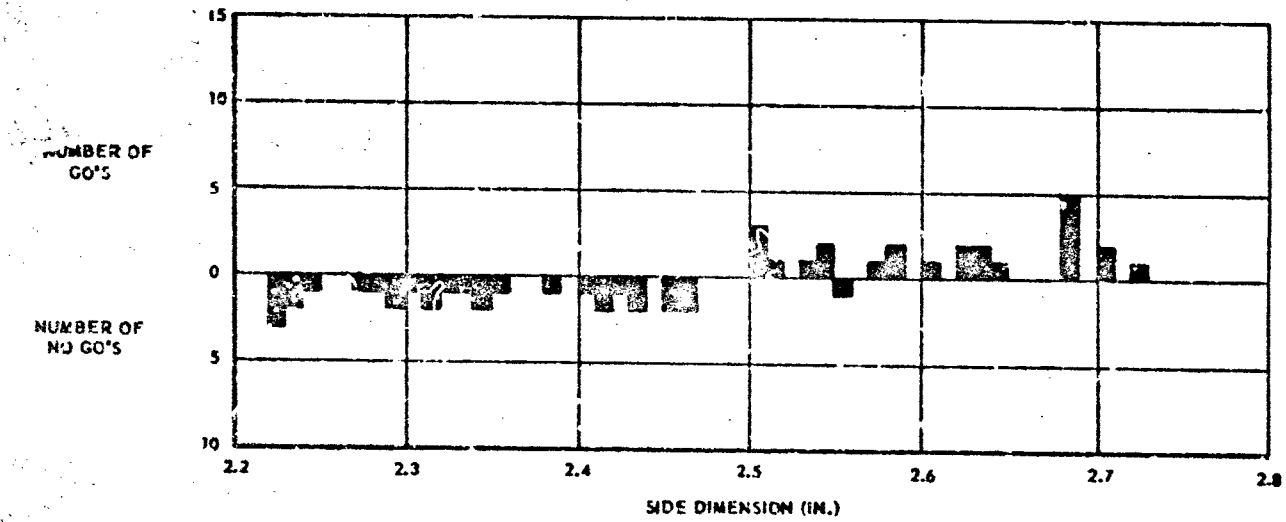


Figure 29. Critical-Geometry Results (Square Columns).

From the results of 21 tests (Figure 30), the maximum likelihood estimate of the mean critical side is 4.50 in., i.e., the mean critical geometry is 2.60 in. The experimental value is 95% of 2.73 in., the predicted critical geometry.

In Figure 30, the abscissa is given both as the side dimension of the triangle and as the geometry of the triangle. The geometry of any shape, defined by generalizing Equation 52, is a dimension given by evaluating

$$\sigma = 4A/P \tag{62}$$

where $\sigma$ is the geometry. This equation allows the size of any shape to be expressed by one number that corresponds to an equivalent diameter, thereby normalizing all data with respect to shape.

The test series could not provide any estimate of the standard deviation because mixed results occurred only at one size. Combining these data with those obtained in SOPHY I, conditional estimates of both the mean and standard deviation can be made. The conditional restriction of the pooled data exists because the critical diameter of the SOPHY I batch that supplied the triangles was not determined to a satisfactory precision. The values that are obtained from the combined triangle data are 4.48 in. mean critical base and 0.042 in. standard deviation. Converted to geometry, these values become 2.58 in. critical geometry and 0.024 in. standard deviation. Although these are conditional estimates, it is apparent that the standard deviation from this acute solid shape is comparable to those that were obtained from circles and squares.

Rectangle

The rectangle is a shape determined by two parameters: width and thickness. Its geometry, by Equation 62, is

$$\sigma = \frac{2\,wt}{w + t} \tag{63}$$

where w is the width and t is the thickness. Differentiating Equation 63 with respect to w and with respect to t,

$$\frac{\partial \sigma}{\partial w} = 2\left(\frac{t}{w + t}\right)^2 \tag{64a}$$

and

$$\frac{\partial \sigma}{\partial t} = 2\left(\frac{w}{w + t}\right)^2 \tag{64b}$$

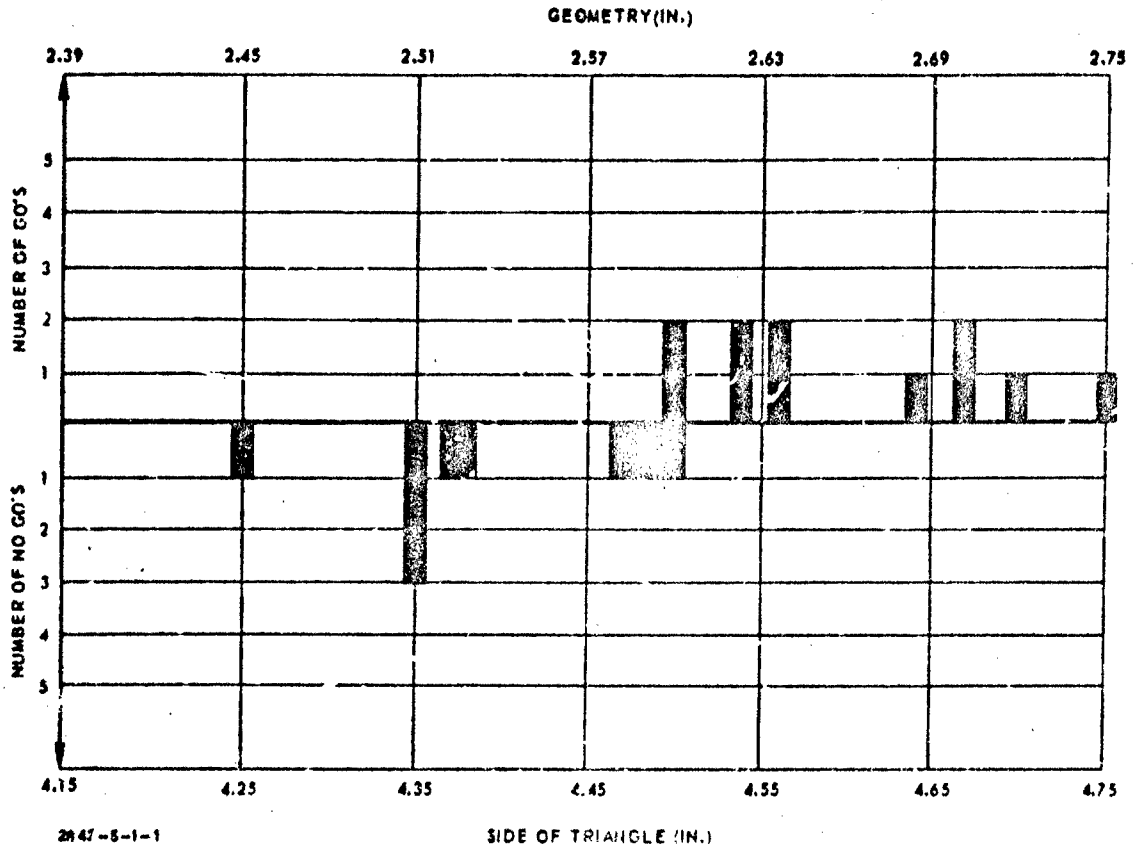


Figure 30. Critical-Geometry Results (Equilateral Triangles).

Equations 64a and 64b show that since w is greater than t by convention, the geometry of a rectangle is less sensitive to w than it is to t. Therefore, to obtain the critical geometry of a rectangle, with one of these dimensions held constant and the other dimension varied in specific increments, greater precision would result from holding t constant and testing rectangles of various widths.

Eighteen critical geometry tests were conducted with rectangles 1.75 in. thick, cast from Batch 4EH-110 ($d_c$ = 2.92 in.). The results are shown in Figure 31, where again the abscissa is shown both as width and as geometry.

The maximum likelihood estimates of the mean critical width and the standard deviation are, respectively, 6.31 in. and 0.26 in. The mean critical geometry, from Equation 52 when t = 1.75 in. and w = 6.31 in., is 2.74 in., and the standard deviation is 0.024 in.

## Perforated Shapes

The critical geometry tests of perforated shapes require a special analytical approach that is peculiar to this general class of shapes. This is due primarily to the interference with the detonation process by high-velocity jet action in the core of the grains. A thorough study of the jetting phenomenon and its effect on grains of the sizes used in this critical geometry program was undertaken in SOPHY II. The study is reported in Appendix IV.

In essence, the conclusion of this investigation was that the high temperature and pressure behind the jet front cause rapid deflagration of the propellant at the inner surface of the grain, which physically reduces the web thickness.

With the proper combination of jet velocity, propellant detonation velocity, initial web thickness, and sample length, it is possible for the web to be reduced to subcritical dimensions ahead of the advancing reactive shock wave in the propellant. Under such circumstances an apparent steady-state detonation could not continue to propagate along the full length of the sample, because the sample geometry has actually become subcritical.

An example of such an occurrence is shown in Figure 32, which is a streak camera record of the reaction of a hollow core sample that was tested in SOPHY I. This record clearly shows the sudden failure of a constant-velocity reaction wave to propagate to the bottom of the charge. The distance over which a reactive shock

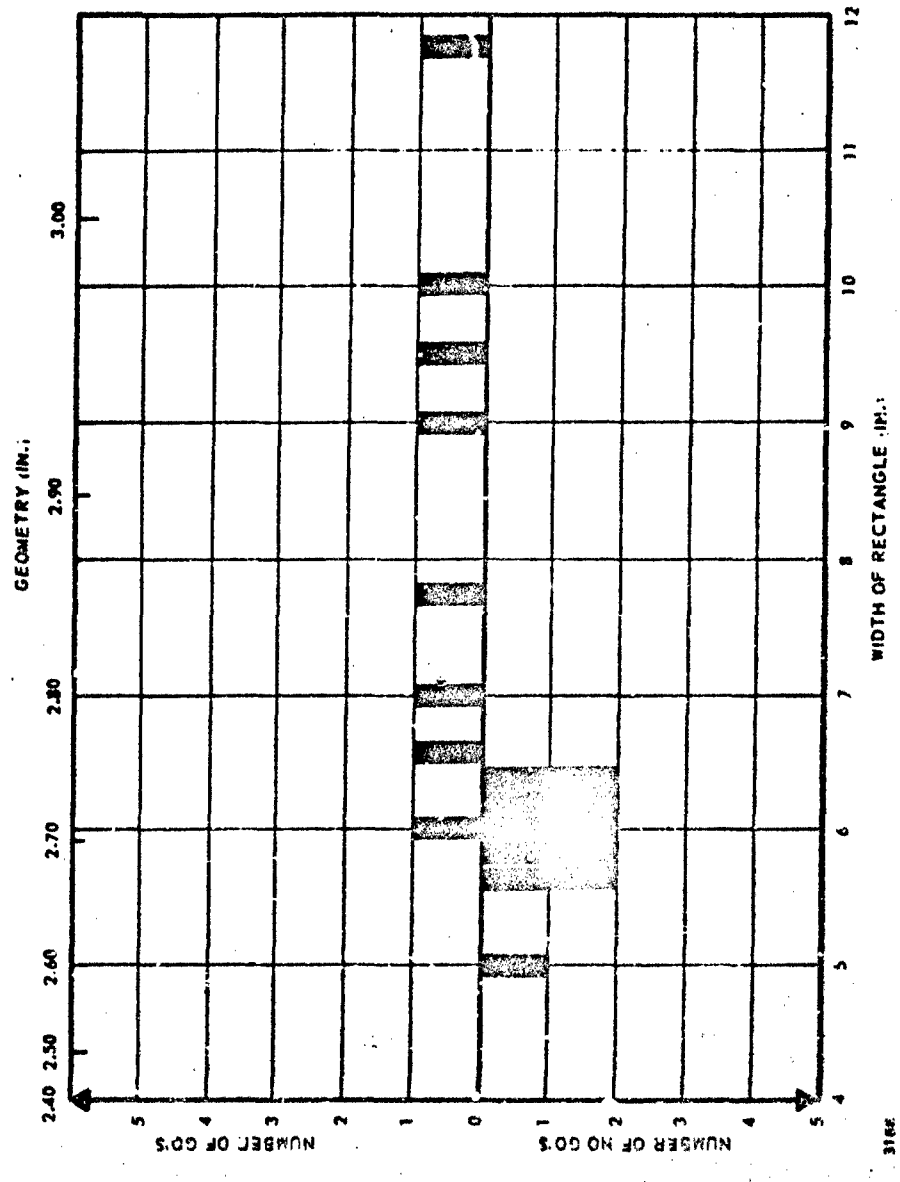


Figure 31. Critical-Geometry Results (1.75-in.-Thick Rectangles).

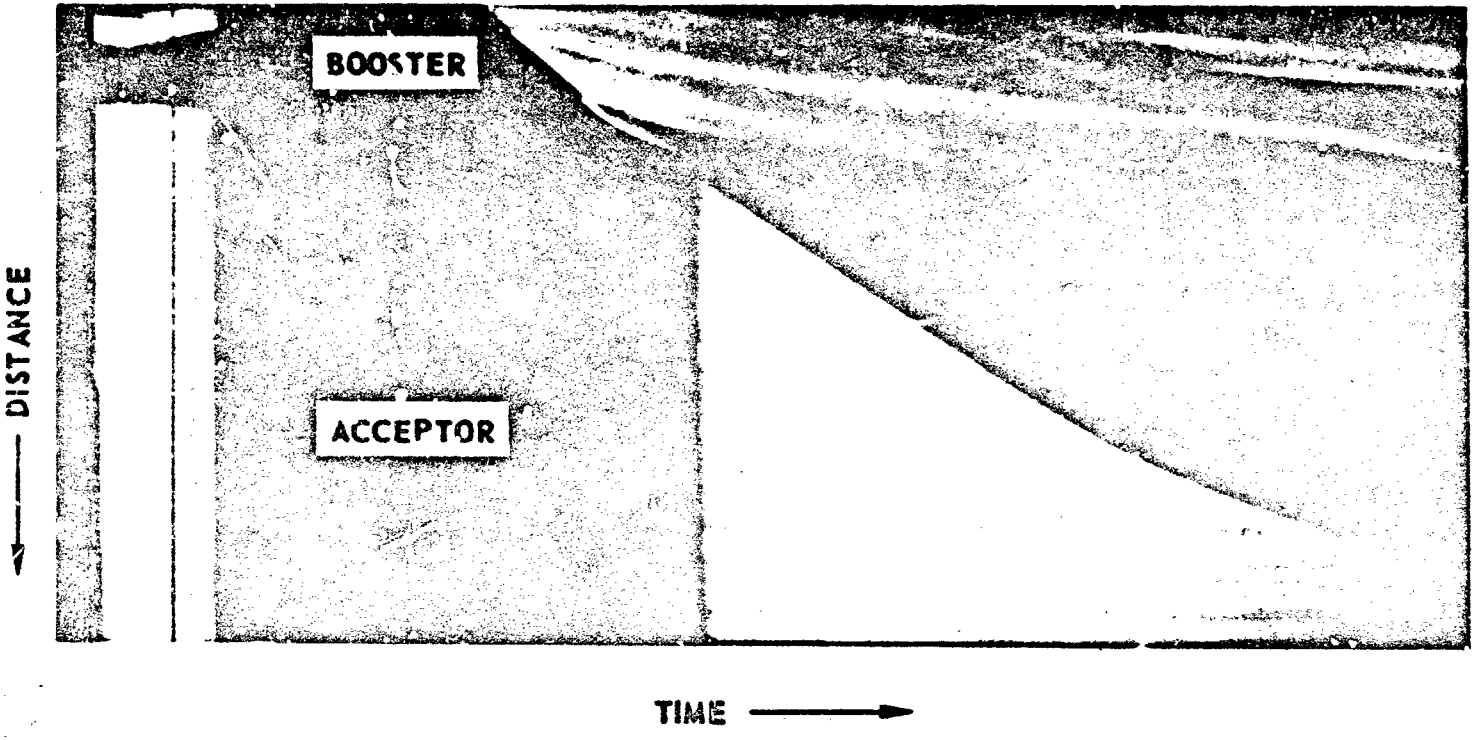


Figure 32. Hollow-Core Cylindrical Charge Undergoing Abortment of Steady-State Detonation.

wave can propagate at a constant velocity depends primarily upon the relative thickness of the web, with respect to the critical thickness. A perforated grain that can sustain steady-state detonation even over a 4 OD charge length cannot, therefore, be necessarily capable of sustaining steady-state detonation over an infinite length, because its geometry may become subcritical at some place farther down the sample.

The concepts of critical size and detonability are restricted to grains of uniform geometry. Since the jet interaction alters the geometry of perforated samples after the reactive shock wave has travelled a variable distance in the grain, it is necessary that the critical geometry tests of perforated grains concentrate on the portion of the sample in which the original geometry is unchanged.

Within this region, the critical web thickness that will support steady-state detonation can be determined. A perforated sample that has a web thickness equal to or greater than the determined critical web thickness cannot be categorized as a critical or supercritical grain for the reasons already discussed. The terms selected in the SOPHY II program to describe such samples are pseudocritical and pseudosupercritical, where the prefix indicates that the sample will not necessarily behave according to conventional interpretation of the meaning of critical and supercritical. To assure that misunderstanding will be minimized, the critical web thickness that is determined experimentally is called the pseudocritical web thickness hereafter and, similarly, the critical geometries of perforated shapes are reported as the pseudocritical geometries.

Determination of the pseudocritical size is accomplished by reducing distance-vs-time data obtained from probes placed in the samples to a depth equal to 1/2-web thickness. The distance over which a sustained detonation occurs is determined from the data for those sizes in which this behavior is observed. A sample is considered to be pseudosupercritical if sustained detonation is noted over a minimal distance of travel (arbitrarily chosen as 2-web thicknesses).

## Test Setup

In testing perforated shapes, the acceptors are not subjected to the full energy of the shock wave emitted from the high-explosive booster. Instead, a 1-in.-thick plate of Plexiglas is used between the booster and acceptor to attenuate the shock pressure. This permits the reactive shock wave in the propellant to stabilize

to its steady-state velocity sooner by reducing the time normally required for the overboostering effects to disappear. The data reduction is greatly facilitated by this modification of the standard critical geometry test setup.

Two other variations from the standard setup are employed. First, the booster is a solid right circular cone, 3 base diameters high. A booster of matching geometry, such as is used with nonperforated shapes, would send a jet into the acceptor core before the propellant was shocked, and in so doing, seriously threaten the generation of any useful data. The conical booster reduces the weight of high explosive needed, without affecting the shape and pressure of the delivered shock wave.

Second, the witness plate has a predrilled, centered hole of a diameter slightly exceeding that of the circle which would circumscribe the core of the sample. The plate is supported at least 1 ft above ground. The hole and the increased elevation of the witness plate prevent the jet produced in the acceptor from physically disturbing the orientation of the charge.

### Circular-Core Cylinders

The critical geometry theory states that for circular core cylinders the pseudocritical geometry is twice the pseudocritical web thickness. Samples were prepared in which the web thickness was varied by changing the OD and holding the ID constant. Two such sets of samples were prepared, with 1.5-in. and 3.0-in. ID's, from Batch 4EH-109 ($d_c$ = 2.97 in.). The results of the tests are shown in Figures 33 and 34.

For the 1.5-in. ID samples, the pseudocritical size is 4.12 in. OD, which corresponds to a pseudocritical geometry of 2.62 in. The pseudocritical size of the 3-in.-ID samples is 5.62 in. OD, which also yields 2.62 in. as the pseudocritical geometry. In both cases the pseudocritical geometry is 88% of the theoretical prediction.

### Cross-Core Cylinders

The cross-core perforation is a square cross, consisting of four square arms (each arm is $\ell$ in. square). The critical geometry theory defines the geometry of a cross-core hollow cylinder as

$$\sigma = \frac{OD^2 - 20\ell^2}{OD + 12\ell} \qquad (65)$$

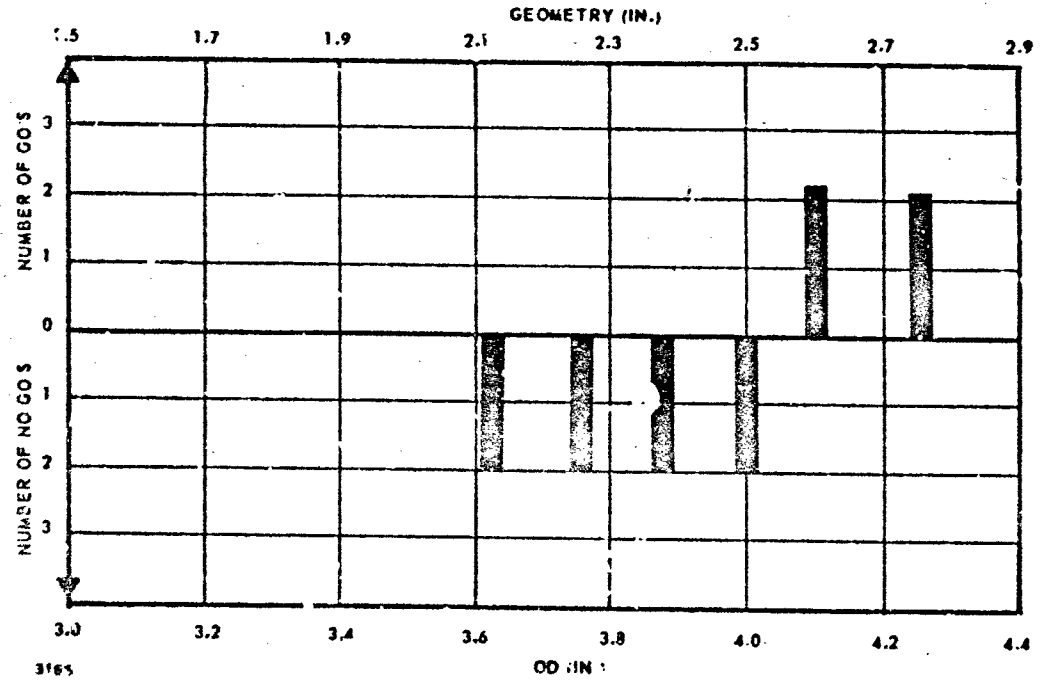


Figure 33. Test Results for 1.5-in. ID Hollow Cylinders.

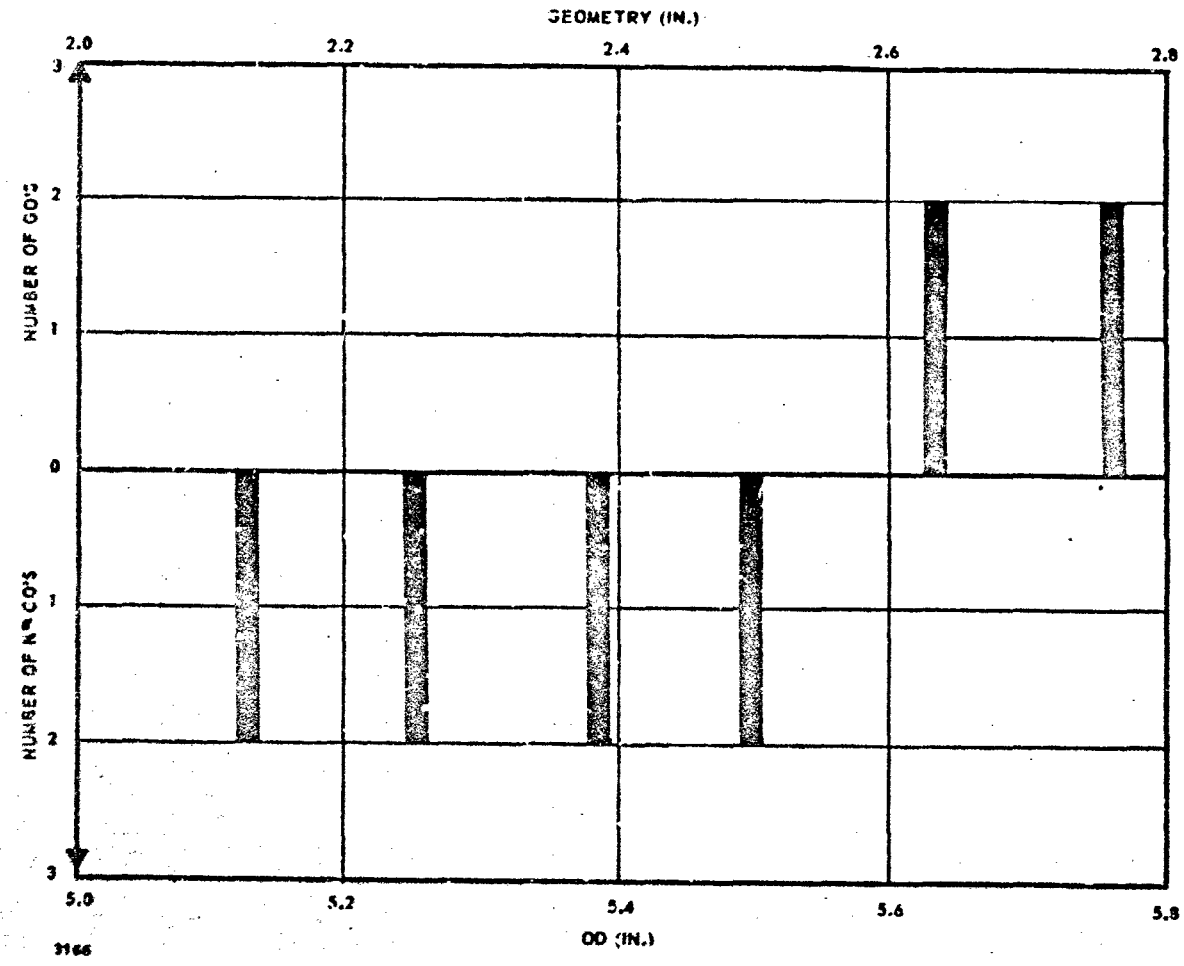


Figure 34. Test Results for 3.0-in. ID Hollow Cylinders.

If $\ell$ is constant, the pseudocritical geometry is a simple function of the pseudocritical outer diameter.

Samples were prepared from Batch 4EH-110 ($d_c$ = 2.92 in.) in two sets ($\ell$ = 0.5 in. and $\ell$ = 1.0 in.), with sample OD being the variable. The results of these tests are shown in Figures 35 and 36. When $\ell$ equals 0.5 in., the pseudocritical OD is 4.12 in., which (by Equation 65), gives a pseudocritical geometry of 2.56 in. For $\ell$ equal to 1.0 in., the pseudocritical OD is 5.50 in., which also yields a value of 2.56 in. for the pseudocritical geometry. In both cases the pseudocritical geometry is 88% of the theoretical prediction.

## CONCLUSIONS

A summary of the analyzed critical-geometry results is given in Table XX, which shows the calculated critical and pseudocritical geometries for square, equilateral triangular, and rectangular columns, and hollow-core cylinders, compared with the critical diameters of the batches from which the samples were cast. These data all have been acquired by testing samples of AAB-3189 propellant.

Table XX. Critical and Pseudocritical Geometries for Various Shapes, AAB-3189.

| Shape | Critical Geometry, $\sigma_c$ (in.) | Batch Critical Diameter, $d_c$ (in.) | $d_c - \sigma_c$ | $\sigma_c / d_c$ |
|---|---|---|---|---|
| Square | 2.49 | 2.71 | 0.22 | 0.92 |
| Equilateral Triangle | 2.60 | 2.73 | 0.13 | 0.95 |
| Rectangle | 2.74 | 2.92 | 0.18 | 0.94 |
| Circular-Core Hollow Cylinder | 2.62* | 2.97 | 0.35 | 0.88 |
| Cross-Core Hollow Cylinder | 2.56* | 2.92 | 0.36 | 0.88 |

Mean ($\sigma_c / d_c$) = 0.92

Standard Deviation = 0.03

*Pseudocritical geometry

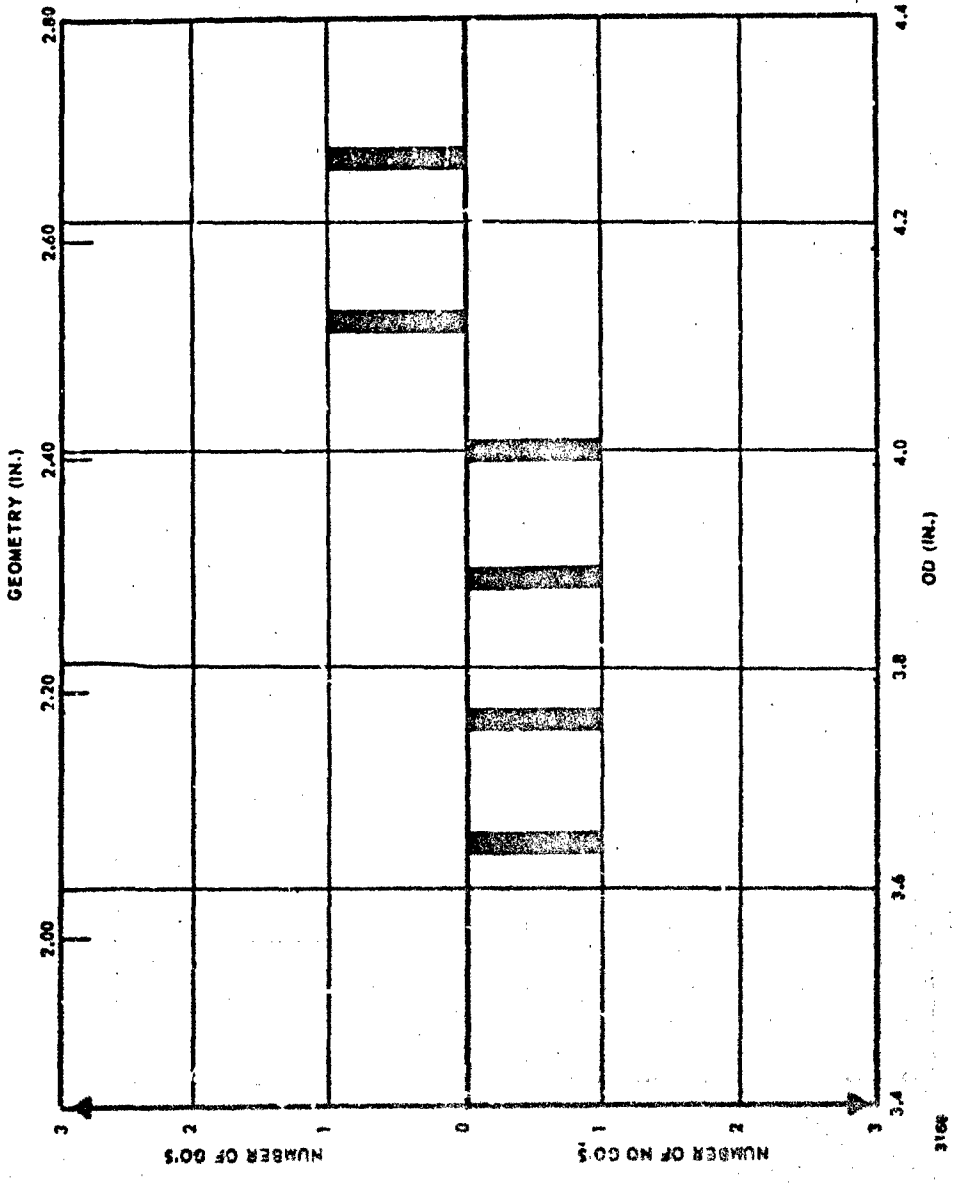


Figure 35. Test Results for Cross-Core Cylinders ($\ell$ = 0.5 in.)

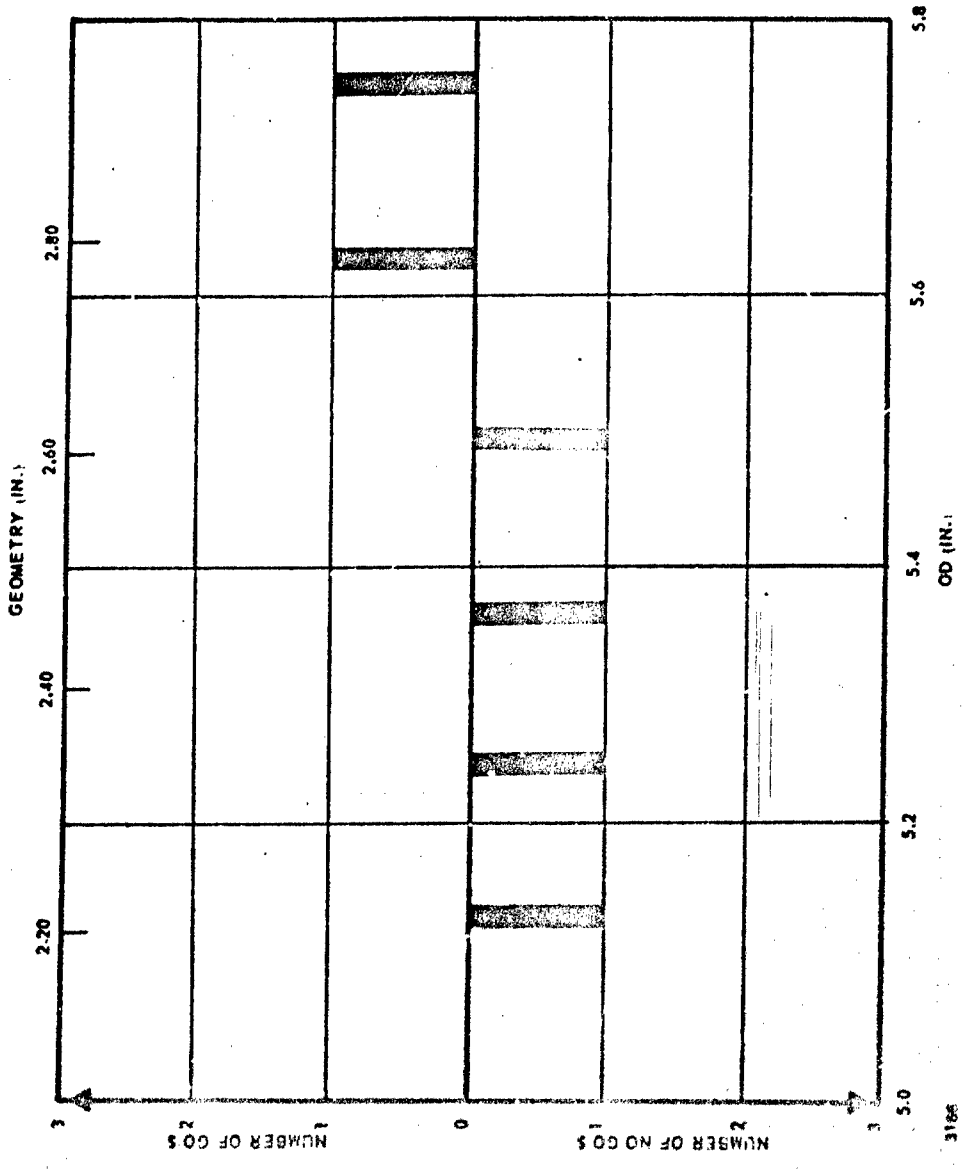


Figure 36. Test Results for Cross-Core Cylinders ($\ell$ = 1.0 in.).

There are many possible ways that the critical and pseudocritical geometries may be correlated with the respective critical diameters. A fundamental approach would have to account for those factors that have been avoided in the development of the model, such as the edge or corner effects and energy losses at concave surfaces. Another, less sophisticated, approach is taken in Table XX, where both the differences and the ratios of $d_c$ and $\sigma_c$ are shown calculated. It appears that since there is less variation among the ratios, the more preferable form of the critical geometry model would be

$$\sigma_c = (0.92 \pm 0.03)\, d_c \qquad (66)$$

This equation is sufficiently accurate that more fundamental (and complicated) correlations are not of any particular value. Equation 66 was derived from tests of only one propellant formulation. It has been evaluated in SOPHY II by a series of tests using a different adulterated propellant (see Section VI).

The assumptions that entered into the development of the model undoubtedly account for the variation of Equations 53 and 66. One assumption, that the detonation velocity at the critical size is independent of the shape, can be tested by comparing the data generated in this program. This is shown in Figure 37, where the average detonation velocities are plotted against the normalized sample size ($\sigma/\sigma_c$) for all six shapes considered in this program. The larger size circle and square data were taken from Table XIV. The critical geometry data are all at normalized sizes less than 1.2 $\sigma_c$) except for the squares. The excellent correlation of velocity data gives strong support to the assumption that shape has no influence on the critical detonation velocity. The square data suggest that this correlation continues to exist beyond the critical region, but again, since squares are the shape most similar to circles, this extended correlation has not been tested sufficiently to justify its general application to all shapes.

It is interesting to compare the critical sizes of the shapes that have been tested on the basis of their minimum cross-sectional dimensions or areas. Minimum critical dimensions range from the 1.31 in. pseudocritical web thickness of the hollow cylinder and the 1.75-in.-thick rectangle to the 3.9-in.-altitude equilateral triangle. Critical cross-sectional areas range from 5.8 $in.^2$ (circle) to 11 $in.^2$ (rectangle) and 17.7 $in.^2$ (3-in. ID hollow cylinder). The critical detonation velocities clearly do not correlate with either the minimum critical dimensions or the minimum critical areas, which lends additional support to the approach that was taken in the critical geometry theory development.

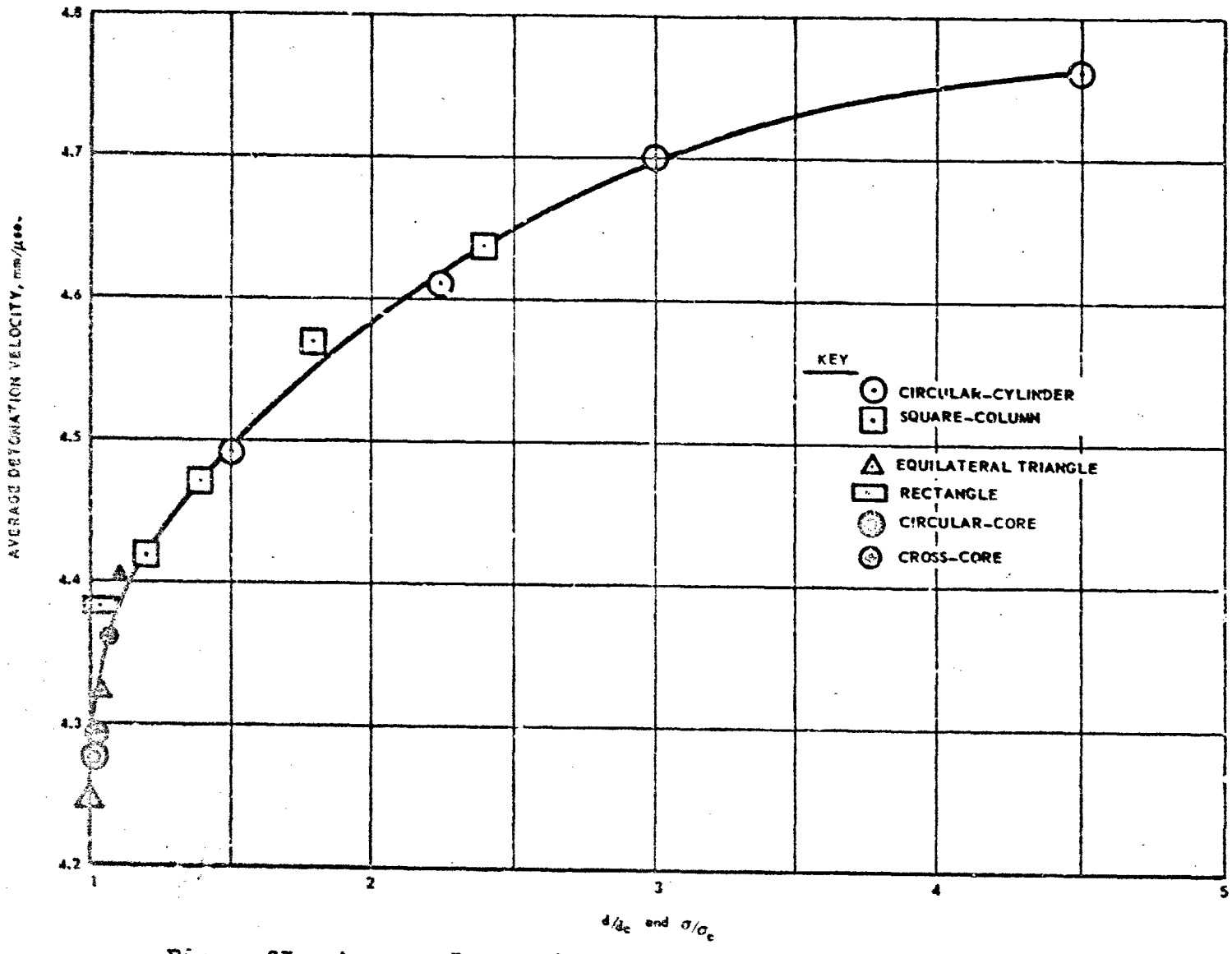


Figure 37. Average Detonation Velocity vs Reduced Size, AAB-3189.

## SECTION VI

## EVALUATION OF THE CRITICAL GEOMETRY THEORY FOR SUSTAINMENT OF DETONATION

### TECHNICAL APPROACH

The ability of the critical geometry theory to predict critical geometries (by Equation 66) was evaluated in this series of experiments by conducting tests with samples of AAB-3225 propellant. This formulation, containing 7.1% RDX, was expected to have a critical diameter near 6 in. The performance of these tests required that the mean critical diameter and the standard deviation be estimated, so that the proper sizes and size increments could be selected for the tests involving these shapes: square column, circular-core cylinder, and cross-core cylinder. Additionally, the estimate of the standard deviation of the critical diameter data could be compared with that obtained using AAB-3189, to determine how the standard deviation may vary with RDX weight fraction. This information can then be extrapolated to 0% RDX to form a crude estimate of the standard deviation expected for unadulterated propellant.

After the mean critical diameter of AAB-3225 was determined, the predicted mean critical geometries of the other shapes were calculated by Equation 66. Using the standard deviation estimate for AAB-3225, sample sizes were computed that lay approximately three standard deviations below and above the predicted mean critical geometries. This approach was taken in preference to actually determining the mean critical geometries because of economic considerations. The statistical uncertainty of each batch's critical diameter would have necessitated preparation of a considerable surplus of samples, covering the six-sigma range in small increments, in order to conduct a standard critical geometry test program. Since these charges are quite large, the total propellant required by such a series and its cost are out of proportion to the task objectives. By testing only at the extremes of the six-sigma region it can be reliably determined whether the theory does function correctly. These tests then are essentially designed to find whether the mean critical geometry is within the predicted range.

## TEST RESULTS

### Critical Diameter Determination

The predicted critical diameter of AAB-3225, using the detonation model of SOPHY I (Reference 1), is 6.00 in. Three batches of this propellant were cast and tested. The experimental results from the first batch indicated a mean critical diameter of 5.21 in., which forced the casting of a second batch to verify this estimate. The second batch ($d_c$ = 6.36 in.) proved to be an outlier, for undetermined reasons, after a third batch was tested and found to have a mean critical diameter of 5.25 in. These batches and their test results are described individually in the following paragraphs.

#### Batch 4EH-44

The results of the 37 tests are shown in Table XXI and in Figure 38. The mean critical diameter is 5.21 in., with a standard deviation of 0.06 in. This critical diameter is about 13% below the theoretically predicted value of 6.00 in. The standard deviation, on the other hand, is the same as that derived for AAB-3189 during the SOPHY I critical-diameter tests. This agreement indicates that variance is relatively constant in the region 7.1% to 9.2% RDX (5.21- to 2.71-in. critical-diameter).

Since the predicted critical diameter was 6.00 in., most of the test samples had to be cut and machined to smaller diameters for these tests. In the process of making these modifications, it was necessary to limit the length of some samples to four-diameter lengths; others were capable of being machined to five-diameter lengths.

The data in Table XXI are arranged in order of decreasing diameter and for samples having the same diameter they are arranged in order of increasing density. The X-ray reports from this batch of propellant showed that every sample had some major voids. All but three samples had these voids in the upper 1- or 2-in. area. It was decided to proceed with the testing of all but the worst sample since the orientation of the sample in the test setup was in the as-cast position, with the major voids at the upper end. The presence of holes at the initiated end did not compromise the data taken over the lower half of the sample.

Table XXI. Critical Diameter Results, Batch 4EH-44.

| Diameter Mean (in.) | Diameter σ (in.) | Density ($gm/cm^3$) | Result (+ = Go 0 = No Go) | Average Detonation Velocity* (mm/μsec) | Test No. |
|---|---|---|---|---|---|
| 6.29 | - | 1.735 | + | 4.2 | 3.2.2.2 |
| 5.65 | - | 1.734 | + | ** | 3.2.2.1 |
| 5.65 | - | 1.734 | + | 4.1 | 3.2.2.3 |
| 5.45 | 0.034 | 1.725 | + | 4.2 | 3.2.2.6 |
| 5.38 | 0.018 | 1.739 | + | 4.2 | 3.2.2.9 |
| 5.37 | 0.011 | 1.740 | + | 4.3 | 3.2.2.11 |
| 5.35 | 0.025 | 1.739 | + | 4.2 | 3.2.2.8 |
| 5.34 | 0.033 | 1.736 | + | 4.2 | 3.2.2.16 |
| 5.34 | 0.031 | 1.740 | + | 4.2 | 3.2.2.14 |
| 5.34 | 0.027 | 1.741 | + | 4.2 | 3.2.2.15 |
| 5.30 | 0.025 | 1.733 | + | 4.3 | 3.2.2.13 |
| 5.29 | 0.024 | 1.730 | + | 4.1 | 3.2.2.21 |
| 5.29 | 0.021 | 1.731 | + | 4.2 | 3.2.2.22 |
| 5.28 | 0.023 | 1.731 | + | 4.2 | 3.2.2.23 |
| 5.28 | 0.036 | 1.731 | + | 4.2 | 3.2.2.26 |
| 5.28 | 0.028 | 1.732 | + | 4.2 | 3.2.2.24 |
| 5.28 | 0.027 | 1.733 | + | 4.2 | 3.2.2.28 |
| 5.28 | 0.010 | 1.735 | + | ** | 3.2.2.12 |
| 5.28 | 0.017 | 1.736 | + | 4.1 | 3.2.2.18 |
| 5.28 | 0.016 | 1.736 | + | 4.2 | 3.2.2.19 |
| 5.28 | 0.011 | 1.736 | + | 4.2 | 3.2.2.20 |
| 5.28 | 0.018 | 1.737 | 0 | *** | 3.2.2.17 |
| 5.28 | 0.008 | 1.739 | 0 | *** | 3.2.2.10 |
| 5.27 | 0.008 | 1.743 | 0 | *** | 3.2.2.5 |
| 5.26 | 0.040 | 1.730 | + | 4.1 | 3.2.2.25 |
| 5.24 | 0.024 | 1.733 | + | 4.0 | 3.2.2.27 |
| 5.24 | 0.025 | 1.733 | + | 4.1 | 3.2.2.29 |
| 5.02 | 0.010 | 1.729 | 0 | *** | 3.2.2.7 |
| 5.02 | 0.016 | 1.736 | 0 | *** | 3.2.2.37 |
| 5.01 | 0.003 | 1.733 | 0 | *** | 3.2.2.4 |
| 5.01 | 0.016 | 1.735 | 0 | *** | 3.2.2.30 |
| 4.86 | 0.011 | 1.739 | 0 | *** | 3.2.2.35 |
| 4.85 | 0.015 | 1.735 | 0 | *** | 3.2.2.34 |
| 4.85 | 0.014 | 1.736 | 0 | *** | 3.2.2.36 |
| 4.75 | 0.011 | 1.738 | 0 | *** | 3.2.2.31 |
| 4.74 | 0.008 | 1.731 | 0 | *** | 3.2.2.32 |
| 4.50 | 0.015 | 1.735 | 0 | *** | 3.2.2.33 |

*Calculated from probe data. Obtained over region from two diameters down to charge bottom. Accuracy of measurement is ± 0.1 mm/μsec.

**No raster record.

***Not applicable.

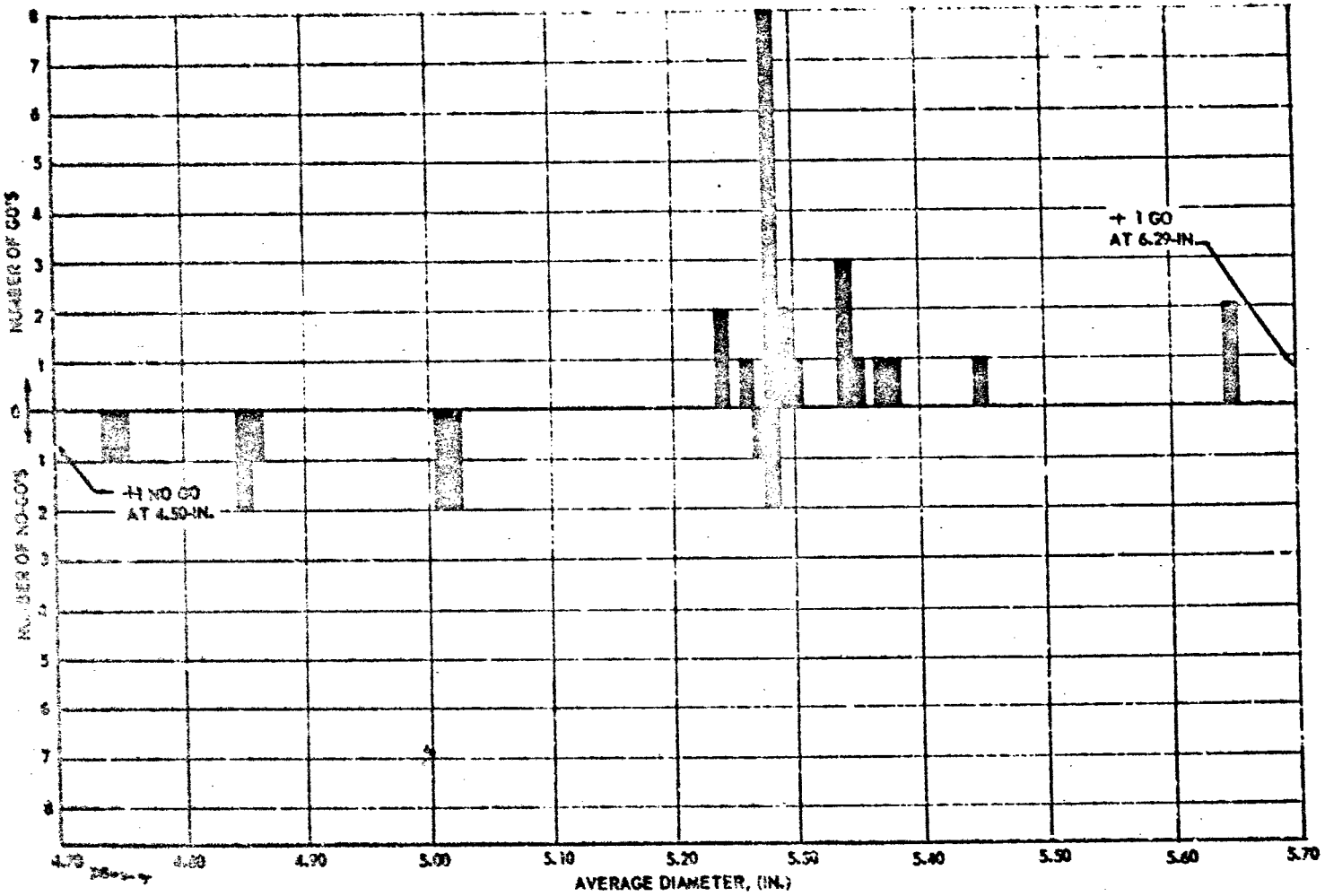


Figure 38. Critical Diameter Results, Batch 4EH-44.

One of the very porous samples and one of the average samples were sent to Aerojet-Sacramento for microscopic analysis to determine whether the distribution of pores visible by X-ray inspection extended significantly down to the microscopic region (10 to 100 μ sizes). If such small pores had existed in the propellant, the unexpectedly low critical diameter of Batch 4EH-44 material could have been understood as being the result of the increase in number of hot-spot initiation sites due to porosity.

The original large samples were prepared for the analysis by cutting them into disc-shaped sections, each of which was subsequently subsectioned. From the subsections, specimens were microtomed and mounted for microscopic examination. Each specimen was approximately 25 to 30μ thick, which placed a lower limit of 12 to 15 μ on the pore sizes that could be observed. Figure 39 shows the sectioning plan used in these analyses. Discussion of the microscopic techniques used in this program is given in Appendix VI.

No pores were discovered in the microscopic region for either sample. Representative photomicrographic mosaics are shown in Figures 40 and 41. In the photographs, the black areas are opaque aluminum particles, the large clear white areas are transparent ammonium perchlorate (AP) crystals, and the small (1 mm) bright or gray spots are RDX crystals. The small voids within the AP crystals are common and must not be thought of as peculiar to the material used in this batch.

Re-evaluation of the predicted pore size that is effective as a hot-spot initiation site has led to the conclusion that pores of 2 to 5 μ diameter can be effective. Their direct observation by microscopic techniques is beyond reach, however, because to prepare microtome specimens of the necessary thickness (4 to 10 μ) and to permit their observation requires chipping a frozen propellant sample. Serious doubts can be raised as to the effect of such action on the physical condition of the sample. This fact, plus the extreme difficulty imposed by requiring a sample of uniform thickness, is further complicated by the fact that the surface area of such a thin specimen must be so small that the number of such specimens required to provide a representative sampling is unmanageably high.

Batch 4EH-84

Batch 4EH-84 was cast to resolve the question of whether the previous data were obtained from acceptable material. The test design was enlarged to cover both the range around the theoretically predicated critical diameter and the range tested with Batch 4EH-44. The test results are shown in Table XXII.

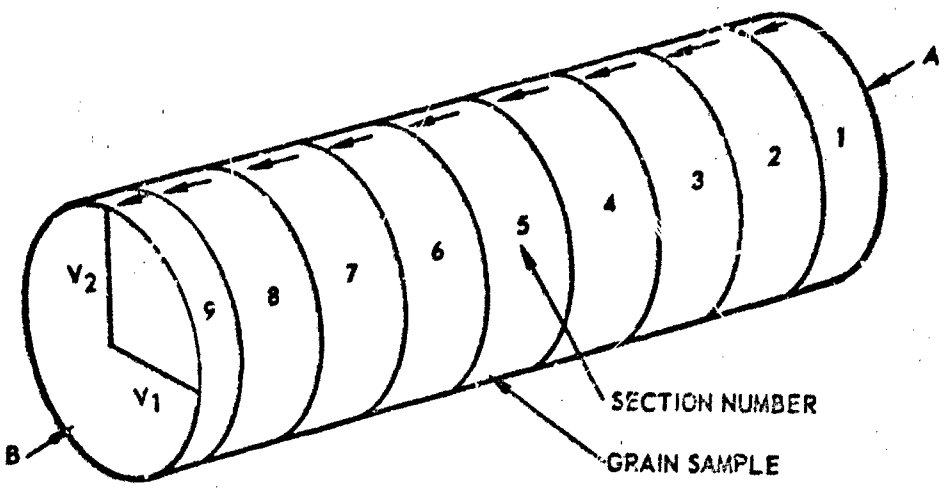


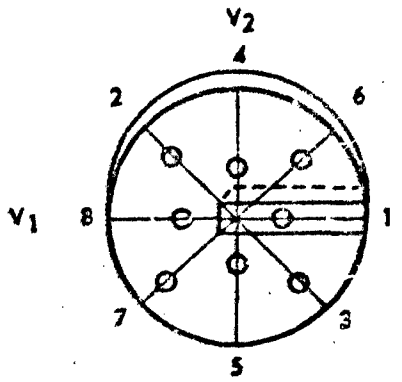


RADIAL SECTION PLAN
1-8 RAY INDEX NUMBER

O - PHOTOMICROGRAPH-MOSAIC LOCATION

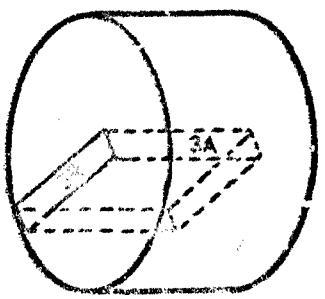


AXIAL SECTION PLAN
CODE NO. SECTION NO.
0.3 A AXIAL
0.3 R RADIAL

Figure 39. Sectioning Plan for Microscopic Analysis.

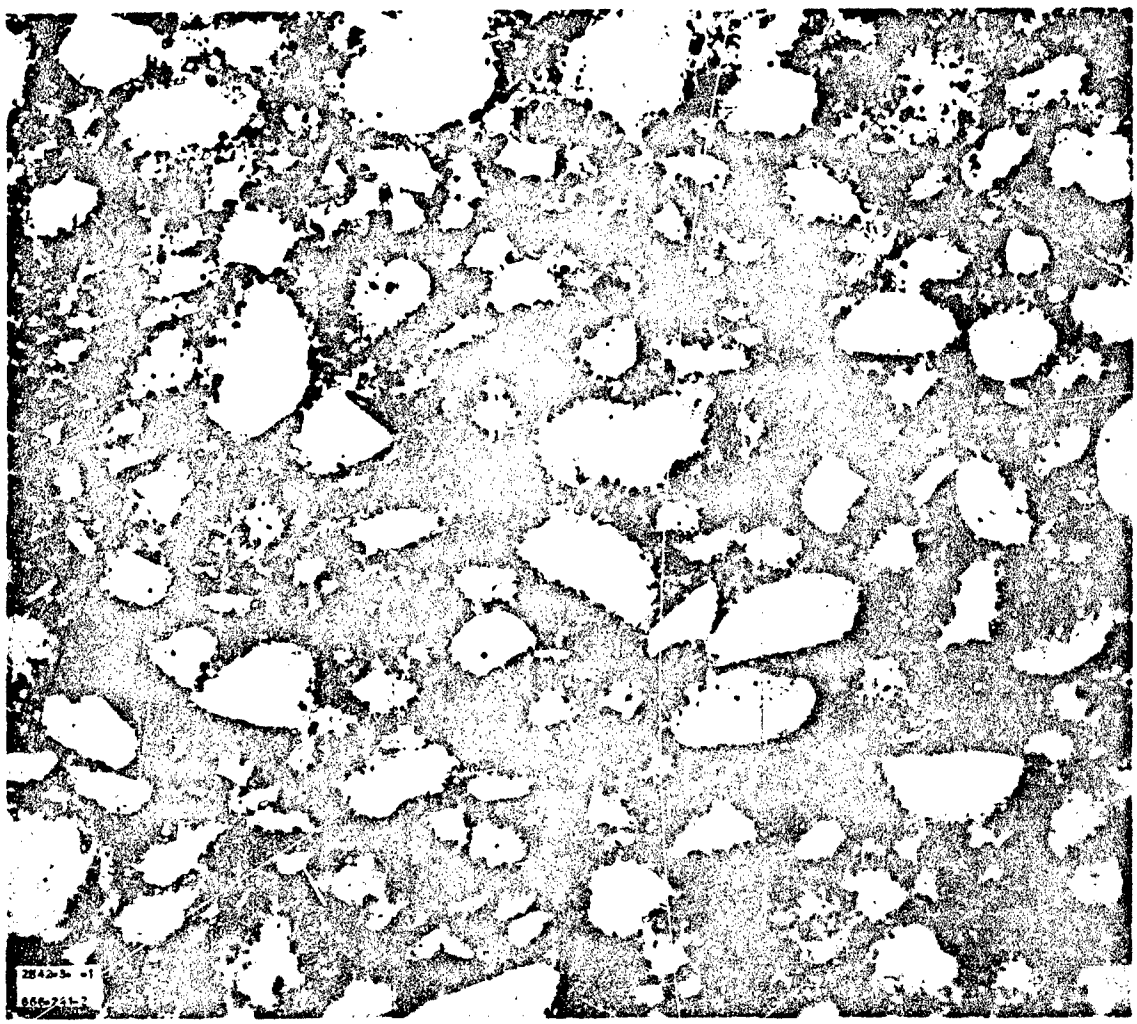

Figure 40. Photomicrograph of AAB-3225 Propellant, Batch 4EH-44 (Specimen 6A).

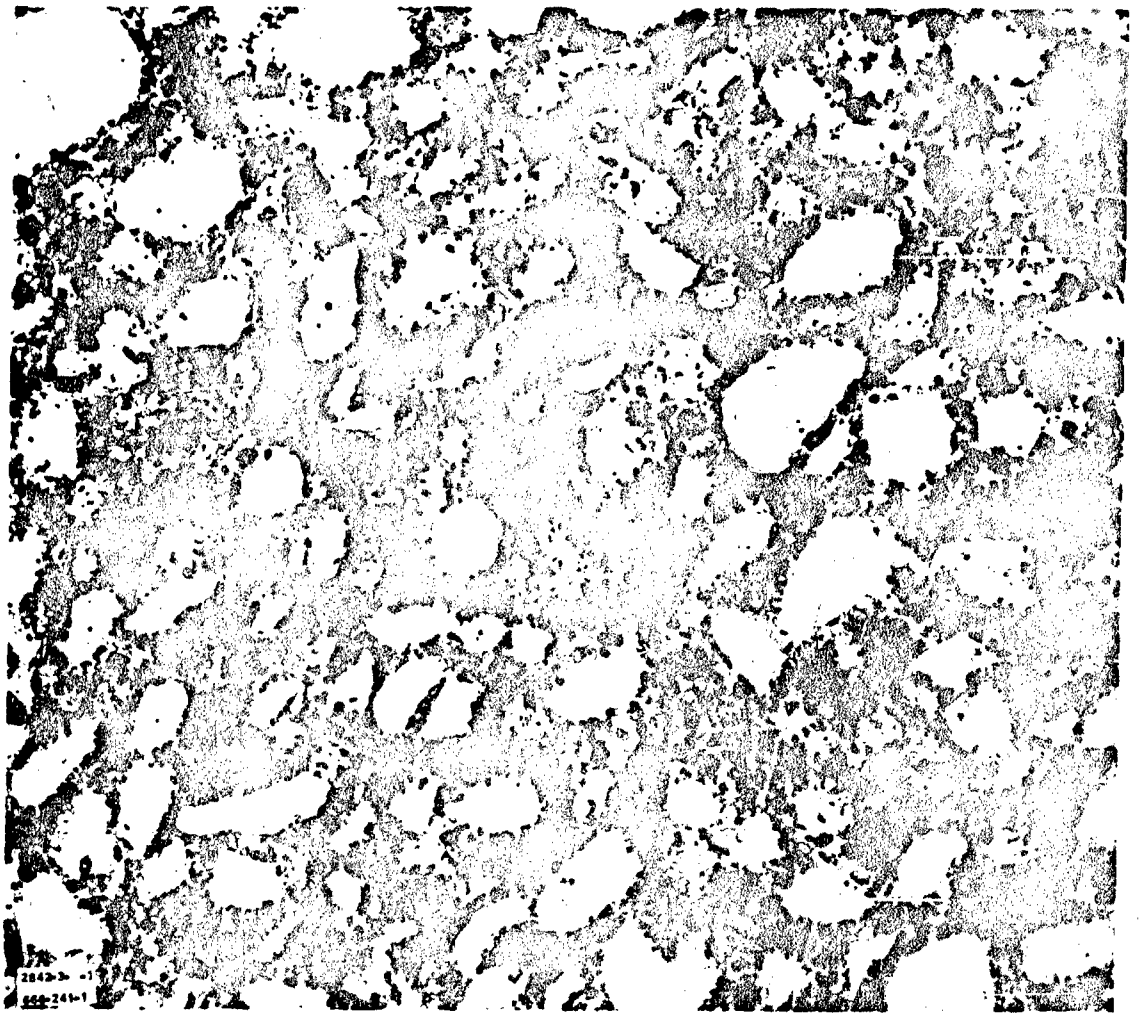

Figure 41. Photomicrograph of AAB-3225 Propellant, Batch 4EH-44 (Specimen 2R).

Table XXII. Critical-Diameter Results, Batch 4EH-84.

| Mean Diameter (in.) | Result (+ = Go) (0 = No Go) | Average Detonation Velocity (mm/μ sec) | Test No. |
|---|---|---|---|
| 5.49 | 0 | -- | 3.2.2.38 |
| 5.49 | 0 | -- | 3.2.2.39 |
| 5.98 | 0 | -- | 3.2.2.40 |
| 5.99 | 0 | -- | 3.2.2.41 |
| 6.09 | 0 | -- | 3.2.2.51 |
| 6.09 | 0 | -- | 3.2.2.52 |
| 6.10 | - | -- | 3.2.2.43 |
| 6.10 | 0 | -- | 3.2.2.50 |
| 6.23 | 0 | -- | 3.2.2.46 |
| 6.24 | 0 | -- | 3.2.2.44 |
| 6.48 | + | 4.25 | 3.2.2.45 |
| 6.48 | + | 4.15 | 3.2.2.47 |
| 6.97 | + | 4.33 | 3.2.2.42 |
| 7.00 | + | Not reduced | 3.2.2.48 |

No overlapping of go and no go results occurred, undoubtedly because of the large increment between diameters at that portion of the test design where the critical diameter was found. No unique maximum-likelihood estimates of $\mu$ and $\sigma$ can be defined. An estimate of $\mu$ would be given best by the midrange diameter between the largest diameter no go and the smallest diameter go. For this set of data, $\mu$ = 6.36 in. No estimate can be made of $\sigma$, but it apparently is not very large.

The wide difference between the critical diameters of these two batches is extremely difficult to explain. That this is the normal batch-to-batch variation to be expected for this formulation is intuitively impossible to accept. Compositional variation in RDX-content, for example, to account for such a shift in the critical diameter, is far beyond the tolerance limits allowed in the batch preparation, and a major discrepancy of this type would appear in the batch preparation records. No such irregularity in composition has been detected following examination of all the batch records.

Batch 4EH-107

The results of the tests are shown in Table XXIII. The need to cover a large range of diameters in this test design precluded the casting of more than two samples at any of these sizes because of their weight and the 2000 lb limit on batch sizes. The test results are composed of nine go-no go data points. Testing at the larger sizes (greater than 5.75 in.) served no purpose once the critical region was established to be at 5.25 in.

Mixed results occurred only at the 5.25-in.-diameter. For results of this type, the maximum likelihood estimate of the mean is given by the test level at which the mixed results occur -- 5.25 in.; the maximum likelihood estimate of the standard deviation must be zero. The latter estimate is difficult to accept. One estimate that appears to be more realistic is that obtained by combining estimates derived from two other estimation techniques, i.e., the minimum overlapping subset method and the two subset method (Reference 11). Applying these techniques to the data yields an estimate of the standard deviation of 0.07 in.

Summary

Statistics from all three batches of 7.1% RDX adulterated solid-cylindrical samples are shown in Table XXIV. It is obvious that the results obtained from Batches 4EH-44 and -107 agree quite closely and that they disagree strongly with the results obtained from Batch 4EH-84.

Table XXIII. Critical-Diameter Results, Batch 4EH-107.

| Mean Diameter (in.) | Result of Test | Average Detonation Velocity (mm/μsec) | Std Dev of Velocity (mm/μsec) | Test No. |
|---|---|---|---|---|
| 5.00 | No Go | - | - | 3.2.2.59 |
| 5.01 | No Go | - | - | 3.2.2.57 |
| 5.24 | No Go | - | - | 3.2.2.58 |
| 5.25 | Go | 4.08 | 0.095 | 3.2.2.56 |
| 5.49 | Go | 4.17 | 0.072 | 3.2.2.55 |
| 5.49 | Go | 4.11 | 0.135 | 3.2.2.60 |
| 5.74 | Go | 4.23 | 0.081 | 3.2.2.61 |
| 5.75 | Go | 4.17 | 0.163 | 3.2.2.54 |
| 5.99 | Go | 4.26 | 0.124 | 3.2.2.53 |

Table XXIV. Comparison of Critical-Diameter Estimates for AAB-3225.

| Estimated Quantity | Symbol | Batch 4EH-44 | Batch 4EH-84 | Batch 4EH-107 | Combined Data Batches 4EH-44 and -107 |
|---|---|---|---|---|---|
| Mean (in.) | $\mu$ | 5.21 | 6.36* | 5.25 | 5.24 |
| Standard Deviation | $\sigma$ | 0.06 | - | 0.07 | 0.08 |
| Covariance | $\sigma_{\mu\mu}$ | 0.00247 | - | - | 0.00031 |
| | $\sigma_{\mu\sigma}$ | -0.00196 | - | - | 0.00026 |
| | $\sigma_{\sigma\sigma}$ | 0.00197 | - | - | 0.00035 |
| ln Likelihood | ln L | -8.15 | - | -1.39 | -10.13 |

*Not maximum-likelihood estimate.

A statistical test of the hypothesis that the data from Batches 4EH-44 and -107 comefrom populations with identical cumulative normal response functions can be made using the likelihood-ratio criterion. For these data, the ln-likelihood ratio is calculated as

$$\ln\lambda = -10.13 + 8.15 + 1.39 \quad (67)$$

$$= 0.59 \quad (68)$$

Therefore,

$$\chi^2 = 1.18 \quad (69)$$

The probability of observing a chi-square value of this size with two degrees of freedom is approximately 0.55. Hence, it is concluded that both sample batches come from populations with the same cumulative normal response function.

An exact statistical comparison of all three batches was difficult since it was impossible to calculate a likelihood for the Batch 4EH-84 samples. However, the fact that the mean of this batch differs significantly from the means of the other two batches is obvious; the batch means differ by more than 1 in. with a within-batch standard deviation of 0.07 in. It is statistically hard to believe that a variation in batch means this large could be attributable to normal batch-to-batch variation. In fact, applying the Dixon-Mood criteria (Reference 12) for extreme means to this data it can be shown at the 0.05 significance level that the Batch 4EH-84 mean is a statistical outlier with respect to the other two means.

Since the large difference in mean critical diameter exists between Batch 4EH-84 and the other two batches, some explanation is required. To this date, all efforts at identifying a chemical or physical difference have been unsuccessful. The compositions of the three batches, as judged from the preparation data, are identical. Furthermore, Batch 4EH-44 was bayonet cast, while the other two were vacuum cast. X-ray reports show that only Batch 4EH-44 samples contained large amounts of pores visible by this technique, yet microscopic examination of samples from this batch could not detect porosity in the 12 to 100 μ-diameter pore-size region.

Density measurements on sections from samples remaining from all three batches were performed to discover whether there was a correlative difference in sample density between the batches. The average densities of these batches were 1.735, 1.724, and 1.729 gm/cc, respectively. No indication of mixing or casting differences between batches was discovered. Since the density data do

not correlate with the critical-diameter data, the difficulty has not been resolved. However, because of the agreement between Batches 4EH-44 and -107, it was concluded that Batch 4EH-84 was not representative of the AAB-3225 formulation. Consequently, the mean critical diameter for AAB-3225 is estimated to be 5.24 in.

## Critical Geometry Verification

Four samples were prepared at each of the two sizes designated for the verification tests of squares and hollow cylinders. The latter were designed with 3 in. ID and 6 in. ID circular cores and with 3 in. by 3 in. and 6 in. by 6 in. cross cores. Of the total of 40 samples that were prepared, 39 were tested. One large ID circular core sample could not be removed from its mold and had to be excluded from testing.

The perforated shapes were tested under the conditions established in the AAB-3189 tests to reduce the level of overboostering, prevent jet formation by the booster, and eliminate obstructions to the jet formed in the propellant.

A hollow-core sample was considered pseudosupercritical if sustained detonation occurred for at least 2 web thicknesses. Unless this was observed, the sample was classified subcritical.

The results of all the tests are given in Table XXV. The larger samples of every shape were found to be supercritical (in the case of the squares) or pseudosupercritical (in the case of the hollow cylinders). The latter showed sustained detonation over distances from 15 to 41 in. The subcritical hollow cylinders were marked in every case by an attenuating shock wave that reached subcritical velocities within 2 in. of travel into the sample.

## CONCLUSIONS

These results show no reason to reject the hypothesis that Equation 66 correctly predicts the critical dimensions of these shapes. The predictions of the critical geometry theory having been demonstrated with AAB-3225 propellant, the theory can be considered to be applicable to all detonable materials.

## Table XXV. Verification-Test Results, Using AAB-3225 Propellant.

| Shape | Inner Dimension (in.) | Outer Dimension (in.) | Length (in.) | Test Result* | Detonation Velocity (mm/μsec) | Propagation Distance (in.) | Test No. |
|---|---|---|---|---|---|---|---|
| Square Column | NA | 4-1/2 by 4-1/2 | 24 | No Go | -- | -- | 3.3.3.3 |
| | | | | No Go | -- | -- | 3.3.3.14 |
| | | | | No Go | -- | -- | 3.3.3.15 |
| | | | | No Go | -- | -- | 3.3.3.17 |
| | | 5-1/8 by 5-1/8 | 24 | Go | No data | -- | 3.3.3.4 |
| | | | | Go | 4.11 | 24 | 3.3.3.5 |
| | | | | Go | 4.19 | 24 | 3.3.3.9 |
| | | | | Go | 4.11 | 24 | 3.3.3.16 |
| Circular-Core Cylinder | 3 | 7-1/4 | 36 | No Go | -- | -- | 3.3.3.1 |
| | | | | No Go | -- | -- | 3.3.3.6 |
| | | | | No Go | -- | -- | 3.3.3.22 |
| | | | | No Go | -- | -- | 3.3.3.23 |
| | | 8 | 36 | Go | 4.29 | 25 | 3.3.3.2 |
| | | | | Go | 4.35 | 30 | 3.3.3.11 |
| | | | | Go | 4.21 | 20 | 3.3.3.24 |
| | | | | Go | 4.29 | 30 | 3.3.3.25 |
| | 6 | 10-1/4 | 48 | No Go | -- | -- | 3.3.3.13 |
| | | | | No Go | -- | -- | 3.3.3.36 |
| | | | | No Go | -- | -- | 3.3.3.37 |
| | | | | No Go | -- | -- | 3.3.3.38 |
| | | 11 | 48 | Go | 4.43 | 41 | 3.3.3.19 |
| | | | | Go | 4.20 | 35 | 3.3.3.30 |
| | | | | Go | 4.21 | 18 | 3.3.3.39 |
| Cross-Core Cylinder | 3 by 3 cross | 7-1/4 | 36 | No Go | -- | -- | 3.3.3.8 |
| | | | | No Go | -- | -- | 3.3.3.10 |
| | | | | No Go | -- | -- | 3.3.3.20 |
| | | | | No Go | -- | -- | 3.3.3.21 |
| | | 8 | 36 | Go | 4.39 | 25 | 3.3.3.7 |
| | | | | Go | 4.38 | 25 | 3.3.3.12 |
| | | | | Go | 4.35 | 25 | 3.3.3.26 |
| | | | | Go | 4.39 | 20 | 3.3.3.27 |
| | 6 by 6 cross | 10-1/4 | 48 | No Go | -- | -- | 3.3.3.28 |
| | | | | No Go | -- | -- | 3.3.3.33 |
| | | | | No Go | -- | -- | 3.3.3.34 |
| | | | | No Go | -- | -- | 3.3.3.35 |
| | | 11 | 48 | Go | 4.40 | 34 | 3.3.3.18 |
| | | | | Go | 4.28 | >15 | 3.3.3.29 |
| | | | | Go | 4.31 | 27 | 3.3.3.31 |
| | | | | Go | 4.32 | 35 | 3.3.3.32 |

*For the hollow-core cylindrical shapes, a go test result is one that shows a sustained detonation velocity over a considerable length of the sample; a no go for these shapes does not exhibit sustained detonation over any measurable portion of the sample length. Therefore, the go's are superpseudocritical; the no-go's are subcritical.

PRECEDING PAGE BLANK-NOT FILMED

# SECTION VII

# INITIATION CRITERION THEORY

## INTRODUCTION

The second major requirement of the SOPHY program is the determination of the conditions required for initiation of detonation in solid composite propellant. The use of high-explosive boosters weighing up to 18,000 lb, in the critical diameter studies, in no way implies that only under such conditions could the propellant samples have detonated. In critical geometry studies, the object is to determine only whether a sample of a given size can support a steady-state detonation. Full-scale boosters are used in critical geometry tests to assure that the test results are due to the sample sizes and not to insufficient shock loading.

The initiation criterion is defined as the minimum necessary and sufficient conditions that must be met by the parameters that describe a shock wave, for that shock wave to initiate detonation in a given material (Reference 1). The shock pressure, shock wave area, and pulse width are those parameters. By the definition given above, if the initiation criterion is not satisfied, detonation of the material will not occur; if it is satisfied, detonation must occur. Similarily, if the propellant sample detonates, the initiating shock wave must have met the initiation criterion. Theoretically, the initiation criterion is a property of the material and independent of sample shape.

In the SOPHY study, this criterion has been determined partially as a relationship between the minimum shock pressure $P^+$ (P-cross) of a plane wave that is required to initiate detonation in a cylindrical sample of area A for samples of several RDX-adulterated propellant formulations ranging in diameters from near-critical to near-ideal, by conducting card-gap tests using Plexiglas[3] as the shock attenuator. By definition, the initiation criterion is a surface in pressure-area-pulse-width space. The criterion that has been determined is actually the projection on the P-A plane of a curve that lies in that surface, since the variation of pulse width with the distance the shock wave travels through the PMMA attenuator has not been established. A series of tests was conducted, however, that showed how the minimum initiating pressure $P^+$ varied with initial pulse width for 4-in. diameter samples of AAB-3189. The need for further study in this area is discussed in Section XII.

[3]Plexiglas is the trade name used by Rohm and Haas for polymethyl methacrylate, hereafter referred to as PMMA.

## INITIATION CRITERIA DETERMINATIONS

Using the card-gap technique to determine the $P^*(A)$ relationship required that several related studies be performed. First, since it would be very difficult to measure the shock velocity in PMMA at the PMMA-propellant interface[4] for each test, especially for the larger tests, an empirical relationship between shock pressure and distance travelled in PMMA was determined. This permitted the reduction of PMMA thickness to incident shock pressure. Second, to calculate the transmitted shock pressure, it was necessary to determine the unreactive Hugoniot equation-of-state for each propellant formulation. The pressure transmitted to the propellant then could be calculated by the Hugoniot-reflection technique, knowing the incident pressure and the Hugoniots of PMMA and the propellant.

### Shock Pressure Attenuation in PMMA

In SOPHY I it was found that the data on shock pressure attenuation in solid cylindrical PMMA rods could be normalized by plotting $P/P_o$ vs $x/d$, where P is the shock pressure, $P_o$ is the initial transmitted shock pressure at the booster-PMMA interface, x is the distance travelled by the shock wave in the PMMA, and d is the diameter of the PMMA column (Reference 1). The SOPHY II program required testing of samples up to 42-in. in diameter which both ruled out the use of solid cylindrical rods for shock attenuation and the use of Composition B for the booster explosive. The PMMA attenuators were constructed instead from stacked square plates and the boosters were cast from TNT.

Using the Hugoniot equation of state for PMMA,

$$P = 5.51\ U^2 - 14.03\ U \quad \text{kbar} \tag{70}$$

where U is the shock velocity in mm/μsec, the shock pressure attenuation can be calculated from shock velocity attenuation data. Measurement of shock velocities in columns of large square plates requires the use of probes and a rasteroscillograph. Optical methods using Argon back-lighting and a Beckman & Whitley streak camera were totally inadequate with 8-in. squares, for example, because of light reflection at the many plate-to-plate interfaces. Even had this problem not arisen with the small squares, attempts to calibrate the larger squares would have faced the additional obstacles of resolution and light intensity, since the camera would have had to be well removed from the test article.

[4] The custom in identifying interfaces is to name first the material from which the shock passes, and name second the material into which the shock is transmitted.

The adopted method used sets of two parallel enamelled-copper wires, at various interfaces in the PMMA column and the PMMA-propellant interface, to obtain time-of-arrival data. This information was recorded on a rasteroscillograph. The success of this method is demonstrated by excellent reproducibility and indicated by the smooth behavior of the distance-time data. The system appears to be limited, however, to sizes below 20 in. because the quality of the results deteriorated beyond that point. At the larger sizes it was found that mechanical target probes inserted in spaced plates gave excellent time-of-arrival information. The distance-time data are given in Table XXVI.

These data were fit to quadratic equations which were differentiated explicitly to provide shock velocity data. (The fits to the distance-time data are shown in Appendix VII.) This method of data reduction was applied instead of numerical differentiation because the data were acquired at unequal increments in both variables. Numerical differentiation of such data is normally accomplished by differentiating the Lagrange or Hermite interpolation formulas, but no estimate of the error is possible when these formulas are applied, so the method is not particularly attractive. Also, these two methods do not function well when there is a large relative difference between successive intervals. Since the quadratic fits to the distance-time data do approximate the data closely, this method was adopted.

The computed initial shock pressure $P_o$ in PMMA from a TNT booster is estimated from the differentiated fits to the square-column data to be 118 kbar.

The shock pressure data can be represented by

$$P/P_o = \exp\left(-2.14504\,\frac{x}{d}\right) \qquad (71)$$

where the standard deviation of the coefficient of x/d is 0.0743 (Figure 42). For comparison, attenuation data have been reported in the literature for 2-in.-diameter columns of PMMA that were shocked with tetryl pellets (References 13, 14, and 15). Figure 43 shows the published tetryl data, plotted as log P vs x/d. For reference, the attenuation of shock pressure in a 3-in.-diameter PMMA column boostered by Composition B is shown, since the SOPHY I and SOPHY II attenuation data are nearly identical, and the $P_o$ for Composition B is considerably higher (211 kbar) than that for tetryl (103 to 123 kbar).

Table XXVI. Attenuation of Shock from TNT Booster by Stacked Squares of Plexiglas.

| Plexiglas Column Cross-Section (in.) | Distance Traveled in Plexiglas (in.) | Time of Arrival (μsec) |
|---|---|---|
| 8 by 8 | 1.00 | 4.37 |
| | 1.31 | 6.25 |
| | 2.00 | 9.44 |
| | 2.81 | 14.05 |
| | 3.00 | 14.63 |
| | 3.53 | 17.5 |
| | 4.00 | 20.1 |
| | 4.28 | 22.2 |
| | 5.00 | 25.6 |
| | 6.47 | 34.85 |
| | 6.70 | 37.5 |
| | 7.25 | 40.9 |
| 10 by 10 | 3.00 | 14.4 |
| | 4.00 | 19.5 |
| | 5.00 | 25.0 |
| | 7.00 | 37.0 |
| | 7.57 | 41.1 |
| | 8.52 | 47.5 |
| | 9.50 | 55.5 |
| | 10.00 | 59.5 |
| 12 by 12 | 2.00 | 9.0 |
| | 5.00 | 25.0 |
| | 9.75 | 54.3 |
| | 10.80 | 61.1 |
| | 11.00 | 63.0 |
| | 11.80 | 70.7 |
| 20 by 20 | 7.00 | 35.0 |
| | 9.50 | 52.5 |
| | 13.50 | 70.0 |
| | 16.50 | 92.1 |
| | 18.50 | 107.0 |
| | 20.65 | 137.5 |
| 24 by 24 | 11.75 | 60.0 |
| | 23.50 | 136.0 |
| 42 by 42 | 25.00 | 125.6 |
| | 27.10 | 142.0 |
| | 31.00 | 166.8 |
| | 32.70 | 177.0 |
| | 34.75 | 191.5 |
| | 38.70 | 220.0 |
| | 40.50 | 235.5 |
| | 42.00 | 248.0 |

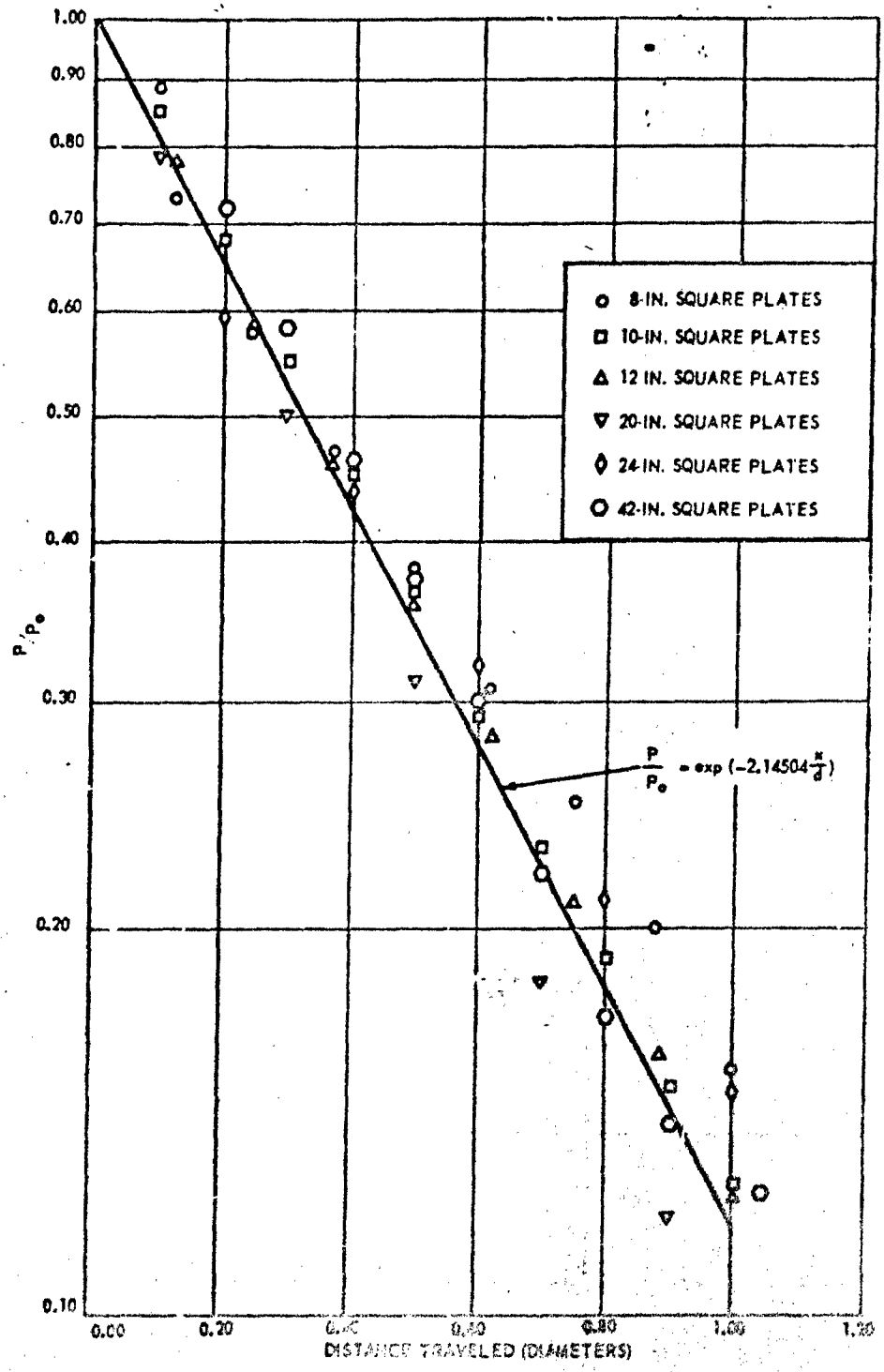


Figure 42. Shock Pressure Attenuation in PMMA, Using TNT Boosters ($P_o$ = 118 kbar).

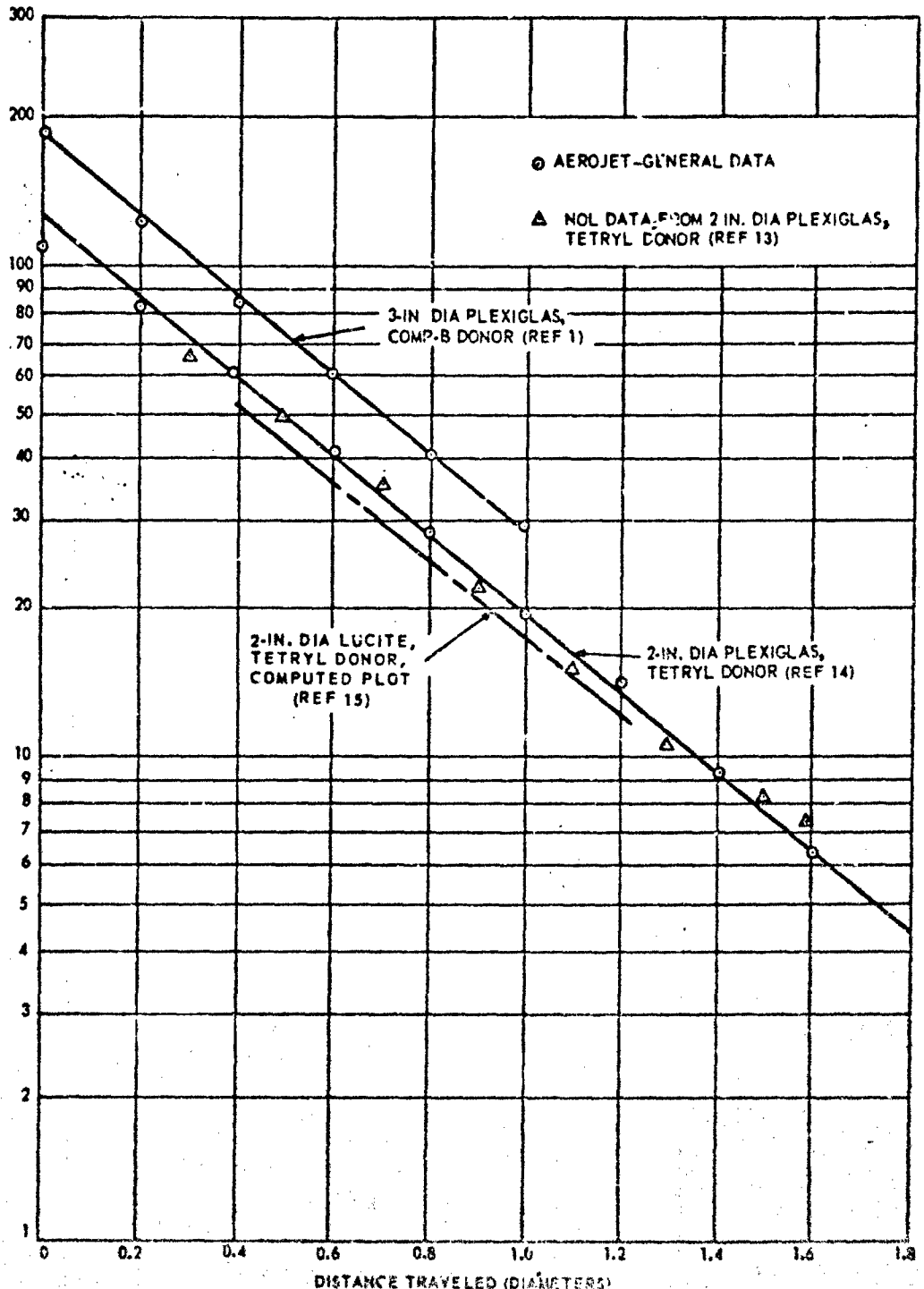


Figure 43. Shock Pressure Attenuation in PMMA - Various Donors.

In Figure 43 the data points of Liddiard (Reference 13) and Aerojet (Reference 14) when fit by linear least squares are indistinguishable from each other because both sets of data extrapolate to $P_o$ = 123 kbar, and their slopes are -1.89704 and -1.86983, respectively.

Price reports that for distances greater than 20mm the shock pressure attenuation in 2-in.-diameter Lucite is approximated by

$$P = 105 \exp(-0.0358\, x) \tag{72}$$

where x is the distance in mm (Reference 15). Converting the independent variable x to x/d requires multiplication of the coefficient of x by d, which is 50.8mm. Equation 72 thus becomes

$$P = 105 \exp\left(-1.8164 \frac{x}{d}\right) \tag{73}$$

The tetryl curves for 2-in. diameter columns and the TNT curve for stacked plates up to 42 in. square are shown in Figure 44. Since $P_o$ in the SOPHY II tests and in the NOL tests is near 100 kbar, the maximum difference in pressures at any x/d predicted from the two sets of data is about 6 kbar.

The SOPHY I attenuation curve for Composition B-boostered PMMA columns and the SOPHY II attenuation curve for TNT-boostered PMMA plates are shown in Figure 45. The correspondence between the two curves supports the contention that attenuation can be represented by a $P/P_o$ vs x/d curve despite the differences in $P_o$ and in the shape of the attenuator. The data from Reference 13 reduced to $P/P_o$ are plotted in Figure 45 along with computed points. The points lay parallel to the SOPHY curves, but slightly above them -- a difference that cannot be identified as significant without a statistical interpretation of all data to determine the errors involved in the pressure estimates and in the curve fitting.

It must be emphasized that although the attenuation data do attain a relationship that may be described by

$$P = P_o \exp\left(-k \frac{x}{d}\right) \tag{74}$$

in the pressure regions being studied, no theoretical justification has been made for Equation 74 and, consequently, it serves only as a curve-fitting tool. Considerably more investigation of the attenuation process with fundamental analysis of the mechanism involved must precede the formation of any mathematical model. It is significant, however, that within the limits of this investigation the attenuation has been adequately approximated by an expression that involves only geometrical considerations.

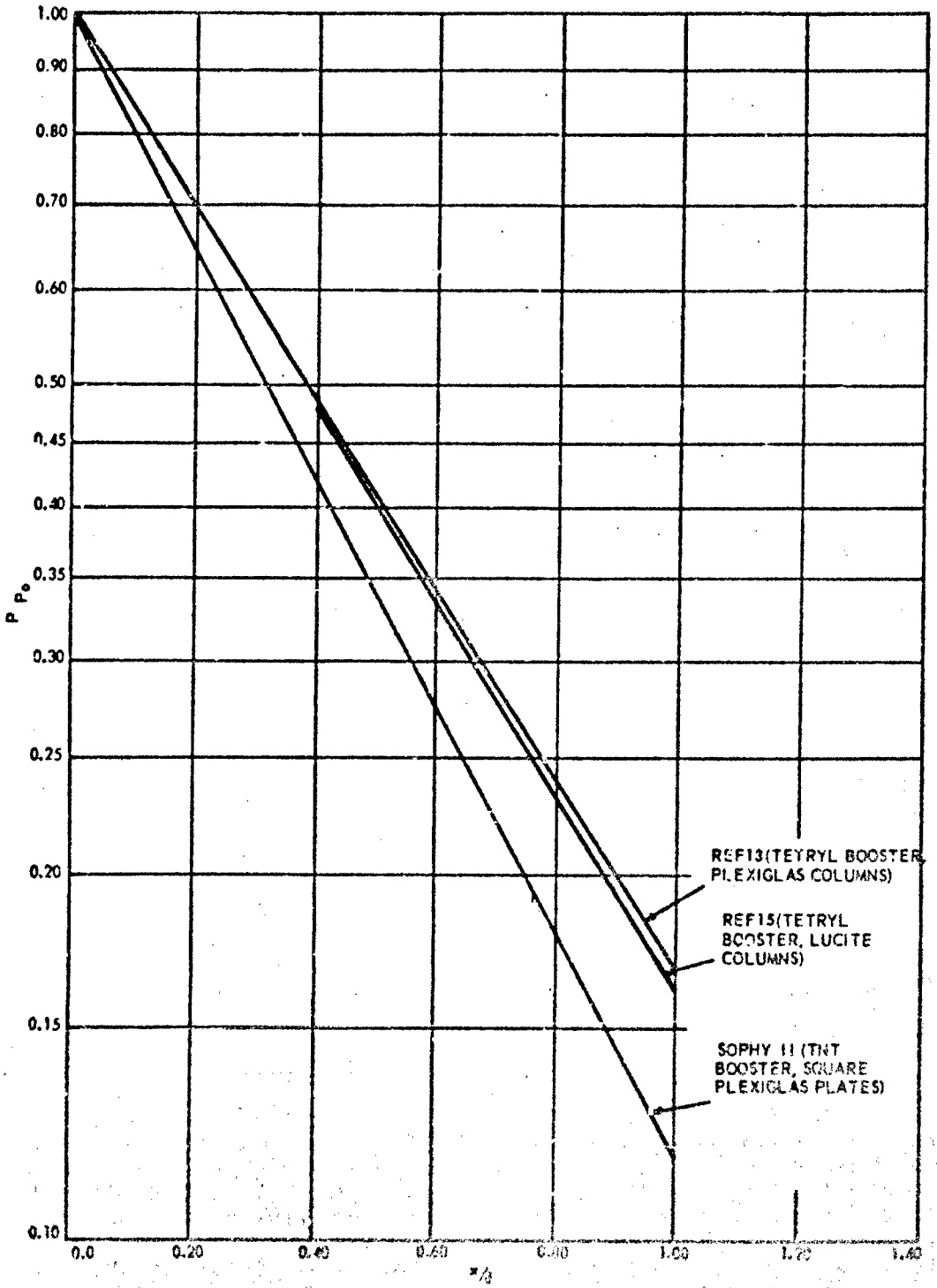


Figure 44. Normalized Shock-Pressure Attenuation Curves for Plexiglas and Lucite.

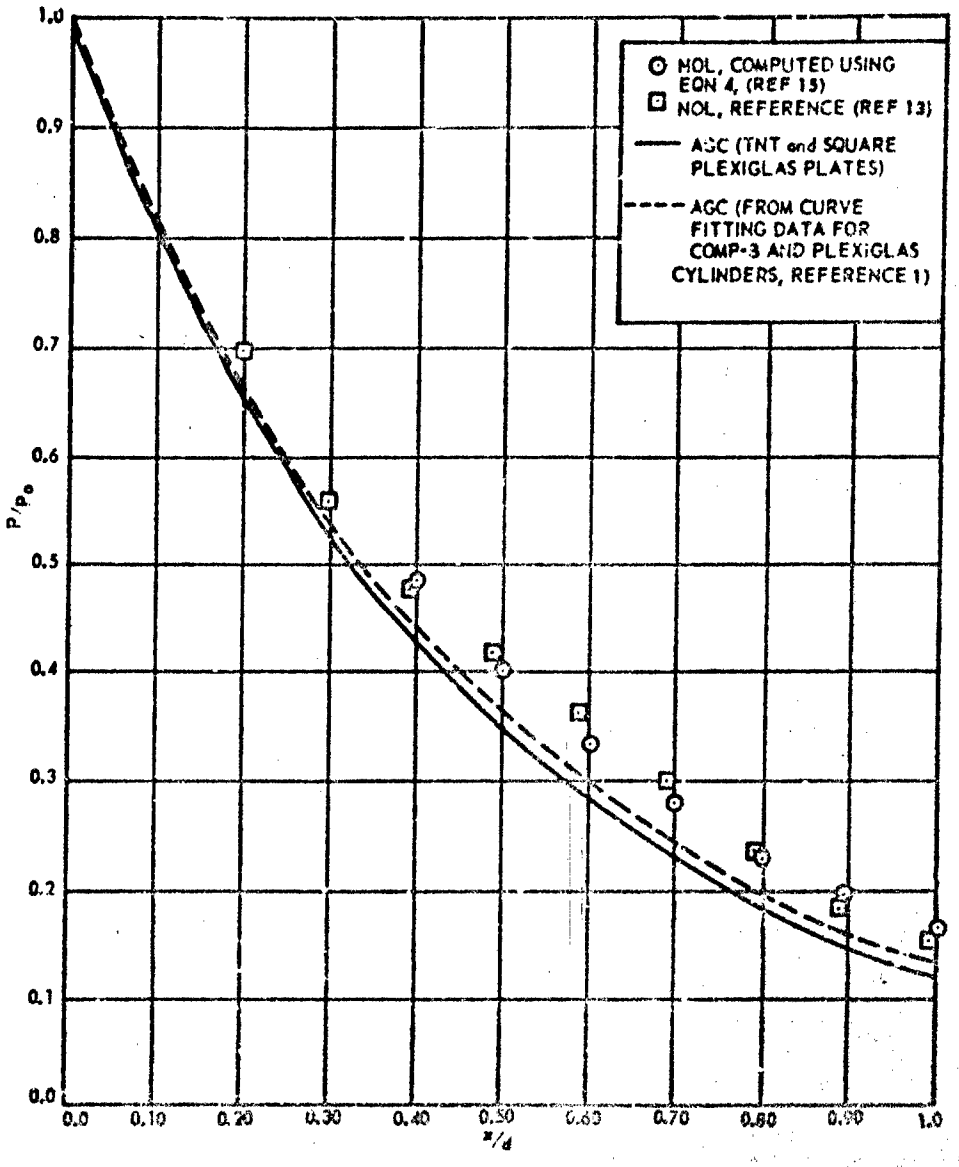


Figure 45. Shock-Pressure Attenuation in PMMA.

## Hugoniot Equations-of State

Three RDX-adulterated propellants were used in the initiation criterion determinations. They were AAB-3189 (9.2% RDX), AAB-3225 (7.1% RDX), and AAB-3267 (5.0% RDX).

The method used to determine the Hugoniot of propellant is identical to that developed in SOPHY I (Reference 1). The charge is prepared by alternately stacking 1/4-in.-thick by 1-in.-diameter PMMA discs and 0.08-in. thick by 1-in.-diameter propellant wafers to form a column approximately 1-1/2 in. high. The column is shocked with a Composition B cylindrical booster, 1 in. in diameter by 2 in. high. The column is backlighted with an Argon bomb and the event is recorded on a Beckman & Whitley streak camera. From the streak record, velocities in the PMMA are determined at each PMMA propellant interface. Average velocities in the propellant are determined by dividing the propellant thickness by the time difference between the moment the shock enters the wafer and the moment it emerges at the propellant-PMMA interface. The streak record thus furnishes data from which the incident-shock velocity $U_i$ in PMMA and the average transmitted shock velocity $U_t$ in propellant are calculated.

The Hugoniot of PMMA can be written

$$P = 30.25\ \mu + 21.56\ \mu^2 \quad \text{kbar} \tag{75}$$

where $\mu$ is the particle velocity in mm/μsec by using the relationships

$$P = 10\ \rho_o\ U\mu \text{ and } \rho_o = 1.188\ \text{gm/cm}^3 \tag{76}$$

A point on the $P(\mu)$ propellant Hugoniot is obtained by solving these two equations:

$$P = 10\ \rho_{o,2}\ \bar{U}_t \mu \tag{77}$$

and

$$P = 21.56\ (2\mu_i - \mu)^2 + 30.25\ (2\mu_i - \mu) \tag{78}$$

where $\rho_{o,2}$ is the density of the propellant and $\mu_i$ is the incident particle velocity in PMMA corresponding to $U_i$. Equation 78 is the reflection of the $P(\mu)$ PMMA Hugoniot about $\mu = \mu_i$. In the SOPHY II program this reflection is performed mathematically, whereas under SOPHY I it was done graphically.

AAB-3189

Using SOPHY I data for $U_i$ and $\bar{U}_t$, the Hugoniot of AAB-3189 was calculated by solving Equations 77 and 78. The results of the calculations are shown in Table XXVII. The best fit to the computed $P_t$ ($\mu_t$) data is

$$P = 32.7\ \mu + 45.4\ \mu^2 \tag{79}$$

from which, assuming $\rho_o = 1.725$ gm/cm$^3$,

$$P = 6.56\ U^2 - 12.42\ U \tag{80}$$

and

$$U = 1.89 + 2.63\ \mu \tag{81}$$

The difference between these equations and those reported earlier (Reference 1) is insignificant in terms of the difference between pressures calculated at any value of U.

AAB-3225

The Hugoniot data and calculations for AAB-3225 are given in Table XXVIII. The best fit to the computed $P_t$ ($\mu_t$) data is

$$P = 27.8\ \mu + 59.8\ \mu^2 \tag{82}$$

Assuming

$$\rho_o = 1.735 \text{ gm/cm}^3,$$

$$P = 5.03\ U^2 - 8.07\ U \tag{83}$$

and

$$U = 1.60 + 3.45\ \mu \tag{84}$$

AAB-3267

The Hugoniot data and calculations for AAB-3267 are given in Table XXIX. The best fit to the computed $P_t$ ($u_t$) data is

$$P = 37.17\ \mu + 37.23\ \mu^2 \tag{85}$$

Assuming $\rho_o = 1.745$ gm/cm$^3$,

$$P = 8.18\ U^2 - 17.4\ U \tag{86}$$

and

$$U = 2.13 + 2.13\ \mu \tag{87}$$

Table XXVII. Hugoniot Computations for AAB-3189.

| $U_i$ | $P_i$ | $\mu_i$ | $\bar{U}_t$ | $P_t$ | $\mu_t$ |
|---|---|---|---|---|---|
| 4.93 | 64.85 | 1.11 | 3.85 | 69.81 | 1.05 |
| 4.53 | 49.59 | 0.92 | 4.37 | 59.86 | 0.79 |
| 5.74 | 101.16 | 1.48 | 5.53 | 122.88 | 1.29 |
| 4.34 | 42.96 | 0.83 | 4.34 | 52.76 | 0.70 |
| 3.39 | 15.79 | 0.39 | 3.27 | 18.82 | 0.33 |
| 3.03 | 8.09 | 0.22 | 2.25 | 8.42 | 0.22 |
| 5.09 | 71.45 | 1.18 | 4.67 | 84.24 | 1.05 |
| 4.02 | 32.70 | 0.68 | 3.64 | 38.02 | 0.51 |
| 3.56 | 19.92 | 0.47 | 2.61 | 20.62 | 0.46 |
| 3.13 | 10.09 | 0.27 | 2.32 | 10.49 | 0.26 |
| 3.05 | 8.48 | 0.23 | 1.66 | 7.43 | 0.26 |

Table XXVIII. Hugoniot Computations for AAB-3223.

| $U_i$ | $P_i$ | $\mu_i$ | $\bar{U}_t$ | $P_t$ | $\mu_t$ |
|---|---|---|---|---|---|
| 4.66 | 54.36 | 0.98 | 4.14 | 63.03 | 0.88 |
| 3.84 | 27.42 | 0.60 | 3.29 | 31.02 | 0.54 |
| 3.30 | 13.73 | 0.35 | 2.71 | 15.12 | 0.32 |
| 3.02 | 7.90 | 0.22 | 2.68 | 9.01 | 0.19 |
| 4.85 | 61.66 | 1.07 | 5.08 | 78.13 | 0.89 |
| 4.23 | 39.31 | 0.78 | 4.17 | 48.00 | 0.66 |
| 3.63 | 21.71 | 0.50 | 4.02 | 24.15 | 0.46 |

Table XXIX. Hugoniot Computations for AAB-3267.

| $U_i$ | $P_i$ | $\mu_i$ | $\bar{U}_t$ | $P_t$ | $\mu_t$ |
|---|---|---|---|---|---|
| 5.02 | 68.69 | 1.15 | 4.54 | 80.77 | 1.02 |
| 5.23 | 77.28 | 1.24 | 4.34 | 86.82 | 1.15 |
| 3.52 | 18.87 | 4.51 | 3.09 | 21.62 | 0.40 |
| 4.91 | 64.09 | 1.10 | 4.20 | 73.07 | 1.00 |
| 5.00 | 11.44 | 1.60 | 5.26 | 132.74 | 1.45 |
| 4.01 | 32.39 | 0.68 | 3.44 | 36.83 | 0.61 |
| 6.10 | 11.96 | 1.55 | 5.32 | 13.85 | 1.49 |

PMMA

There are several published Hugoniot equations of state for Plexiglas, Perspex, and Lucite. These equations are given in Table XXX.

Table XXX. Hugoniot Equations of State for Polymethylmethacrylate.

| Coded Source* | Hugoniot Equation |
|---|---|
| BJT (16) | $U = 3.13 + 1.04\ \mu$ |
| A-AFSWC (17) | $U = 3.06 + 1.04\ \mu$ |
| B-AFSWC (17) | $U = 2.38 + 1.56\ \mu$ |
| Air Red (18) | $U = 2.73 + 1.57\ \mu$ |
| AGC (14) | $U = 2.546 + 2.153\ \mu$ |
| BW (19) | $U = 2.50 + 1.61\ \mu$ |
| A-JBA (20) | $U = 2.33 + 1.66\ \mu$ |
| B-JBA (20) | $U = 2.62 + 1.52\ \mu$ |
| A-Lidd (13) | $U = 2.56 + 1.69\ \mu$ ($\mu$ >0.5mm/μsec) |
| B-Lidd (13) | $U = 2.95 + 0.85\ \mu$ ($\mu$ <0.5mm/μsec) |
| C-JBA (21) | $U = 2.588 + 1.514\ \mu$ |
| Cole (22) | $U = 2.710 + 1.568\mu - 0.307\ \mu^2$ |

*Number in parentheses indicates reference number. Sources are abbreviated. Where two equations are taken from one source, they are distinguished by prefixes A-, B-, C-, .... as necessary.

The PMMA Hugoniot is used in the SOPHY program to determine the Hugoniots for each of the propellant formulations subjected to card-gap sensitivity tests, and subsequently, to determine the shock pressure transmitted into the propellant at the PMMA/propellant interface (incident shock pressures at the interface are derived from the universal attenuation curve). The differences among the PMMA Hugoniots are a potential source of difficulty in determining the correct transmitted pressures, because there is no objective basis on which to choose the correct Hugoniot.

To evaluate the effect of using each of these Hugoniots on the transmitted pressure values, each equation in Table XXX was applied to the experimental data by which the Hugoniot for AAB-3189 was determined. The similarity of this Hugoniot to those for AAB-3225 and AAB-3267 prompts the assumption that comparable results would be obtained with the Hugoniot data for the other formulations.

After each Hugoniot for AAB-3189 was determined for the corresponding Plexiglas Hugoniot, transmitted pressures were calculated for several values of incident pressure. A representative sample of the results of these calculations is shown in Table XXXI. All Plexiglas Hugoniots were used except that shown in Reference 13 for $\mu \leq 0.5$ and that in Reference 22. The two omitted Hugoniots are not significantly different from those that were used. Table XXXI shows that indeed there is no reason to reject the reported transmitted pressures calculated from the Aerojet Hugoniot because all of the equations produce nearly identical data.

## Card-Gap Tests

PMMA card-gap tests are conducted in the standard manner by testing whether a certain thickness of PMMA attenuates the shock wave delivered by a high-explosive booster to a level insufficient to initiate a supercritical cylindrical acceptor charge. If detonation is not achieved, less PMMA is used in the next test. This sequence continues until a thickness is found that allows detonation to be initiated. At this point the sequence reverses, using smaller incremental changes in the PMMA thickness, until no detonation occurs. The process again is reversed. The testing continues in this fashion, decreasing the increments after each reversal, until the go-no go range has been reduced to the desired limit.

The test setup includes the cylindrical propellant acceptor charge, which is 2 diameters long (except the 10-in. diameter charges, which were 40-in. long), the PMMA attenuator, and a conical TNT booster that is 3 base diameters high. The 42-in. diameter setup is shown in Figure 46. The acceptor is instrumented with ionization probes for determination of the reactive shock velocity in the propellant, which is the basis for judging whether or not the sample detonates. The results of the card-gap tests, performed in this subtask, bracket $P^+$ at certain diameters within a 5 to 6 Kbar range, which is the largest range in all the data. In general, at the other diameters, $P^+$ has been bracketed within 1 to 2 Kbars. The results of the card-gap tests define the initiation criteria of these propellants quite adequately.

Table XXXI. Transmitted Shock Pressures in AAB-3189 for Several Incident Shock Pressures in PMMA, Using Various Hugoniot Equations of State.

| Incident Pressure (kbar) | Transmitted Pressure (kbar)* | | | | | | | | | |
|---|---|---|---|---|---|---|---|---|---|---|
| | BJT (Ref. 16) | A-AFSWC (Ref. 17) | B-AFSWC (Ref. 17) | AIR RED. (Ref. 18) | Aerojet (Ref. 14) | SW (Ref. 19) | A-JBA (Ref. 20) | B-JBA (Ref. 20) | A-LITO (Ref. 13) | GULF. (Ref. 22) |
| 0 | 0 | 0 | 0 | 0 | 0 | 0 | 0 | 0 | 0 | 0 |
| 6 | 6.5 | 6.6 | 6.3 | 6.5 | 6.5 | 6.3 | 6.3 | 6.5 | 6.5 | 6.5 |
| 12 | 13.2 | 13.3 | 12.9 | 13.3 | 13.2 | 12.9 | 12.9 | 13.2 | 13.2 | 13.1 |
| 18 | 19.9 | 20.1 | 19.7 | 20.1 | 20.1 | 19.7 | 19.7 | 20.0 | 20.0 | 20.1 |
| 24 | 26.7 | 27.0 | 26.6 | 27.1 | 27.2 | 26.5 | 26.6 | 26.9 | 26.9 | 26.8 |
| 30 | 33.6 | 33.9 | 33.6 | 34.1 | 34.2 | 33.5 | 33.6 | 33.9 | 34.0 | 33.5 |
| 36 | 40.5 | 40.9 | 40.6 | 41.1 | 41.4 | 40.5 | 40.6 | 40.9 | 41.0 | 40.9 |
| 42 | 47.4 | 47.9 | 47.7 | 48.2 | 48.6 | 47.5 | 47.8 | 48.0 | 48.1 | 48.0 |
| 48 | 54.4 | 54.9 | 54.9 | 55.4 | 55.8 | 54.6 | 54.9 | 55.2 | 55.3 | 54.9 |
| 54 | 61.4 | 62.0 | 62.1 | 62.6 | 63.1 | 61.7 | 62.1 | 62.4 | 62.5 | 62.5 |
| 60 | 68.5 | 69.1 | 69.3 | 69.7 | 70.3 | 68.9 | 69.4 | 69.6 | 69.6 | 69.8 |
| 66 | 75.5 | 76.3 | 76.5 | 77.0 | 77.7 | 76.0 | 76.6 | 76.8 | 77.0 | 77.0 |
| 72 | 82.6 | 83.4 | 83.8 | 84.2 | 85.0 | 83.2 | 83.9 | 84.0 | 84.3 | 84.6 |
| 78 | 89.7 | 90.6 | 91.1 | 91.5 | 92.4 | 90.4 | 91.3 | 91.3 | 91.6 | 92.0 |
| 84 | 96.9 | 97.7 | 98.4 | 98.8 | 99.8 | 97.7 | 98.6 | 98.6 | 98.9 | 98.8 |
| 90 | 104.0 | 105.0 | 105.7 | 106.1 | 107.2 | 104.9 | 106.0 | 106.0 | 106.3 | 105.8 |

*Column headings refer to coded sources given in Table XXX.

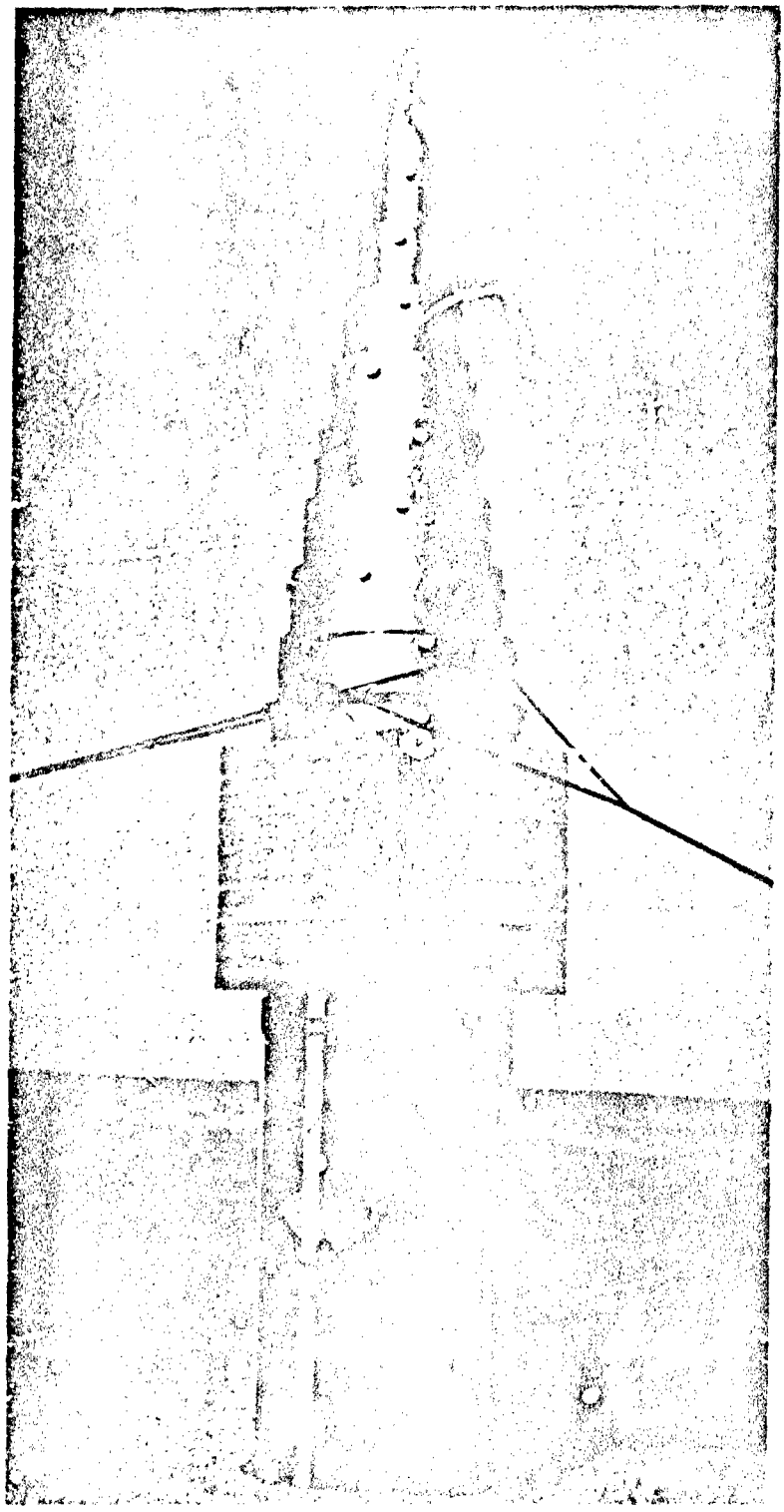

Figure 46. 42-in. Diameter Card-Gap Setup.

These results are given in Tables XXXII through XXXIV. The initiation criteria for the three propellants are shown individually in Figures 47 through 49, and are combined (using a reduced-diameter abscissa, $d/d_c$) in Figure 50.

## EVALUATION OF THE INITIATION CRITERION FOR AAB-3189

If the initiation criterion theory is correct, the area, average pressure, and pulse width of a shock wave in a supercritical acceptor must exceed the minimum conditions established by the criterion if sustained detonation is to be initiated. They must not exceed these conditions if detonation of the acceptor is not initiated. Since the initiation criteria that have been determined have been defined only in terms of the average shock pressure and the area of the shock wave, it must be assumed that under the conditions of the tests described below the variation in pulse width does not have a significant effect on the pressure-area criterion. This assumption is made by considering that the pulse width of the shock wave entering the propellant directly from a high-explosive booster is not significantly different from that of an explosively-driven shock wave that has been attenuated by PMMA. The latter case describes the shock waves that were applied in the card-gap tests, by which the initiation criteria were developed.

The experimental program to evaluate the validity of the initiation criterion consisted of tests that involved solid circular cylindrical samples and rectangular samples. Both shapes were shocked by explosive boosters centered on the end of the acceptors.

### Cylindrical Acceptor Tests

The initiation criterion evaluation tests were conducted with 6-in. diameter right circular cylindrical samples cast from AAE-3189 propellant ($d_c$ = 2.71 in.). Several values of the initial shock pressure and area were selected. By choosing cylindrical boosters of various diameter and by using various lengths of PMMA attenuators, the initial wave area and pressure were varied over the desired region. The initial conditions and the go-no go results of the tests are shown in Table XXXV. Detonation was achieved with boosters as small as 1.75 in. diameter, as in SOPHY I (Reference 1).

Table XXXII. Card-Gap Test Results, AAB-3189 Propellant.

| Propellant Diameter (in.) | Plexiglas Thickness (dia) | Incident Pressure in Plexiglas* (kbar) | Transmitted Pressure in Propellant* (kbar) | Test Result | Test Number |
|---|---|---|---|---|---|
| 10 | 0.752 | 25 | 28 | Go | 3.3.5.21 |
| | 0.856 | 20 | 22 | Go | 3.3.5.22 |
| | 0.856 | 20 | 22 | Go | 3.3.5.24 |
| | 0.950 | 17 | 19 | No go | 3.3.5.20 |
| | 0.950 | 17 | 19 | No go | 3.3.4.23 |
| 12 | 0.823 | 22 | 25 | Go | 3.3.5.26 |
| | 0.907 | 20 | 22 | Go | 3.3.5.27 |
| | 0.907 | 20 | 22 | Go | 3.3.5.29 |
| | 0.979 | 16 | 18 | No go | 3.3.5.25 |
| | 0.979 | 16 | 18 | No go | 3.3.5.28 |

*At Plexiglas-propellant interface.

Table XXXIII. Card-Gap Test Results, AAB-3325 Propellant.

| Propellant Diameter (in.) | Plexiglas Thickness (dia) | Incident Pressure in Plexiglas* (kbar) | Transmitted Pressure in Propellant* (kbar) | Test Result | Test Number |
|---|---|---|---|---|---|
| 6 | 0.618 | 34 | 41 | Go | 3.3.5.1 |
| | 0.742 | 26 | 31 | Go | 3.3.5.3 |
| | 0.809 | 23 | 27 | Go | 3.3.5.11 |
| | 0.816 | 22 | 26 | No go | 3.3.5.7 |
| | 0.840 | 21 | 24 | No go | 3.3.5.9 |
| | 0.860 | 20 | 23 | No go | 3.3.5.2 |
| 7 | 0.778 | 24 | 28 | Go | 3.3.5.14 |
| | 0.833 | 21 | 24 | Go | 3.3.5.15 |
| | 0.858 | 20 | 23 | Go | 3.3.5.18 |
| | 0.889 | 19 | 22 | No go | 3.3.5.13 |
| 8 | 0.881 | 19 | 22 | Go | 3.3.5.4 |
| | 0.925 | 18 | 21 | Go | 3.3.5.10 |
| | 0.956 | 17 | 20 | No go | 3.3.5.8 |
| | 1.000 | 15 | 17 | No go | 3.3.5.6 |
| | 1.112 | 13 | 15 | No go | 3.3.5.5 |
| 12 | 0.823 | 22 | 26 | Go | 3.3.5.31 |
| | 0.901 | 18 | 21 | Go | 3.3.5.52 |
| | 0.912 | 18 | 21 | Go | 3.3.5.32 |
| | 0.995 | 15 | 17 | No go | 3.3.5.51 |
| | 1.073 | 11 | 16 | No go | 3.3.5.30 |
| 20 | 0.828 | 22 | 26 | Go | 3.3.5.33 |
| | 0.922 | 18 | 21 | Go | 3.3.5.35 |
| | 0.956 | 17 | 20 | Go | 3.3.5.39 |
| | 0.969 | 16 | 19 | Go | 3.3.5.53 |
| | 1.017 | 15 | 17 | No go | 3.3.5.34 |
| 24 | 0.896 | 19 | 22 | Go | 3.3.5.37 |
| | 0.938 | 17 | 20 | Go | 3.3.5.38 |
| | 0.938 | 17 | 20 | Go | 3.3.5.54 |
| | 0.977 | 16 | 18 | No go | 3.3.5.36 |
| | 0.977 | 16 | 18 | No go | 3.3.5.50 |

*At Plexiglas-propellant interface.

Table XXXIV. Card-Gap Test Results, AAB-3267 Propellant.

| Propellant Diameter (in.) | Plexiglas Thickness (dia) | Incident Pressure in Plexiglas* (kbar) | Transmitted Pressure in Propellant* (kbar) | Test Result | Test Number |
|---|---|---|---|---|---|
| 12 | 0.646 | 32 | 36 | Go | 3.3.5.57 |
| | 0.732 | 27 | 30 | No go | 3.3.5.58 |
| | 0.818 | 22 | 25 | No go | 3.3.5.56 |
| 42 | 0.914 | 16 | 18 | Go | 3.3.5.59 |
| | 0.966 | 14 | 16 | Go | 3.3.5.60 |
| | 1.006 | 12 | 13 | No go | 3.3.5.55 |

*At Plexiglas-propellant interface

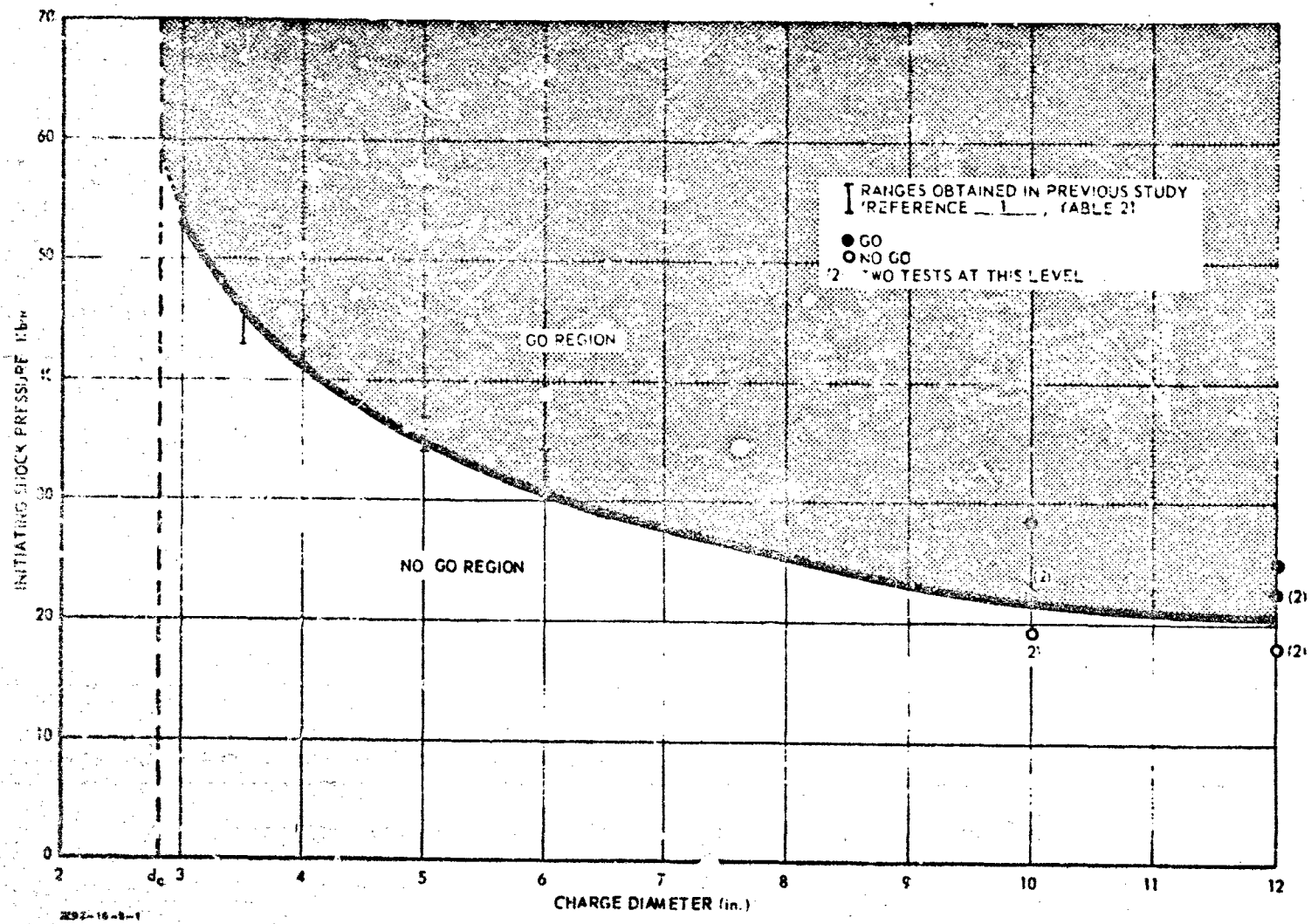


Figure 47. Initiation Criterion for AAB-3189.

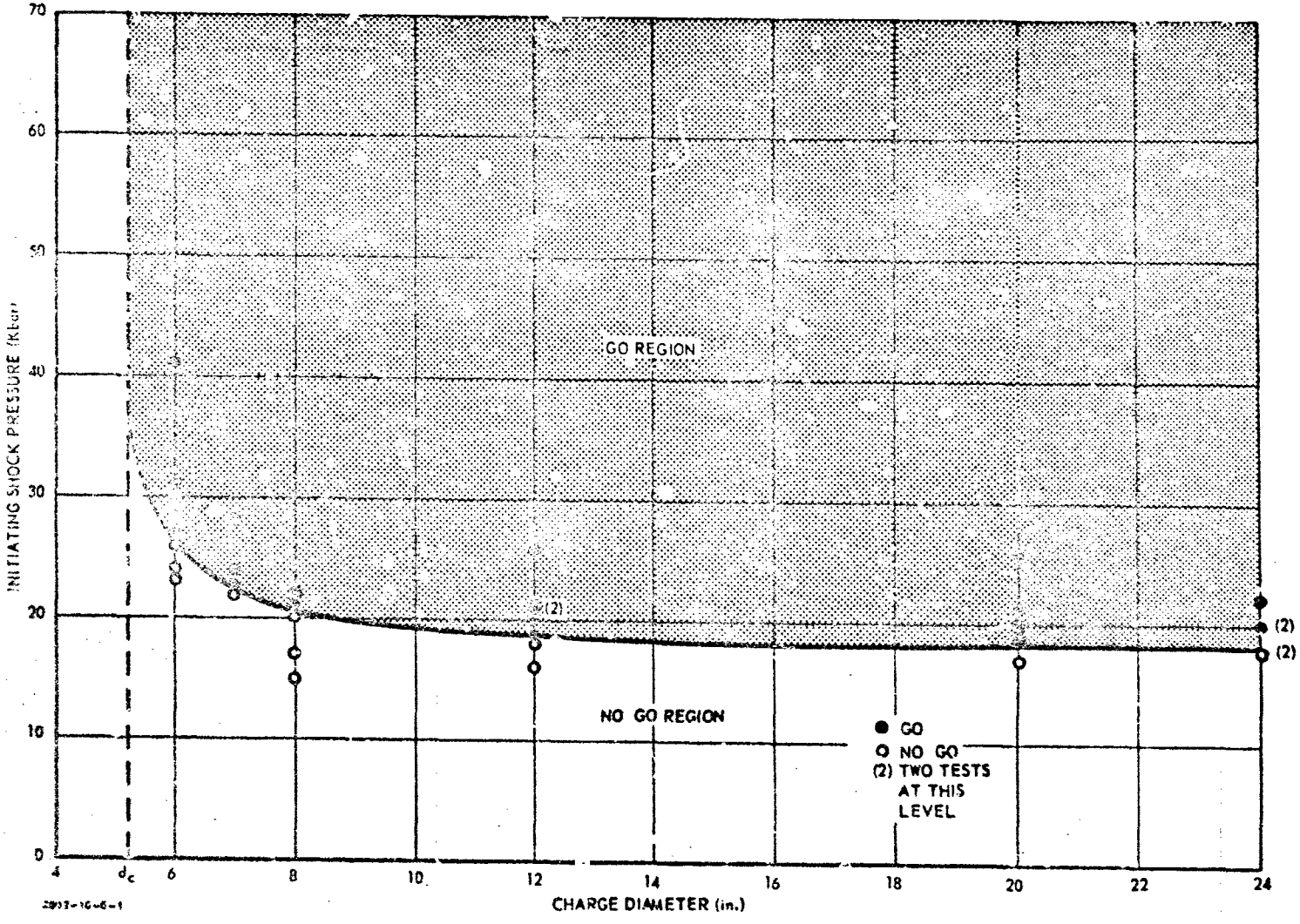


Figure 48. Initiation Criterion for AAB-3225.

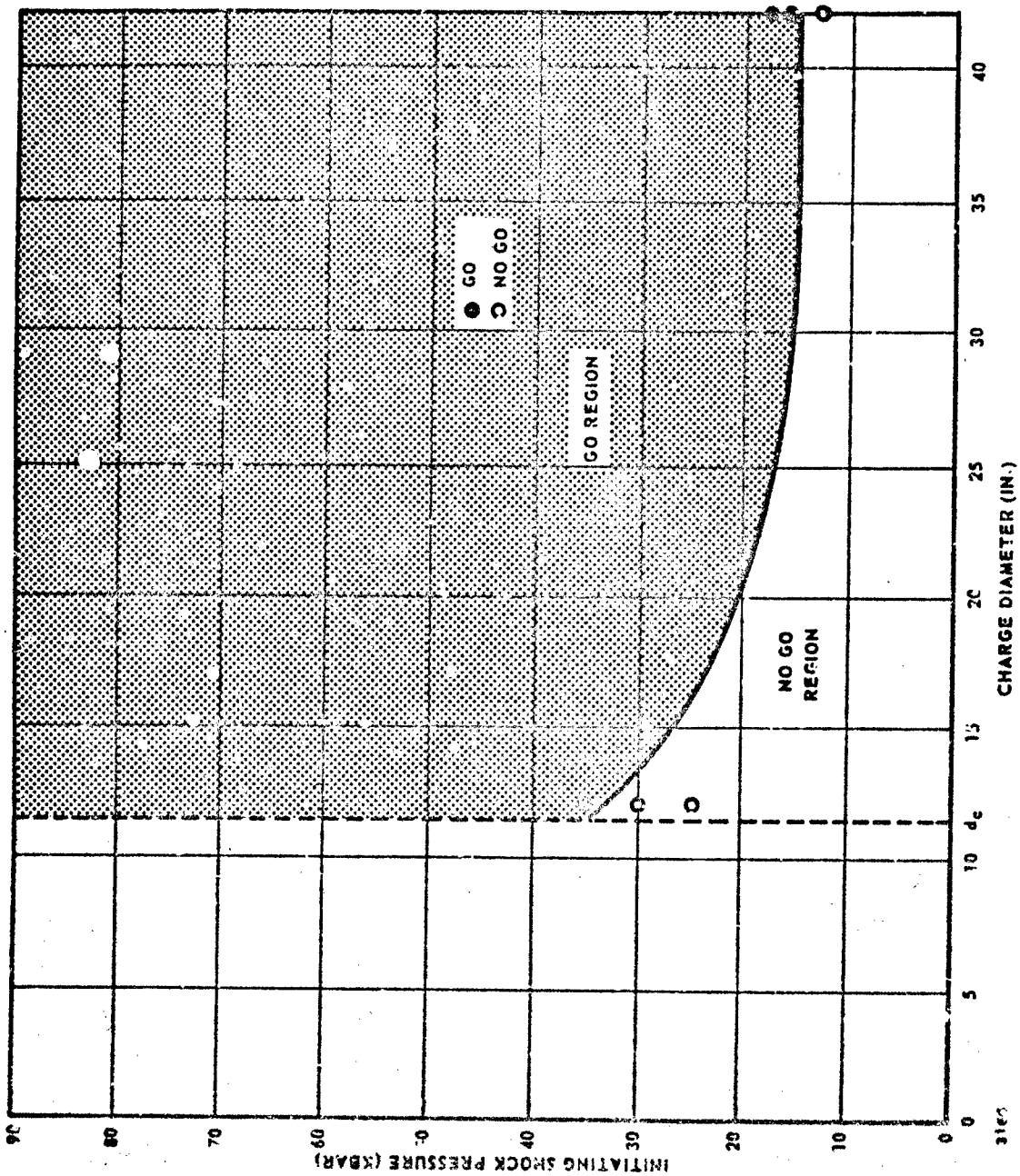


Figure 49. Initiation Criterion for AAB-3267.

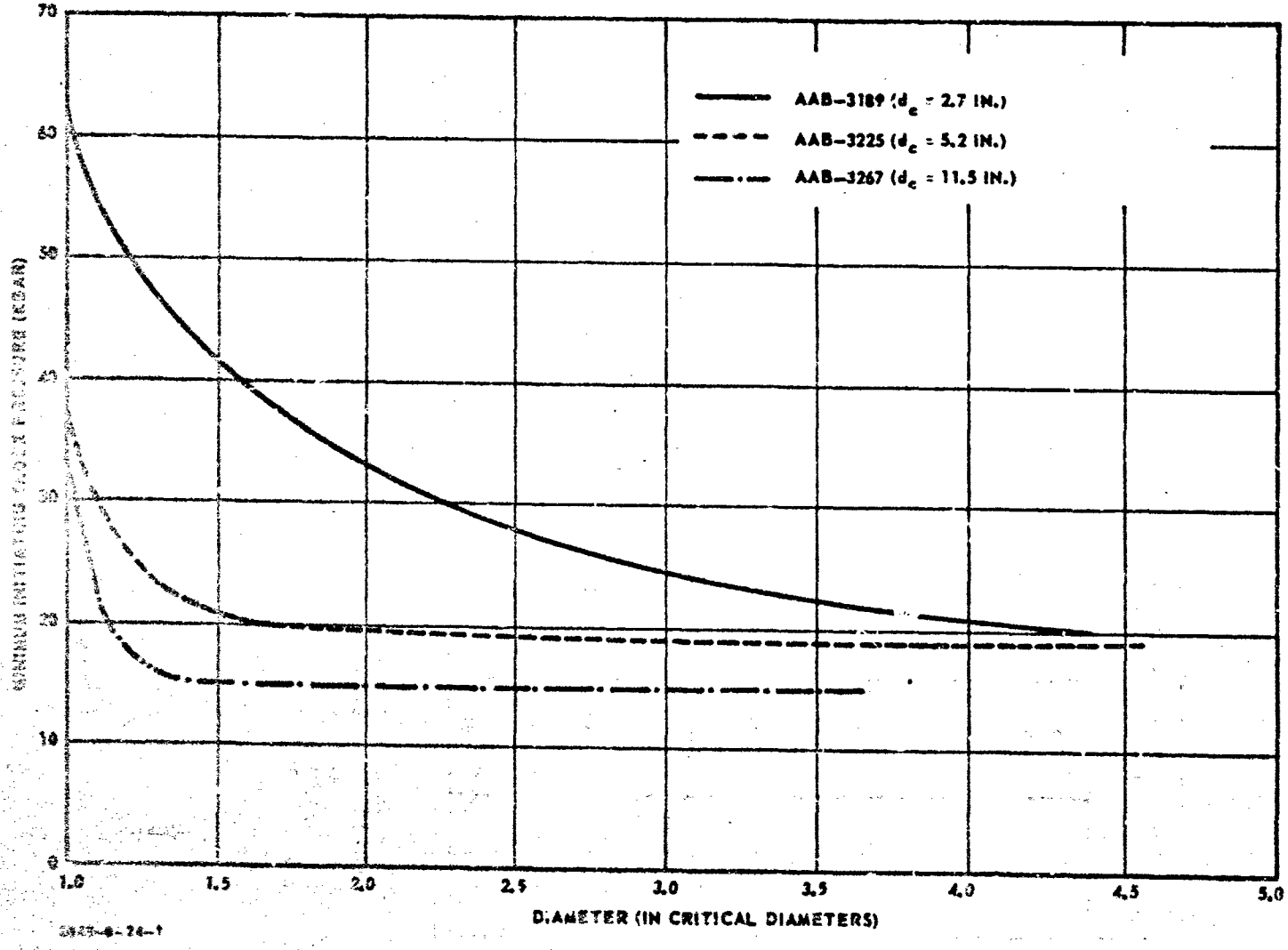


Figure 50. Normalized Initiation Criteria.

Table XXXV. Initiation Criterion Evaluation for Cylindrical Acceptor.

| Booster Diameter (in.) | PMMA Length (in.) | Initial Average Shock Pressure (kbar) | Initial Shock Wave Area ($in.^2$) | Test Result | Test Number |
|---|---|---|---|---|---|
| 3.0 | 2.04 | 50 | 7.07 | No go* | 3.3.7.9 |
| 3.0 | 2.04 | 50 | 7.07 | No go* | 3.3.7.13 |
| 3.0 | 2.28 | 43 | 7.07 | No go | 3.3.7.8 |
| 2.0 | None | 250 | 3.14 | Go | 3.3.7.5 |
| 2.0 | 0.390 | 150 | 3.14 | Go | 3.3.7.7 |
| 2.0 | 0.390 | 150 | 3.14 | No go | 3.3.7.14 |
| 2.0 | 0.390 | 150 | 3.14 | Go* | 3.3.7.15 |
| 2.0 | 0.580 | 125 | 3.14 | No go | 3.3.7.6 |
| 2.0 | 0.580 | 125 | 3.14 | No go | 3.3.7.12 |
| 1.75 | None | 250 | 2.41 | Go | 3.3.7.2 |
| 1.75 | None | 250 | 2.41 | Go* | 3.3.7.10 |
| 1.75 | 0.342 | 150 | 2.41 | No go | 3.3.7.4 |
| 1.75 | 0.342 | 150 | 2.41 | No go* | 3.3.7.11 |
| 1.5 | None | 250 | 1.77 | No go | 3.3.7.3 |
| 1.0 | None | 250 | 0.79 | No go | 3.3.7.1 |

*Shock wave pressures and areas could not be computed, due to insufficient data retrieval.

The acceptor charges were instrumented with ionization probes, with their tips located in four columns down the charge; on the axis and 0.75 in., and 1.75 in., and 2.50 in. from the axis. Each column of probes was connected electrically to a mixer box and rasteroscillograph. Distance-time data were generated along each of these columns.

Choosing an X-Y coordinate system with the origin at the center of the initiated end of the acceptor and the X-axis coincident with the charge axis, the location of points on the shock wave is determined at any time t by the x (t), y data. At times selected in 5 μsec intervals, the shock wave pressure and area are determined by assuming a spherical wave shape. Symmetry allows the analysis of the data in 2-dimensions, i.e., the wave is represented by the equation of a circle of radius r, centered at (h, 0):

$$(x-h)^2 + y^2 = r^2 \tag{88}$$

The velocity of the shock wave in the X direction, at any y greater than zero, is only an apparent velocity. The true shock velocity is taken in directions normal to the wave front at various points on the surface. The true shock velocity $U_x$ at any x is calculated by

$$U_x = U_o \left(\frac{x - h}{r}\right) \tag{89}$$

where $U_o$ is the velocity in the X direction. The shock pressure at any (x,y) point on the wave surface is given by the Hugoniot equation of state:

$$P_x = 6.56\, U_x^2 - 12.42\, U_x \tag{90}$$

The average shock pressure $\bar{P}$ of the wave is given by

$$\bar{P} = (r + h - x_1)^{-1} \int_{x_1}^{r+h} P\,dx \tag{91}$$

where $x_1$ is the value of x on the surface of the wave that will satisfy the geometric limitations:

$$\left.\begin{aligned} x_1 &= 0 \quad \text{if } r^2 \leq h^2 + 9 \\ x_1 &= \sqrt{r^2 - 9} + h \quad \text{if } r^2 > h^2 + 9 \end{aligned}\right\} \tag{92}$$

$$\left.\begin{aligned} x_1 &= h \quad \text{if } r \leq 3 \\ x_1 &= \sqrt{r^2 - 9} + h \quad \text{if } r > 3 \end{aligned}\right\} \tag{93}$$

and the shock-velocity limitation, given by solving Equation 89 for x where $U_x = U_s$, the sonic velocity in AAB-3189:

$$x_1 = r\frac{U_s}{U_o} + h \tag{94}$$

The larger of the geometric and shock-velocity limits on $x_1$ is the final choice for $x_1$. The value of x on the X-axis is equal to r + h.

The surface area A of the wave is given by

$$A = 2\pi r (r + h - x_1) \tag{95}$$

The average shock pressure and wave area are computed at each t, and the pressure-area data are compared with the initiation criterion. The computed pressure and area of the waves in each test at various values of t are presented in Appendix VIII.

The test design required a set of tests in which the initial shock pressure was held constant and the initial wave area was varied by using boosters of several different diameters. The results of this set of tests are shown in Figure 51. It was found that detonation of the propellant was achieved with 1-3/4-in. diameter boosters, but not with 1-1/2-in. diameter boosters. The same results were reported in the SOPHY I program, in which 4-in. diameter acceptors were used (Reference 1). The shock pressure-area curves from the two tests in which detonation was initiated (Tests No. 3.3.7.2 and 3.3.7.5) show that after a certain time, the average pressure begins to increase as the wave area begins to diminish. This hook in the curves is expected from a detonating charge initiated under the conditions of these tests. The detonation velocity (hence, pressure) first decreases from the initial level and then increases to the steady-state value. The wave area increases as the wave expands in the acceptor but then decreases slightly as the wave flattens out during its approach to steady-state conditions. The wave area approaches that of a 6-in. diameter circle: 28.3 $in.^2$.

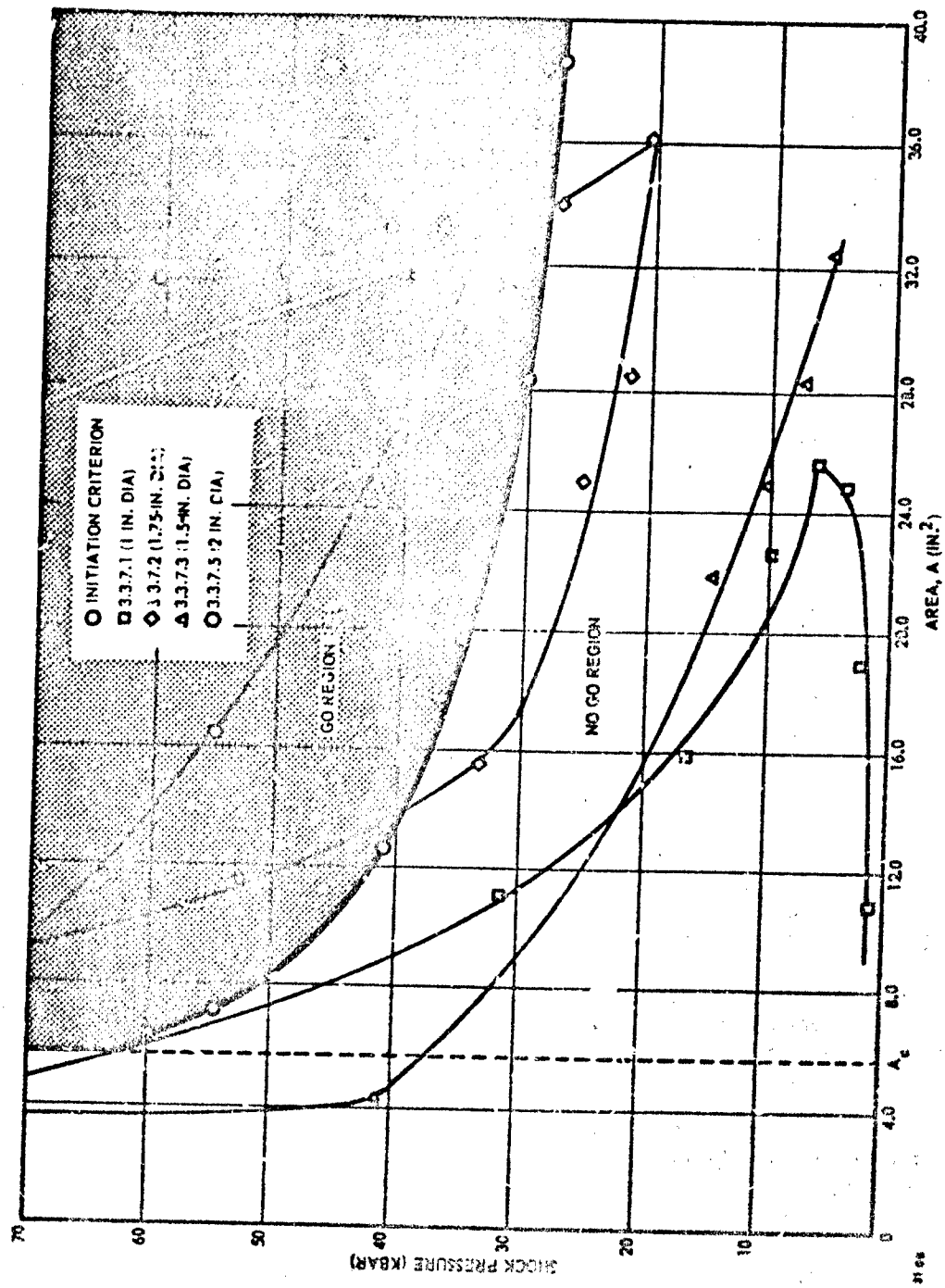


Figure 51. Evaluation of Initiation Criterion with Unattenuated Booster Shock Wave.

A hook in the opposite direction is shown by the curve from Test No. 3.3.7.1 (1.0 in. diameter booster), but it is not yet evident in Test No. 3.3.7.3 (1.5 in. diameter booster). In a no go, the shock wave area can decrease if the wave shape becomes more acute near the end of the shock wave life, since that portion travelling at supersonic velocity will diminish with time.

In Figure 52 are presented the curves from the second set of tests, in which the initial shock wave area was held constant and the average initial pressures were varied by using several different lengths of PMMA to attenuate the shock wave from the booster. The data are for 2-in. diameter boosters with 2-in. diameter PMMA rod attenuators. Detonations were initiated with average initial pressures as low as 150 kbar. No detonations resulted when the average initial pressure was 125 kbar. The area of these initial waves is less than 60% of the cross sectional area of the acceptor.

The results of Test No. 3.3.7.5 have been discussed above. Test No. 3.3.7.7 resulted in a detonation. When the same conditions were repeated in Test No. 3.3.7.14 the result was a no go, which indicates that 150 kbar must be near the minimum initial shock pressure required of a 2-in.-diameter wave to initiate detonation. The data from Test 3.3.7.7 indicate that the shock wave was not flattening out and that the wave was not even large enough to cover the full diameter of the charge. This information is certainly erroneous, because the sample did detonate. The poor data from this test is probably due to one column of probes, but there is no objective basis by which to select the faulty data. The curve proceeds toward the go region but does not enter. Considering the poor raw data and the completely illogical pressure-area relationship at times greater than 20 μsec, the apparent contradiction of the initiation criterion theory that is implied by this test should not be heavily weighted.

The results from two other tests, both no go's, are shown in Figure 53. Both curves miss the initiation criterion. The hook observed in the data from Test No. 3.3.7.8, which lie below the other data, is similar to that found in Test No. 3.3.7.1. In reporting shock pressures less than 10 kbar, where the shock velocity (2.5 mm/μsec) is nearly sonic causing considerable scatter in probe response, the accuracy of the pressure data is no better than ± 4 kbar. This potential error does not affect the evaluation of the initiation criterion theory; it must be remembered, however, if any extensive interpretation of the attenuation curves should be attempted.

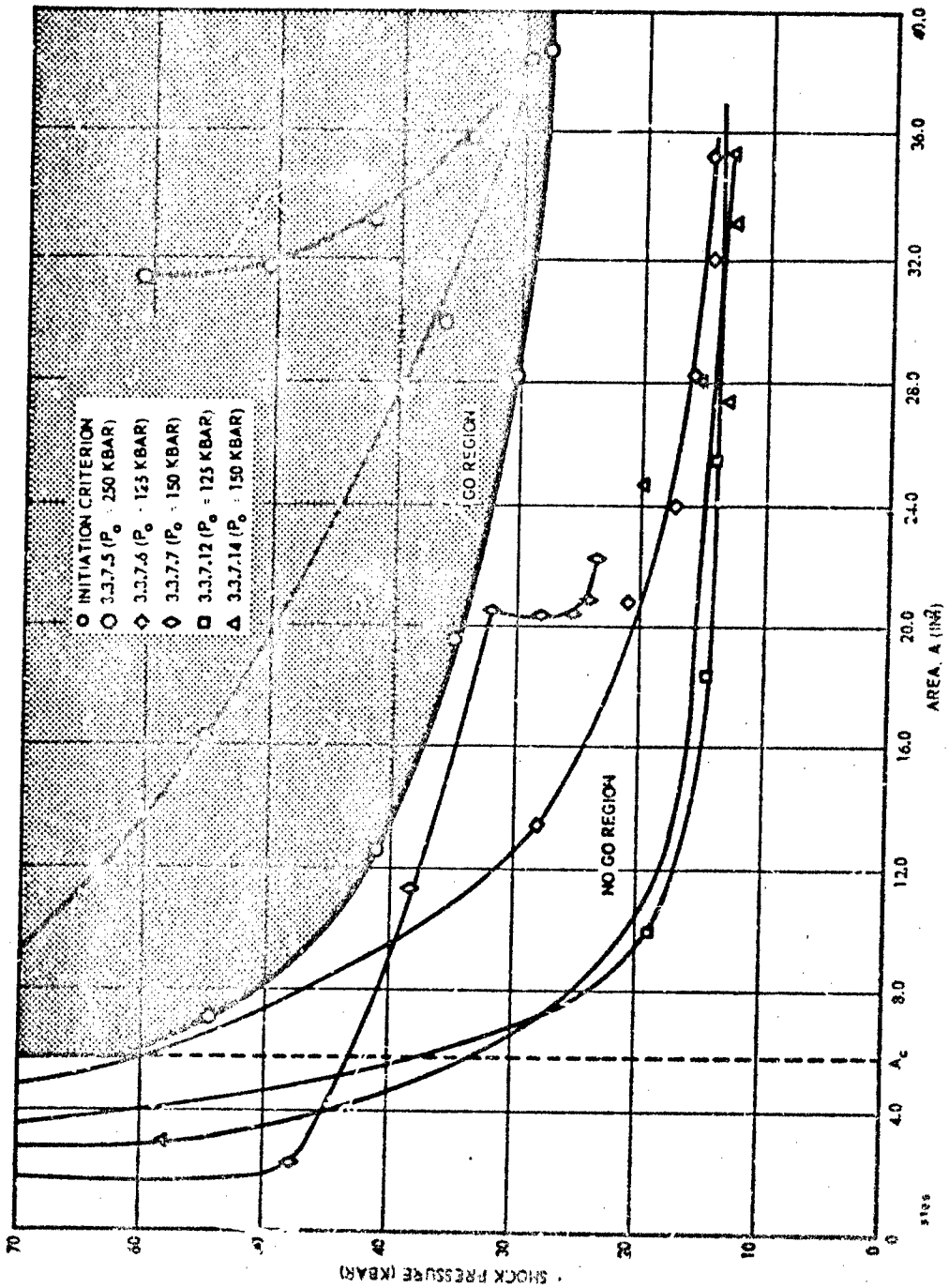


Figure 52. Evaluation of Initiation Criterion with Attenuated Booster Shock Wave.

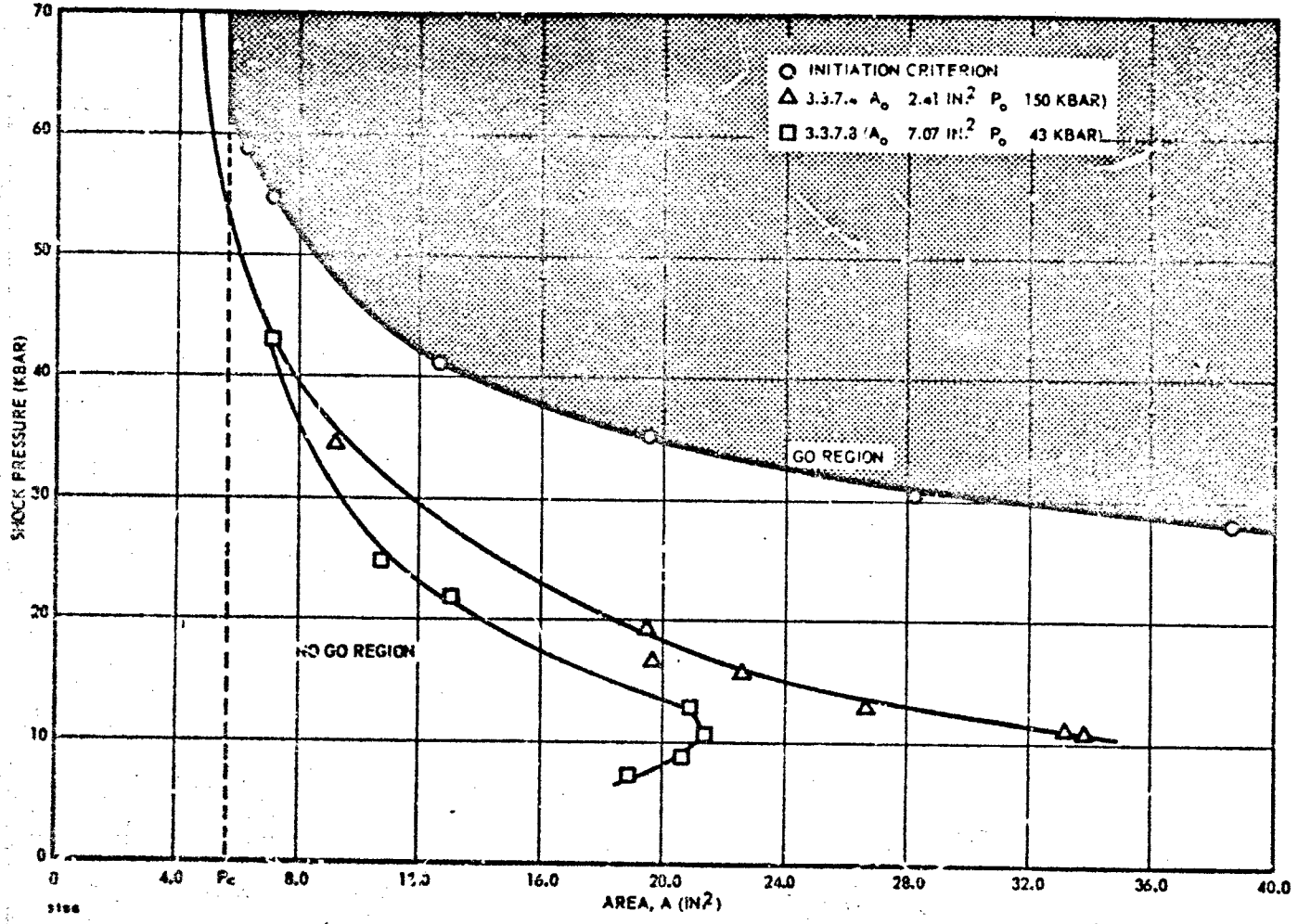


Figure 53. Evaluation of Initiation Criterion, Miscellaneous Tests.

## Rectangular Acceptor Tests

The initiation theory requires that the criterion be independent of sample shape. To investigate this, a small number of tests were performed with supercritical rectangular acceptors cast from AAB-3189 propellant. These rectangular samples were 4-in. thick by 8-in. wide by 12-in. long, and the booster charges were located at the center of the 4-in. by 8-in. top end of the samples.

Five tests were conducted. The details of the initial test conditions and the results are shown in Table XXXVI. Two samples each failed to detonate when shocked by 1-in. thick by 2-in. wide by 4-in. long Composition B boosters. Two samples each detonated when shocked by 1-1/4-in. thick by 2-1/2-in. wide by 5-in. long Composition B boosters. The fifth sample was shocked by a 2-in. diameter by 6-in. long cylindrical Composition B booster with the wave attenuated by PMMA to 125 kbar. This sample did not detonate.

Table XXXVI. Evaluation of Initiation Criterion, Using 4-in. by 8-in. Rectangular Acceptors.

| Booster Size (in.) | PMMA Length (in.) | Maximum Initial Shock Pressure (kbar)* | Minimum Initial Wave Area ($in.^2$)* | Test Result | Test Number |
|---|---|---|---|---|---|
| 1 by 2 | None | 250 | 2.00 | No go | 3.3.8.1 |
| 1 by 2 | None | 250 | 2.00 | No go | 3.3.8.4 |
| 1-1/4 by 2-1/2 | None | 250 | 3.12 | Go | 3.3.8.2 |
| 1-1/4 by 2-1/2 | None | 250 | 3.12 | Go | 3.3.8.3 |
| 3 dia | 0.580 | 125 | 7.07 | No go | 3.3.8.5 |

*Assuming plane wave.

The instrumentation of the rectangular acceptors was established by assuming the detonation wave to be approximated by a torus. It was expected that the wave would have a larger radius of curvature in the width-length plane than in the thickness-length plane, because of the charge geometry. A coordinate system was chosen which made the center of the top of the acceptor the origin. The

X-axis was directed through the sample, perpendicular to the top surface, the Y-axis was directed toward the larger side, and the Z-axis toward the smaller side. The rectangle was defined by

$$\begin{aligned} 0 &\leq x \leq 12 \quad \text{in.} \\ -2 &\leq y \leq 2 \quad \text{in.} \\ -4 &\leq z \leq 4 \quad \text{in.} \end{aligned} \tag{96}$$

By assuming symmetry, the shock wave was analyzed only in the quarter where x, y, and z are nonnegative. Probes were placed at uniform distances down the length of the charge in the X-Y plane and in the X-Z plane. The equation of the torus generated by rotating the circle

$$(x - k)^2 + y^2 = r^2 \qquad (z = 0) \tag{97}$$

about the line (h, y, 0) is

$$\left[\sqrt{(x - h)^2 + z^2} - k + h\right]^2 + y^2 = r^2 \tag{98}$$

$$(k > h + r)$$

If R is the radius of curvature in the X-Z plane, Equation 98 can be written

$$\left[\sqrt{(x - h)^2 + z^2} - R + r\right]^2 + y^2 = r^2 \tag{99}$$

where r is the radius of curvature in the X-Y plane. Programing the computer to solve Equation 99 requires adoption of a nonlinear least squares analysis to the (x, y, z) data. In lieu of this, the (x,y) data were fit to Equation 97, and the (x,z) data were fit to

$$(x - h)^2 + z^2 = R^2 \tag{100}$$

Comparison at each t of the two values of x at (x,0,0) predicted by the fits of Equations 97 and 100 revealed correspondence to within 0.02 in., so that the data were compatible with a toroidal shape. The pressure distribution was calculated using the experimental data and simple geometric analysis of the surface shape. The area of the wave was calculated by determining the S(y,z) boundary of its projection on the Y-Z plane and integrating over this region by the equation

$$A = \iint_S \left[1 + \left(\frac{\partial x}{\partial z}\right)^2 + \left(\frac{\partial x}{\partial y}\right)^2\right]^{1/2} dzdy \qquad (101)$$

Regrettably, the no go's each failed to produce sufficient data for an analysis to be made. The difficulties included loss of data from entire columns of probes and, more commonly, very erratic data. Probe data from nondetonating charges always becomes erratic as the shock wave attenuates to low pressures. In these rectangular tests the data were very poor within 5 μsec after the shock wave entered the sample, except when detonation occurred. It is apparent that in future tests of this type the probes must be grouped very near the area that is being shocked.

The two tests that resulted in detonation produced excellent data that could be fit to the assumed toroidal wave shape. The best fits of the shock wave at various times are given in Appendix VIII for Tests No. 3.3.8.2 and 3.3.8.3, including the calculated average shock pressures and wave areas.

The results clearly show that in both tests the shock wave pressure and area exceeded the initiation criterion (Figure 54).

With a wave delivered by a rectangular booster twice as wide as it is thick it could be assumed that the shock wave in the propellant will expand so that its projection on the Y-Z plane will always have (y,z) dimensions in the same proportion. This assumption arises from the fact that the expansion in the Y-direction may be slower than that in the Z-direction because the wave has a smaller radius of curvature in the X-Y plane. The critical area of a rectangular sample having width equal to 2 thicknesses is given by the critical geometry theory:

$$t_c = \frac{3}{4}\sigma_c$$

$$w_c = 2t_c = 3/2\ \sigma_c \qquad (102)$$

$$\therefore A_c = \frac{9\ \sigma_c^2}{8} \qquad (103)$$

Assuming $\sigma_c = 0.92\ d_c$, the critical area is 6.98 $in.^2$.

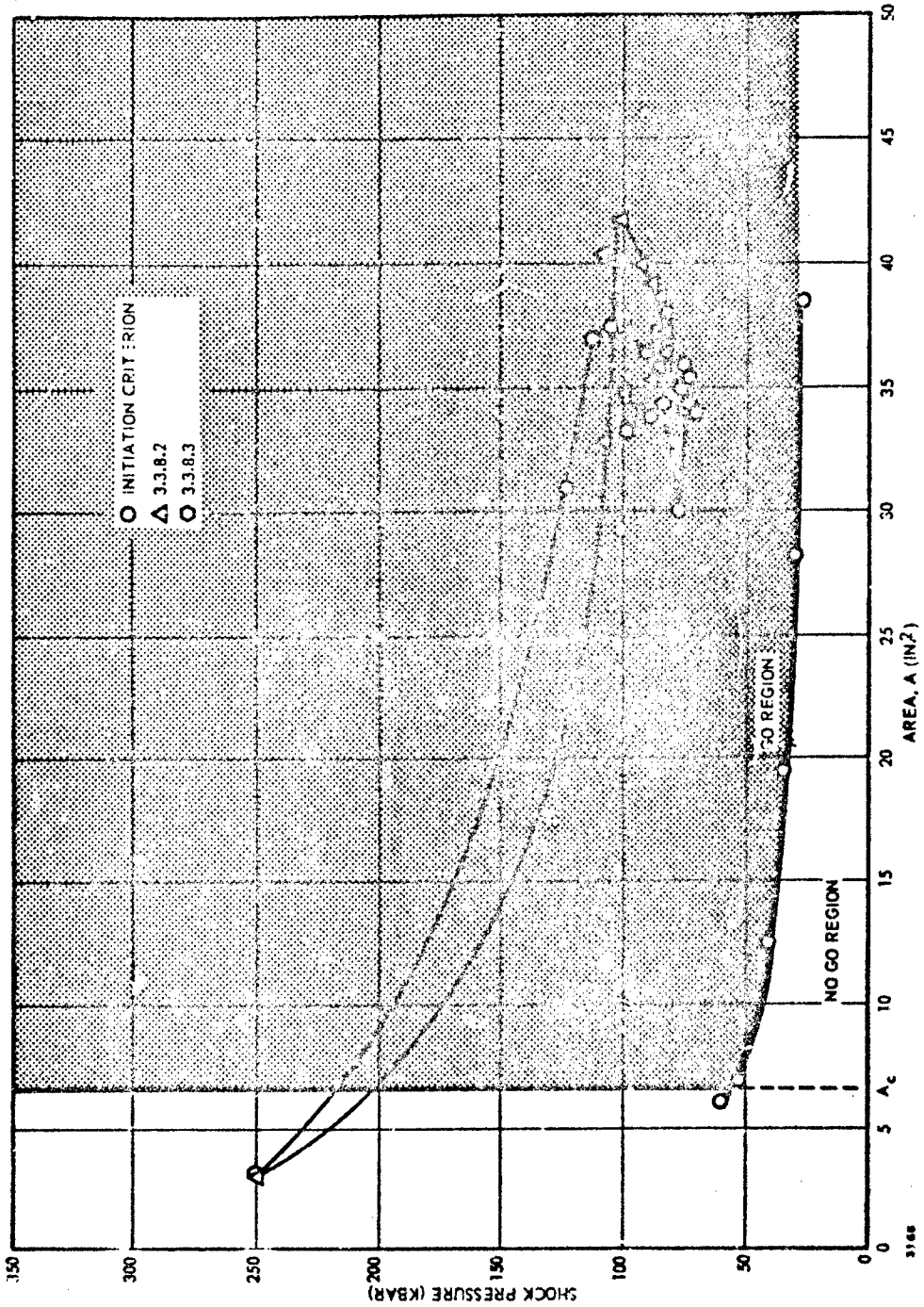


Figure 54. Evaluation of Initiation Criterion, Rectangular Acceptor.

If one assumes that the wave expands with equal velocity in the Y- and Z-directions, the wave will essentially have a rectangular cross section at any time t before |y| = 2 in. that is given by

$$|y| = y_o + \Delta$$
$$|z| = z_o + \Delta \qquad (104)$$

where the subscript o refers to the initial size of the wave and $\Delta$ is one-half of the increase in either width or thickness. The proportions of this rectangular shape change with time and are dependent on the booster size. It can be shown that with a 1-1/4-in. by 2-1/2-in. booster, the critical value of $\Delta$ is 0.39 in., and $A_c$ = 6.61 in.$^2$. Since the data indicate that the wave expands in both the Y and Z directions at about the same velocity, this value for $A_c$, the critical area of the rectangle, is indicated in Figure 54.

It may be noted that the smaller the booster dimensions are, the larger the value of $A_c$ becomes, because the wave expanding as indicated must reach critical proportions that agree with the critical geometry theory. The thinner the booster is, the greater the critical width of a rectangle must be and, in terms of area, the larger the critical area must be. If $\xi$ is the ratio of width to thickness,

$$A_c = \frac{(\xi + 1)^2}{\xi}\left(\frac{\sigma_c}{2}\right)^2 \quad (\xi \geq 1) \qquad (105)$$

and

$$\frac{\partial A_c}{\partial \xi} = \left(\frac{\xi^2 - 1}{\xi^2}\right)\left(\frac{\sigma_c}{2}\right)^2 \geq 0 \qquad (106)$$

The minimum critical area for a rectangle is that of the critical square ($\xi$ = 1), which for AAB-3189 is 6.20 in.$^2$.

## INITIATION PRESSURE vs PULSE WIDTH

The objective of this subtask was to investigate the relationship between the shock pressure required to initiate detonation and the pulse-width of the shock wave. This study was a preliminary study for the broadened initiation criterion that considers shock pressure, shock wave area, and pulse width to be the three determining parameters of initiation to detonation. In the study of the pressure-pulse width relationship, the flyer-plate technique was applied.

## Background

When one condensed material impacts another, the shock pressure and pulse duration are calculated from knowledge of the test conditions and the Hugoniot equations of state of the two materials. In this particular case, aluminum plates were propelled at 4-in. diameter samples of AAB-3189. Knowing the flyer-plate velocity, the shock pressure generated on impact at the plate-propellant interface can be determined by the Hugoniot reflection method. The shock velocity in the aluminum, $U_{Al}$, and in the propellant, $U_{PBAN}$, can then be calculated directly from the Hugoniots of these materials.

The time of contact, neglecting any attenuation of the shock wave in the flyer plate, is given by

$$t = \frac{2x}{U_{Al}} \tag{107}$$

where t = contact time and x = flyer plate thickness. The duration time of the pulse entering the propellant will be equal to t, and if attenuation in the propellant is neglected,

$$t = \frac{w}{U_{PBAN}} \tag{108}$$

where w = the pulse width in the propellant. By equating Equations 107 and 108 and rearranging,

$$w = \frac{2xU_{PBAN}}{U_{Al}} \tag{109}$$

Shock pressures transmitted at impact as a function of $u_f$ are shown in Figure 55, and the pulse width (mm) as a function of $u_f$ and x is shown in Figure 56.

## Test Description

Aluminum flyer plates 5-in. square were propelled at 4-in. diameter cylindrical samples of AAB-3189 (critical diameter = 2.7 in.) The pulse width and shock pressure were varied from test to test by proper selection of flyer plate velocity and thickness.

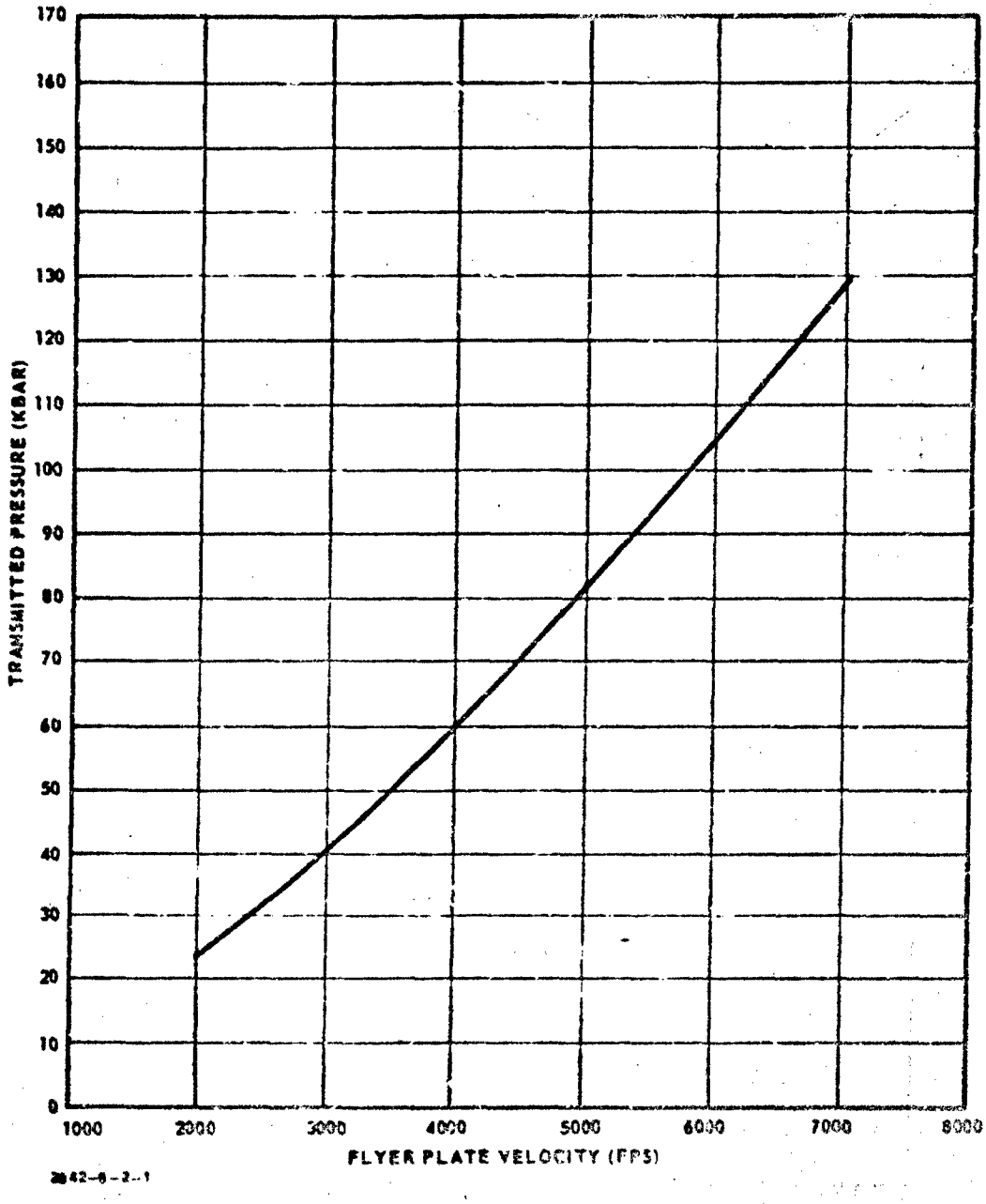


Figure 55. Pressure in PBAN Propellant as a Function of Flyer Plate Velocity.

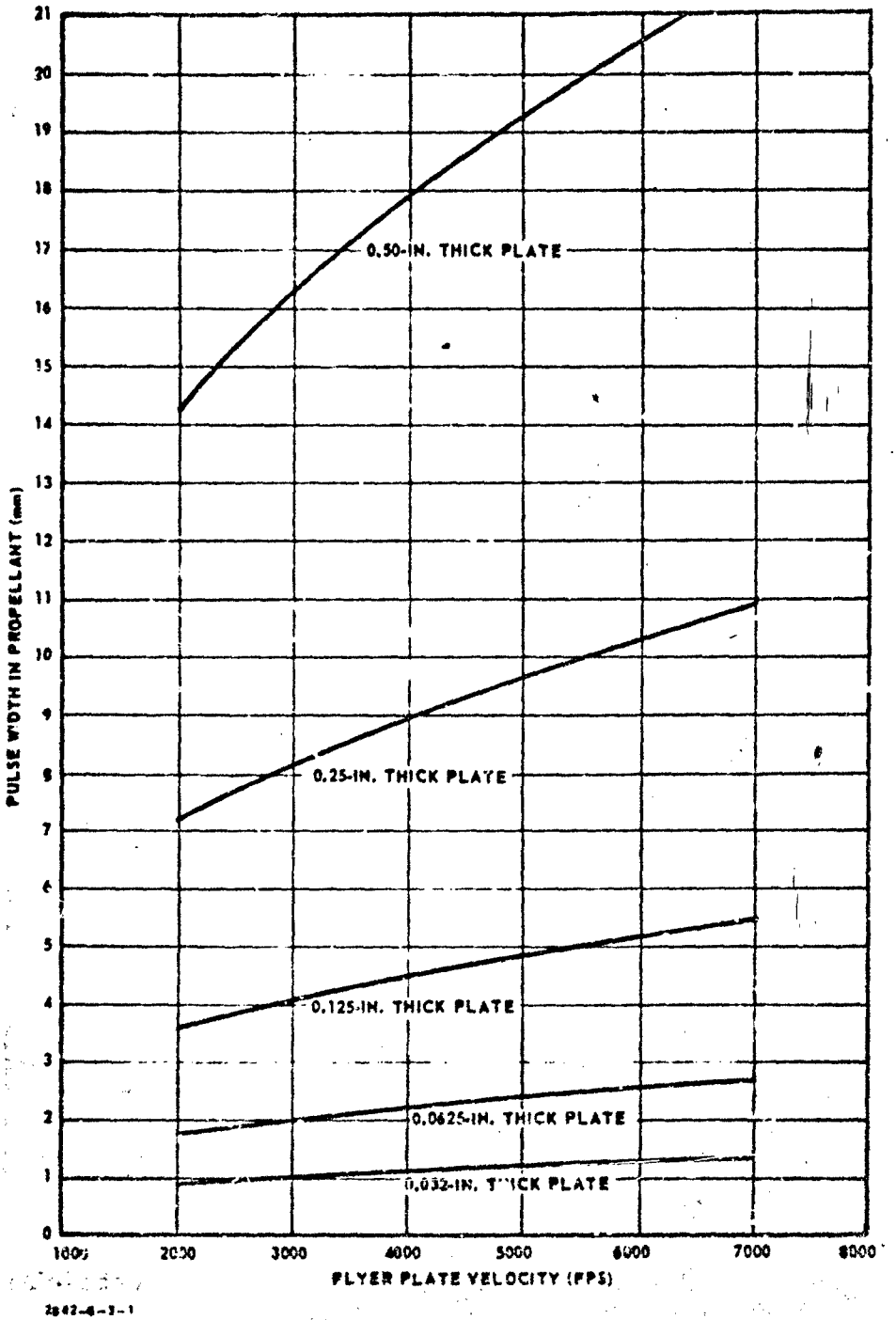


Figure 56. Pulse Width of Shock Wave in PBAN Propellant.

Figure 57 shows the test orientation. The T-1 target switches are located in the path of the plate at a measured separation from each other so that the velocity of the plate can be determined. A 6- by 6- by 1/2-in. steel plate placed against the rear of the acceptor charge functions as a witness plate to facilitate interpretation of the test results.

## Flyer-Plate Technique

An experimental method was developed to accelerate aluminum flyer plates to velocities ranging from 2000 to 7000 fps. This velocity range is required to obtain a shock pressure range suitable for the propellant initiation-to-detonation study. A flash-X-ray system is used to monitor the flight of the flyer plate. The flyer-plate velocity and the angle of tilt required to obtain simultaneous impact of the flyer plate against a target were then determined from the radiographs. The experimental setup is shown in Figure 58.

Initially, the tests were performed with a single sheet of Detasheet C explosive. Only a limited amount of Detasheet of different thicknesses was available at the Chino Hills Ordnance Laboratory, and a 10 to 12-week lead time was required to obtain the explosive from the vendor. Therefore, multiple layers of Detasheet C-1 (0.042-in. thick) explosive were used. The flyer-plate velocities obtained with the multiple layers of explosive were different from the velocities obtained with one layer of the thicker Detasheet. The flyer-plate velocities, a family of curves describing flyer-plate velocity as a function of plate thickness, using 1 to 4 layers of Detasheet C-1 and angle-of-tilt data for the flyer plate as a function of plate velocity, are shown in Appendix IX.

During the program, it was found that the flyer-plate velocity, using a specific explosive weight per square inch, could be reduced by using a plywood test stand instead of steel. This increased the range of flyer-plate velocities obtainable with the limited supply of explosives.

## Results

Sixteen tests were conducted after the developmental experiments were concluded. Aluminum plates from 1/32 to 1/2-in. thick were flung at velocities from 1868 to 6897 fps. The results of these tests are given in Table XXXVII and Figures 59 and 60. Examination of the figures reveals an expected relationship between the

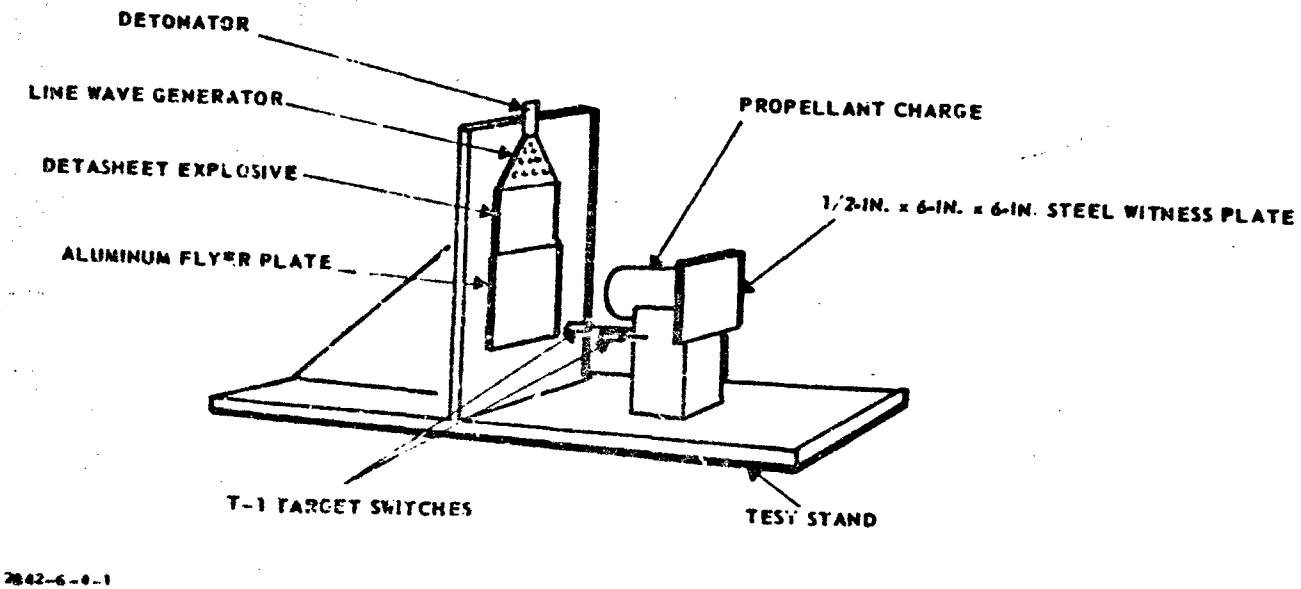


Figure 57. Experimental Test Configuration.

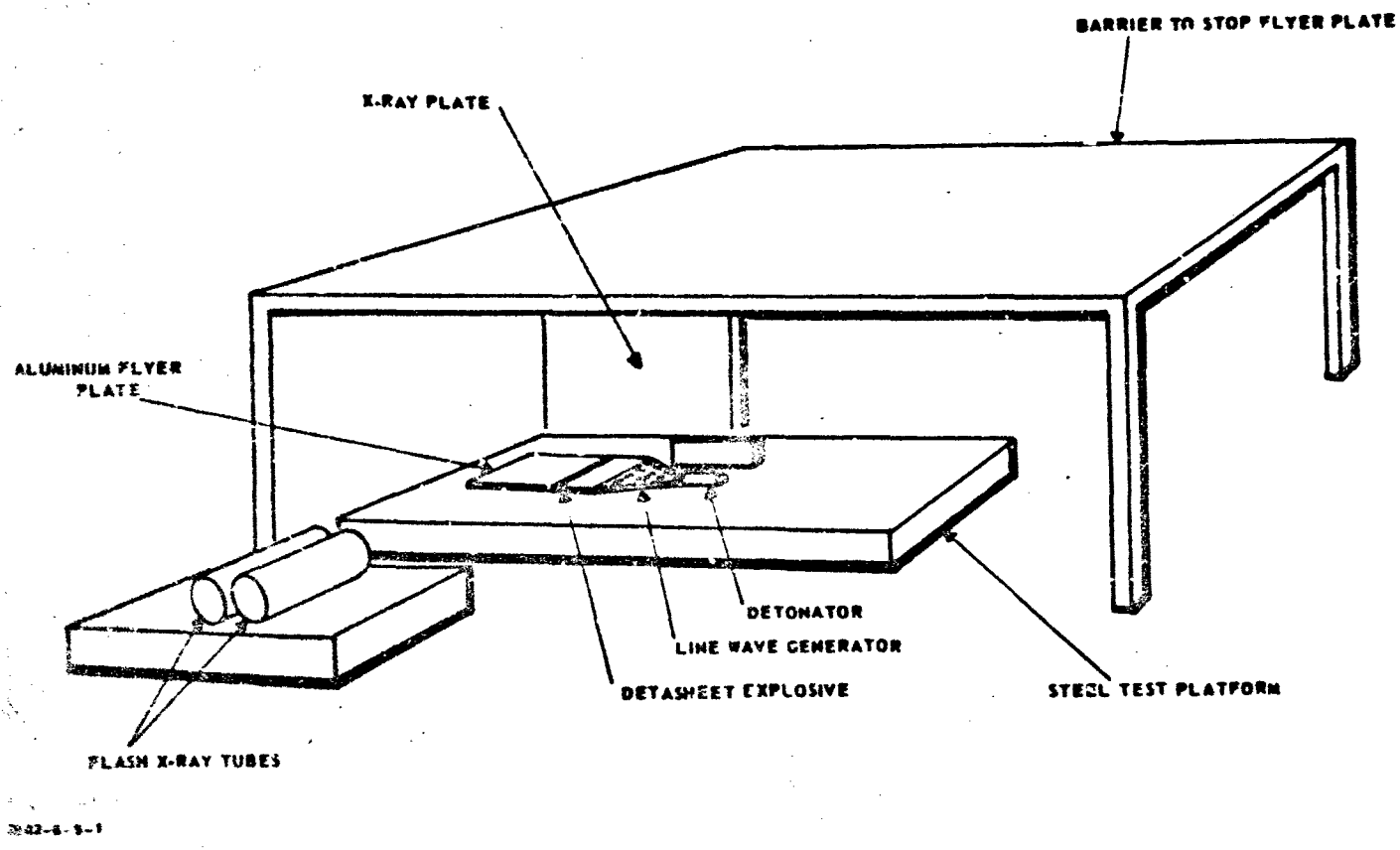


Figure 58. Test Setup Using Flash X-Ray.

## Table XXXVII. Results of Flyer-Plate Tests.

| Test Number | Detasheet Explosive | Flyer Plate Thickness (in.) | Distance Between Pins (in.) | Time Between Pulses (μsec) | Velocity (fps) | Pressure (kbar) | Pulse Width in Propellant (mm) | Time (usec) | Detonation of Propellant | Test Stand |
|---|---|---|---|---|---|---|---|---|---|---|
| 3.3.4.46 | Two-thickness C-1 | 1/8 | 0.87 | 20.7 | 3502 | 49.5 | 4.25 | 1.25 | Yes | Steel |
| 3.3.4.47 | One-thickness C-1 | 1/8 | 1.07 | 34.6 | 2577 | 32.5 | 3.85 | 1.21 | No | Steel |
| 3.3.4.48 | Three-thickness C-1 | 1/4 | 1.21 | 35.3 | 2857 | 37.5 | 7.95 | 2.44 | Yes | Steel |
| 3.3.4.49 | Two-thickness C-1 | 1/4 | 1.12 | 39.7 | 2351 | 28.8 | 7.45 | 2.36 | No | Steel |
| 3.3.4.50 | Two-thickness C-1 | 1/8 | 0.82 | 29.6 | 2309 | 28.2 | 3.71 | 1.18 | No | Plywood |
| 3.3.4.51 | One-thickness C-1 | 1/16 | 0.98 | 27.2 | 3002 | 40.5 | 2.02 | 0.61 | No | Steel |
| 3.3.4.52 | Three-thickness C-1 | 1/8 | 1.01 | 28.7 | 2933 | 39.5 | 4.45 | 1.35 | No | Plywood |
| 3.3.4.53 | Two-thickness C-1 | 1/16 | 1.02 | 17.8 | 4775 | 76 | 2.38 | 0.64 | Yes | Steel |
| 3.3.4.54 | One-thickness C-4 | 1/4 | 1.04 | 46.4 | 1868 | 21.5 | 7.90 | 2.31 | No | Plywood |
| 3.3.4.55 | Three-thickness C-1 | 1/4 | 0.79 | 25.4 | 2592 | 33 | 7.70 | 2.40 | Yes | Steel |
| 3.3.4.56 | Two-thickness C-1 | 1/16 | 1.01 | 20.0 | 4206 | 64 | 2.27 | 0.64 | Yes | Steel |
| 3.3.4.57 | Four-thickness C-1 | 1/2 | 1.29 | 54.3 | 1980 | 23.5 | 14.2 | 4.62 | No | Steel |
| 3.3.4.58 | One-thickness C-1 | 0.032 | 0.98 | 23.3 | 3505 | 49.5 | 2.12 | 0.62 | No | Steel |
| 3.3.4.59 | Two-thickness C-1 | 0.032 | 1.44 | 17.4 | 6897 | 126 | 1.40 | 0.34 | Yes | Steel |
| 3.3.4.60 | Five-thickness C-1 | 1/2 | 1.22 | 46.2 | 2201 | 26.5 | 14.7 | 4.73 | No | Steel |
| 3.3.4.61 | Six-thickness C-1 | 1/2 | 1.29 | 33.6 | 3199 | 43.5 | 16.55 | 4.97 | Yes | Steel |

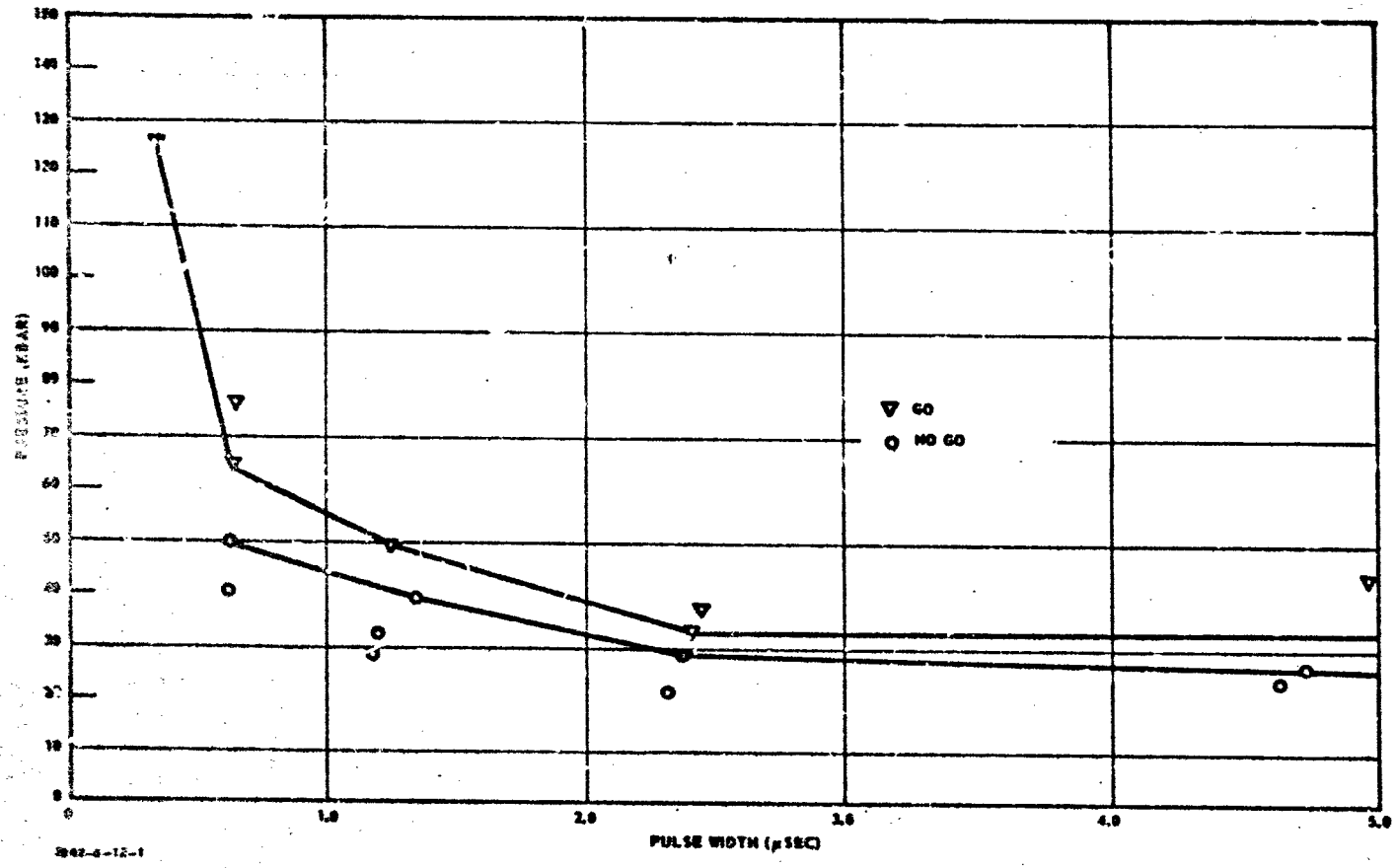


Figure 59. Effect of Pulse Width on Minimum Initiating Shock Pressure.

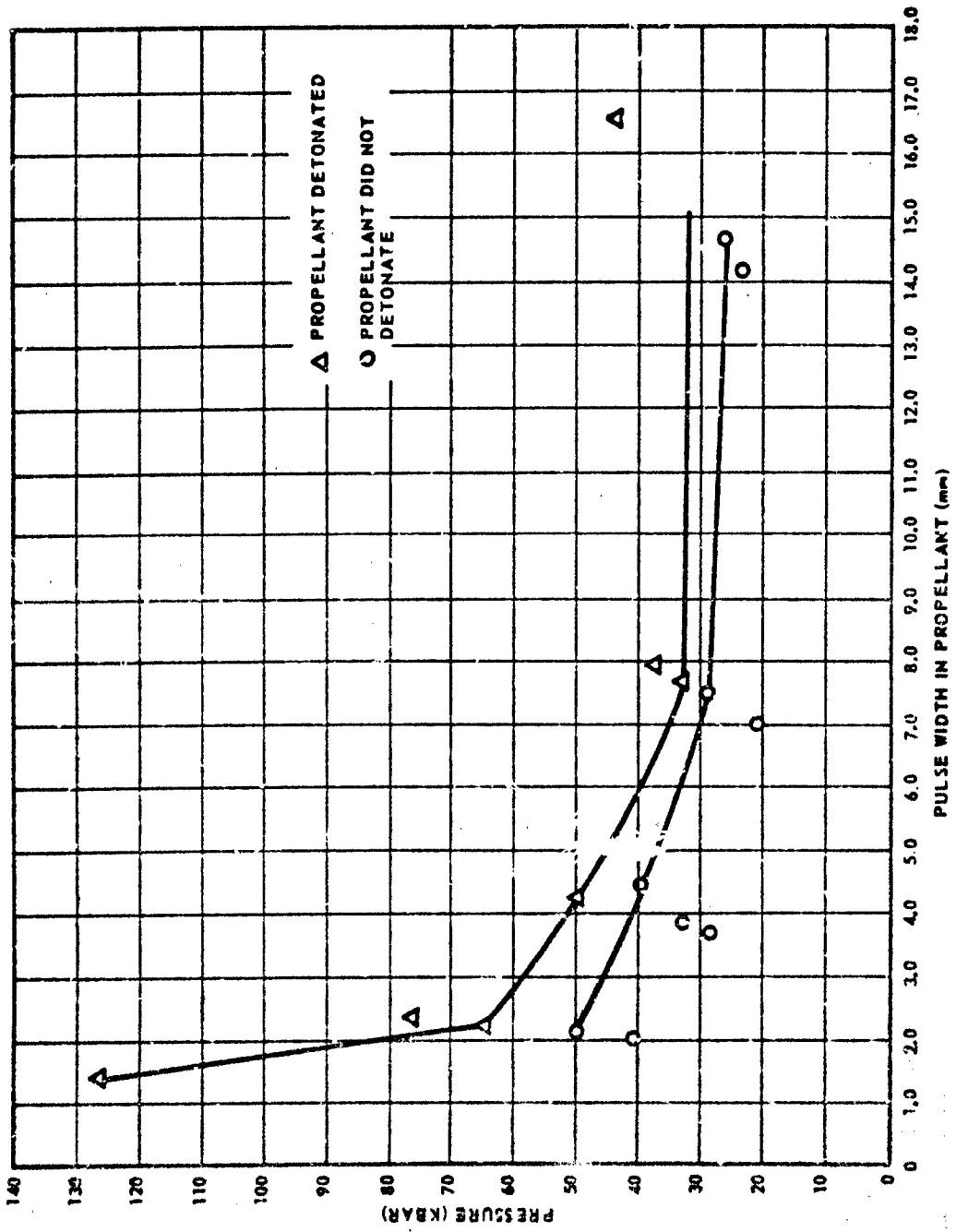


Figure 60. Effect of Pulse Width (mm) on Minimum Initiating Shock Pressure.

shock pressure and pulse width required to initiate detonation. Pulses of smaller width require higher pressure to achieve initiation of the acceptor. It is furthermore indicated that a minimum pressure exists below which initiation is impossible with any width pulse. For the 4-in. diameter samples this minimum pressure is near 30 kbar.

## PREDICTED INITIATION CRITERION FOR UNADULTERATED PROPELLANT

The normal technique that is used to generate the initiation criterion for a detonable material has been described in detail. Requiring, as it does, card-gap tests of supercritical samples, this technique is only practical when applied to materials of reasonably small critical diameters. The critical diameter of ANB-3226 is between 5 and 6 ft. Any estimate of the initiation criterion for this propellant could only be accomplished through use of a new experimental technique or by theoretical analysis and prediction. Both approaches were taken in SOPHY II.

An experimental technique was suggested in which the minimum shock pressure at ideal diameter, P*, could be measured directly from tests involving subcritical samples only. A theoretical prediction of the initiation criterion was developed, also, by extrapolating the initiation criteria of RDX-adulterated formulations.

### Axial-Probe Technique

In this subtask the objective was to evaluate the use of the axial resistance-probe technique as a means to arrive at the minimum critical shock pressure, and, if the technique did succeed, to determine P* for unadulterated propellant ANB-3226.

#### Background

The axial resistance probe has been used for some time in the study of deflagration-to-detonation in high explosives (References 23, 24, and 25). The probes usually consist of a Nichrome wire and a copper wire, cast in the sample either parallel to, and equidistant from, the axis or wrapped one about the other to form a coaxial probe on the axis. The probe is shorted by the highly-ionized medium immediately behind the shock front. As the detonation wave moves down the sample the resistance of the probe is reduced in direct proportion to the reduction in the length of the probe lying ahead of the shock front. The resistance probe is in a

constant-current circuit, with the changing voltage being monitored on an oscilloscope. As the length of the probe ahead of the advancing wave diminishes, the resistance in the circuit diminishes and, since the current is held constant, the voltage in the circuit drops. The oscilloscope records voltage vs real time and, since the current level is known, the resistance vs time data are easily computed. Since the probe is made to a known resistance per unit length, it is a straightforward step to convert to distance-time data. The axial resistance probe thus supplies a continuous record of the behavior of the detonation wave at the axis.

There are three major assumptions involved in the theoretical justification for applying the axial resistance-probe technique to subcritical sensitivity tests. First, the material near the axis of a subcritical cylindrical charge will not react differently from that in a supercritical or ideal diameter charge until the effects of the incoming rarefaction regions are communicated to it. Experimental evidence obtained in SOPHY I during the testing of supercritical samples initiated by boosters that had diameters below the critical diameter of the acceptor suggested such to be the case (Reference 1). In a test that resulted in failure to initiate detonation because the booster was too small, the detonation wave attenuation profile in the acceptor revealed that along the axis the wave was sustained at a constant velocity over the first diameter of the sample (4 in.). Finally the wave began to attenuate. The important fact is that momentary sustainment did occur and at a velocity equal to the detonation velocity in AAB-3189 propellant.

The second assumption is that in the card-gap testing of a very subcritical sample the small diameter will not reduce the time during which the velocity is sustained along the axis to an immeasurably small value. In the example cited above, the sample diameter was nearly 60% above $d_c$ and the shock wave from the booster was not attenuated before reaching the propellant surface. Under these initial conditions, the sustainment lasted approximately 20 μsec.

The third assumption is that P*, the minimum shock pressure required to initiate detonation in an infinite-diameter sample, is not significantly different from the minimum shock pressure required to initiate chemical reaction in the material.

If the second assumption holds, one would expect to find a shock pressure above which the velocity stabilizes for a few microseconds and below which the velocity continuously decreases. In this event, determination of this pressure would be by noting the lowest pressure that produces a linear portion in the output of the probe. This pressure should be related to, or equivalent to P*.

If the third assumption is true, below P* there may be insufficient ionization produced to electrically short the probe, and the minimum pressure at which any pulse was generated could be considered as an estimate of P*.

## Test Plan

The hypotheses stated previously needed experimental evaluation before any investigation could be conducted with ANB-3225 propellant. Since the initiation criterion for AAB-3189 (9.2% RDX) adulterated propellant had been determined in SOPHY I, a reasonable estimate of P* already existed for this material: 20 kbar.

The experimental task therefore consisted of conducting card-gap tests of axially-probed, subcritical, cylindrical samples of AAB-3189, particularly selecting initial transmitted-shock pressures in the immediate region of 20 kbar. The output pulse from each test had to be analyzed for evidence of a sustained velocity over a short distance along the axis. Outputs received from tests that were conducted at pressures lower than 20 kbar would be analyzed to determine whether any characteristic of their appearance differentiated them from those obtained from tests at higher initial transmitted shock pressures. In all, tests would be performed at initial pressures as high as 60 kbar, so that if the break point were not at 20 kbar, its exact position of the initiation criterion could be established.

Following a successful identification of the minimum shock pressure necessary to cause a subcritical AAB-3189 sample to detonate momentarily along its axis, the axial-probe method would be applied to instrumented samples of the unadulterated propellant and attempts to estimate a point on the initiation criterion of ANB-3226 would be made.

## Test Results

Samples 2-in. diameter by 8-in. long of AAB-3189 were cast with a coaxial resistance probe (Figure 61) located on the axis of each sample. The probes were constructed of 40-gage Nichrome wire tightly wrapped around a 20-gage wire. Initial resistance of this probe was found to be 486 ± 2 ohms.

Card-gap tests were conducted, with transmitted shock pressures ranging from less than 20 kbar to more than 100 kbar, in search of a distinguishing change in the probe outputs. No evidence could be found that might identify a minimum shock pressure to cause

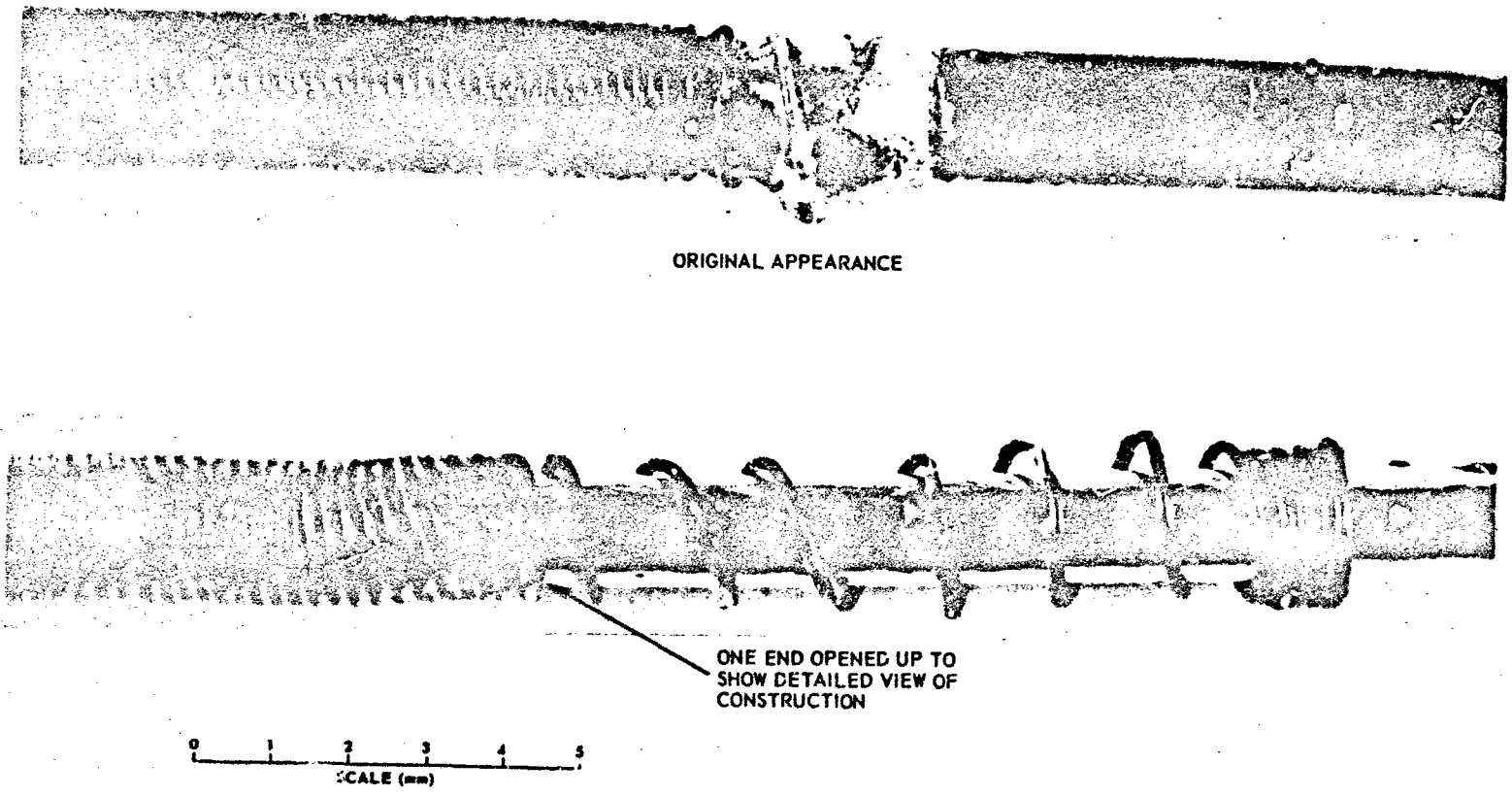


Figure 61. Axial-Resistance Probe.

propellant detonation in a supercritical sample. The analysis of the pulses produced, in several instances, unrealistically high apparent shock wave velocities in the acceptors. It was noted furthermore that considerable extraneous noise was being picked up by the probe, to further complicate interpretation of the results.

To check out probe behavior in a detonating charge, a test was conducted with an axially-probed Composition B charge. This test produced a linear trace that indicated a detonation velocity of 7.40 mm/μsec, which is about 5% below published values for Composition B. However, the test was designed to be a qualitative evaluation of the probe, and the charge density was not determined, so this velocity discrepancy should not be taken too seriously.

The probe system appears to work well when a sustained detonation is in progress but to fail to operate satisfactorily under the transient conditions of a subcritical test. Whether this failure is due to the probe design itself or to unwarranted assumptions about the behavior of subcritical samples has not been determined. Perhaps another design would yield usable data. The SOPHY II study was limited to this design and its evaluation. Consequently, there was no attempt made to determine a point on the ANB-3225 initiation criterion by subcritical testing of axially-probed samples.

## Extrapolation Technique

The data shown in Figure 50 compare the initiation criteria of AAB-3189, -3225, and -3267 propellants with the abscissa normalized by dividing the charge diameters by the critical diameters of the respective formulations. The steepness of the initiation criterion in the region near the critical diameter makes it difficult to estimate $P^+$ at the critical diameter. Experiments cannot be conducted with samples having diameters very near to the critical diameter because it could not be established whether failure were due to insufficient shock loading or to insufficient diameter.

Nevertheless, the estimated values of $P^+$ at the critical diameter for these propellants, in order of increasing critical diameter, are 62, 37, and 34 kbar. The last value is the most uncertain of all. It can be seen, however, that with increasing critical diameters the value of $P^+$ at the critical diameter decreases. Assuming no reversal in direction as the RDX content is reduced further, the value of $P^+$ for a critical-diameter, unadulterated sample may be 25 to 30 kbar.

Comparing $P^+$ for these propellants, the values are all within 5 kbar of each other: AAB-3189, 20 kbars; AAB-3225, 18 kbar; and AAB-3267, 15 kbar. Extrapolating these values, the estimated minimum transmitted shock pressure required to initiate detonation of an ideal-diameter unadulterated sample may be as low as 3 to 10 kbar.

The predicted initiation criterion for ANB-3226 has a relative maximum of 25 to 30 kbar and a minimum of 8 to 10 kbar. These values are completely dependent upon the corresponding values obtained from the adulterated propellants. Since greater uncertainty exists with the near-critical values used in the extrapolation, the 25 to 30 kbar pressure estimate is extremely tentative. Hopefully, there will be additional data generated in future studies that will resolve this uncertainty.

A certain degree of support exists for the findings that the minimum initiating shock pressures required decrease with an increase in critical diameter. The estimated value of $P^+$ at the critical diameter for AAB-3189 is 62 kbar. The spike detonation pressure for this propellant calculated from its Hugoniot is 65 kbar. For AAB-3225 the respective pressures are 37 and 50 kbar; for AAB-3267, they are 34 kbar and 48 kbar. In each case, the $P^+$ value is somewhat less than the detonation pressure. Since the P(U) Hugoniots for these propellants are almost the same in the low-pressure region (P less than 25 kbar) the spike detonation pressure of ANB-3226 could be estimated roughly by substituting $U = 3.2$ mm/μsec (see Section IV) in any of the Hugoniots. This produces an estimated value of 29 kbar. It can be assumed from this argument that the value of $P^+$ near the critical diameter for ANB-3226 is less than 29 kbar. The extrapolated prediction agrees well with this restriction.

## CONCLUSIONS

The initiation criterion has been determined and evaluated in terms of minimum shock pressure and wave area. The data have been extrapolated to predict the corresponding criterion for unadulterated propellant. Since the criterion is a function of pulse width as well, each curve generated in this study is actually the projection on the P-A plane of a curve that lies on the initiation criterion surface. In order to define this surface for each material it is necessary that the pulse-width effect be known. The pulse-width data that were generated for 4-in. diameter AAB-3189 samples indicate that, as expected, the minimum pressure required to initiate detonation is inversely related to the pulse width of the shock wave, with the limitation that, regardless of the magnitude of the pulse width, there is a minimum shock pressure required to initiate detonation of any particular size sample. The pulse-width studies only determined the minimum applied pulse widths necessary for initiation of detonation, which is similar to the evaluation tests of the pressure-area criterion in that the minimum area required of a 250 kbar shock wave was found to be between 1.77 $in.^2$ and 2.41 $in.^2$, and the minimum pressure required of a 3.14 $in.^2$ wave

was found to be approximately 150 kbar. These data are not strictly properties of the material because they describe the initial conditions only. As the initiation criterion is defined, the conditions for initiation of detonation are met if, and only if, the shock wave meets or exceeds the initiation criterion. Clearly initiation is not assured when the shock pressure equals 150 kbar and the area equals 3.14 $in.^2$, since the AAB-3189 sample will not detonate unless it is supercritical, and the illustrated conditions are below those required for sustainment of detonation, i.e, acceptor area must be greater than 5.77 $in.^2$, the area of a critical diameter sample.

Judging from the fact that for both 4-in. and 6-in. diameter samples the minimum booster diameter required to initiate detonation is between 1-1/2-in. diameter and 1-3/4-in. diameter, it might be presumed that the actual size of the supercritical acceptor does not affect the minimum initial pressure-area conditions required to initiate detonation. If such is the case, and an extensive study certainly would be demanded to verify this assumption, the theory of initiation could be restated in such a way that would allow the definition of a pressure-area-pulse width surface that described the minimum conditions required to initiate detonation of any supercritical grain. This surface would extend into the region $A < A_c$, and it would still be a property of the material because its shape in this region would depend on the manner in which the shock wave pressure and pulse width change as the wave expands to a supercritical area. The acquired data on the minimum initial shock wave area and pressure required to initiate detonation of supercritical cylindrical and rectangular samples of AAB-3189, obtained from the card-gap tests and the initiation criterion evaluation tests, generate the composite curve shown in Figure 62. This curve has been defined most thoroughly by the 6-in. diameter evaluation tests, but no exception to the curve is found in the 4-in. by 8-in. rectangle tests or in the 4-in. diameter tests of SOPHY I.

To assume that the curve in Figure 62 may apply to all supercritical samples, regardless of shape, requires one to assume that the expansion of the shock wave in a sample is independent of the sample shape. This assumption cannot be justified. In the case of the rectangles that were tested their thickness was greater than the critical diameter of AAB-3189, so that the results obtained from these tests do not constitute a sufficient test for the independence of sample shape.

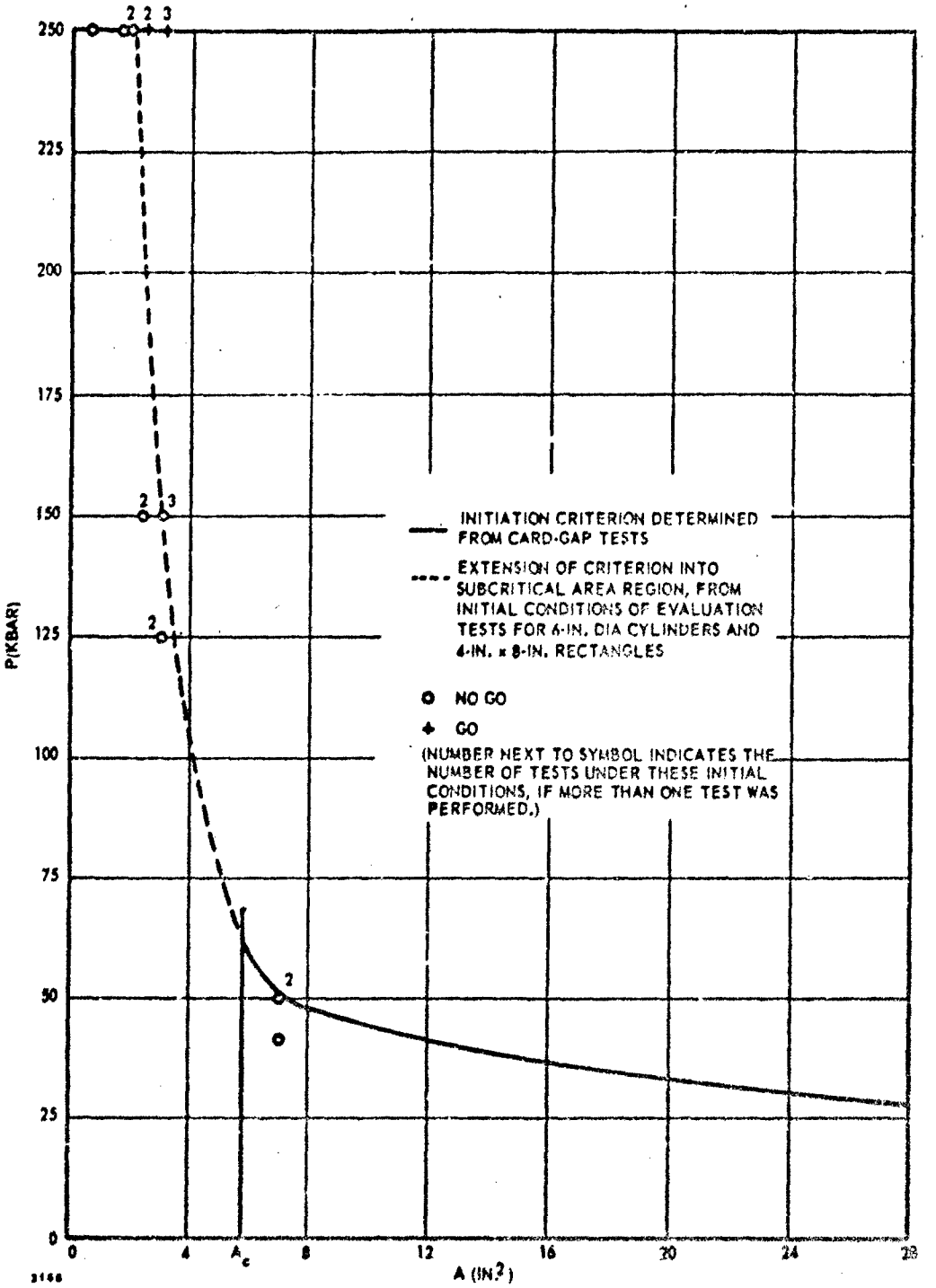


Figure 62. Minimum Initial Pressure-Area Requirements for Shock Initiation of Detonation in AAB-3189.

Before the initiation criterion can be categorically applied to any grain shape it is imperative that (1) the theory be tested for several noncircular shapes and (2) the effect of pulse width on the pressure-area criterion be studied extensively.

A third area of investigation, which like the others is crucial to the acceptance of the hypothesis, must be performed. That study must deal with shock application at other locations on a grain. The SOPHY studies have provided ample verification of the validity of the initiation criterion hypothesis for the circular cylinder and for a specific rectangle when the sample is subjected to a shock wave entering at the center of one end of the sample. Similar tests must be made to determine the validity of the initiation criterion when a shock wave is applied to the side of the sample or to the end but off the center (such as on the web at one end of a hollow-core cylinder).

The importance of analyzing the initiation criterion further is not only to satisfy the curiosity of the theoretician, but to meet the present requirements of solid propellant hazards evaluation. Since the critical geometry and critical diameter test results prove that large solid motors of present design do reach supercritical proportions, it is vital to the interpretation of detonation hazards that the minimum conditions for initiation of detonation be fully established..

PRECEDING PAGE BLANK-NOT FILMED

# SECTION VIII

# SYNTHESIS OF DEFECTIVE PROPELLANT

## INTRODUCTION

The objectives of this program were to develop methods of preparing propellant with defects as listed below and to develop methods of analyzing these propellants.

- Propellant with connected voids with propellant surface areas of 10 to 15 $cm^2/cm^3$ and 40 to 50 $cm^2/cm^3$.
- Propellant with unconnected pores with porosity ranges of 5 to 10% and 20 to 30% with pore diameter ranges of 1 to 10 μ and 0.1 to 1 mm.

The following report describes the experiments which resulted in propellants with pores from a few percent to as high as 23%. There were many variations of procedures with and without additives which made significant differences in porosity. The analytical and microscopic methods for establishing porosity and the technique developed for measuring propellant surface area are also described.

## PRODUCTION OF PROPELLANT WITH UNCONNECTED PORES

The production of pores in propellant may be accomplished by several methods. While the production without additive ingredients is desirable, additives which do not alter the physical or chemical nature of the propellant are acceptable.

Propellants containing 5 to 13% pore volume can be produced by mechanical means alone. Propellants with pore volumes to 23% can be produced with the addition of additives.

### Mechanical Techniques

#### Gas Aeration of Binder

Cowles Dissolver Techniques. The Cowles dissolver is a motor-driven blade creating a very high shear at its peripheral edge. If a gas is supplied to this edge the blade teeth will incorporate small bubbles into the liquid surrounding the blade. This

technique was used to produce foams for propellant study. A study was made of the effect of Cowles dissolver blade speed during premix mixing on the pore volume of the propellant made from the premix. Table XXXVIII indicates that a slight increase in pore volume is obtained at speeds of 3400 rpm and above. Indication of incomplete mixing at 2000 rpm led to a higher standard speed of 4900 rpm.

Table XXXVIII. The Effect of Cowles Dissolver Speed.

| Premix Technique | Casting Vacuum (in. Hg) | Cure Temp (°F) | Propellant Density (gm/ml) | Pore Volume (%) |
|---|---|---|---|---|
| Cowles dissolve all ingredients except oxidizer at 5400 rpm | No vacuum | 110 | 1.6357 | 5.6 |
| Cowles dissolve all ingredients except oxidizer at 3400 rpm | No vacuum | 110 | 1.6362 | 5.5 |
| Cowles dissolve all ingredients except oxidizer at 2000 rpm | No vacuum | 110 | 1.6413 | 5.1 |

A second study was undertaken to determine if the use of the complete binder technique, combining all liquid ingredients including the catalyst with aluminum into a complete premix, would give more pore volume than a separate catalyst addition. Table XXXIX indicates that no effect was found on a 10-lb scale. Results, discussed later, on 60-lb batches indicated an effect did exist.

A vortex must be formed in the premix during Cowles dissolving which will allow gas to be drawn to the periphery of the blade. When the diameter of the blade is slightly less than the diameter of the Cowles vessel and the height of the vessel is twice its diameter, good aeration results.

In order to scale up from 10-lb to 60-lb batches it was necessary to duplicate the Cowles dissolving technique used in the 10-lb size. The Cowles speed of the blade is given by multiplying $\pi D$ times the shaft speed, where D is the diameter of the blade.

Table XXXIX. The Effect of Cowles Dissolver and Aeration Technique.

| Premix or Mixing Technique | Casting Vacuum (in. Hg) | Cure Temp (°F) | Propellant Density (gm/ml) | Pore Volume (%) |
|---|---|---|---|---|
| Cowles dissolve all ingredients except DER and oxidizer | No vaccum | 110 | 1.6382 | 5.4 |
| | 25 | 110 | 1.6754 | 3.3 |
| | 25 | 135 | 1.6852 | 2.7 |
| | 25 | 150 | 1.6928 | 2.2 |
| Cowles dissolve all ingredients except oxidizer | No vacuum | 110 | 1.6478 | 4.9 |
| | 25 | 110 | 1.6823 | 2.9 |
| | 25 | 135 | 1.7190 | 0.8 |
| | 25 | 150 | 1.7185 | 0.9 |
| Cowles dissolve all ingredients except DER and oxidizer. Aerate in the mixer with $N_2$ for 30 min at 20 gas flow meter units | No vacuum | 110 | 1.6477 | 4.9 |
| | 25 | 110 | 1.7215 | 0.7 |
| | 25 | 135 | 1.7187 | 0.8 |
| | 25 | 150 | 1.7199 | 0.7 |
| Cowles dissolve all ingredients except oxidizer. Aerate in the mixer with $N_2$ for 30 min at 20 gas flow meter units | No vacuum | 110 | 1.6396 | 5.3 |
| | 25 | 110 | 1.7188 | 0.8 |
| | 25 | 135 | 1.7213 | 0.6 |
| | 25 | 150 | 1.7249 | 0.4 |

The peripheral speed of a 3-in.-diameter blade rotating at 4900 rpm is equivalent to a 6-in. blade rotating at 2450 rpm.

Nitrogen Entrainment. In order to prepare foams of ANB-3226 binder the viscosity of this binder was determined (Figure 63) with a Haake Rotoviscometer at several temperatures at and above ambient. The lower viscosities at elevated temperatures allowed the production of foams with smaller bubbles than at ambient. The foam was produced by aerating the binder with dry nitrogen through a gas flow meter and orifice. Foam produced at 80°F contained bubbles approximately 1mm in diameter while that produced at 140°F contained significantly smaller bubbles. The propellant prepared from this foam had pores of 1mm and 0.1mm, respectively.

Gas flow studies shown in Table XL indicate no effect on the pore volume due to a change in gas-flow rate in the range of 10 to 55 ml/sec.

Premix and Mixing Cycle Sequence

The normal mode of mixing is the preparation of a submix and charging it into the mixer, followed by a dry aluminum addition, then a catalyst addition, followed by an oxidizer addition. This allows bubbles in the less viscous submix to coalesce during aluminum and catalyst additions. Table XLI shows that no improvement occurred with the elimination of these steps, indicating the need for a premixing or complete-binder technique.

A complete-binder technique involves the Cowles dissolving of all binder ingredients including the catalyst with the aluminum so that the only mixing step required in the mixer is the addition of oxidizer. Table XLII indicates that this technique and additional bubbling of nitrogen through the premix in the mixer (which may have served to further coalesce the bubbles) did not improve the pore volume in 10-lb batches.

The complete-binder technique requires the use of a Cowles pot with adequate cooling capacity to prevent exothermic reaction between the catalyst and other binder ingredients. One 60-lb batch was produced before the cooling coils could be added to the Cowles pot. Consequently the catalyst (DER-322, the diepoxide curing agent) was not added to this batch. During the catalyst-addition cycle of the mixing an undue amount of coalescing and defoaming was noted in the mixer. Subsequent batches were mixed with the complete binder technique and mixing in the mixer began with the oxidizer addition. Table XLII shows the improvement in the percent pore volume resulting from the use of this technique.

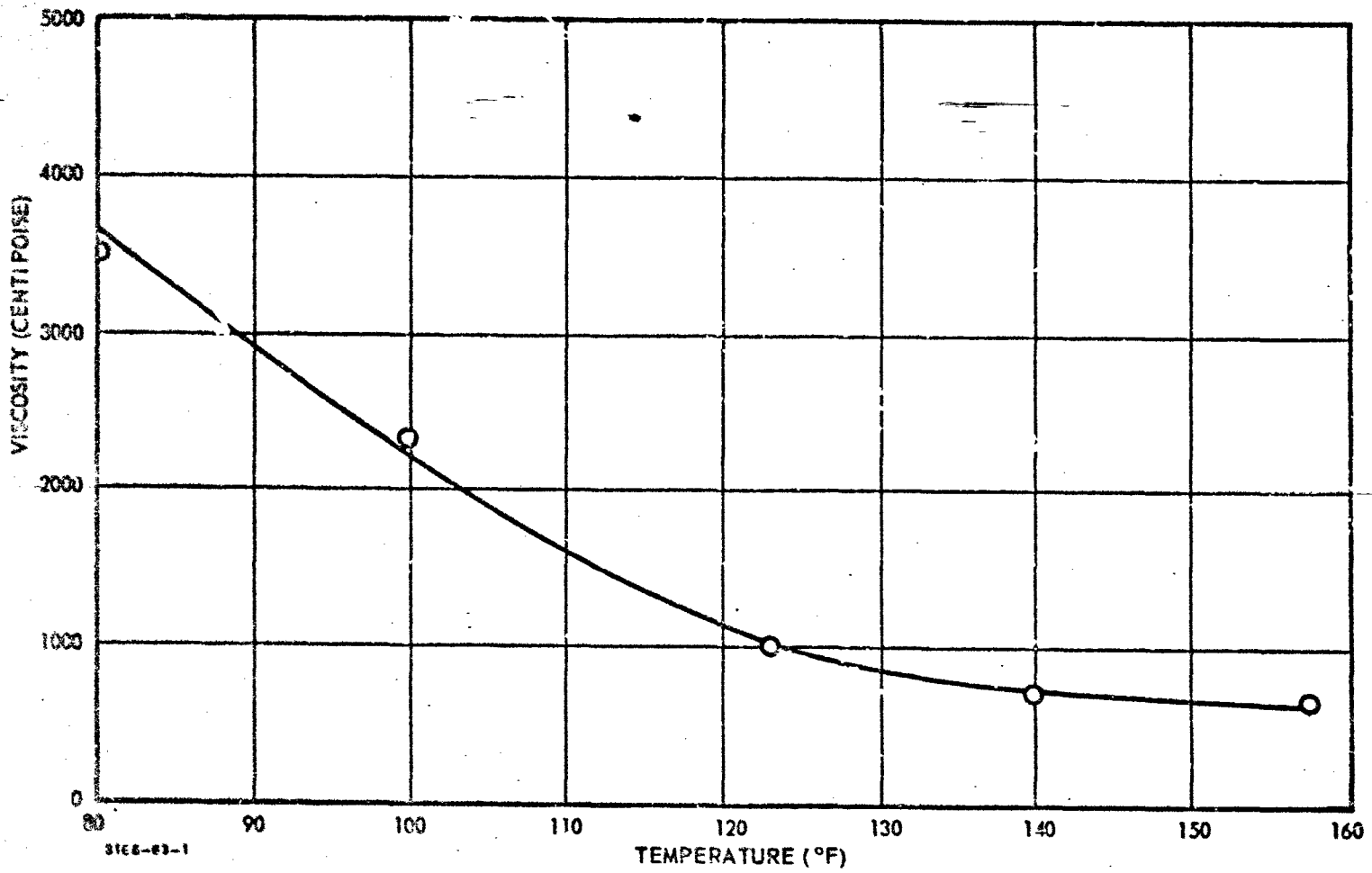


Figure 63. The Effect of Temperature on the Viscosity of ANB-3226 Binder.

Table XL. The Solid Density of ANB-3226 Propellant Prepared from Aerated Binder with Various Aeration Methods.

| Set* | Batch No. | Binder Temp During Aeration (°F) | Gas Flow Rate Flowmeter Units | Cure Temperature (°F) | Propellant Solid Densities (gm/ml) | Average | Pore Volume (%) |
|---|---|---|---|---|---|---|---|
| 1 | 6416 | 140 | 10 | 110 | 1.6305 | | |
| | | 140 | 10 | 135 | 1.6371 | 1.6361 | 5.5 |
| | | 140 | 10 | 150 | 1.6406 | | |
| | 6417 | 77 | 10 | 110 | 1.6484 | | |
| | | 77 | 10 | 135 | 1.6589 | 1.6545 | 4.5 |
| | | 77 | 10 | 150 | 1.6601 | | |
| 2 | 6613 | 140 | 10 | 110 | 1.6477 | | |
| | | 140 | 10 | 135 | 1.6533 | 1.6522 | 4.8 |
| | | 140 | 10 | 150 | 1.6556 | | |
| | 6614 | 140 | 10 | 110 | 1.6464 | | |
| | | 140 | 10 | 135 | 1.6532 | 1.6501 | 4.5 |
| | | 140 | 10 | 150 | 1.6507 | | |
| | 6534 | 77 | 20 | 110 | 1.6457 | | |
| | | 77 | 20 | 135 | 1.6573 | 1.6537 | 4.8 |
| | | 77 | 20 | 150 | 1.6571 | | |
| | 6535 | 77 | 5 | 110 | 1.6426 | | |
| | | 77 | 5 | 135 | 1.6496 | 1.6495 | 4.5 |
| | | 77 | 5 | 150 | 1.6564 | | |

*Set 1 samples cast without vibration.
Set 2 samples vibrated after casting.

Table XLI. The Effect of Mixing Conditions.

| Batch No. | Change in Mixing Conditions | Cure Temp (°F) | Propellant Density (gm/ml) | Pore Volume (%) |
|---|---|---|---|---|
| 1 | Control | 110 | 1.6340 | 5.7 |
| | Control | 135 | 1.6483 | 4.8 |
| | Control | 150 | 1.6523 | 4.6 |
| 2 | Same as Control except Al is added with DER. | 110 | 1.6441 | 5.1 |
| | Same as Control except Al is added with DER. | 135 | 1.6512 | 4.6 |
| | Same as Control except Al is addded with DER. | 150 | 1.6530 | 4.5 |
| 3 | Same as Batch 2 except new submix and new day of mixing is involved. | 110 | 1.6309 | 5.8 |
| | Same as Batch 2 except new submix and new day of mixing is involved. | 135 | 1.6411 | 5.2 |
| | Same as Batch 2 except new submix and new day of mixing is involved. | 150 | 1.6581 | 3.0 |

Table XLII. Effect of Mixing Technique on 60-lb Batches of ANB 3226 Propellant.

| Mixing Technique | Cure Temp (°F) | Casting Vacuum (in. Hg) | Curing Vacuum (in. Hg) | Pore Volume (%) |
|---|---|---|---|---|
| Cowles dissolve premix without DER-332 | 110 | None | None | 7.9 |
| Cowles dissolve premix with DER-332 | 110 | None | None | 11.9 |
| Cowles dissolve premix with DER-332 and addition of chloroform | 110 | None | None | 14.6 |

### Dissolving of Gaseous Nitrogen Under Pressure

ANB-3226 binder was subjected to nitrogen pressure at 3000 psig for time periods of 3 to 24 hr and 325 psig for 22 hr. The data in Table XLIII and Figure 64 indicate that at 3000 psig the nitrogen dissolves into the binder in 3 hr and produces pores in the resulting propellant. These pores are smaller and of a more uniform distribution than those produced by Cowles dissolving. At 325 psig the pore formation is similar but slightly less than at 3000 psig.

Propellant was also mixed in the normal manner (Cowles dissolve technique) and then the uncured propellant exposed to 3000 psig nitrogen 16 hr prior to cure. The effect of the treatment was to increase the pore-volume content of the uncured propellant to 11.7 to 13.6%, compared to 7.0 to 9.3% for the untreated control.

## Addition of Additive Material

### Foaming Agents

Physical (Phase Change). Several foaming or blowing agents were used to produce gas or vapor in the propellant for the purpose of increasing the pore formation. These agents were of two types: those undergoing a phase change from a liquid to a vapor (chloroform, methyl chloroform, and Freon TF), and those which either react or decompose to form a gas (toluene di-isocyanate/water and hydroxylamine acid sulfate). The first type is more feasible since the blowing effect can be more readily controlled by the vacuum and temperature conditions of the mixing, casting, and curing process.

Chloroform was incorporated at 2 and 4 wt % of the binder. The effects on the pore content when the propellant was cast and cured under different conditions of temperature and pressure are shown in Table XLIV. A slight improvement over the control prepared by the Cowles dissolver technique (14.9% vs 13.4% pore content) was observed when propellant containing 4 wt % chloroform was cured at 110°F under atmospheric pressure. Curing at 150°F showed no increase in pore content. Casting and curing under vacuum conditions caused a decrease in porosity as compared to the control, except when vacuum cure was delayed until the propellant was partially cured. This resulted in an increase in porosity to 23.2%. Table XLIV also shows the blowing effect due to chloroform.

Table XLIII. Effect of Dissolved Nitrogen, in ANB-3226 Binder, on Pore Formation.

| Time Binder Under 3000 psi (hr) | Cure Temperature (°F) | Casting Vacuum (in. Hg) | Curing Vacuum (in. Hg) | Pore Volume (%) |
|---|---|---|---|---|
| 0, Control | 110 | None | None | 13.4 |
| 24 | 110 | None | None | 12.1 |
| 15 | 110 | None | None | 12.5 |
| 12 | 110 | None | None | 14.0 |
| 3 | 110 | None | None | 13.3 |
| 22* | 110 | None | None | 9.4 |
| 24 | 150 | None | None | 12.7 |
| 15 | 150 | None | None | 11.5 |
| 12 | 150 | None | None | 13.0 |
| 3 | 150 | None | None | 13.1 |
| 22* | 150 | None | None | 10.8 |
| 24 | 110 | 15 | 15 | 9.5 |
| 15 | 110 | 15 | 15 | 7.0 |
| 12 | 110 | 10 | 10 | 8.8 |
| 3 | 110 | 10 | 10 | 11.4 |
| 22* | 110 | None | 10 | 15.2 |
| 24 | 150 | 15 | 15 | 15.3 |
| 15 | 150 | 15 | 15 | 15.1 |
| 12 | 150 | 10 | 10 | 7.7 |
| 3 | 150 | 10 | 10 | 8.2 |
| 22* | 150 | None | 10† | 19.6 |

* This binder held at 325 psig

† After curing 24 hr without vacuum

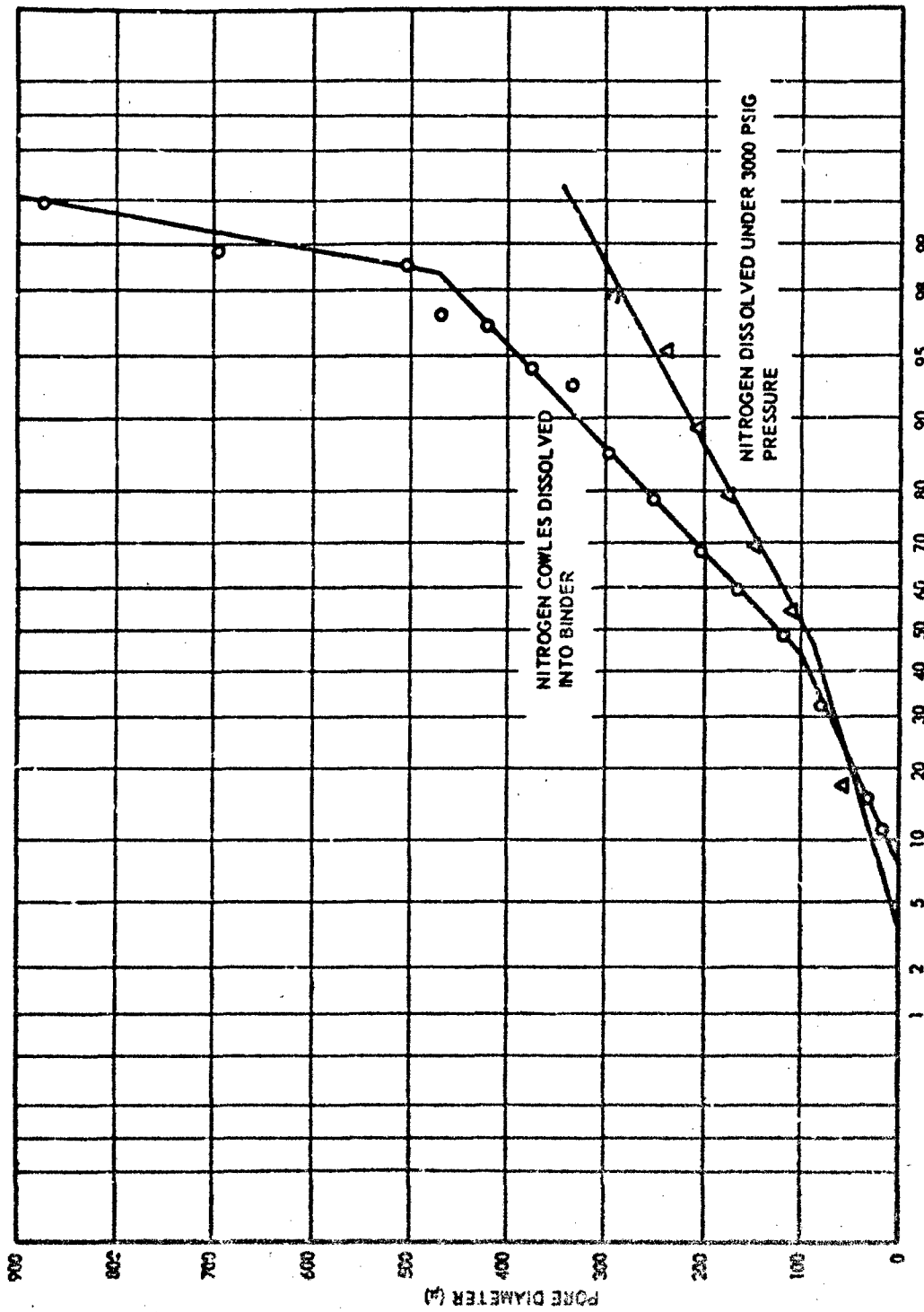


Figure 64. Distributions of Pore Diameters.

Table XLIV. The Effect of Chloroform on Pore Formation.

| Chloroform (Wt % of Binder) | Cure Temperature (°F) | Casting Vacuum (in. Hg) | Curing Vacuum (in. Hg) | Pore Volume (%) |
|---|---|---|---|---|
| 0, Control | 110* | None | None | 13.4 |
| 2 | 110* | None | None | 14.1 |
| 4 | 110* | None | None | 14.9 |
| 4† | 110* | None | None | 14.6 |
| 2 | 110* | 15 | None | 9.7 |
| 4 | 110* | 15 | 15** | 11.1 |
| 4† | 110* | 15 (approx) | None | 15.6 |
| 2 | 150 | None | None | 13.0 |
| 4 | 150 | None | None | 14.1 |
| 4† | 150 | None | 15†† | 23.2 |
| 2 | 150 | 15 | None | 5.9 |
| 4 | 150 | 15 | 15** | 11.8 |

* Cure 1 week at 110°F followed by 1 week at 135°F.

† Sixty-lb batch, others 10-lb batches.

** The propellant surface rose and bubbled over during vacuum cure.

†† After a delay of 24 hr at ambient pressure 15 in. Hg vacuum was applied.

Propellant containing Freon-TF (a duPont fluorocarbon) and methyl chloroform (4 wt % of binder) was mixed in a similar fashion and the resulting data are listed in Table XLV. Where indicated the propellant was cured at 110°F for 24 and 48 hr under atmospheric pressure prior to vacuum cure. Neither of these two blowing agents was as effective as chloroform in causing pore formation.

Table XLV. The Effect of Freon-TF and Methyl Chloroform on Pore Formation.

| Ingredient* | Cure Temp (°F) | Casting Vacuum (in. Hg) | Curing Vacuum (in. Hg) | Pore Volume (%) |
|---|---|---|---|---|
| Control | 110 | None | None | 13.4 |
| Freon-TF | 110 | None | None | 13.0 |
| Freon-TF | 110 | None | 5 | 10.1 |
| Freon-TF | 110 | None | 5† | 10.5 |
| Freon-TF | 110 | None | 10 | 10.0 |
| Methyl Chloroform | 110 | None | None | 12.4 |
| Methyl Chloroform | 150 | 10 | 5 | 9.0 |
| Methyl Chloroform | 110 | 10 | 10† | 11.6 |
| Methyl Chloroform | 110 | 10 | 10** | 10.6 |

* 4 wt % of binder
† After 24 hr at atmospheric pressure
** After 48 hr at atmospheric pressure

Chemical Decomposition. Decomposition of additives to form gases is another method of blowing a foam. Since decompositions are accompanied by exotherms, each system was investigated before use in propellant systems.

These hydroxylamine acid sulfate and toluene di-isocyanate/water systems were investigated as blowing agents in this study. The TDI/$H_2O$ combination forms $CO_2$ gas while the hydroxylamine acid sulfate reaction with Paracril generates nitrogen decomposition products.

Neither toluene di-isocyanate ($TDI/H_2O$) nor hydroxylamine acid sulfate was effective as a blowing agent at the levels used: 0.05 and 0.1 wt % of propellant for $TDI/H_2O$; and 0.05, 0.1, and 0.2 milliequivalents hydroxylamine acid sulfate per gram of Paracril in the binder. At the 0.2 meq/g level the hydroxylamine acid sulfate shortens the pot life to the extent that the batch is uncastable.

### Surface Active Agent

In normal production of ANB-3226 propellant, DC-200 (a Dow-Corning surface-active agent) is added to this formulation to aid in the removal of pores during vacuum mixing. Removal of DC-200 from the formulation improves the production of pores.

## Discussion

### Casting of Propellant

When propellant is cast without vacuum, entrapment of air produces large irregular casting pores. Vibration assists in the removal of these pores without markedly affecting the micropore content.

Large castings cannot be produced free of casting pores when vibration alone is used. Therefore it is desirable to determine the highest possible vacuum that will not destroy the micropores created in the propellant, but which will prevent casting pores. ANB-3226 propellant was cast under vacuum, which was varied from 10 to 29 in. of mercury, to determine the optimum conditions. The effect of the vacuum casting conditions on the pore content of the propellant is shown in Figure 65. The percent pore content remaining under testing conditions was determined as follows:

$$\frac{\text{Pore Content After Vacuum Casting}}{\text{Pore Content After Ambient Pressure Casting}} \times 100$$

These data indicate that a vacuum level of 10 in. of mercury or less does not appreciably affect the micropore content. However, it was noted that the large casting pores are not removed at this vacuum level, and the distribution and size of the pores were unsatisfactory for the program requirements. It is possible that vibration during casting would improve this condition.

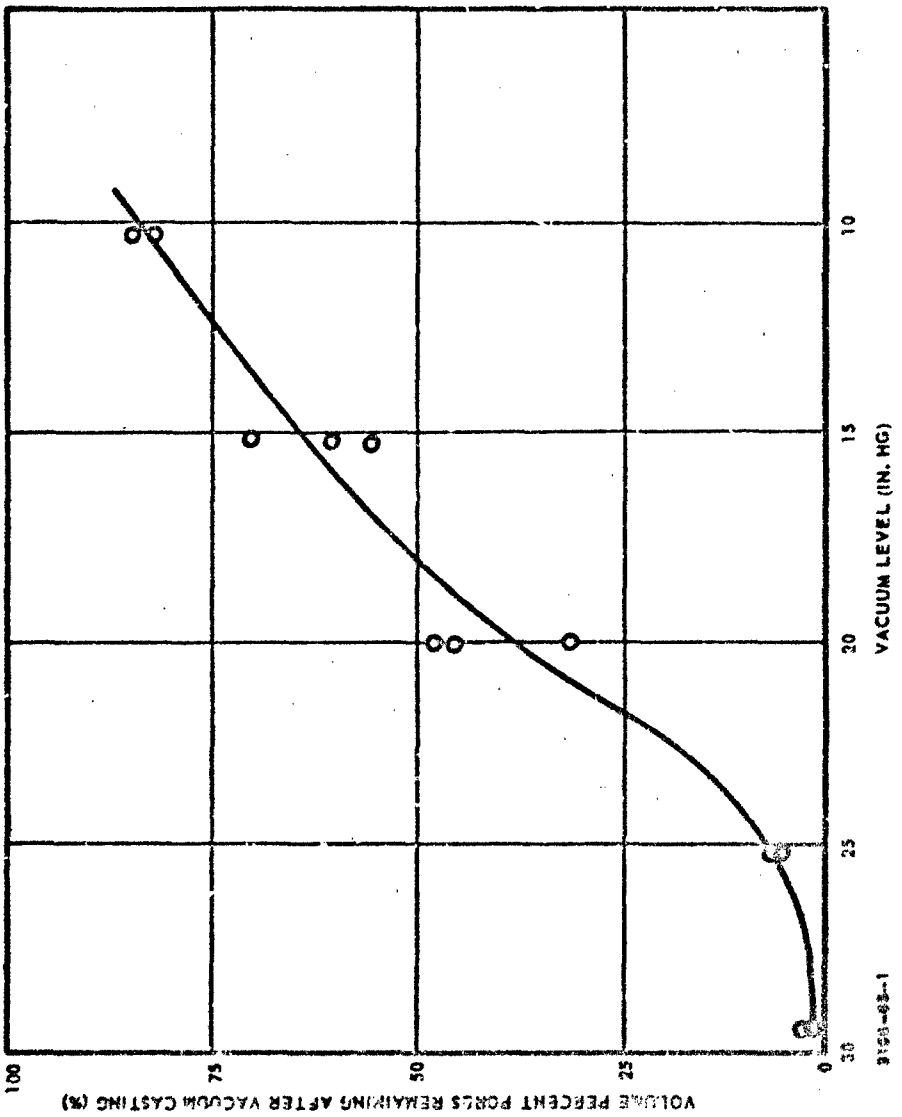


Figure 65. The Effect of Vacuum Level During Casting on Pore Formation.

Propellant Cure

Because of the P-V relationship that must be obeyed by gas pores in an uncured propellant matrix, curing at elevated temperature and negative and positive pressure should give variations in the pore volume of propellant. Propellant cured at 110° (followed by 135°F cure), 135°, and 150°F, under vacuum conditions, loses pore volume if not preceded by partial cure of the propellant before vacuum cure is begun. This is shown in Table XLVI.

Table XLVI. The Effect of Delay in the Vacuum Cure of ANB-3226 Propellant.

| Batch No. | Hours Delay Before Start of Vacuum | Cure Temperature (°F) | Curing Vacuum (in. Hg) | Pore Volume (%) |
|---|---|---|---|---|
| 1 | 0 | 110 | None | 7.9 |
| 1 | 0 | 110 | 10 | 5.9 |
| 1 | 24 | 110 | 10 | 7.9 |
| 2 | 0 | 110 | None | 11.9 |
| 2 | 0 | 110 | 15 | 9.2 |
| 2 | 0 | 150 | None | 11.1 |
| 2 | 48 | 150 | 15 | 14.2 |

When propellant containing micropores is cured under positive pressure the pore volume is reduced and the pore diameter distribution is lowered.

Propellant containing approximately 14% pore volume at ambient pressure was cured under pressures of 25, 50, and 87 psig at 150°F. The effect on pore volume shown in Figure 66 is the hyperbolic function expected from a P-V relationship. Propellant cured at 87 psig cracked at the propellant pore interfaces when the pressure was released to atmospheric pressure.

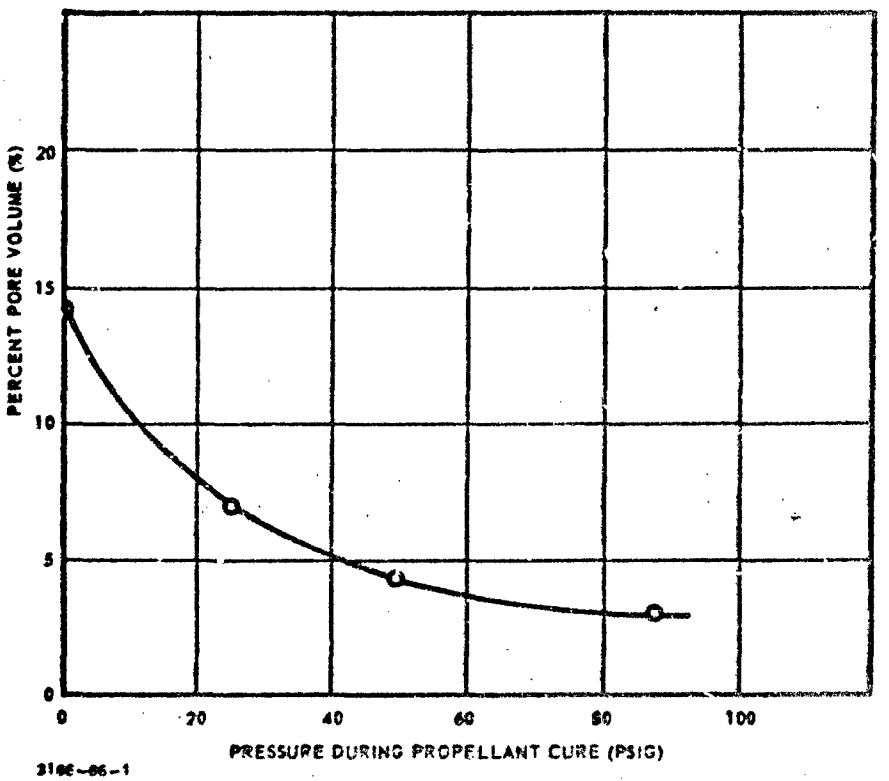


Figure 66. The Effect of Pressure Cure on ANB-3226 Propellant Containing Micropores.

## PRODUCTION OF CONNECTED VOIDS

### Casting Onto Honeycomb

Voids are connected pores, or cracks, within the propellant matrix that form channels throughout the propellant. One method of obtaining a partial channeling is to cast propellant upon two layers of honeycomb and remove the honeycombs after the propellant has been cured. This propellant can be cut in circles and packed into a cylinder for surface area measurements. Several experimental samples were cast with S-122 (a fluorocarbon release agent) and 190°F wax-coated aluminum honeycomb. S-122-coated honeycomb would not release and 190°F wax-coated honeycomb released only with difficulty. Aluminum honeycomb does not have the necessary strength to maintain structural integrity during the removal operation. However, this method could be used with the proper modification to produce large quantities of acceptable propellant.

### Fracture by Pressure Differential

Attempts to produce channels by shattering propellant samples (with and without unconnected pores) with gas pressure yielded negative results. The propellant was placed under 1800 to 2200 psig of nitrogen pressure and released instantaneously. Propellant not containing pores remained unchanged. Propellant containing pores increased in size by 25% but failed to shatter.

### Fracture by Thermal Shock

Small cylinders of propellant were shattered into smaller pieces by thermal shock when treated three times with liquid nitrogen and allowed to return to ambient temperature between each treatment.

## SECTION IX

## CHARACTERIZATION OF DEFECTIVE PROPELLANT

### PORE VOLUME MEASUREMENT

The principal technique for measurement of pore volume for this program made use of the standard density measurement with a large propellant sample. A comparison of the weight in air and the weight in oil yields the density, which is converted into the percent pore volume in the propellant by comparing it to the density of propellant without pores according to the following equation:

$$\text{Percent Pore Volume} = \frac{1.7340 - (\text{Density of Propellant with Pores})}{1.7340} \times 100 \qquad (107)$$

The sample reproducibility is within ± 0.1% pore volume, between slabs within the same carton. Greater accuracy is possible with more homogeneous samples.

The line intercept method is used on a thin section under a microscope and consists of measuring along a random line in the sample the ratios of chord lengths intersected in the pores to the total length of the line transversed.

Using the above techniques, percent pore volumes were determined on Cowles dissolved and nitrogen pressure dissolved samples with the following results:

Percent Pore Volume Determination

| Sample | Analytical Technique for % Pore Volume Displacement | Microscopic Planimetric |
|---|---|---|
| Cowles Dissolved | 12.5 | 11.4 |
| Nitrogen Pressure Dissolved | 13.3 | 13.3 |

### PORE DIAMETER DISTRIBUTION

In studying pores in thin sections of propellant at high magnification it was noted that the walls of the pores passing through the thin section were cusped up or down and a few walls were vertical. From the geometry of these pores it is apparent that

cusped walls are formed by minor circles in a sphere and the vertical walls are from a great circle. The pores that do not pass through the section always give great circle projections. Thus by scanning the thin section and measuring the diameter of the pores with great circles, the pore-size distribution can be recorded. These pore diameters can be reduced statistically and plotted as a distribution on normal probability paper. A complete discussion of the line-intercept and planimetric methods is presented in Appendix VI.

Two samples of pore-diameter distributions are shown in Figure 64. One propellant sample was prepared with binder mixed by the Cowles dissolving technique and one with binder which had nitrogen dissolved in it at 3000 psig pressure. The difference in slopes of the pore-diameter distributions is readily apparent. The propellant produced with a binder that had nitrogen dissolved in it under pressure had significantly smaller pores and a narrower pore-size distribution than that produced with a binder mixed by Cowles dissolving.

Propellant samples cured under pressures of 25, 50, and 87 psig undergo the expected reduction in pore volume as shown in Figure 66. Pore-diameter distributions are shown in Figure 67. No pores of less than 90 μ were found on microscopic examination. The sample cured at 87 psig had too few pores to make a distribution count. Its position on this graph was calculated from the pore volume data in Figure 66, and is shown as a dotted line. It can be seen that very little pore distribution lies above 90 μ, thus accounting for the few pores found in this sample. No explanation can be given for the lack of pores below 90 μ size. However, the absence of small pores at a threshold value and the lower slope may make this sample of more interest in detonation studies.

## MEASUREMENT OF SURFACE AREA

Surface area measurements can be made by adsorption of vapor onto the surface of the propellant. The apparatus used is shown in Figures 68 and 69.

The sample chamber and remaining system volumes are determined by using the gas burette and the pressure gauge. The system is evacuated with a vacuum pump, and the sample chamber is closed off. Gas is admitted to the remainder of the system and the gas burette until a pressure P is reached. The sample chamber is opened and the gas pressure is restored to P by mercury displacement, using the gas burette.

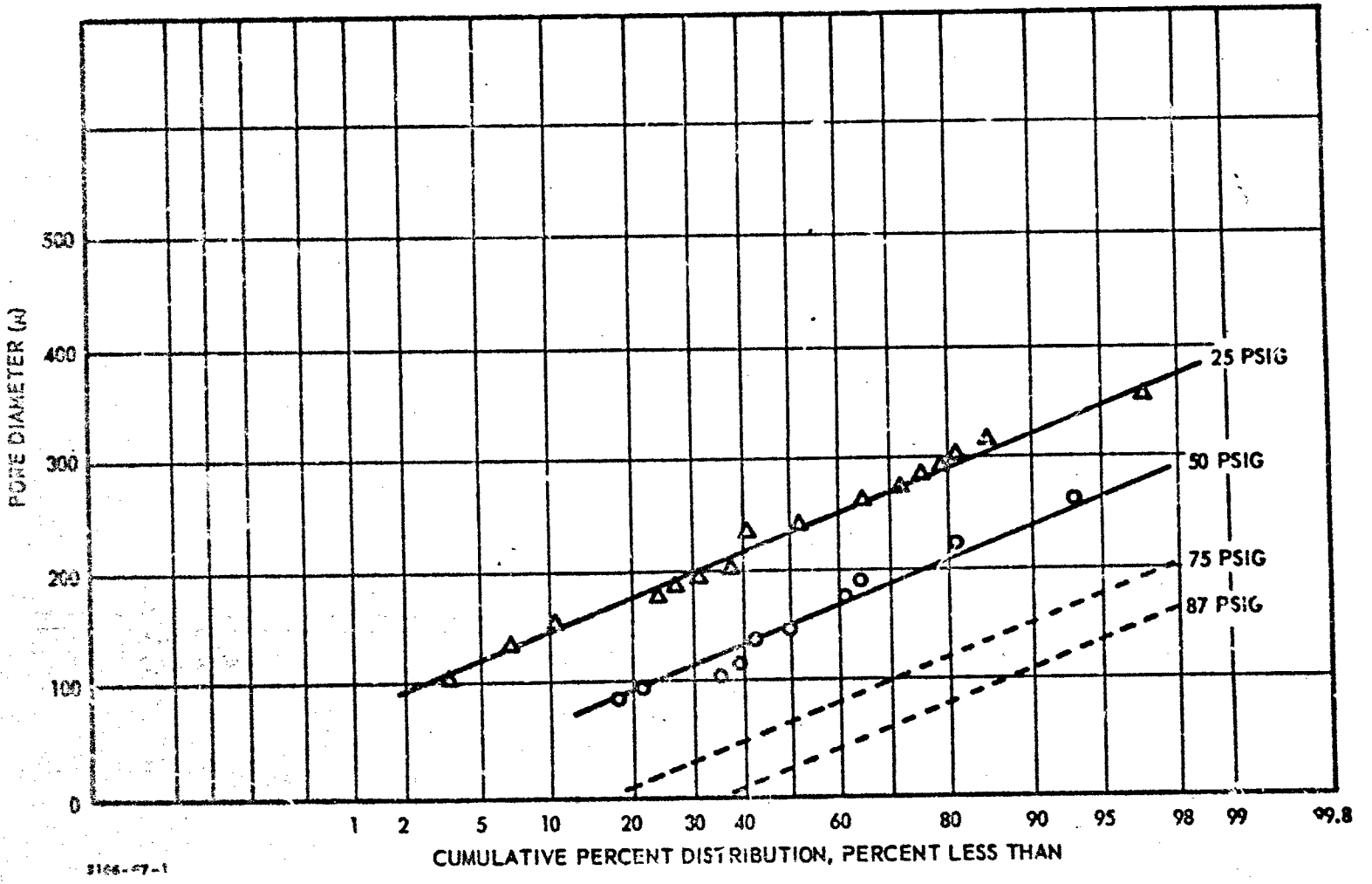


Figure 67. Distributions of Pore Diameters in ANB-3226 Propellant Cured Under Pressure.

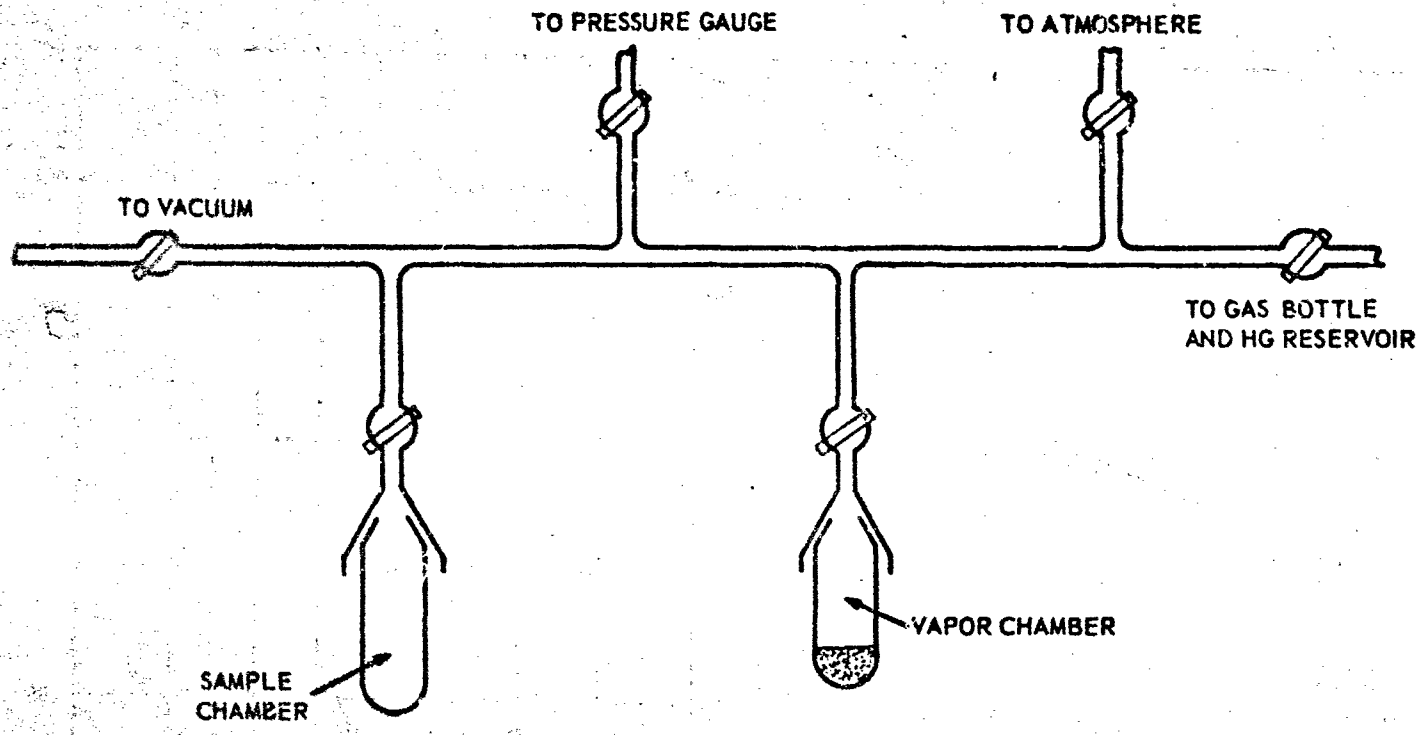




Figure 68. Apparatus for Surface Area Determination.

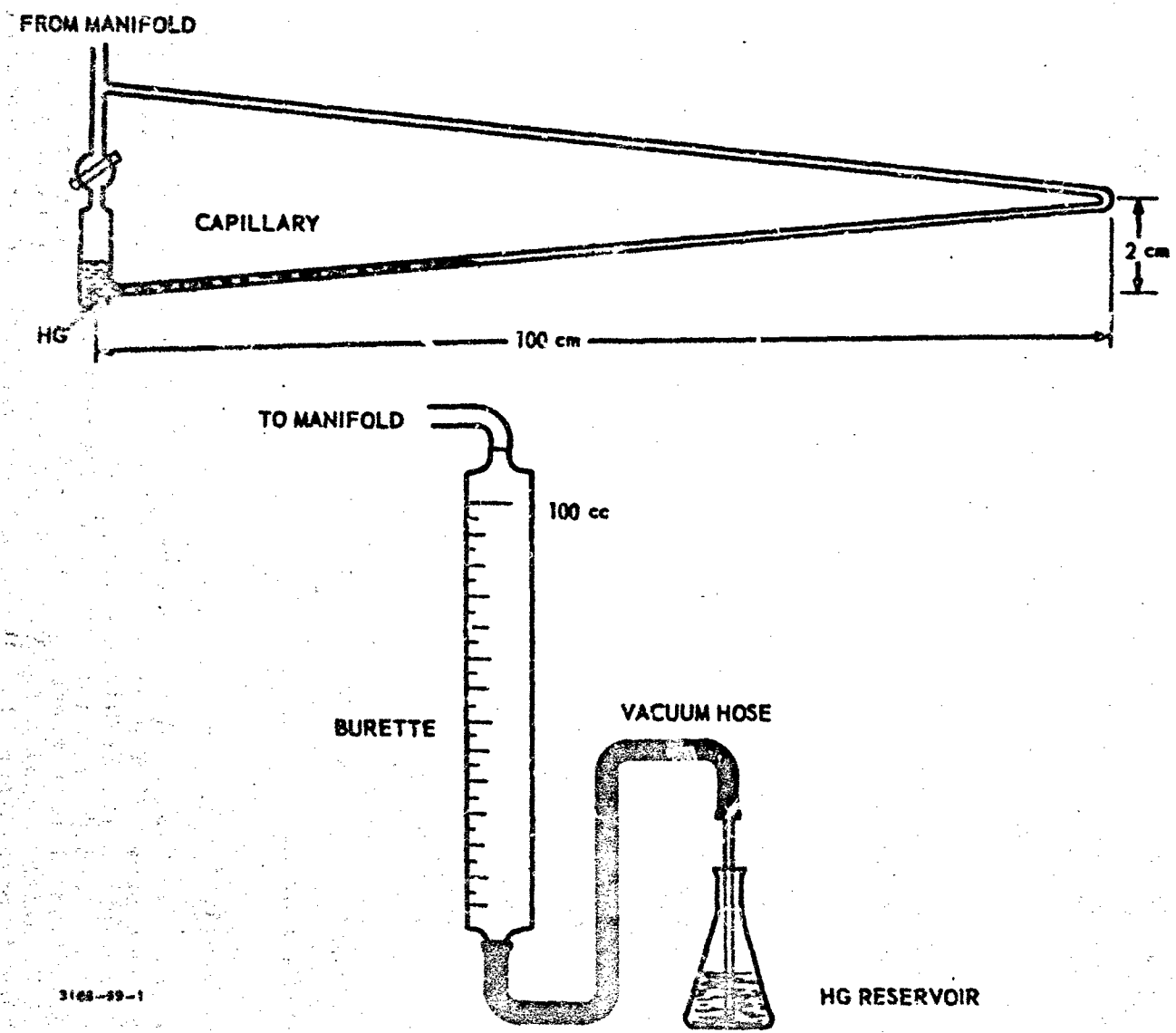


Figure 69. Inclined-Tube Pressure Gauge.

A propellant sample is loaded into the sample chamber and the system is pumped down to 0.1mm Hg pressure. The sample chamber is sealed off and vapor admitted to the system at $P_1$ and $V_1$. When equilibrium is reached, the sample chamber is opened to the system and the new pressure $P_2$ (for volume $V_2$) is obtained. The $\Delta$ PV is calculated by

$$\Delta PV = P_1V_1 - P_2 (V_2 - V_s) \qquad (108)$$

Where:

P = Pressure, mm Hg

V = Volume, cc

$V_s$ = Volume of sample, cc

## Water Vapor

Several attempts were made to utilize water vapor in this adsorption study. The water vapor appears to diffuse slowly into the capillaries in the glass. At pressures that would have given reasonable differentiation, an excess of water vapor was adsorbed during blank runs. Therefore, the use of water vapor was discontinued.

## Toluene Vapor

The measurement of propellant surface area was improved with the use of toluene, and with 3 to 4 repeat measurements on the same sample, adequate resolving power exists. Coefficients of variation have been measured in the 18 to 20% range. Table XLVII lists the parameters found for two samples of cut cubes. These data indicate that a larger $\Delta$ PV was found for samples with a larger surface area.

## CONCLUSIONS

Foams have been produced by several methods, and propellants with percent pore volumes of less than 1 to 23% have been produced. Propellant with the highest pore contents was achieved when chloroform was added as a blowing agent, the complete premix was Cowles dissolved at high speed and the mixed propellant was cured at 150°F under vacuum after ambient pressure curing at 150°F for 24 hr. Pore diameters from 15 $\mu$ to 30 $\mu$ have been detected by microscopic

Table XLVII. Adsorption of Toluene Vapor.

| Sample A -- Cut cubes approximately 6 mm on a side | | |
|---|---|---|
| | Measurement | PV |
| (Measured average area of 20 cubes is 0.240 in.$^2$/cube. There were 80 cubes in Sample A which weighed 17.44 gm. The total cut area exposed of Sample A was 19.2 in.2) | 1 | 360 |
| | 2 | 360 |
| | 3 | 397 |
| | 4 | 250 |
| Mean | | 344 |
| Standard Deviation | | 64 |
| Coefficient of Variation | | 18.5% |

| Sample B -- Cut cubes approximately 2 mm on a side | | |
|---|---|---|
| | Measurement | PV |
| (Measured average area of 20 cubes is 0.015 in.$^2$/cube. There were 2738 cubes in Sample B which weighed 14.8153 gm. The total exposed cut surface area of Sample B was 40.5 in.$^2$) | 1 | 535 |
| | 2 | 440 |
| | 3 | 605 |
| | 4 | 525 |
| Mean | | 521 |
| Standard Deviation | | 66 |
| Coefficient of Variation | | 12.8% |

examination and can be differentiated from spherical aluminum and other particles. Propellants with pore-diameter distributions have been prepared which are within the required range of 0.1 to 1 mm. Propellants with narrow pore-diameter distributions are achieved when nitrogen is added to premix under pressure. Pore diameters and percent pore volumes in propellent have been changed by vacuum and pressure curing. Surface areas measurements have been studied and a method developed which can differentiate surface areas. Propellant with numerous surface channels has been prepared and partially meets the interconnected-voids requirement.

## SECTION X

## REPORTED MISHAPS OF SOLID MOTORS

It is well known that while essentially void-free composite propellant will not propagate a steady-state detonation in diameters of less than 5 or 6 ft, the introduction of only a small amount of porosity drastically lowers the minimum (critical) diameter for detonation. Experience also indicates that random cracks in a propellant grain can serve as paths for propagation of a flame front throughout the grain, and that such internal burning leads to the very rapid generation of exceedingly high pressures with consequent explosion of the motor.

The type and severity of a catastrophic failure resulting from an operational incident with degraded propellant will depend upon the nature and extent of the degradation as well as the type of initiating stimulus. Degradation of the propellant grain can occur through a wide variety of accidents during its storage, transportation, launch, and flight. It was therefore proposed at the inception of this contract that reported mishaps with solid motors be examined to attempt to determine the probable nature of the propellant defects created by a particular type of incident. To aid predictions of the probable extent and nature of fracturing resulting from various operational mishaps, it was further proposed that published investigations of solid propellant fracture mechanisms be examined.

It has not yet been possible to obtain access to actual records of solid rocket motor incidents. Pending the examination of such records, published studies of the potential operational hazards of large solid propellant motors, as well as pertinent references on solid propellant aging and fracture mechanics, have been accumulated for future analysis. Some of the most significant of these reports are listed below:

a. Hazards of Large Solid Propellant Motors


1. Amster, A. B., Hazards Study of Large Solid Propellant Motors (U), Final Report (Confidential), Stanford Research Institute, 28 Sept. 1962.

2. Amster, A. B., R. W. Van Dolah, D. Price, and L. Zernow, "A Proposed Program for the Evaluation of the Explosive Hazards of Titan III." Titan III Explosive Hazards Ad Hoc Committee (1 July 1963).

3. Rattin, E. J., Summary of 1964 Conference on Large Solid Motor Explosion Hazards, (Confidential), Aerospace Corporation (10 November 1964).

4. Settles, J. E., "The Hazard Classification of Missile Propellants in Relation to Explosions, Detonations, and TNT Equivalence," (U), (Confidential); Bulletin of the 20th Interagency Solid Propulsion Meeting (U), Hercules Powder Company (July 1964).

5. McDevitt, J. A., Potential Operational Mishaps of Large Solid Motors, U.S. Naval Propellant Plant, Indian Head, Md (26 January 1966).

6. McDevitt, J. A. and M. F. Zimmer, Problems Involved in Assessing the Explosion Hazards of Very Large Solid Motors, U.S. Naval Propellant Plant, Indian Head, Md; presented at the meeting of the States Section of the Combustion Institute, La Jolla, Calif (April 1967).

b. Fracture Mechanics of Composite Propellants

1. Irwin, Dr. O. R., Susceptability of Solid-Composite Propellants to Explosion or Detonation (U); Aerojet-General Corporation, Program Summary Report 0253-05(02)FP (Confidential) (14 April 1964).

2. Fracture Mechanics of Solid Propellants (U), Eastern Laboratory, E. I. duPont de Nemours Company, Progress Report No. F Lab-A-19 (Confidential) (16 Feb. 1959 - 15 Feb. 1960).

c. Solid-Propellant Aging

1. Harris, C., Development of Nondestructive Testing Techniques for Large Solid-Propellant Rocket Motors, United Technology Corp. Final Report U21-2015-QP-2 (14 Sept. 1962).

2. Meyers, J. L., E. L. Moon, and L. R. Allen, Bibliography of Solid Rocket Component Aging (U) (Confidential), TRW Systems, Redondo Beach, Calif (April 1966).

3. Solid Rocket Structural Integrity Abstracts, edited by R. A. Westmann, Graduate Aeronautical Laboratories, California Institute of Technology; Vol. 2, No. 2 (April 1965); Vol. 2, No. 3 (July 1965); Vol. 2, No. 4 (Oct. 1965).

4. Danziger, L., A. H. Klein, and P. R. Mosher, Monitoring Internal Stresses in Solid-Propellant Motors. U.S. Naval Propellant Plant, Indian Head, Md., Technical Memorandum Report 232 (20 Oct. 1965).

5. Carkey, D. E., Solid Propellant Structural Integrity Investigations: Dynamic Response and Failure Mechanisms (U); Lockheed Propulsion Company, Redlands, Calif., LPC Report No. 667-F, Final Report (Confidential) (Nov. 1965).

## SECTION XI

## BLAST AND FIREBALL CORRELATION

The blast and fireball data that have been gathered from large critical diameter tests in the SOPHY I and SOPHY II projects have been analyzed to determine explicit expressions and correlation coefficients relating their parameters to propellant size, RDX content, test result, etc. The raw data obtained from these tests include peak side-on overpressure, positive impulse, shock wave times-of-arrival, maximum fireball height, maximum fireball diameter, time to maximum fireball height, time to maximum fireball diameter, and total fireball-duration time.

### AIRBLAST DATA

A complete summary of the air blast parameters for the 22 tests that are included in this analysis is given in Appendix X.

#### Analysis of Overpressure Data

Peak side-on overpressure measurements were derived from Kistler transducer measurements taken during 22 of the larger diameter tests. These values were reduced further to determine the propellant-contributed overpressures, both at each Kistler station and at midpoint distances between stations. Midpoint values were calculated using time-of-arrival data and an equation derived from the Rankine-Hugoniot equations:

$$p = \frac{2\gamma}{\gamma + 1} P_o \left( \frac{U^2}{C_o^2} - 1 \right) \qquad (109)$$

where

$p$ = peak overpressure at the shock front
$\gamma$ = ratio of specific heats for air
$P_o$ = test-site atmospheric pressure
$U$ = velocity of shock front
$C_o$ = sound velocity at test site

The propellant-contributed overpressures were determined by substituting the calculated overpressures into the Kingery equation (Reference 26), which expresses TNT overpressure as a function of ground range divided by weight to the 1/3 power. The weight of TNT that would be required to produce the total overpressure measured at each range is determined. The booster weight is subtracted from this apparent TNT weight. The resulting weights and ground ranges are then substituted into the Kingery equation to calculate the propellant-contributed overpressures.

The propellant-contributed overpressures calculated from all tests are pooled, independent of test result. The 530 data points were fit to an equation of the form

$$\ln P = A_o + A_1 \ln \lambda \qquad (110)$$

where

$$\lambda = R/W^{1/3}$$

The resulting equation was

$$\ln P = 7.4228 - 1.9925 \ln \lambda \qquad (111)$$

This fit explained over 96% of the total variation in the data. The average relative error for this fit was 3%. Approximately 50% of the individual relative errors were less than 10%. Figure 70 shows a plot of this equation along with the Kingery equation for TNT. The lines are shown only for overpressures between 0.8 and 400 psi, since this was the range of the measured data.

In order to determine whether or not there was any effect due to test result (go or no go) the data were divided into two groups, and individual fits were made to both the go and no go data.

$$\text{Go's:} \quad \ln P = 7.53 - 2.0113 \ln \lambda \qquad (112a)$$

$$\text{No go's:} \quad \ln P = 7.25 - 1.9961 \ln \lambda \qquad (112b)$$

Both equations explained 96% of the total variation and both had standard errors of estimate of 1.43 psi (0.36 with respect to ln P). Obviously the test result has no measurable effect on the overpressure.

Propellant TNT-equivalence is given by the cube of the ratio of the $\lambda$ for propellant to the $\lambda$ for TNT at any given overpressure level. Figure 70 shows the propellant curve to be almost uniformly

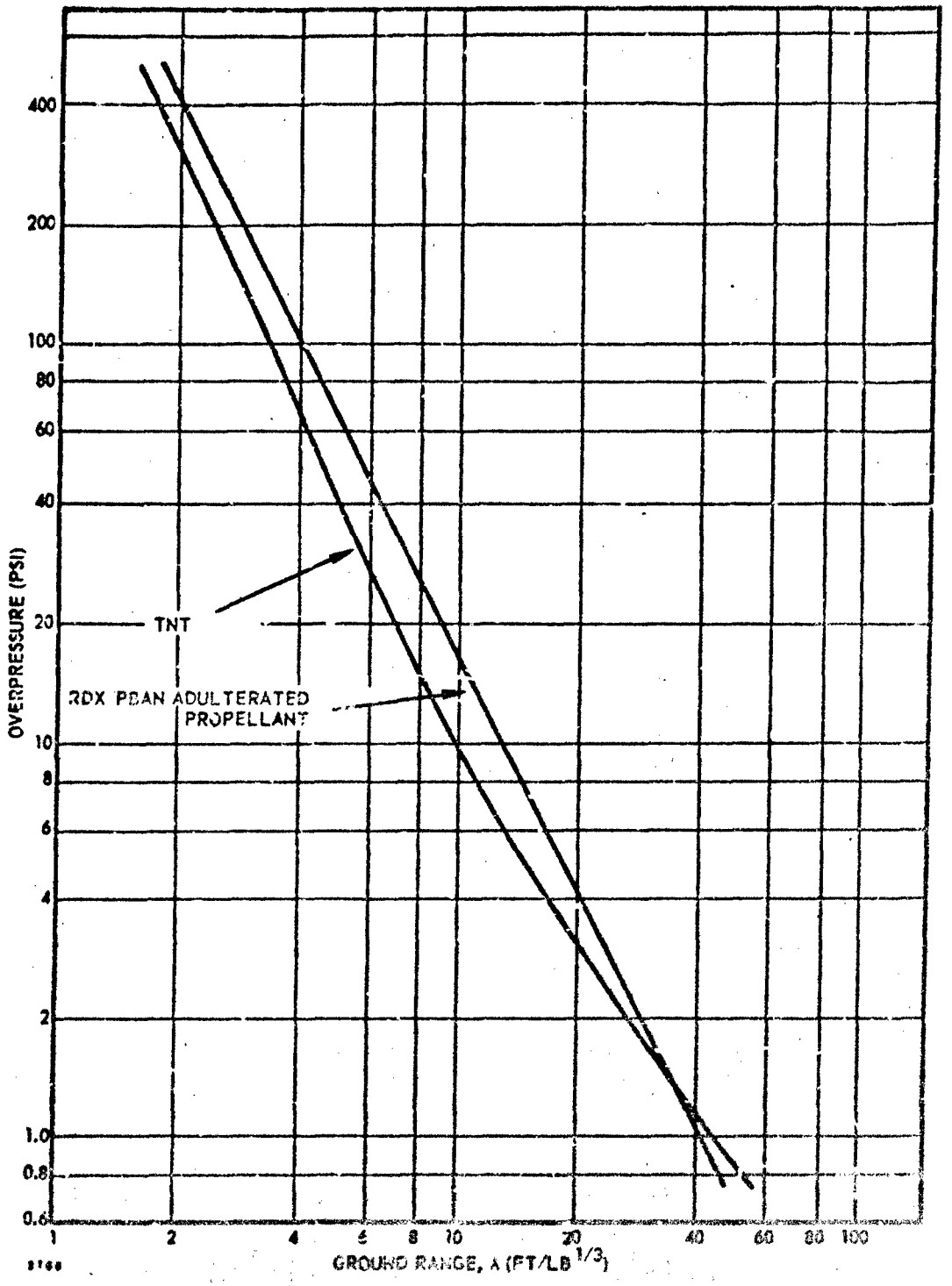


Figure 70. Peak Overpressure vs Scaled Distance, TNT and RDX-Adulterated PBAN Propellants.

greater than the TNT curve except for low overpressure values. At P equal to 200 psi, the TNT equivalence is 173%; at P equal to 50 psi, the TNT equivalence is 200%; and at P equal to 10 psi, the TNT equivalence is 220%. The average TNT equivalence is approximately 197% over the entire range of overpressures.

## Analysis of Impulse Data

For each of the 22 tests for which blast-wave parameters are recorded, impulse calculations were made at each of the Kistler stations. These calculations are made by integrating the side-on overpressure with respect to time. The propellant-contributed impulses are determined using a procedure similar to that used to determine the propellant-contributed overpressures. The TNT base equation was determined using data given in Reference 27. These data indicate a linear relationship when $\ln (I/W^{1/3})$ is plotted vs $\ln (R/W^{1/3})$. This linear equation is

$$\ln\left(\frac{I}{W^{1/3}}\right) = 4.17 - 0.9547 \ln\left(\frac{R}{W^{1/3}}\right), \text{ or} \qquad (113)$$

$$I = 64.8\, W^{0.6515}\, R^{-0.9547} \qquad (114)$$

As in the case for the overpressure data, all propellant-contributed impulses were pooled, independent of test result, and the 148 data points were fit to a function of the same form as that given for TNT. The resulting equation is:

$$\ln\left(\frac{I}{W^{1/3}}\right) = 4.09 - 0.869 \ln\left(\frac{R}{W^{1/3}}\right) \qquad (115)$$

This fit accounted for 69% of the total variation. The average relative error for this fit was 3%, with 42% of the individual relative errors being less than 10%. Figure 71 shows a plot of this equation along with the corresponding equation for TNT. The maximum and minimum measured values for propellant-contributed impulse were 55 and 1.84 psi-μsec, respectively. (The maximum and minimum measured values, in terms of $I/W^{1/3}$ were 19.9 and 0.28.)

As in the case for the overpressure data, the impulse data were divided into two categories, go's and no go's. Individual fits were made to both sets. These equations were estimated as

$$\text{go's:} \quad \ln\left(\frac{I}{W^{1/3}}\right) = 3.71 - 0.717 \ln\left(\frac{R}{W^{1/3}}\right) \qquad (116)$$

$$\text{no go's:} \quad \ln\left(\frac{I}{W^{1/3}}\right) = 4.25 - 0.953 \ln\left(\frac{R}{W^{1/3}}\right) \qquad (117)$$

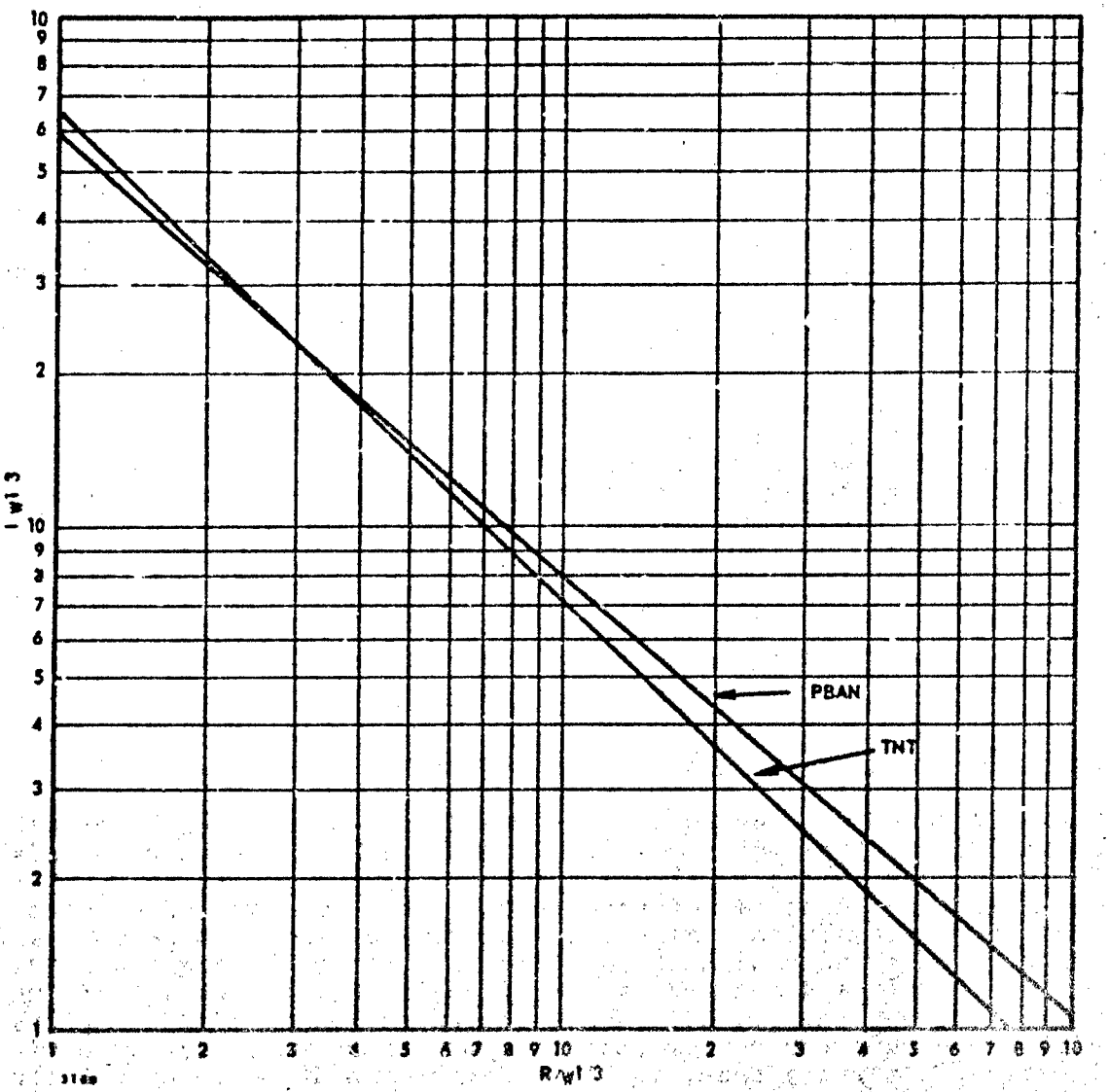


Figure 71. Comparison of TNT Impulse with Best Fit of the Pooled Propellant Data.

The equation for the go's explained 56% of the total variation in the data, whereas the equation for the no go's explained 78% of the total variation.

The standard error of estimate in terms of ln $(I/W^{1/3})$ is 0.46 for both fits. The estimated standard deviation for the intercept coefficients is 0.20, and the estimated standard deviation for the slope coefficients is 0.066. The two intercepts differ by more than 2.7 standard deviations and the two slopes by more than 3.5 standard deviations. Therefore it is concluded that the two estimated curves are statistically different. These curves along with the TNT curve are shown in Figure 72.

Percent TNT impulse-equivalents for RDX-PBAN adulterated propellants were calculated for each fit -- go's and no go's, pooled go's only, and no go's only -- at various ranges and for various weights. These results are shown in Table XLVIII. These values vary substantially both with range and weight. The average values over these ranges and weights for each fit are 125, 138, and 114% respectively. On this basis, the go tests indicate higher impulse than the no go tests even though for some range/weight combinations the no go tests produce higher impulses than the go tests.

Defining terminal yield as the average of the TNT equivalences, based on peak overpressure and on impulse over the ranges that these tests included, the terminal yield of detonating adulterated and unadulterated propellant is 168%. The terminal yield for the nondetonating propellant is 156% remembering that the nature of these tests biases these data because all samples are nearly critical and those that failed to detonate still contributed most of their energy to the fading detonation. Much smaller samples certainly would have correspondingly lower TNT equivalents and terminal yields.

## ANALYSIS OF FIREBALL DATA

Fireball data were recorded and reduced from a total of 16 of the larger critical-diameter tests. Fireball-history plots were made for each test, using a Cal-Comp plotter. These graphs showed both the height and diameter of the fireball as a function of elapsed time after detonation. Fireball diameter was taken to be the maximum horizontal dimension of the fireball; fireball height was the maximum vertical dimension of the fireball, not the height of the fireball above the ground. While the exact shapes of these plots differed considerably from test to test there were certain similarities. In every case, both the height and diameter of the fireball

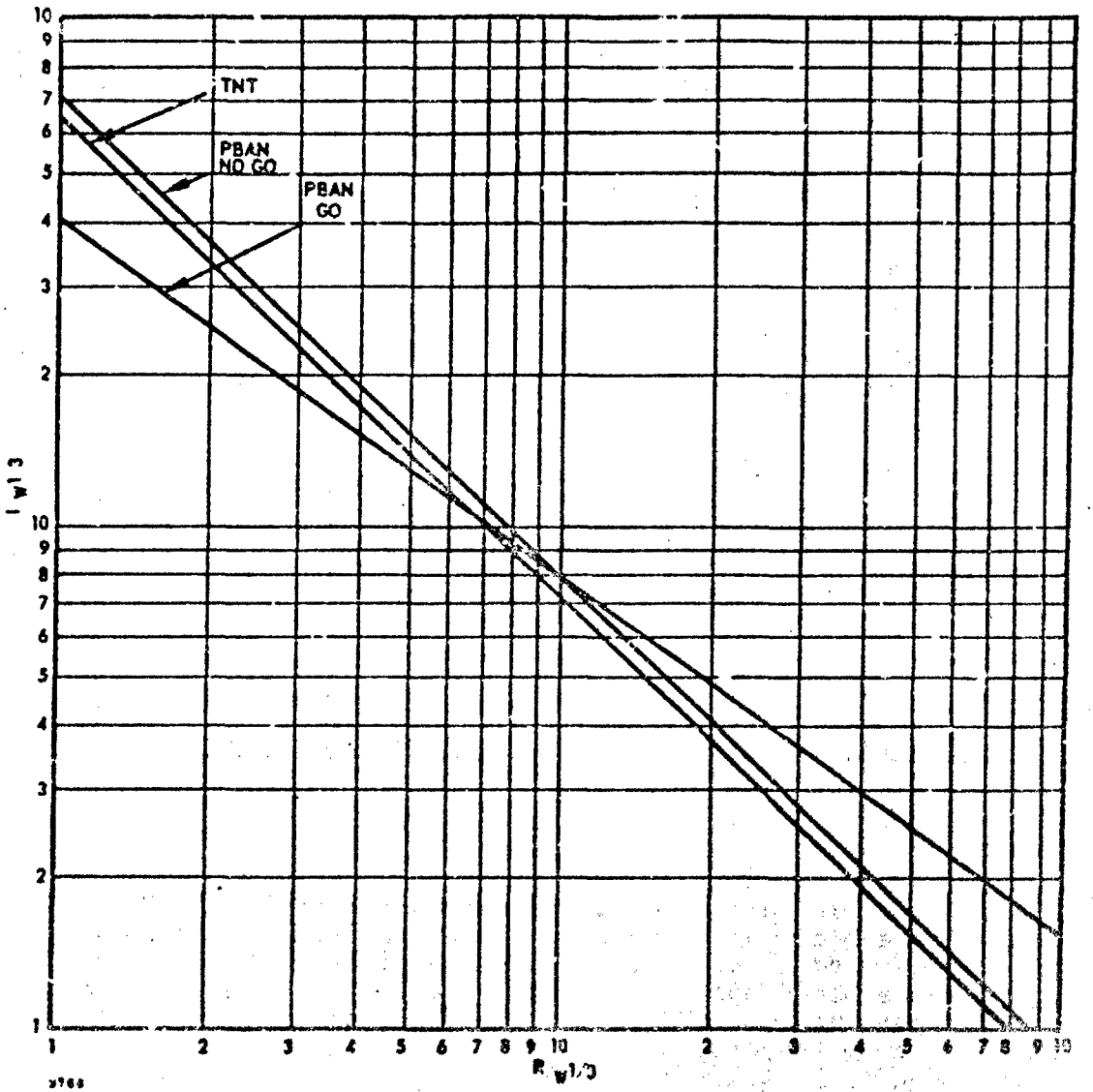


Figure 72. Comparison of TNT Impulse with Best Fits of Propellant Go and No Go Data.

Table XLVIII. Percent TNT Impulse Equivalences for RDX-Adulterated PBAN Propellants.*

| Range (ft) | Weight (lb) | | | | | |
|---|---|---|---|---|---|---|
| | 2,500 | 5,000 | 10,000 | 25,000 | 50,000 | 75,000 |
| 50 | 105 | 102 | 99 | 95 | 92 | 90 |
| | 79 | 73 | 67 | 60 | 55 | 52 |
| | 113 | 113 | 113 | 113 | 113 | 113 |
| 100 | 115 | 111 | 108 | 104 | 101 | 99 |
| | 102 | 94 | 86 | 77 | 71 | 68 |
| | 114 | 113 | 113 | 113 | 113 | 113 |
| 250 | 130 | 126 | 122 | 117 | 114 | 117 |
| | 143 | 131 | 121 | 108 | 99 | 94 |
| | 114 | 114 | 114 | 114 | 114 | 113 |
| 500 | 142 | 138 | 134 | 128 | 125 | 122 |
| | 184 | 169 | 155 | 139 | 128 | 122 |
| | 114 | 114 | 114 | 114 | 114 | 114 |
| 1000 | 156 | 151 | 146 | 141 | 136 | 134 |
| | 237 | 218 | 200 | 179 | 164 | 157 |
| | 114 | 114 | 114 | 114 | 114 | 114 |
| 1500 | 164 | 159 | 154 | 148 | 144 | 141 |
| | 274 | 252 | 232 | 207 | 191 | 181 |
| | 114 | 114 | 114 | 114 | 114 | 114 |

*The upper value in each cell represents the percent TNT impulse equivalence based upon the fit of the combined go and no go data. The middle value represents the percent TNT impulse equivalence based upon the fit of go data only; and the lower value represents the TNT impulse equivalence based upon the fit to the no go data.

increased rapidly to a maximum value, or plateau. However, the fireball-decay pattern differed markedly from test to test. It was decided to characterize the fireball size and rate of growth by five parameters. These were

a. Maximum fireball height

b. Maximum fireball diameter

c. Time to maximum height

d. Time to maximum diameter

e. Total duration of the fireball

The summary values for the 16 tests are presented in Table XLVIX. This table also shows the test result (go or no go), sample diameter, weight fraction RDX, and total sample weight (propellant weight plus booster weight) for each test. Total sample weight had to be used since it was impossible to isolate that portion of the fireball due to the propellant from that due to the TNT. Plots of each of these summary parameters, as a function of sample diameter, are shown in Figures 73 through 77. With the exception of time to maximum diameter (Figure 76) a strong linear relationship with sample diameter is indicated for each parameter. For this parameter, however, there appear to be three outlier observations: Test No. CD-81 (350 msec time for an 18-in. diameter sample); Test No. CD-85 (500 msec time for a 23.5-in. diameter sample); and Test No. CD-88 (750 msec time for a 44-in. diameter sample). The latter two tests were no go's. If these three tests are ignored, there is a significant linear association with diameter. Omitting these test values to time-to-maximum-diameter, but using all data for the other parameters, correlation coefficients were calculated between each of the various independent and dependent variables. These coefficients are shown in Table L with the starred values indicating those correlations which are statistically significant.

All correlations with respect to total weight were conducted using the transformed variable as almost totally redundant with diameter. The most important conclusion to be drawn from the coefficients is that there is no effect of test result (go or no go) upon the fireball parameters. This may be explained by the fact that in each test approximately 1/5 of the total sample weight was composed of TNT, and even in the cases of no go's the major portion of the propellant was involved in a fading detonation, contributing to the fireball as the detonation wave attenuated.

Table XLVIX. Fireball Data.

| Test Number | Test Result | Diameter (in.) | Weight Fraction RDX | Total Sample Weight (lb) | Maximum Fireball Height (ft) | Maximum Fireball Diameter (ft) | Time to Maximum Height (msec) | Time To Maximum Diameter (msec) | Total Fireball Duration (msec) |
|---|---|---|---|---|---|---|---|---|---|
| CD-79 | No go | 11 | 0.0475 | 353 | 48 | 85 | 300 | 50 | 950 |
| CD-80 | Go | 12 | 0.0475 | 467 | 50 | 93 | 300 | 50 | 1200 |
| CD-81 | Go | 18 | 0.034 | 1,531 | 75 | 160 | 400 | 350 | 2000 |
| CD-82 | Go | 24 | 0.029 | 3,545 | 85 | 185 | 450 | 75 | 1250 |
| CD-83 | Go | 27 | 0.034 | 4,951 | 100 | 225 | 850 | 95 | 2400 |
| CD-84 | Go | 24 | 0.034 | 3,558 | 100 | 195 | 600 | 80 | 1800 |
| CD-85 | No go | 23.5 | 0.018 | 3,903 | 120 | 190 | 750 | 500 | 3400 |
| CD-86 | Go | 23.5 | 0.024 | 3,909 | 125 | 212 | 750 | 75 | 2700 |
| CD-88 | No go | 44 | 0.00 | 18,715 | 210 | 300 | 1000 | 750 | 2900 |
| CD-89 | Go | 48 | 0.0073 | 27,704 | 150 | 380 | 750 | 112 | 2250 |
| CD-90 | Go | 48 | 0.0050 | 27,834 | 200 | 380 | 1000 | 112 | 2500 |
| CD-91 | No go | 11 | 0.0175 | 353 | 60 | 95 | 350 | 75 | 1170 |
| CD-92 | No go | 48 | 0.0025 | 27,846 | 218 | 330 | 1400 | 250 | 4300 |
| CD-93 | Go | 13 | 0.06 | 580 | 48 | 116 | 420 | 40 | 1500 |
| CD-96 | Go | 72 | 0.00 | 92,000 | 325 | 480 | 1500 | 250 | 4300 |
| CD-98 | No go | 60 | 0.00 | 53,500 | 300 | 400 | 1500 | 370 | 4250 |

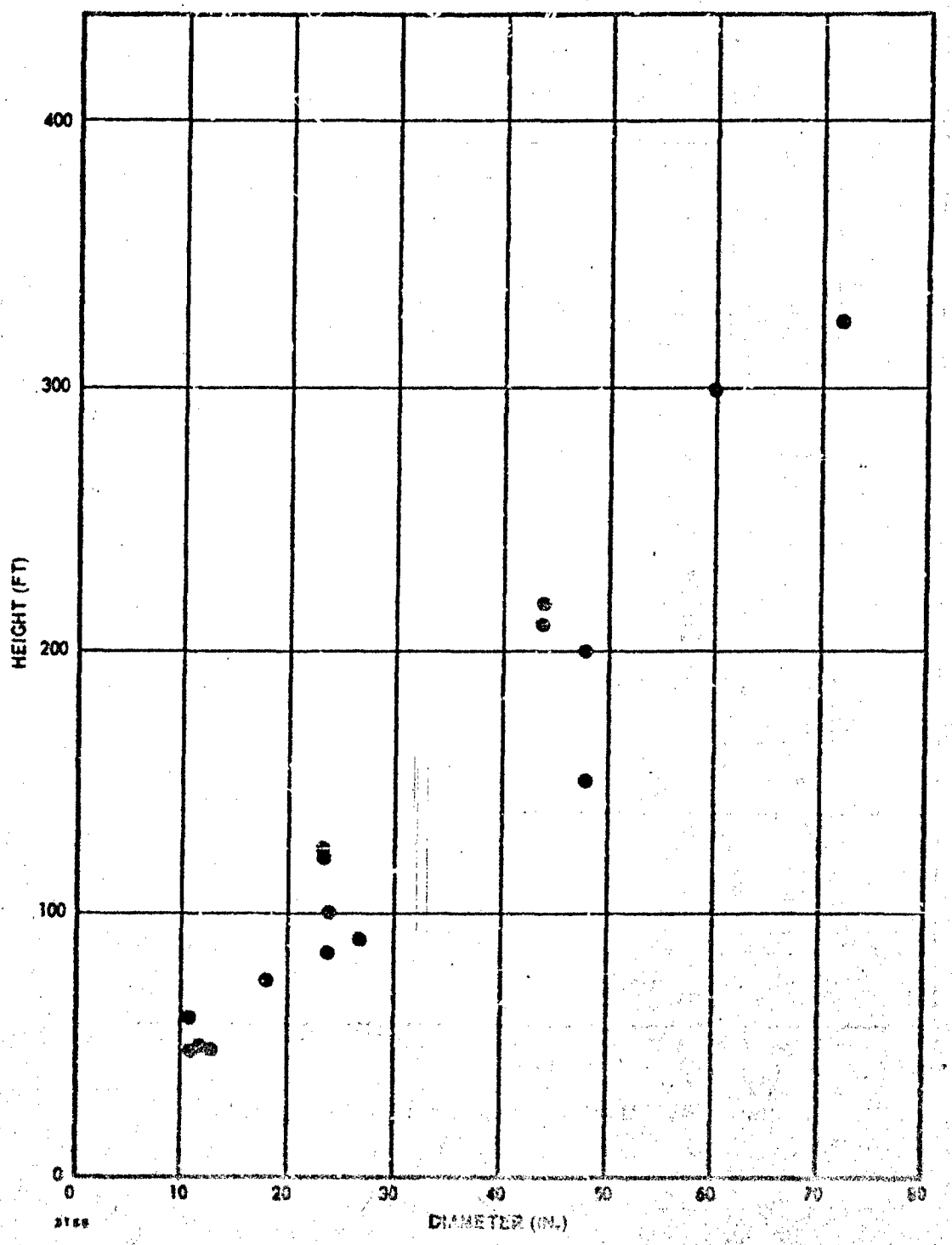


Figure 73. Maximum Height of Fireball.

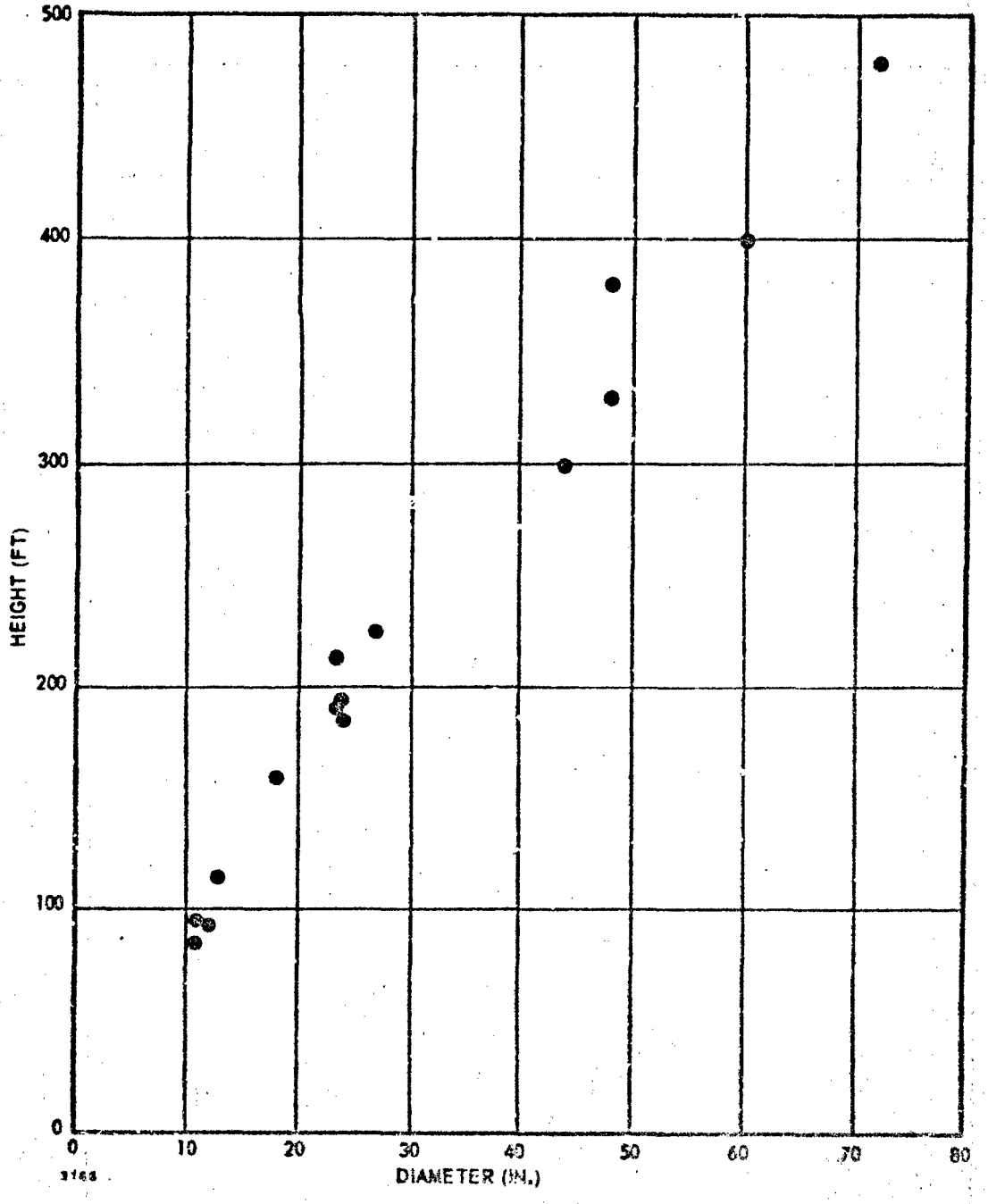


Figure 74. Maximum Diameter of Fireball.

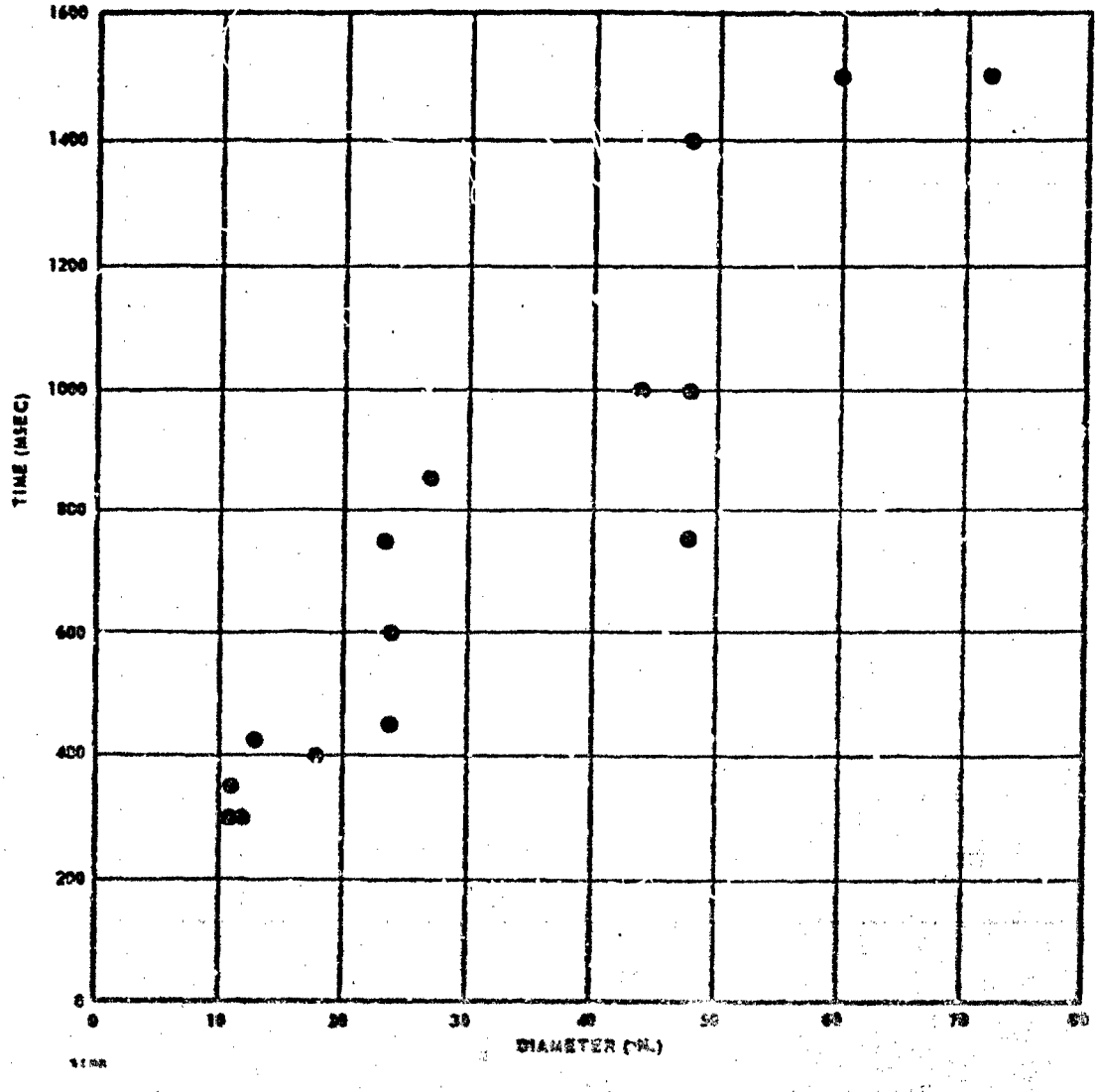


Figure 75. Time to Maximum Height.

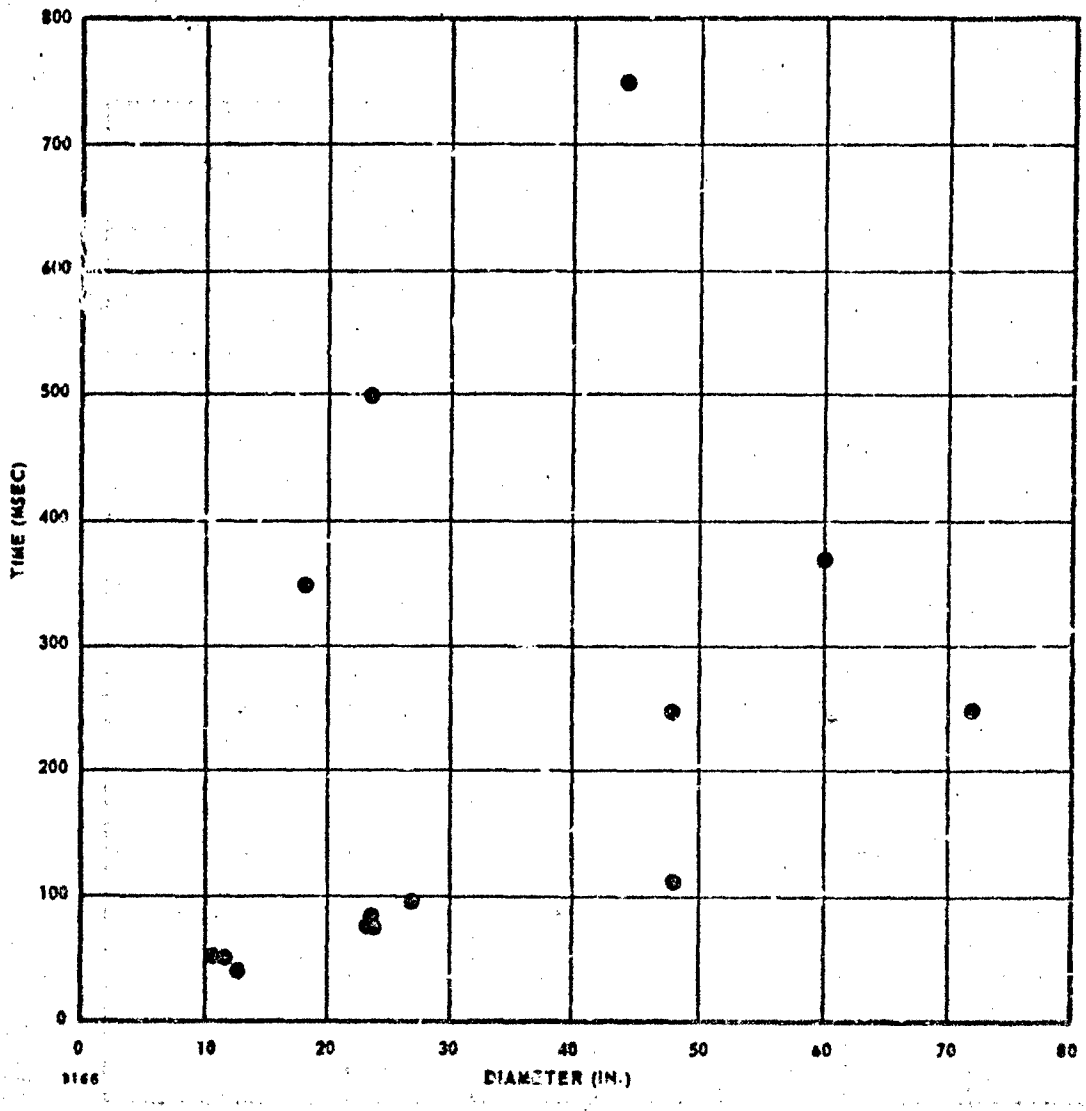


Figure 76. Time to Maximum Diameter.

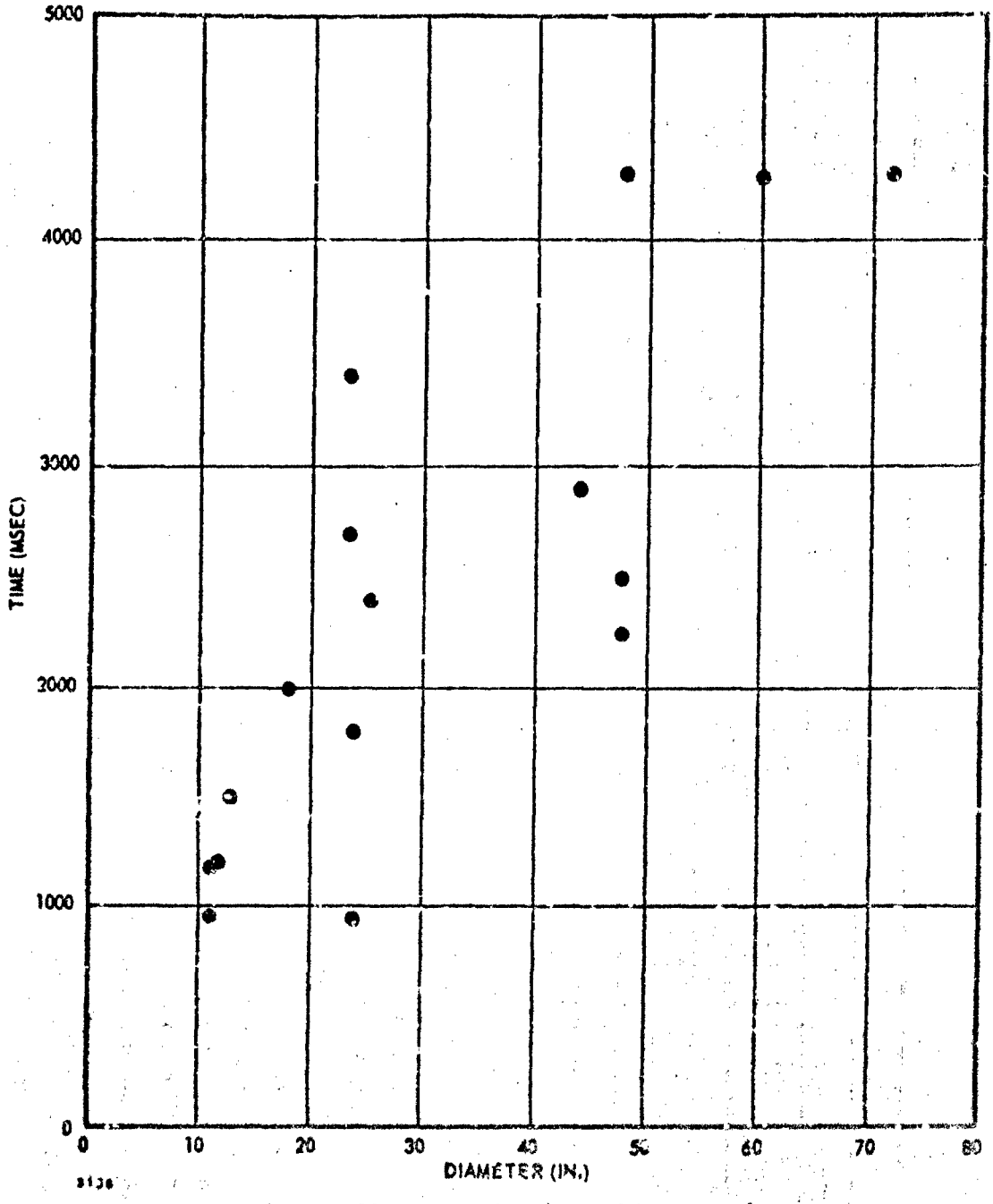


Figure 77. Total Fireball Duration.

Table L. Correlation Coefficients, Fireball Data.

| Variable | 1 | 2 | 3 | 4 | 5 | 6 | 7 | 8 | 9 |
|---|---|---|---|---|---|---|---|---|---|
| 1 | 1.0 | -0.836* | 0.996* | -0.052 | 0.967* | 0.987* | 0.925* | 0.834* | 0.824* |
| 2 | | 1.0 | -0.824 | 0.342 | -0.848* | -0.834* | -0.799* | 0.754* | -0.752* |
| 3 | | | 1.0 | -0.027 | 0.961* | 0.988* | 0.926* | 0.834* | 0.831* |
| 4 | | | | 1.0 | -0.195 | 0.037 | -0.218 | -0.419 | -0.278 |
| 5 | | | | | 1.0 | 0.931* | 0.955* | 0.905* | 0.884* |
| 6 | | | | | | 1.0 | 0.897* | 0.763* | 0.797* |
| 7 | | | | | | | 1.0 | 0.912* | 0.945* |
| 8 | | | | | | | | 1.0 | 0.900* |
| 9 | | | | | | | | | 1.0 |

Variable

*Indicates significance at the 5% level.

Variable
1 - Diameter (in.)
2 - Weight fraction RDX
3 - Total weight of sample to 1/3 power (lb)
4 - Test result dummy variable: 0 for no go; 1 for go
5 - Maximum fireball height (ft)
6 - Maximum fireball diameter (ft)
7 - Time to maximum height (msec)
8 - Time to maximum diameter (msec)
9 - Total duration of fireball (msec)

Linear equations for predicting the fireball parameters as a function of either diameter or total weight to the 1/3 power were calculated. The coefficients for these equations are given in Table LI. These equations are of the form

$$Y = A_o + A_1 X \qquad (118)$$

where Y is the fireball parameter in the units designated and X is the independent variable, either diameter or total weight of the 1/3 power. The coefficients of determination, $R^2$ (the proportion of the total variation explained by regression), are also given for each fit.

Table LI. Coefficients of Fireball Equation.

| Independent Variable - Diameter | | | |
|---|---|---|---|
| Dependent Variable | $A_o$ | $A_1$ | $R^2$ |
| Maximum Height (ft) | -4.93 | 4.503 | 0.935 |
| Maximum Diameter (ft) | 35.09 | 6.439 | 0.974 |
| Time to Maximum Height (msec) | 130.408 | 20.184 | 0.856 |
| Time to Maximum Diameter (msec) | -6.866 | 4.088 | 0.696 |
| Total Duration (msec) | 857.08 | 49.619 | 0.679 |
| Independent Variable - $(\text{Weight})^{1/3}$ | | | |
| Dependent Variable | $A_o$ | $A_1$ | $R^2$ |
| Maximum Height (ft) | -6.937 | 7.270 | 0.924 |
| Maximum Diameter (ft) | 30.824 | 10.466 | 0.976 |
| Time to Maximum Height (msec) | 117.165 | 32.801 | 0.857 |
| Time to Maximum Diameter (msec) | -8.873 | 6.546 | 0.694 |
| Total Duration (msec) | 810.150 | 81.356 | 0.692 |

Figure 78 shows a plot of the fireball size history for Test CD-98 (60-in. diameter, 0.0% RDX, total weight 53,500 lb). Superimposed on this graph are the estimates of the fireball parameters predicted from the equations using diameter as the independent variable. The predicted values fall very close to their corresponding measured values. Tables LII and LIII present tabular evaluations of these equations for various diameters and total weights, respectively. Both of these tables extrapolate the fireball parameters to diameters and total weights much greater than the values tested during the SOPHY program. In the case of diameter as the dependent variable the extrapolations go out to as much as twice the maximum diameter tested; in the case of total weight as the dependent variable they extend to over five times the total weight tested.

## CONCLUSIONS

The data have shown that, regardless of whether the sample detonates or not, the peak overpressure correlates with the propellant weight and range. Similarly, the fireball size correlates with the total weight (booster plus acceptor) and range and is independent of the test result. These correlations are only applicable either to propellant sample sizes that are near the critical diameter or to tests in which the applied shock pressure and shock wave area are not far below the minimum required to initiate detonation. Under such conditions, the propellant is involved either in a fading detonation that proceeds through most of the sample or in a steady-state detonation that continues through the entire sample. Only if the test conditions are such that even in those tests in which the sample fails to sustain detonation most of the propellant is involved in a fading-detonation reaction, can statistically insignificant differences between the relative outputs of the go's and the no go's be expected.

Under weaker conditions, i.e., when the sample diameter is more subcritical or when the applied shock pressure and/or shock wave size are farther below the minimum level required to initiate detonation, the fraction of the total propellant weight that is involved in the fading detonation diminishes. The peak overpressures produced, when related to the total propellant weight, will yield lower apparent TNT equivalences because part of that weight is of material that does not participate in the fading-detonation reaction. The fireball data should behave similarly. Therefore, to predict blast and fireball output under a specific set of test conditions requires, in addition to knowledge of the critical geometry and the initiation criterion, an understanding of fading detonation reactions, so that the weight of propellant that is expected to react can be estimated. Then Figure 70 and Table XLVIII could be used to predict the output for any propellant composition similar to ANB-3226.

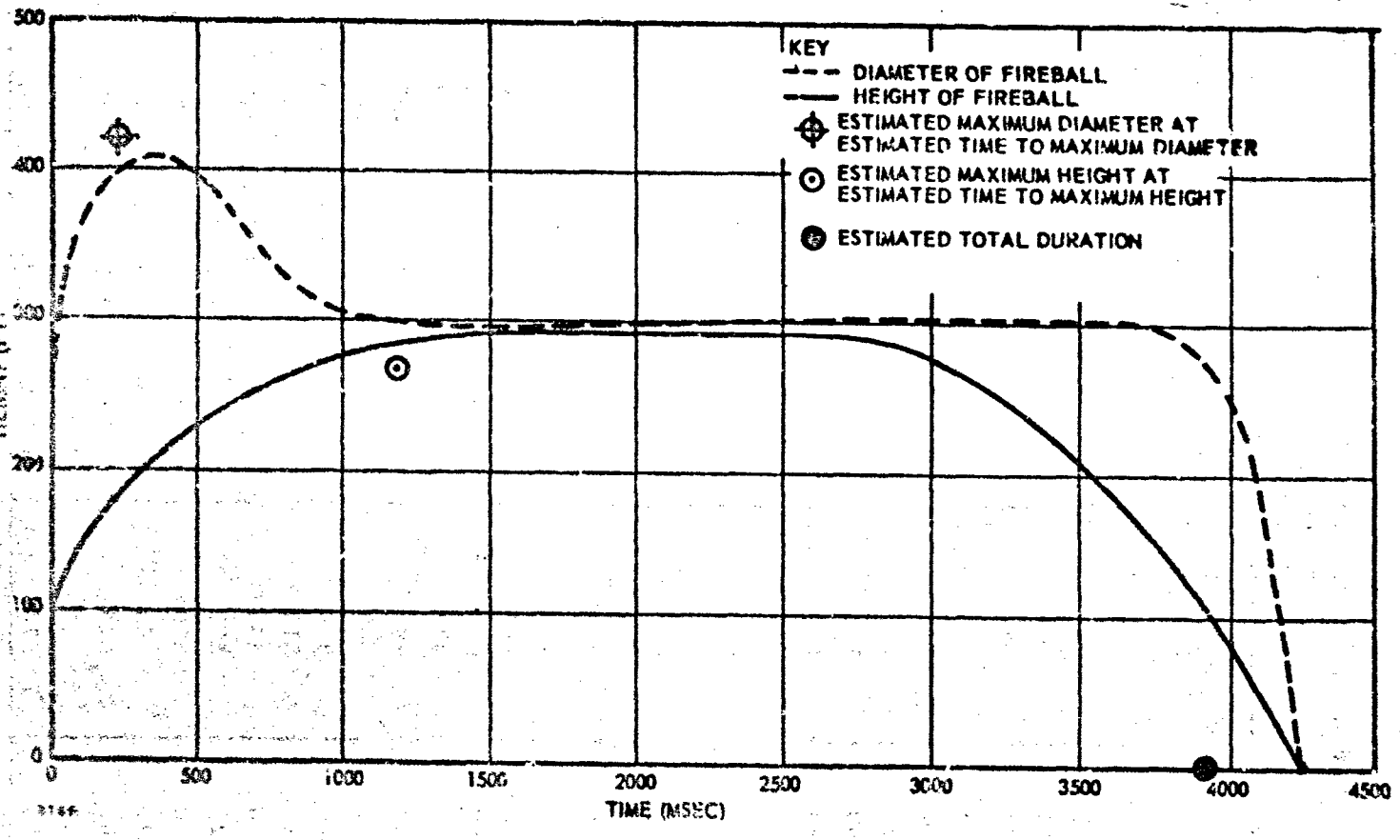


Figure 78. Fireball Size History (Measured vs Predicted), Test CD-98.

Table LII. Estimates of Fireball Characteristics as a Function of Diameter.

| Diameter (in.) | Maximum Height of Fireball (ft) | Maximum Diameter of Fireball (ft) | Time to Maximum Height (msec) | Time To Maximum Diameter (msec) | Total Duration (msec) |
|---|---|---|---|---|---|
| 5 | 18 | 67 | 231 | 14 | 1105 |
| 10 | 40 | 99 | 332 | 34 | 1353 |
| 15 | 63 | 132 | 433 | 54 | 1601 |
| 20 | 85 | 164 | 534 | 75 | 1849 |
| 25 | 108 | 196 | 635 | 95 | 2098 |
| 30 | 130 | 228 | 736 | 116 | 2346 |
| 35 | 153 | 260 | 837 | 136 | 2594 |
| 40 | 175 | 293 | 938 | 157 | 2842 |
| 45 | 198 | 325 | 1039 | 177 | 3090 |
| 50 | 220 | 357 | 1140 | 198 | 3338 |
| 55 | 243 | 389 | 1241 | 218 | 3586 |
| 60 | 265 | 421 | 1341 | 238 | 3834 |
| 65 | 288 | 454 | 1442 | 259 | 4082 |
| 70 | 310 | 486 | 1543 | 279 | 4330 |
| 75 | 333 | 518 | 1644 | 300 | 4578 |
| 80 | 355 | 550 | 1745 | 320 | 4827 |
| 85 | 378 | 582 | 1846 | 341 | 5075 |
| 90 | 400 | 614 | 1947 | 361 | 5323 |
| 95 | 423 | 647 | 2048 | 382 | 5571 |
| 100 | 445 | 679 | 2149 | 402 | 5819 |
| 105 | 468 | 711 | 2250 | 422 | 6067 |
| 110 | 490 | 743 | 2351 | 443 | 6315 |
| 115 | 513 | 775 | 2452 | 463 | 6563 |
| 120 | 535 | 808 | 2553 | 484 | 6811 |
| 125 | 558 | 840 | 2653 | 504 | 7059 |
| 130 | 580 | 872 | 2754 | 525 | 7308 |
| 135 | 603 | 904 | 2855 | 545 | 7556 |
| 140 | 625 | 936 | 2956 | 566 | 7804 |
| 145 | 648 | 969 | 3057 | 586 | 8052 |
| 150 | 670 | 1001 | 3158 | 606 | 8300 |

Table LIII. Estimates of Fireball Characteristics as a Function of Weight.

| Weight ($lb \times 10^3$) | Maximum Height of Fireball (ft) | Maximum Diameter of Fireball (ft) | Time To Maximum Height (msec) | Time To Maximum Diameter (msec) | Total Duration (msec) |
|---|---|---|---|---|---|
| 10 | 150 | 256 | 824 | 132 | 2562 |
| 20 | 190 | 315 | 1007 | 169 | 3018 |
| 30 | 219 | 356 | 1136 | 194 | 3338 |
| 40 | 242 | 389 | 1239 | 215 | 3592 |
| 50 | 261 | 416 | 1326 | 232 | 3807 |
| 60 | 278 | 440 | 1401 | 247 | 3995 |
| 70 | 293 | 462 | 1469 | 261 | 4163 |
| 80 | 306 | 482 | 1530 | 273 | 4316 |
| 90 | 319 | 500 | 1587 | 284 | 4456 |
| 100 | 330 | 517 | 1640 | 295 | 4586 |
| 125 | 356 | 554 | 1757 | 318 | 4878 |
| 150 | 379 | 587 | 1860 | 339 | 5032 |
| 175 | 400 | 616 | 1952 | 357 | 5361 |
| 200 | 418 | 643 | 2036 | 374 | 5568 |
| 225 | 435 | 667 | 2112 | 389 | 5758 |
| 250 | 451 | 690 | 2183 | 403 | 5935 |
| 275 | 466 | 711 | 2250 | 417 | 6101 |
| 300 | 480 | 731 | 2313 | 429 | 6256 |
| 325 | 493 | 750 | 2372 | 441 | 6403 |
| 350 | 505 | 768 | 2429 | 452 | 6544 |
| 375 | 517 | 785 | 2482 | 463 | 6677 |
| 400 | 529 | 802 | 2534 | 475 | 6804 |
| 425 | 540 | 818 | 2583 | 483 | 6927 |
| 450 | 550 | 833 | 2631 | 493 | 7044 |
| 475 | 560 | 847 | 2676 | 502 | 7158 |
| 500 | 570 | 861 | 2720 | 511 | 7267 |

The impulse data showed significant statistical difference between the correlations with respect to the propellant reaction. The no go's produced impulse-range data that were uniformly equivalent to 114% TNT over the entire region (Figure 72). The correlation of the go data shows that the propellant is equivalent to less than 100% TNT at close range, but that the TNT equivalence increases, becoming greater than 100% at long range. The differences between the detonation reactions of TNT and composite propellant should account for the behavior of the impulse data generated by detonating propellant. The complex kinetics that characterize propellant detonation reactions produce a blast wave profile different from that generated by TNT. In the latter material, the principal reaction is simply the decomposition of trinitrotoluene, whereas in propellant the reactions include ammonium perchlorate decomposition and subsequent oxidation of the aluminized fuel. The aluminum oxidation reaction is particularly slow compared to all the other reactions. Consequently, one expects that the blast wave attenuation in terms of impulse should differ for these two materials.

This difference is indicated by the line for the propellant go data in Figure 72, which has a slope greater than that for TNT, so that

$$\left(\frac{d \ln I}{d \ln R}\right)_P > \left(\frac{d \ln I}{d \ln R}\right)_T \tag{119}$$

where the subscripts P and T refer to propellant and TNT. The rate of attenuation of impulse with range, for a specified weight of either TNT or propellant, is -(dI/dR), which may be evaluated at any R by Equations 113 or 116, and 120:

$$-\frac{dI}{dR} = -\frac{I}{R}\frac{d \ln I}{d \ln R} \tag{120}$$

It is obvious by Equation 120 that at ranges greater than that at which the TNT and propellant lines intersect,

$$\left(-\frac{dI}{dR}\right)_P < \left(-\frac{dI}{dR}\right)_T \tag{121}$$

since over that region, at any R,

$$I_P > I_T \tag{122}$$

Equation 121 holds for smaller ranges as well, the shortest range being determined by finding the range at which $I_P$ and $I_T$ satisfy Equation 123:

$$I_P = I_T \frac{\left(\frac{d \ln I}{d \ln R}\right)_T}{\left(\frac{d \ln I}{d \ln R}\right)_P} \qquad (123)$$

The use of Figures 70 and 72 and Table LI to predict the blast and fireball characteristics of a propellant detonation must be restricted to propellant formulations similar to ANB-3226, specifically with respect to the weight fractions of total oxidizer (69%) and aluminum (15%). No data have been acquired in SOPHY regarding the effects of the constituents on the blast and fireball parameters, since all formulations tested contained these specific weight fractions of total oxidizer and aluminum. It is reasonable to expect that each of these ingredients is influential in determining the blast and fireball parameters, but there has been no attempt made to obtain information regarding these relationships. Such an investigation obviously would be extremely valuable to the SOPHY purpose. However, ANB-3226 is a representative formulation, and many other composite formulations contain approximately the same weight fractions of oxidizer and aluminum, so that the estimates that could be made from the present data should be relatively accurate.

Equation 121 holds for smaller ranges as well, the shortest range being determined by finding the range at which $I_P$ and $I_T$ satisfy Equation 123:

$$I_P = I_T \frac{\left(\frac{d \ln I}{d \ln R}\right)_T}{\left(\frac{d \ln I}{d \ln R}\right)_P} \qquad (123)$$

The use of Figures 70 and 72 and Table LI to predict the blast and fireball characteristics of a propellant detonation must be restricted to propellant formulations similar to ANB-3226, specifically with respect to the weight fractions of total oxidizer (69%) and aluminum (15%). No data have been acquired in SOPHY regarding the effects of the constituents on the blast and fireball parameters, since all formulations tested contained these specific weight fractions of total oxidizer and aluminum. It is reasonable to expect that each of these ingredients is influential in determining the blast and fireball parameters, but there has been no attempt made to obtain information regarding these relationships. Such an investigation obviously would be extremely valuable to the SOPHY purpose. However, ANB-3226 is a representative formulation, and many other composite formulations contain approximately the same weight fractions of oxidizer and aluminum, so that the estimates that could be made from the present data should be relatively accurate.

[illegible]

# SECTION XII

# CONCLUSIONS AND RECOMMENDATIONS

## SUSTAINMENT OF DETONATION

The ability of solid composite propellant cast in a large rocket motor to sustain detonation has been established by the results of the critical diameter and critical geometry tasks. In the former, a theoretical and experimental technique developed in SOPHY I was proven to be capable of accurately predicting the critical diameter of a composite propellant. During the SOPHY II program the theoretical model for detonation was generalized and the validity of its basic theoretical assumption regarding the relationship between diameter and detonation velocity was proven by experimental studies. In the critical geometry task, a simple relationship between critical diameter and the critical dimensions of any shape was tested intensively for several shapes. The critical geometry theory was successfully applied to an adulterated propellant of larger critical diameter than that of the material with which it had been developed. The results of tests with hollow-core samples required the adoption of special criteria to interpret the behavior of these grains to shock stimuli, but this concept of pseudocriticality may be extraneous to the discussion of rocket motor detonability. Because of the large core and finite length of such grains and the probability that a particular rocket motor will rarely be of exactly critical proportions, the need to modify the original concept of detonability should not arise.

To summarize the conclusions of the SOPHY II program regarding the ability of composite propellant ANB-3226 to sustain detonation, the critical diameter of this propellant was found to be greater than 60 in. and less than 72 in. The critical geometry theory predicts that the critical dimensions for this propellant, in any shape, will be given by

$$55 \text{ in.} \leq \left(\frac{4A}{P}\right)_c \leq 66 \text{ in.} \qquad (124)$$

so that a circular-core grain would be of supercritical size if its web thickness were greater than 27 to 33 in. There are several rocket motors presently in operation or in development that exceed this web-thickness range.

It is recommended that the techniques developed in SOPHY for estimating the critical diameter be applied to other composite propellants, both to estimate their critical diameter and to gain experimental knowledge about the effect of propellant composition on the critical diameter. With the knowledge of the effect of propellant composition on its critical diameter, new formulations might be tailored to meet specific objectives regarding detonability. Aside from assisting in the design of new formulations, such information would facilitate prediction of the critical diameter of any propellant before any tests had been conducted. The only experimental study necessary to confirm the prediction would be the determination of the critical diameter of one adulterated form of the parent formulation.

## INITIATION OF DETONATION

Various suggestions were made at the conclusion of Section VI regarding the initiation criterion theory. Those conclusions deserve repetition because frequently their importance is overlooked.

The fact that ANB-3226 propellant sustained detonation in the 72-in. diameter test does not signify that 18,000 lb of TNT is required to initiate detonation of composite propellant merely because that amount was used to booster the sample. In the critical-diameter task it was necessary to overbooster each sample so that if it were of supercritical size it would sustain detonation. The size of the booster in those tests has no bearing on the sensitivity of the material.

The sensitivity of propellant to initiation of detonation is defined in SOPHY by the initiation criterion theory, which postulates that the initiation criterion for any detonable material is a function of the minimum shock pressure, minimum shock wave area, and minimum pulse width necessary to initiate detonation.

The tests conducted in SOPHY II have shown that within the limitations of the data and the test conditions the theory is valid. The initiation criterion has been determined by card-gap tests in terms of minimum pressure and area. The evaluation of the criterion offers conclusive evidence for its validity. Beyond that, it suggests that either the pulse width of a shock wave entering propellant from a PMMA attenuator is not significantly different from that entering from a high explosive charge, or the effect of these two pulse widths on the minimum pressure required for initiation is negligible, because pressures delivered under both conditions were consistent in their effect on the propellant.

From the initiation criteria (pressure-area) of three adulterated propellant formulations, the initiation criterion for ANB-3226 was estimated. The minimum shock pressure estimated to be necessary to initiate detonation of an ideal diameter solid circular-cylindrical charge of this propellant is 8 to 10 kbar. The shock pressure required for a sample of near-critical diameter is estimated to be less than 29 kbar. This is the maximum shock pressure on the initiation criterion for ANB-3226. Its exact value could not be estimated accurately from the available data.

The importance of understanding the pulse-width effect is illustrated in the data obtained from near-ideal samples. The extreme case in point is the 42-in. diameter card-gap test of AAB-3267. If the shock wave pulse width increases with distance travelled through PMMA, the pulse delivered to the 42-in. diameter propellant sample was much longer than that delivered to much smaller samples. The minimum pressure required in a wave that has a large pulse width should be less than that required in a thinner wave. Consequently, the pressure values used to estimate the minimum shock pressure required to initiate ideal diameter samples of ANB-3226 may be biased. The pulse width studies conducted in this program, while extremely limited, do indicate that beyond a certain pulse width the minimum pressure required remains constant, so that the bias in the case of the 42-in. sample may not be large at all.

The initiation criterion has been tested only for solid samples, symmetrically initiated on their end surface. Under these conditions the theory has not been found in error. The data from rectangular acceptors were of limited usefulness since those samples that failed to detonate also failed to provide intelligible data.

It is recommended that in order to obtain a better estimate of the initiation criterion for ANB-3226, further tests be conducted near the critical diameter of several adulterated propellants to determine the respective minimum initiating shock pressures, for extrapolation to unadulterated propellant. It is further recommended that the study of pulse width be continued beyond the SOPHY II program so that a better understanding of this vital parameter may be achieved. It is apparent that the initiation criterion must be established in terms of all three variables, and that until this is accomplished the application of the available initiation principles to tangible problems will not provide a completely accurate appraisal of the probability that initiation may occur.

Lastly, it is recommended that the validity of the initiation criterion be determined for those cases in which the shock wave is delivered at the side or off-centered at the end of samples. Admittedly a formidable challenge, such tests nevertheless must be performed on both solid and perforated shapes. The solid rocket motor on a launch pad is more likely to be shocked from the side or obliquely than from one end, and information must be available for estimating the propellant reaction under such loading conditions.

## PROPELLANT WITH DEFECTS

The SOPHY study is concerned equally with detonation hazards and thermal explosion hazards of composite propellant. It also recognizes that propellant may be physically modified by shock, impact, and thermal stresses, and that its reaction to subsequent shock or ignition will be greatly affected by the modification it has undergone.

Attempts to manufacture and characterize porous and cracked propellant are necessary for a scientific investigation of modified-propellant response. Considerable progress in this area has been reported in Sections VIII and IX. Before any further development of technology in creating such propellant is attempted, it is recommended that an experimental program be developed to study the effect of weak shock waves, low- and high-velocity impact, and exposure to high thermal energy upon the physical integrity of solid propellant. With such information in hand, the test design and the defect requirements will be defined more easily.

## BLAST AND FIREBALL

The blast and fireball data obtained from 22 tests, some resulting in detonation, others not, have been correlated on the basis of sample weight. The blast data (peak overpressure and positive-phase impulse) were correlated with propellant weight; the fireball data, with total weight of booster plus propellant. From these correlations it is possible to predict the following, knowing the weight of propellant involved: (1) peak overpressure vs range, (2) positive-phase impulse vs range, (3) maximum diameter of fireball, (4) maximum height of fireball, and (5) duration of fireball.

All the blast and fireball data were generated by samples that were nearly critical or supercritical. Care must be exercised in using the correlations, because they only apply to samples that meet these conditions. Very subcritical samples cannot be expected to produce equivalent data.

## REFERENCES


1. Large Solid Propellant Boosters Explosive Hazards Study Program (Project SOPHY), Technical Documentary Report No. AFRPL-TR-65-211, Aerojet-General Report No. 0866-01(01)FP (24 November 1965).

2. Apin, A. Ya., and L. N. Stesik, "Mechanism of the Chemical Reaction in the Detonation of Solid Explosives," Z. prik. mekh. tekh. fiz., No. 2, pp 146-149 (1965).

3. Levine, H. B., and R. E. Sharples, "Operator's Manual for RUBY," UCRL 6815 (20 March 1962).

4. Evans, M. W., B. O. Reese, L. B. Seely, and E. L. Lee, "Shock Initiation of Low-Density Pressings of Ammonium Perchlorate," The Fourth Symposium on Detonation (Preprints, Vol. II), U.S. Naval Ordnance Laboratory, White Oak, Silver Springs, Md., pp C-78 through C-89 (12-15 October 1965).

5. Calculations of Detonation Parameters with the RUBY Code, NOLTR 63-205 (31 March 1965).

6. Andersen, W. H., and R. E. Pesante, "Reaction Rate and Characteristics of Ammonium Perchlorate in Detonation," Eighth Symposium (International) on Combustion, The Williams and Wilkens Co., Baltimore, Md., pp 705-710 (1962).

7. Cook, M. A. , The Science of High Explosives, American Chemical Society Monograph Series, Reinhold Publishing Company, New York, N. Y., pp 144f. (1958).

8. Price, D., Large Scale Gap Tests: Interpretation of Results for Propellants, NOL-323, NAVWEPS 7401 (15 March 1961).

9. 22-Inch Critical-Diameter Tests of Minuteman Stage II, Wing VI, Propellant, Aerojet-General Corporation Final Report 0713-53-511, Contract AF04(694)258, CCN 28 (20 March 1964).

10. Correlation of Small and Large Diameter Card-Gap Sensitivity Tests, Aerojet-General Corporation Summary Report IWA 7641-25-313 (8 July 1963).

11. The Design and Analysis of Sensitivity Experiments, Rocketdyne Report R-6152 (May 1965).

12. Dixon, W. J., "Analysis of Extreme Values," Ann Math Stat, Vol. 21, 488-506 (1950).

13. Liddard, T. P., Jr., "The Compression of Polymethylmethacrylate by Low Amplitude Shock Waves," The Fourth Symposium on Detonation, Preprints Vol. I, 12-15 October 1965.

14. Analysis of Shock Attenuation for 0.5- and 2.0-Inch Diameter Card-Gap Sensitivity Tests, Aerojet-General Corporation Report SRP-289 (Special), January 1962.

15. Price, D., and I. Jaffe, "Large-Scale Gap Test: Interpretation of Results for Propellants," ARS Journ, Vol. 31, 595-599 (May 1961).

16. Buchanan, J. S., H. J. James, and G. W. Teague, Phil. Mag., Vol. 3, 1432 (1958).

17. Determination of Hugoniot Equation-of-State for Polymers and Re-entry Vehicle Materials and Investigations of Fracture Phenomena, Air Force Special Weapons Center, Kirtland AFB, New Mexico, TDR-62-66, Vol. I (August 1962).

18. Advanced Test Methods for Determining Operational Characteristics of Propellants, Air Reduction Company Report RPL-TDR-64-20 (June 1963).

19. "High-Speed Ideas," Beckman and Whitley, Inc. Applications Newsletter, Vol. II, No. 1 (1964).

20. Jaffe, I., R. L. Beauregard, and A. B. Amster, The Attenuation of Shock in Lucite, U.S. Naval Ordnance Laboratory, White Oak, Md., NAVORD Report 6876 (May 1960).

21. Jaffe, I., R. L. Beauregard, and A. B. Amster, ARS Journ., Vol. 32, 22-25 (1962).

22. Coleburn, N. L., "Sensitivity of Composite and Double-Base Propellants to Shock Waves," AIAA Journ., Vol. 4, No. 3, 521-525 (March 1966).

23. Gibson, F. C., M. L. Bowser, and C. M. Mason, "Method for the Study of Deflagration to Detonation Transition," Rev. Sci. Inst. Vol. 30, No. 10, 916-919 (October 1959).

24. Jaffe, I., D. Price, Progress Report on Adaption of Continuous Wire Method for Measuring Transient Phenomena, NOLTR-63-136. U.S. Naval Ordnance Laboratory, White Oak, Md. (7 June 1963).

25. Price, D., I. Jaffe, and J. P. Toscano, Development of the Continuous Wire Method, Progress Report II, NOLTR 66-21, U.S. Naval Ordnance Laboratory, White Oak, Md. (17 March 1966).

26. Kingery, C. N., and B. F. Pannill, Peak Overpressure vs Scaled Distances for TNT Surface Bursts (Hemispherical Charges), BRL Memorandum Report 1518, Ballistic Research Laboratories. (April 1964). AD 443 102.

27. Operation SNOW BALL Project Descriptions, Vol. I (U), DASA Data Center Special Report 24-1, DASA 1516-1. (1964) AD 441 974.